

## Section 3 Contents

3.	Scientific Basis for Predictive Model Development .....	3-1
3.1	Spent-Fuel Cladding Failure .....	3-2
3.1.1	Parameters for Failure Models .....	3-6
3.1.2	Failure Models .....	3-13
3.2	Spent-Fuel Oxidation .....	3-14
3.2.1	Experimental Parameters for Oxidation Models .....	3-16
3.2.2	Oxidation Models .....	3-36
3.2.2.1	Summary .....	3-36
3.2.2.2	Introduction .....	3-36
3.2.2.3	Oxidation Response of $\text{UO}_2$ to $\text{U}_4\text{O}_9$ .....	3-38
3.2.2.4	Oxidation Response of $\text{U}_4\text{O}_9$ to $\text{U}_3\text{O}_8$ .....	3-49
3.2.2.5	Comparison of Model Response to Oven Drybath Data .....	3-59
3.2.2.6	Model Predictions of Spent-Fuel Oxidation in a Constant 100°C Temperature Environment .....	3-63
3.2.2.7	Chemical and Physical Alteration of Spent Fuel .....	3-64
3.2.2.8	Oxidation Studies of Spent Fuel .....	3-66
3.2.2.9	Model Enhancements .....	3-69
3.2.2.10	Model Predictions of $\text{U}_4\text{O}_9 \rightarrow \text{U}_3\text{O}_8$ with TGA Experiments .....	3-70
3.2.2.11	Model Predictions of $\text{U}_4\text{O}_9 \rightarrow \text{U}_3\text{O}_8$ with Oven Drybath Experiments ...	3-80
3.2.2.12	Discussion of Modeling Comparisons with Experimental $\text{U}_4\text{O}_9 \rightarrow \text{U}_3\text{O}_8$ Histories .....	3-89
3.2.2.13	Environmental Impacts of Oxidation of $\text{UO}_2$ .....	3-89
3.2.2.14	References .....	3-92
3.3	Spent Fuel Fission Gas Release .....	3-94
3.3.1	Parameters for Fission Gas Release .....	3-95
3.3.2	Fission Gas Release Models .....	3-100
3.4	Spent Fuel Dissolution .....	3-103
3.4.1	Parameters for Dissolution .....	3-105
3.4.1.1	Dissolution Rates .....	3-108

3.4.1.2	Solubility Limits .....	3-115
3.4.1.3	Solubility Limiting Phases .....	3-116
3.4.2	Spent Fuel Dissolution Models .....	3-119
3.4.2.1	Introduction .....	3-119
3.4.2.2	Nonequilibrium, Thermodynamic Dissolution-Rate Function Forms .....	3-120
3.4.2.3	Regression Fit of Data to Models .....	3-129
3.4.2.4	Aqueous-Release-Rate Response for Spent Fuels .....	3-135
3.4.2.5	Release-Rate Model and Preliminary Analysis of Radionuclide Release in Unsaturated Drip Tests .....	3-143
3.4.2.6	References .....	3-160
	Section 3.4.2 Appendix .....	3-163
3.5	Glass Dissolution .....	3-169
3.5.1	Experimental Parameters for Glass Dissolution .....	3-170
3.5.1.1	Introduction .....	3-170
3.5.1.2	Rate Equation for Simplified Glass-Dissolution Model .....	3-170
3.5.1.3	Parameters for Simplified Glass Dissolution Model .....	3-171
3.5.1.4	Example Calculation .....	3-176
3.5.1.5	Limitations of the Simplified Model .....	3-176
3.5.1.6	Incorporation of Simplified Glass Model into Performance-Assessment Models .....	3-176
3.5.1.7	Solubility-Limited Radionuclide Release from Glass .....	3-187
3.5.1.8	Comparison With Laboratory Results .....	3-192
3.5.1.9	Effect of Dissolved Iron on Borosilicate Glass Dissolution .....	3-194
3.5.1.10	References .....	3-197
3.5.2	Glass Dissolution Models .....	3-199
3.5.2.1	Overview of Glass Dissolution .....	3-199
3.5.2.2	Modeling of Glass Corrosion .....	3-202
3.5.2.3	Limitations of Current Models .....	3-210
3.5.2.4	Conclusions .....	3-211
3.5.2.5	Assessment of Current Methods for Estimating Glass-Dissolution Rates under Silica-Saturated Conditions .....	3-211
3.5.2.6	References .....	3-218

3.6	Other Release Sources of Radionuclides .....	3-224
3.6.1	Crud .....	3-225
3.6.2	Hardware .....	3-228
3.6.3	Cladding .....	3-229

### 3. Scientific Basis for Predictive Model Development

### 3.1 Spent-Fuel Cladding Failure

The Zircaloy cladding that already exists on the fuel rod may be an important barrier that contributes in a performance evaluation of waste forms to their ability to meet the radionuclide release requirement. Several potential mechanisms of Zircaloy cladding degradation during dry storage have been identified, such as hydride reorientation, stress corrosion cracking, creep, and creep fracture.

At the present time three distinct time periods can be identified during repository storage:

1. A high-temperature period (above 250°C) during which the container is probably unbreached, the fuel rods are surrounded by inert gas or air, and no liquid water is present.
2. An intermediate-temperature period (250° to 100°C) when the container is probably unbreached and liquid water (from breached fuel rods containing water) may be present in contact with the fuel rods (90 to 1000 years).
3. A lower-temperature period (below 100°C) when the container may be breached and air, water vapor, and liquid water may be in contact with the spent fuel rods.

#### Cladding Failure Model

**Model equations.** LLNL is currently formulating quasi-static rate of displacement and rate of stress equations for a Zircaloy tube with an adjacent thin zirconium oxide film. The equations include contributions from elastic, creep, thermal, and hydride precipitation dependent strains. Given initial conditions and expected repository environmental histories to derive boundary conditions, we will integrate the set of rate equations to assess cladding failure. Our simplest and most conservative modeling assumption, with respect to cladding failure, is a stress or strain limit at which the zirconium oxide film fractures. This failure modeling concept is motivated because of the known large volume change that occurs when zirconium in the Zircaloy is oxidized to zirconium oxide. Hence, the oxide film is expected to remain in a compressive state of hoop stress for the expected large number of fuel rods that initially have low fission gas releases (<1%). This compressive hoop stress will prevent stress corrosion cracking from being initiated. In addition to the strain contribution of hydride precipitate, another potential mechanism of cladding failure is fluoride-Zircaloy corrosion, which is not stress dependent. The available data for fluoride-Zircaloy corrosion are preliminary, but suggest a pin-hole pitting uniformly distributed on the surface.

There have been no activities to evaluate stainless steel cladding failure response. The amount of stainless steel cladding is very small compared to the amount of Zircaloy cladding.

**Measured quantities.** Initial conditions are required for a rate displacement-stress formulation; thus, measurements for the initial dimensions and state of stress of the Zircaloy and zirconium oxide film are necessary to characterize the cladding. The boundary condition for a rate displacement-stress formulation of the cladding are the inside and outside pressure histories. This means that the fission gas content (released from  $\text{UO}_2$  spent fuel matrix) inside the cladding is required for the fuel rods. This data will also have a statistical character because the different  $\text{UO}_2$  fuels and burnup cycles may result in different amounts of fission gas content in the fuel rods. We would like to see this expressed as a probabilistic density function  $f(g,b,t)$ , where the density function,  $f$ , is the number of fuel rods per unit fission gas content per unit burnup with fission gas content,  $g$ , and burnup,  $b$ , at time,  $t$ . At  $t=0$ , this density function would characterize the initial distribution of fission gas content in fuel rods emplaced in the repository. At later times, the fission gas content may increase

because of helium produced due to decaying actinides. Thus, to predict the expected stress state in the Zircaloy and in the oxide film, the expected fission gas released from the  $\text{UO}_2$  matrix is a required initial condition that must be measured.

Considerable information on material properties for the elastic strain, creep strain, thermal strain, and fracture responses of Zircaloy cladding is available from reports and analysis for the Dry Storage Spent Fuel Program, reactor design documents, and the open literature. Some of this data may require additional confirmation tests for purposes of QA Level I input to models and analysis. Much of the data is not particularly useful because of the relatively low temperatures expected in a repository compared to in-reactor temperatures and the tensile hoop stress state expected in a repository compared to in-reactor compressive hoop stress state. Also, some testing to establish material properties of zirconium oxide failure is anticipated; again, this may be confirmation tests. The problem of hydride precipitation strains will require measurement of the initial concentrations of hydrogen as well as low temperature hydride platelet orientation statistics in each class of Zircaloy cladding. Additional testing and model development for hydride precipitation and re-orientation and its associated dependence on the state of stress are currently being planned. The initial hydrogen content data may have a statistical character similar to the fission gas content data. Hence, we are interested in it being expressed as a probabilistic density function,  $h(H, a_r, a_\theta, b)$ , where the density function,  $h$ , is the number of fuel rods per unit hydrogen content per unit size in the radial direction per unit size in the theta direction per unit burnup with hydrogen content  $H$ ,  $a_r$  length of hydride platelets in the radial direction,  $a_\theta$  length of hydride platelets oriented in the theta (hoop) direction, and burnup,  $b$ . Note that time is not a variable here as we do not anticipate additional hydrogen pickup by the cladding in the low temperature environment of the repository.

With this statistical information on initial hydrogen content and low temperature orientation, a time-dependent model is being planned to predict the precipitation kinetics of hydride platelets and the effect of stress on the hydride platelet orientation as the repository temperature decreases. The strain contribution from hydride platelet precipitation is a required part of the model development for assessing probable cladding failure rate.

Finally, the proposed quasi-static displacement-stress rate model assumes that the Zircaloy cladding and its adjacent zirconium oxide film are initially pristine. This assumption must be supported as part of the MCC characterization of spent fuel rods. Certainly there will be a statistical character to the initial qualities of the fuel rods with respect to defects and surface flaws. We will need to have data on flaw size, flaw surface density, etc. We plan to support tests that will subject flawed and defected cladding to temperature and stress states that will provide failure data for additional failure rate models for the number of fuel rods that are not initially pristine.

The following list of references address the progress that has been accomplished in testing, modeling, and understanding the complexities of spent fuel cladding failure response and a range of environmental conditions that may need to be addressed in the design of a geological repository.

## References

- Ardell, A.J. "On the Calculation of Melting Temperatures for Low-Temperature Phases of Polymorphic Metals," *Acta Metall.*, 11, 591-594 (June, 1963).
- Blackburn, L.D., et al. "Maximum Allowable Temperature for Storage of Spent Nuclear Fuel: An Interim Report," HEDL-TME 78-37, UC-70 (1978).

- Chen, I.-W. "Implications of Transformation Plasticity in ZrO<sub>2</sub>-Containing Ceramics: II, Elastic-Plastic Indentation," J. Am. Ceram. Soc. 69(3), 192 (1986).
- Christian, J.W. "Phase Transformations," in Physical Metallurgy, R.W. Chan, ed., North-Holland Pub. Co., Ch. 10, pp. 443 (1965).
- deGroot, S.R. "Thermodynamics of Irreversible Processes," North-Holland Pub. Co. Amsterdam (1957).
- Dieter, G.E. Mechanical Metallurgy, second edition, McGraw Hill (1976).
- Einzig, E.R., D.M. Bozi, and A.K. Miller. "Transactions," Waste Form Development and Processing, American Nuclear Soc. p. 131 (1980).
- Einzig, R.E. and R. Kohli. "Low-Temperature Rupture Behavior of Zircaloy-Clad Pressurized Water Reactor Spent Fuel Rods Under Dry Storage Conditions," Nuc. Tech., 67, 107 (1984).
- Ells, C.E. "Hydride Precipitates in Zirconium Alloys," N. Nuc. Mat., 28, 129 (1968).
- Ells, C.E. "The Stress Orientation of Hydride in Zirconium Alloys," J. Nuc. Mat., 34, 306 (1970).
- Eringen, A.C. "Mechanics of Continua," John Wiley Pub. New York (1967).
- Farwick, D.G. and R.A. Moen. "Properties of Light Water Reactor Spent Fuel Cladding," Westinghouse Hanford Report HEDL-TME 78-70 (Aug. 1979).
- Gibbs, J. "The Scientific Papers of J. Willard Gibbs," Vol. 1, Dover Pub. Inc., New York (1961).
- Hardy, H.K. and T.J. Heal. "Report on Precipitation," in Progress in Metal Physics, 5, 143, 2nd printing, Pergamon Press (1961).
- Khan, M.A., N.H. Madsen, and B.A. Chin. "Fracture Predictions in Zircaloy Fuel Cladding: Effects of Radiation on Materials," Twelfth International Symposium, ASTM Stg 870, Philadelphia, pp. 642-655 (1985).
- Leger, M. and A. Donner. "The Effect of Stress on Orientation of Hydrides in Zirconium Alloy Pressure Tube Materials," Canadian Meta. Qu., 24, 235 (1984).
- Lupis, C.H.P. "Chemical Thermodynamics of Materials," Elsevier Science Pub., New York (1983).
- Lustman, B. and F. Kerze, Jr., eds. "The Metallurgy of Zirconium," McGraw Hill, first edition, p. 354 (1955).
- Miller, A.K. "Application of the SCCIG Model to Dry Storage of Spent Fuel," Workshop on Spent Fuel Integrity in Dry Storage, Seattle, WA, (Jan 20, 1982).
- Onsager, L. "Reciprocal Relations in Irreversible Processes; I and II," Phys. Rev. 37 405, and 38 2265 (1931).
- Ostberg, G. "Crack Propagation in Hydrided Zircaloy-2," Int. J. Fract. Mech., 4 95 (1968).
- Parfenov, B.G., V.V. Gerasimov, and G.I. Vendiktova. "Corrosion of Zirconium and Zirconium Alloys," (translated from Russian), Israel Program for Scientific Translations, Jerusalem, p. 87 (1969).
- Pearson, W.B. "Handbook of Lattice Spacings and Structures of Metals and Alloys," 1, 130.

- Pescatore, C., M.G. Cowgill, and T.M. Sullivan. "Zircaloy Cladding Performance Under Spent Fuel Disposal Conditions," Brookhaven National Laboratory Report BNL-52235 (Progress Report May 1 - October 31, 1989).
- Rothman, A.J. "Potential Corrosion and Degradation Mechanisms of Zircaloy Cladding on Spent Nuclear Fuel in a Tuff Repository," UCID-20172 (Sept. 1984).
- Sawatzky, A. J. Nucl. Mat, 2,321 (1960).
- Smith, C.F. and W.B. Crandall, J. Amer. Ceramic Soc., 47(12), 624-627 (Dec., 1964).
- Smith, H.D. "Initial Report on Stress Corrosion Cracking Experiments Using Zircaloy-4 Spent Fuel Cladding Rings," Westinghouse Hanford Company, Richland, WA.
- Smith, H.D. "Zircaloy Cladding Corrosion Degradation in a Tuff Repository," HEDL-7455, Rev. 1, p. 12 (July, 1985).
- Stehle, H., F. Garzarolli, A.M. Garde, and P.G. Smerde. "Zirconium in the Nuclear Industry," Sixth International Symposium, ASTM STP 824, pp. 483-506 (1984).
- Stout, R.B. "A Deformation and Thermodynamic Model for Hydride Precipitation Kinetics in Spent Fuel Cladding," Lawrence Livermore National Laboratory, UCRL-100860, (submitted to Symp. on Scientific Basis for Nuclear Waste Management XII, Boston MA, Nov. 27-30, 1989).
- Stout, R.B. "Deformation and Thermodynamic Response for a Crack Dislocation Model of Brittle Fracture," Eng. Fract. Mech., 19, 545 (1984).
- Stout, R.B. "Modeling the Deformations and Thermodynamics for Materials Involving a Dislocation Kinetics," Cryst. Latt. Def. 9, 65 (1981).
- Yaggee, F.L., R.F. Mattas, and L.A. Neimark. "Characterization of Irradiated Zircaloys" Susceptibility to Stress Corrosion Cracking," NP-1557, Research Project 1027, prepared by Argonne National Laboratory for EPRI, pp. 4-27, Fig. 4-7 (Oct., 1980).



### 3.1.1 Parameters for Failure Models

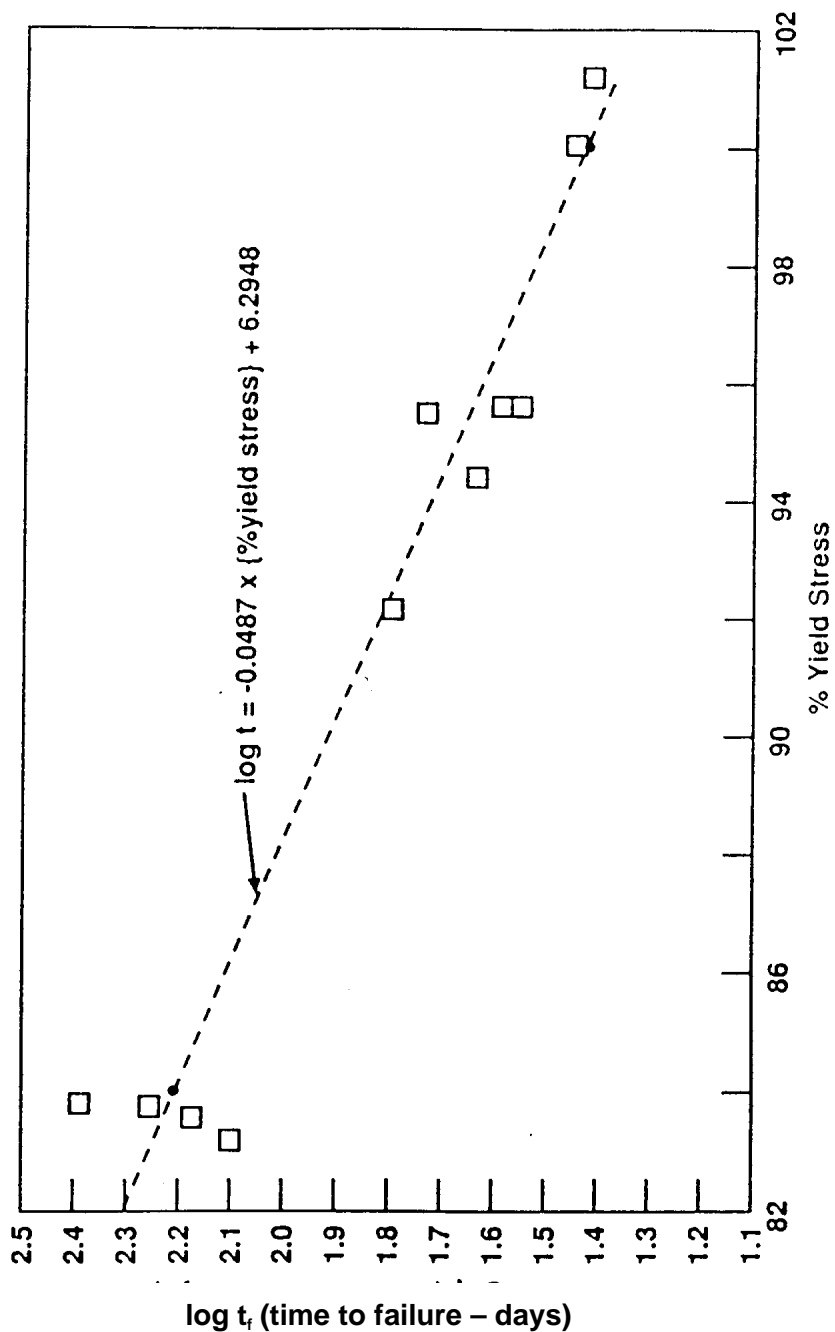
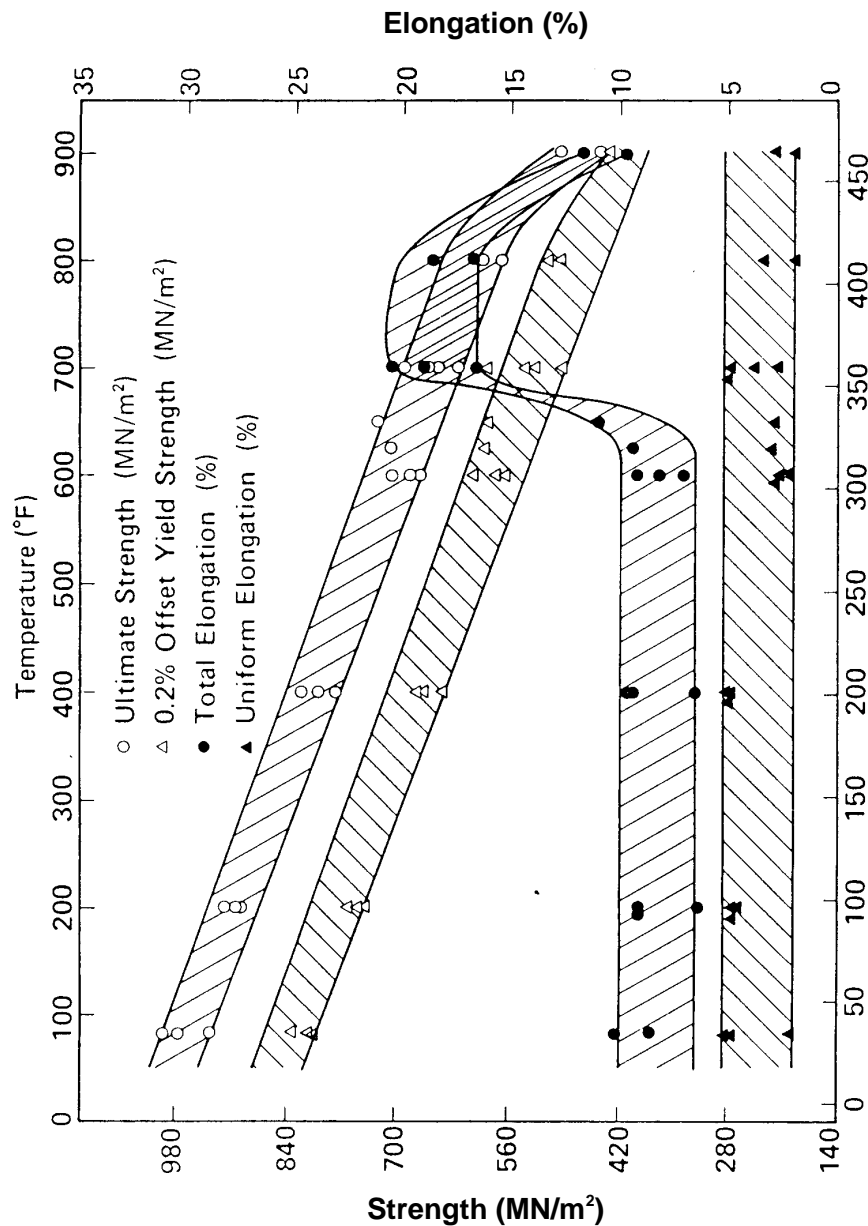
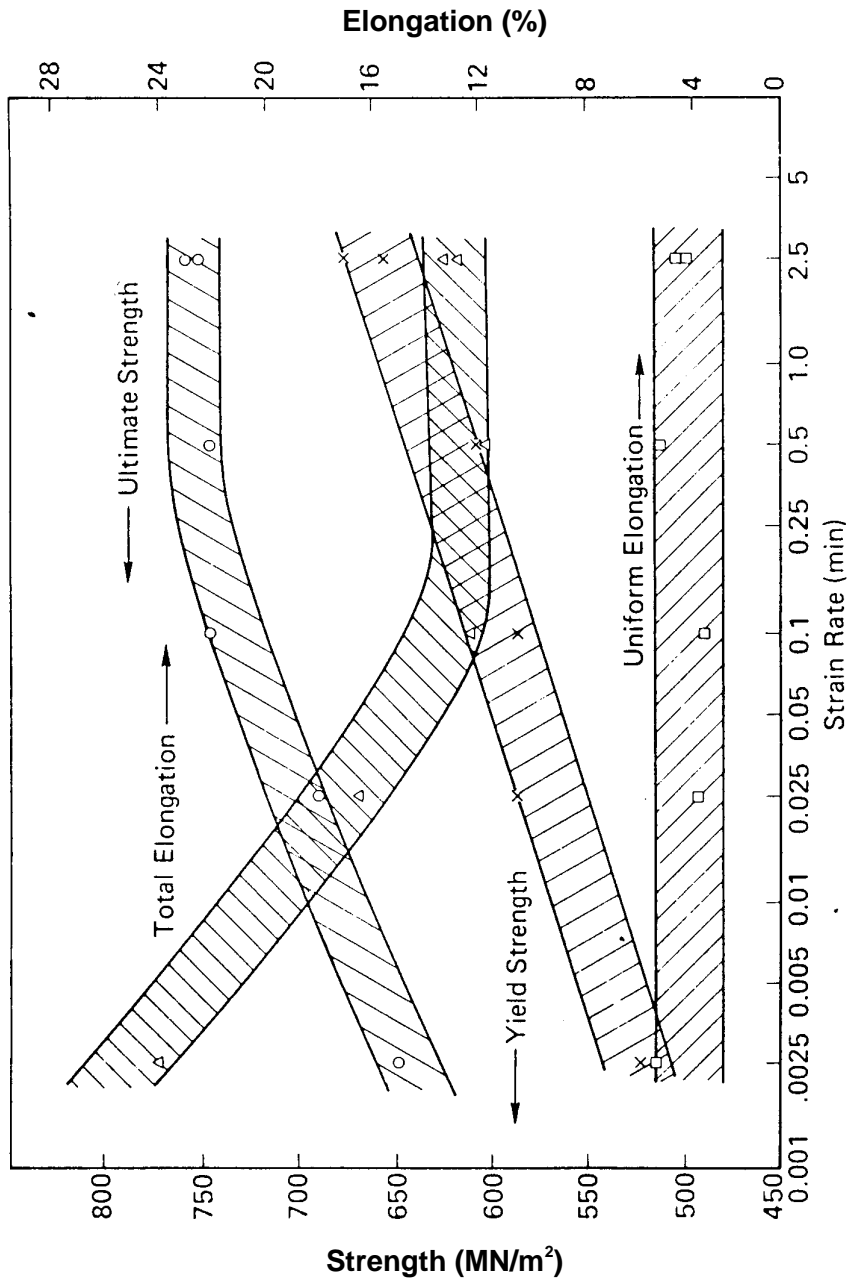


Figure 3.1.1-1 Observed relationship: log t<sub>f</sub> (time to failure) vs. stress (% of yield stress) (H.D. Smith, *Spent Fuel Cladding Degradation*, presented to the Nuclear Waste Technical Review Board, August, 1990)



**Figure 3.1.1-2** Effect of temperature on the tensile properties of H.B. Robinson spent fuel cladding (strain rate = 0.025/min) (Figure 2 from A.A. Bauer, L.M. Lowry, "Tensile Properties and Annealing Characteristics of H.B. Robinson Spent-Fuel Cladding," *Nuclear Technology*, Vol. 41, Dec. 1978, pp. 359-372.)



**Figure 3.1.1-3** Effect of strain rate on the tensile properties of H.B. Robinson spent-fuel cladding (test temperature was 371°C) (Figure 3 from A.A. Bauer, L.M. Lowry, "Tensile Properties and Annealing Characteristics of H.B. Robinson Spent Fuel Cladding," *Nuclear Technology*, Vol. 41, Dec. 1978, pp. 359-372.)

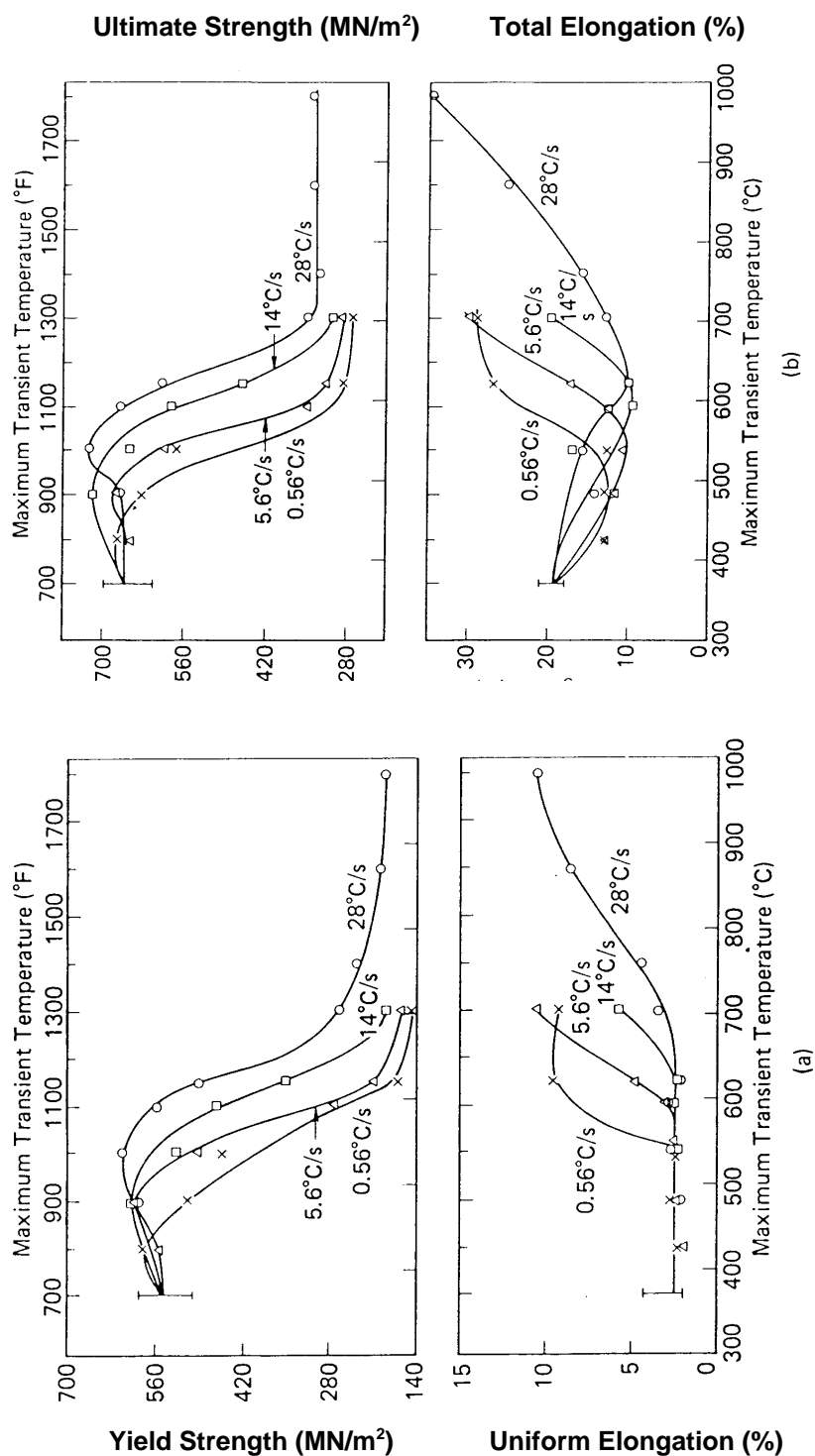


**Figure 3.1.1-4** Response of spent fuel cladding to transient annealing (test temperature was 371°C) (a) Yield strength and uniform elongation and (b) ultimate strength and total elongation (Figure 4 from A.A. Bauer, L.M. Lowry, "Tensile Properties and Annealing Characteristics of H.B. Robinson Spent Fuel Cladding," *Nuclear Technology*, Vol. 41, Dec. 1978, pp. 359-372.)

### 3.1.1 Parameters for Failure Models

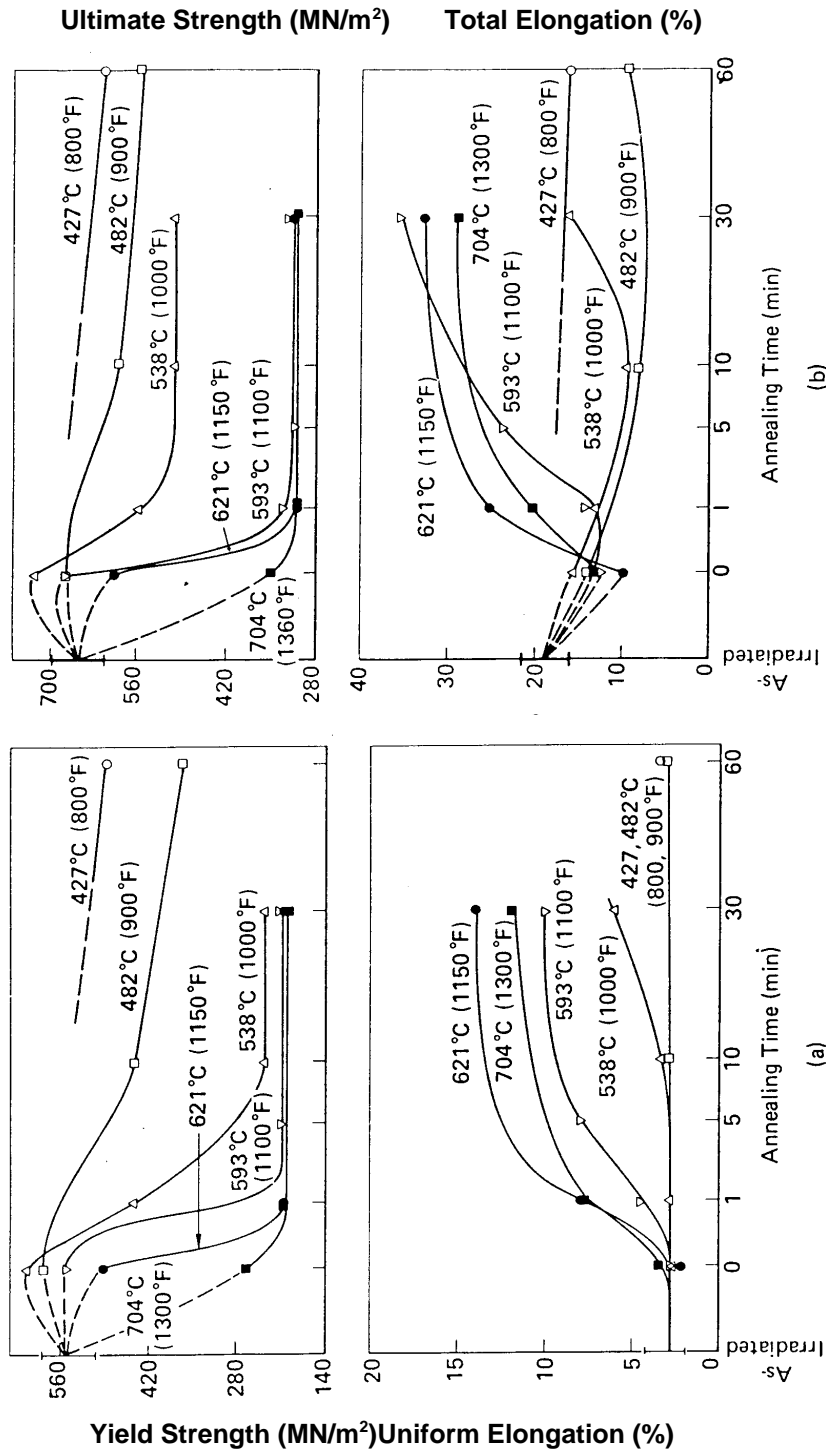


**Figure 3.1.1-5** Response of spent fuel cladding to isothermal annealing (test temperature was 371°C. (a) Yield strength and uniform elongation, and (b) ultimate strength and total elongation (Figure 5 from A.A. Bauer, L.M. Lowry, "Tensile Properties and Annealing Characteristics of H.B. Robinson Spent Fuel Cladding," *Nuclear Technology*, Vol. 41, Dec. 1978, pp. 359-372.)

Table 3.1.1-1 Rates and oxidation depths occurring in the low-temperature corrosion of Zircaloy cladding (Table A1)

Temperature (°C)	Corrosion Rate (mg/dm <sup>2</sup> ·day)		Oxidation Depth (μm)*	
	Eq. 1	Eq. 2	Eq. 1	Eq. 2
250	$4.45 \times 10^{-3}$	$1.75 \times 10^{-3}$	0.071	0.028
300	$3.60 \times 10^{-2}$	$2.35 \times 10^{-2}$	0.577	0.377
350	$2.08 \times 10^{-1}$	$2.09 \times 10^{-1}$	3.33	3.35
400	$9.25 \times 10^{-1}$	1.34	14.8	21.5

\*Under isothermal conditions for one year.

#### References

- A1. E. Hillner, "Corrosion of Zirconium-Base Alloys - An Overview," Zirconium in the Nuclear Industry, ASTM STP 633, American Society for Testing and Materials, Philadelphia, PA, 1977.
- A2. A. B. Johnson Jr, E. R. Gilbert and R. J. Guenther, Behavior of Spent Nuclear Fuel and Storage System Components in Dry Interim Storage, PNL-4189, Pacific Northwest Laboratory, Richland, WA, August 1982.
- A3. D. G. Boase and T. T. Vandergraaf, "The Canadian Spent Fuel Storage Canister: Some Material Aspects," Nucl. Tech. 32, p. 60, 1977.

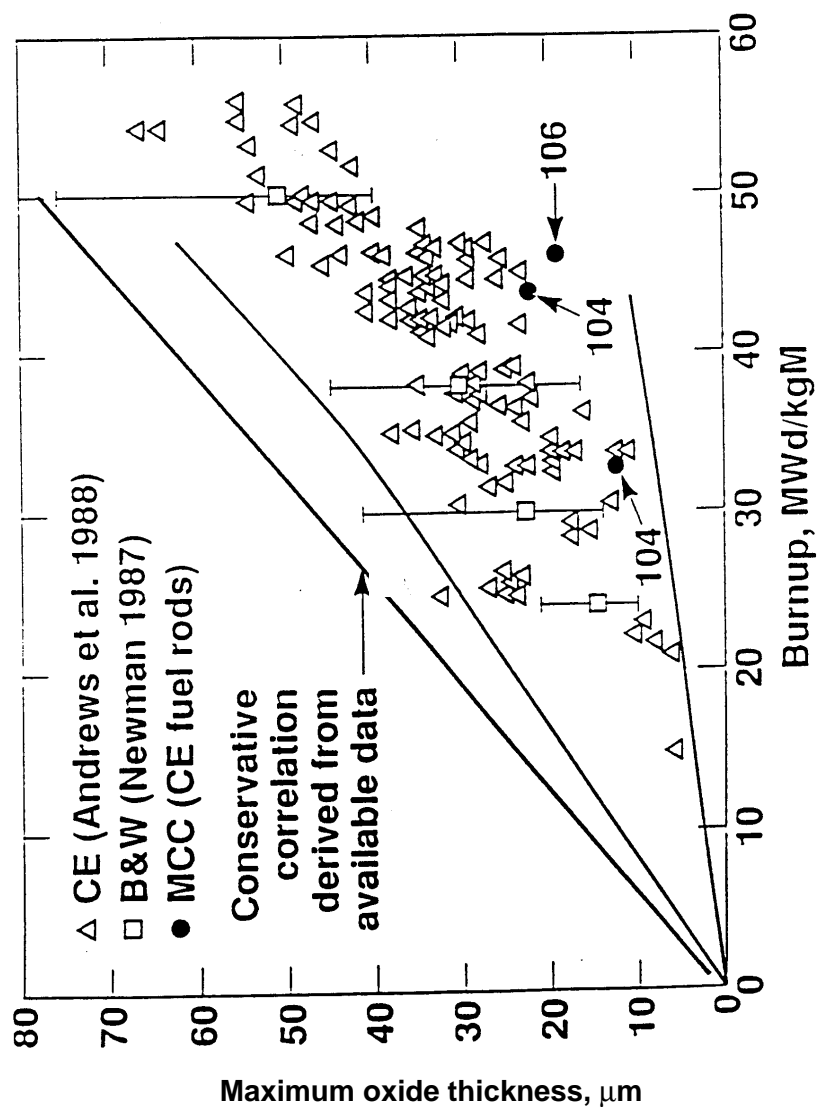


Figure 3.1.1-6 Method for correlating maximum oxide thickness with burnup (R.B. Stout, *Spent Fuel Characteristics Overview*, presented to the Nuclear Waste Technical Review board, August, 1990.)

### **3.1.2 Failure Models**

Both the experimental testing and the model development activities for cladding failure response are incomplete. At this time only the report by L. Santanam, H. Shaw and B.A. Chin (Modeling of Zircaloy Cladding Degradation Under Repository Conditions, Lawrence Livermore National Laboratory Report UCRL-100211, July, 1989) contains a preliminary analysis for Zircaloy cladding failure during the high temperature time period. The analysis used a deformation and fracture map methodology that is an extension of the methods applied to analyze Zircaloy cladding deformation and fracture for the dry storage of spent fuel waste form program established by the nuclear utility industry. Substantial testing and model development activities remain to be completed to support creditable repository design that would include the cladding as a long term barrier to the  $\text{UO}_2$  spent fuel waste form. It is believed, however, that the Zircaloy clad fuel rods that have low internal pressures will have low failure rate through both the high temperature and intermediate temperature periods.



### 3.2 Spent-Fuel Oxidation

In any proposed nuclear waste repository for spent fuel from nuclear power reactors, the potential release rates of many radionuclides over a 10,000 year design lifetime depends on the oxidation rate and the oxidation state of any irradiated  $\text{UO}_2$  fuel pellets that may be exposed to the atmosphere. This is because  $\text{UO}_2$  spent fuel can oxidize into  $\text{U}_4\text{O}_9 \rightarrow \text{U}_3\text{O}_8 \rightarrow \text{UO}_3$ , and possibly other oxides, which could influence the surface area and the dissolution rates of any spent fuel that may be exposed to water in a repository. Therefore, experiments to provide both data and a physical basis for rational model development for  $\text{UO}_2$  oxidation kinetics are necessary in order to eventually predict potential radionuclide release rates from spent fuel in a repository.

Results from tests at this time imply that the grain boundaries of irradiated  $\text{UO}_2$  oxidized more rapidly than the grain volumes at low temperatures (less than  $200^\circ\text{C}$ ). This two-rate oxidation process of  $\text{UO}_2$  spent fuel is difficult to represent mathematically because classical diffusion models with their associated classical initial conditions and external boundary conditions do not physically describe certain geometrical aspects of the experimental observations.

Furthermore, the vast majority of the spent fuel rods placed in the repository will have intact Zircaloy cladding, but approximately 0.01% of the rods will contain cladding defects, usually in the form of small splits or pin holes. Some of the breached rods may contain water. If cladding with small breaches is to provide a barrier function, then it will be necessary to determine if fuel oxidation occurs rapidly enough under repository conditions to split the cladding and expose additional fuel with an oxidation state higher than  $\text{UO}_2$  before significant credit can be taken for pin-hole-defected cladding as a barrier to radionuclide release. Thus, spent fuel oxidation time response is also an input function for modeling the extent and amount of exposed  $\text{UO}_2$  spent fuel in failed cladding.

Spent LWR fuel consists primarily of  $\text{UO}_2$  pellets, whose density is 92-95% of the theoretical density, enclosed in a Zircaloy sheath. When  $\text{UO}_2$  oxidizes in excess oxygen, it passes through certain possibly metastable states, such as  $\text{U}_4\text{O}_9$  and  $\text{U}_3\text{O}_8$ , before it totally oxidizes to  $\text{UO}_3$ . The rate at which the fuel oxidizes through the various phases depends on the temperature. The rate may also depend on the moisture content of the atmosphere, previous radiation history of the fuel, and radiation level during storage. The densities of the phases range from a high of  $10.3 \text{ g/cm}^3$  for 93% dense  $\text{UO}_2$  to  $7.3 \text{ g/cm}^3$  for  $\text{UO}_3$ . Until  $\text{U}_3\text{O}_8$ , with a density of  $8.3 \text{ g/cm}^3$ , is formed, intermediate phases have densities approximately equal to that of  $\text{UO}_2$ . Therefore, as the  $\text{UO}_2$  oxidizes through  $\text{U}_3\text{O}_8$ , the fuel pellets will swell and put a tensile hoop stress on the cladding. Several studies have shown that cladding placed under a hoop stress, caused by the formation of  $\text{U}_3\text{O}_8$ , will enlarge existing breaches and, in some cases, will fracture where there had been on previous pin hole (small) breaches.

In the following Section 3.2.1, information and data are provided from TGA (Thermogravimetric Apparatus) Tests and ODB (Oven Dry Bath) tests. The temperature-time response with spent fuel oxidation testing below  $260^\circ\text{C}$  remains to be completed. Above  $260^\circ\text{C}$ , it appears that the oxidation time response is sufficiently rapid to be instantaneous relative to repository time duration. Thus, atmospherically exposed  $\text{UO}_2$  spent fuel in failed waste packages as a model for kinetics, transforms instantly to  $\text{U}_3\text{O}_8$  (or  $\text{UO}_3$ ) above  $260^\circ\text{C}$ .

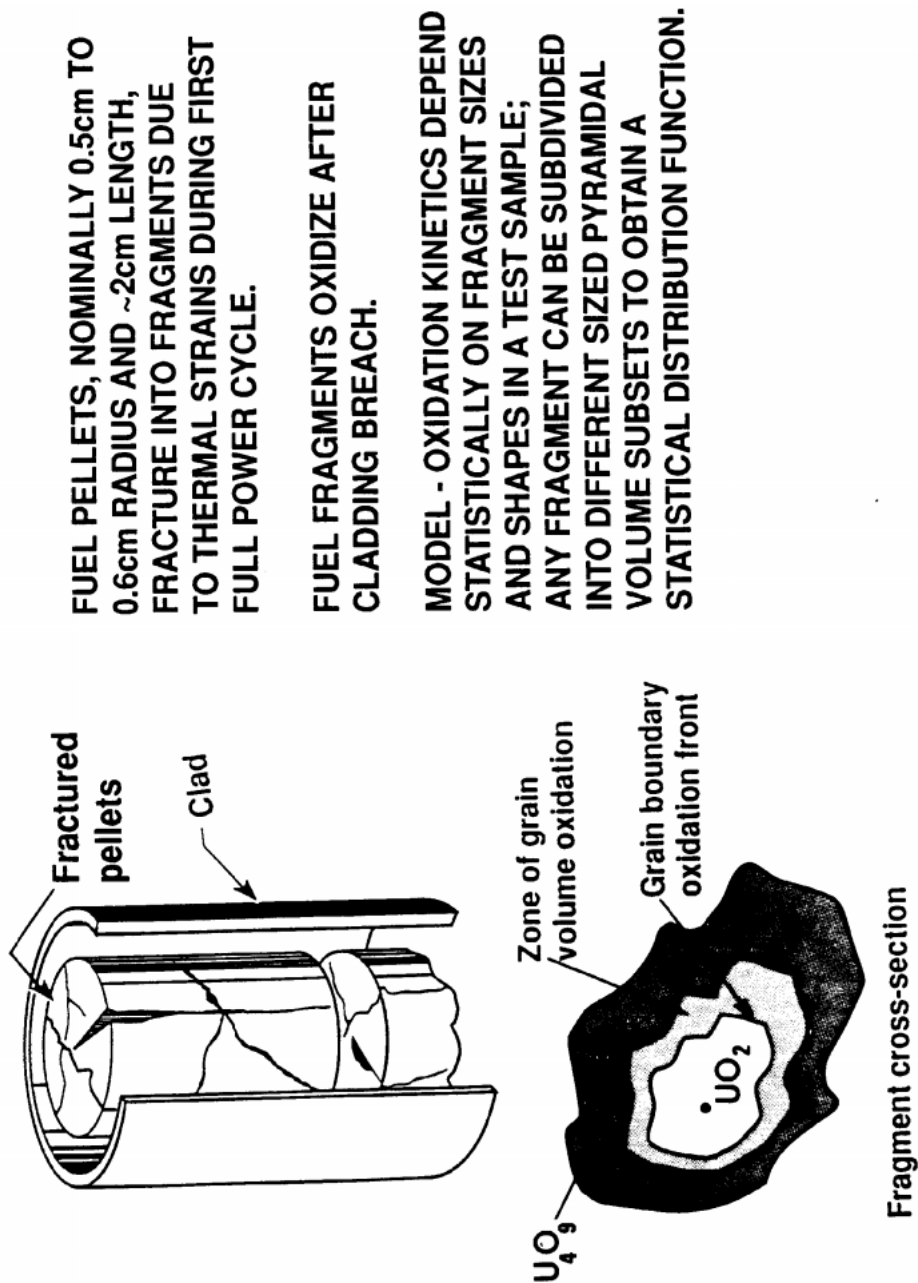
The temperature-time response of oxidizing  $\text{UO}_2$  below  $260^\circ\text{C}$  will be described with a preliminary model in Section 3.2.2. This model represents two time sub-domains. The first sub-domain is the time interval for oxidizing spent fuel to a  $\text{U}_4\text{O}_9$  lattice structure and to attain the O to U of  $\sim 2.4$  plateau that has been observed. The time interval will be evaluated based on the time for the  $\text{U}_4\text{O}_9$  front to propagate to the center of a spent fuel grain. This is a conservative model as it assumes that all grain boundaries oxidized and crack open instantaneously when the  $\text{UO}_2$  spent fuel is initially exposed to atmospheric oxygen. The model can also describe the weight gain time response during partial oxidation of  $\text{UO}_2$  grains to  $\text{U}_4\text{O}_9$  grains.

The second sub-domain is the time interval on the  $\sim 2.4$  O/U plateau before a transition away from the plateau level appears. This transition in oxygen weight gain is conjectured to be the result of the initial formation of the  $\text{U}_3\text{O}_8$  phase, which would occur most likely on the outer boundary of the existing  $\text{U}_4\text{O}_9$  grains. At the present time, no data are available on the subsequent time response or geometrical character of the  $\text{U}_3\text{O}_8$  oxidation response. Thus, it is conservative to assume that the total time interval for  $\text{UO}_2$  spent fuel to transform to  $\text{U}_3\text{O}_8$  is the sum of the two sub-domain time intervals. However, it is conservative to assume that the total time interval for  $\text{UO}_2$  spent fuel to transform to  $\text{U}_3\text{O}_8$  is the sum of the two sub-domain time intervals (time to reach  $\text{U}_4\text{O}_9$  plus time to initiate the  $\text{U}_3\text{O}_8$  phase). Note that a critical part of the assumption is that an individual grain must all be at an O/U of  $\sim 2.4$  before the phase transition to  $\text{U}_3\text{O}_8$  can be initiated. Once the relatively low (compared to  $\text{UO}_2$ ) density state of  $\text{U}_3\text{O}_8$  has been attained, the dissolution/release performance of spent fuel has been significantly decreased because of the large ( $\sim$ potentially three orders of magnitude) increase in exposed spent fuel surface area, relative to the initial surface area of fragmented spent fuel pellets. Thus, the time-temperature-phase transformation responses for the different spent fuel oxidation processes can significantly impact the potential release rate of radionuclides from spent fuel waste forms.

### 3.2.1 Experimental Parameters for Oxidation Models

The testing activities to determine oxidation response are thermogravimetric analysis (TGA) method and oven dry bath (ODB) method. Both methods provide measurements of weight gain due to oxidation of the sample during the time interval of the testing and under controlled temperature and some controlled atmospheric gas variations. In the case of TGA testing, the sample size is small, around 200 mg, and this initial weight is typical of an average fragment from a spent fuel pellet. In the case of ODB testing, the sample size is considerably larger, around 10 grams of spent fuel. (The larger initial sample weights of ODB testing provides a well-controlled procedure to obtain oxidized spent fuel samples for future oxidized spent fuel dissolution testing.) In each testing method, the weight gain time response is measured, and samples can be obtained for microscopic examinations at various oxidation stages (times) during the weight gain time response. The weight gain time response is usually reported as the oxygen to heavy metal atomic ratio, with an O to U or O to M ratio notation (the first is oxygen to uranium and the second is oxygen to heavy metal, which ideally would include all actinide atoms but is dominated by the uranium atomic number density). For example, an O/U of 2.0 is  $\text{UO}_2$ . The microscopic analyses are performed on samples to identify the sequence of crystallographic lattice structures that occur during the oxidation of spent fuel. From the weight gain measurements and the phase identification analysis, the oxidation response for the existing test matrix of spent fuel samples has shown that  $\text{UO}_2$  spent fuel transforms first to a non-stoichiometric  $\text{U}_4\text{O}_9$  lattice structure phase with an O/U of  $\sim 2.4$  at temperatures below  $200^\circ\text{C}$ . Transitions to higher oxidation phases ( $\text{U}_3\text{O}_8$  and  $\text{UO}_3$ ) have not yet been observed in ODB tests below  $200^\circ\text{C}$ . Higher temperature TGA and ODB testing are being initiated to determine the phases and the kinetics of oxidation plus phase transformation mechanisms. The critical temperature range to establish oxidation response and phase change kinetics (stable versus metastable transformations) is between  $200^\circ\text{C}$  and  $260^\circ\text{C}$ . Both TGA and ODB testing activities are in progress to provide additional data in the  $200^\circ\text{C}$  to  $260^\circ\text{C}$  temperature interval. Above  $260^\circ\text{C}$ , the rate of spent fuel oxidation and the phase transformations proceed rapidly to  $\text{U}_3\text{O}_8$  and  $\text{UO}_3$  lattice structures in short periods of time (weeks/years) relative to repository disposal time periods (100 to 1000 years).

The following set of figures present a visual and brief statement format that provides information and data obtained with the existing spent fuel oxidation testing methods. The oxidation response of spent fuel is not believed to be a radionuclide release process (there is a possible gaseous release mechanism which remains to be characterized). Rather, the oxidation response of spent fuel is considered primarily a degradation process which transforms the physical and chemical state of the waste form. As a result, the oxidation phases  $\text{UO}_2$ ,  $\text{U}_4\text{O}_9$ ,  $\text{U}_3\text{O}_8$ , or  $\text{UO}_3$  have potentially different intrinsic dissolution rates that determine the aqueous release rate response. In addition to the dissolution rates, the potential magnitude of surface area exposed greatly increases as  $\text{UO}_2$  oxidizes to the higher phases. In going from  $\text{UO}_2$  to  $\text{U}_4\text{O}_9$ , grain boundaries between grain volumes crack open because of the slight volume decrease during this phase transformation. Furthermore, the phase transformations from the  $\text{U}_4\text{O}_9$  lattice structure to  $\text{U}_3\text{O}_8$  and  $\text{UO}_3$  have significant volume increases which can microcrack and flake grain volumes to smaller particles and/or powdered forms. Thus, the aqueous radionuclide release rate is potentially increased for higher oxidized phases if groundwater access occurs to wet the increased exposed surfaces of oxidized spent fuel.



SCHEMATIC 4-16/18-20/20-01 2/5

Figure 3.2.1-1 Spent fuel oxidation response

- **UO<sub>2</sub> fuel pellets (initially ~0.5 cm radius and ~1–3 cm length) break into fragments during reactor operation. This fragmentation increases the surface area of spent fuel for oxidation and dissolution responses.**
- **A fragment of UO<sub>2</sub> spent fuel will oxidize to higher oxidation weight gains (UO<sub>2+x</sub>) and at low temperatures other oxidation state phases (U<sub>4</sub>O<sub>9</sub>, U<sub>3</sub>O<sub>7</sub>, U<sub>3</sub>O<sub>8</sub>, UO<sub>3</sub> plus possible hydrates).**
- **A fragment of spent fuel (oxidized or not) will dissolve in aqueous solutions.**

Figure 3.2.1-2 Spent fuel waste form characteristics observations

- Small fraction (< 0.1%) of rods will enter repository breached and be available for oxidation when container is compromised
  - Cladding corrosion may lead to additional breaches
  - High temperature data indicate that low-density  $U_3O_8$  can form, destroying fuel and cladding
  - Four oxidation effects:
    - Change phase of fuel
    - Open additional internal fuel surfaces to leachant
    - Release trapped fission gas
    - Split cladding; change path for radioisotope release
- Question?**  
 **$\Delta(O/M)$  as a function of time, temperature,  
and atmosphere**

Figure 3.2.1-3 Why study spent fuel oxidation?

- **Temperature was an important variable**
- **Effect of atmospheric moisture and burnup is uncertain**
- **Low-temperature oxidation data were not available**
- **Assumed  $\text{UO}_2$  and spent fuel had similar oxidation behavior**

Figure 3.2.1-4 Basis for YMP spent fuel oxidation testing from early work

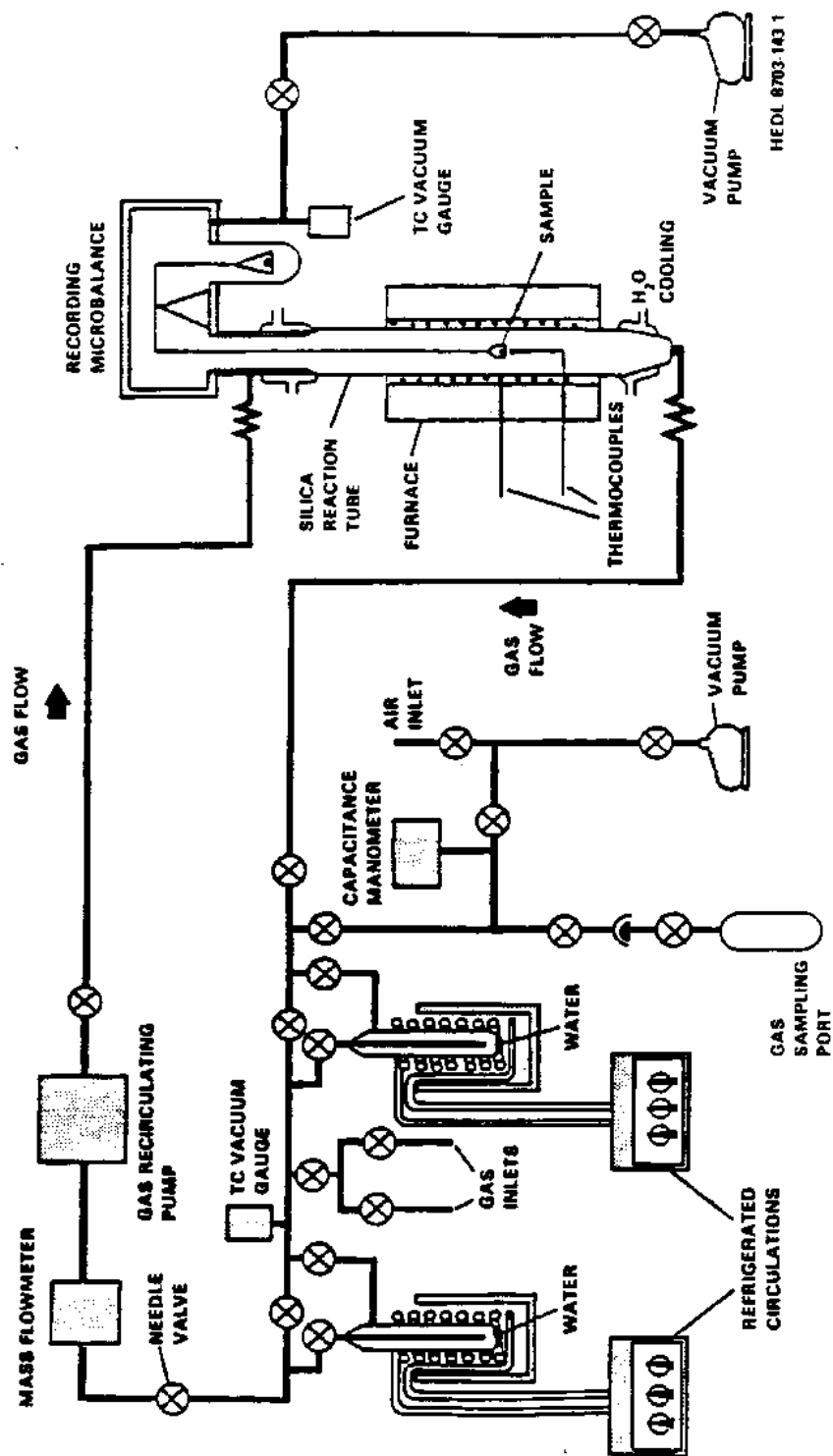


Figure 3.2.1-5 TGA apparatus



<b>ASSUMPTIONS</b>	
1. UNIFORM SPHERICAL GRAINS	
2. GRAINS OXIDIZE INDEPENDENTLY	
3. PLANAR OXIDATION FRONT	
<b>DESCRIPTION</b>	
$1 - [1 - 3 \Delta(O/M)]^{1/3} = (k't)^{1/2}$	
<b>WHERE</b>	
$\Delta(O/M)$	= CHANGE IN OXYGEN TO METAL RATIO
$k'$	= OXIDATION RATE CONSTANT
$t$	= OXIDATION TIME

Figure 3.2.1-6 TGA data analysis

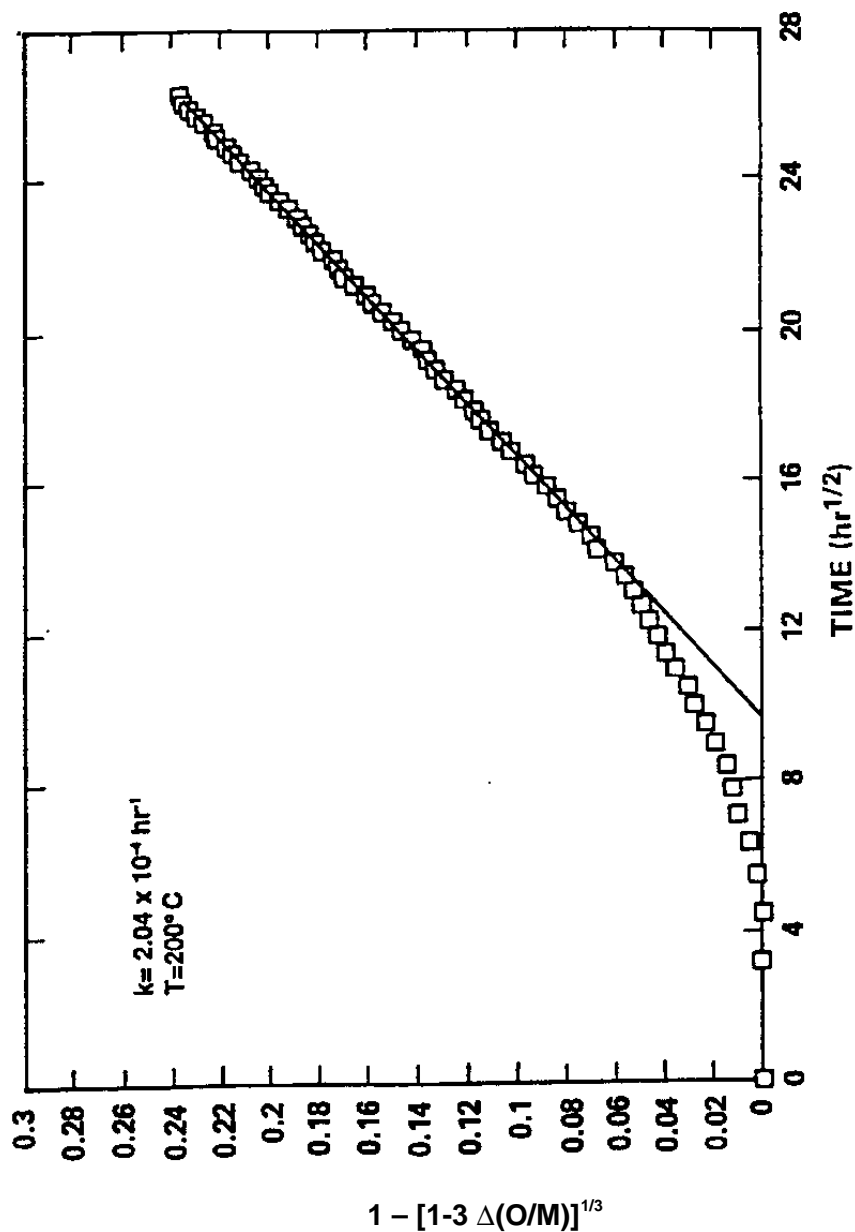


Figure 3.2.1-7 Fitting TGA data to obtain rate constant

- Different oxidation behavior in unirradiated  $\text{UO}_2$
- Spent fuel oxidation is a two-step process: oxygen penetration of the grain boundaries followed by oxidation of the bulk grains
- Arrhenius dependence on temperature. The activation energy is consistent with  $\text{O}_2$  diffusion into  $\text{UO}_2$ .
- Moisture level has little effect
- Oxidation more rapid at the pellet surface
- The majority of the mechanistic data comes from the microstructural examination of the oxidized fuel

Figure 3.2.1-8 TGA oxidation summary

- **To provide rate data for oxidation model**
- **Determine long-term oxidation behavior**
- **Source of fuel for leach testing**

Figure 3.2.1-9     Dry-Bath oxidation  
program

<b>Temperature:</b>	195°, 175°, 130°, 110°C
<b>Dew Points:</b>	-55, +80°C
<b>Sample Configuration:</b>	As-irradiated fragments pulverized fuel
<b>Fuels:</b>	HB Robinson PWR (ATM-101) Turkey Point PWR Cooper BWR (ATM-105) Calvert Cliffs PWR (ATM-103, -104, -106)
<b>Grain Size Range:</b>	5 to 30 μm
<b>Burnup Range:</b>	25 to 48 GWd/MTU
<b>FGR Range:</b>	0.1% to 18%
<b>Current Test Times:</b>	Up to 40 kh (5.0 yr)

Figure 3.2.1-10 Test variables

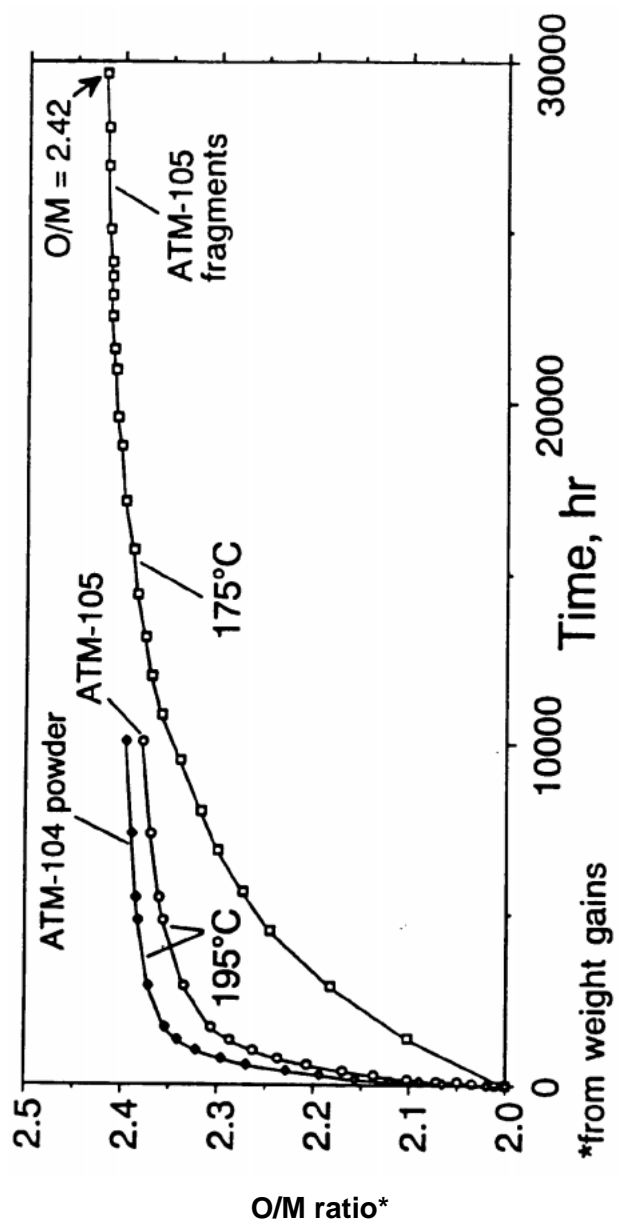


Figure 3.2.1-11 Oxidation of LWR spent fuel

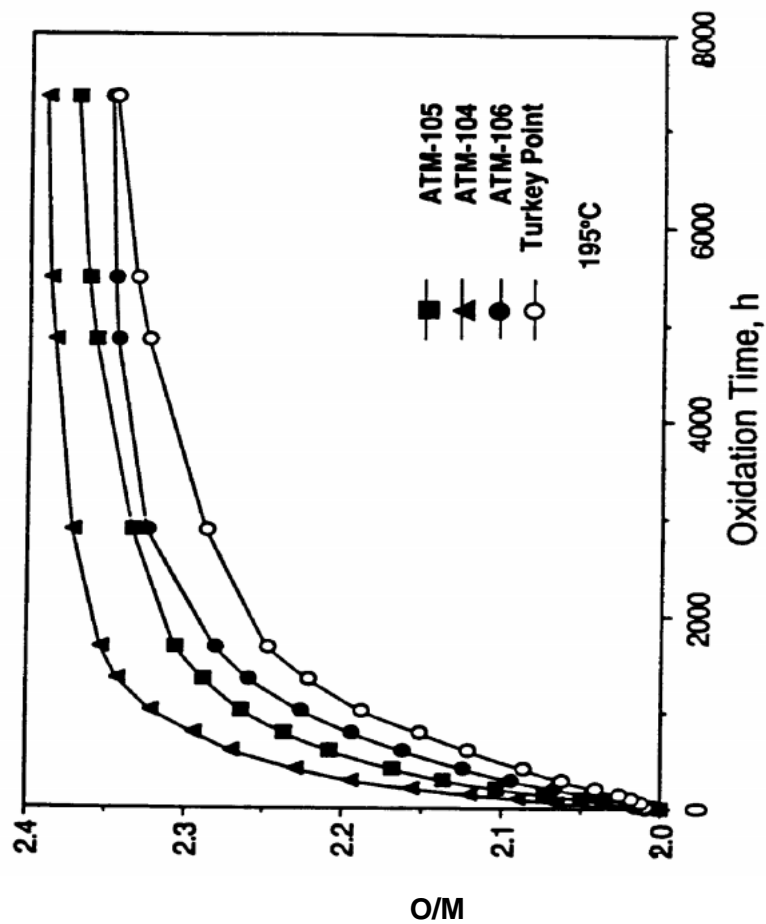


Figure 3.2.1-12

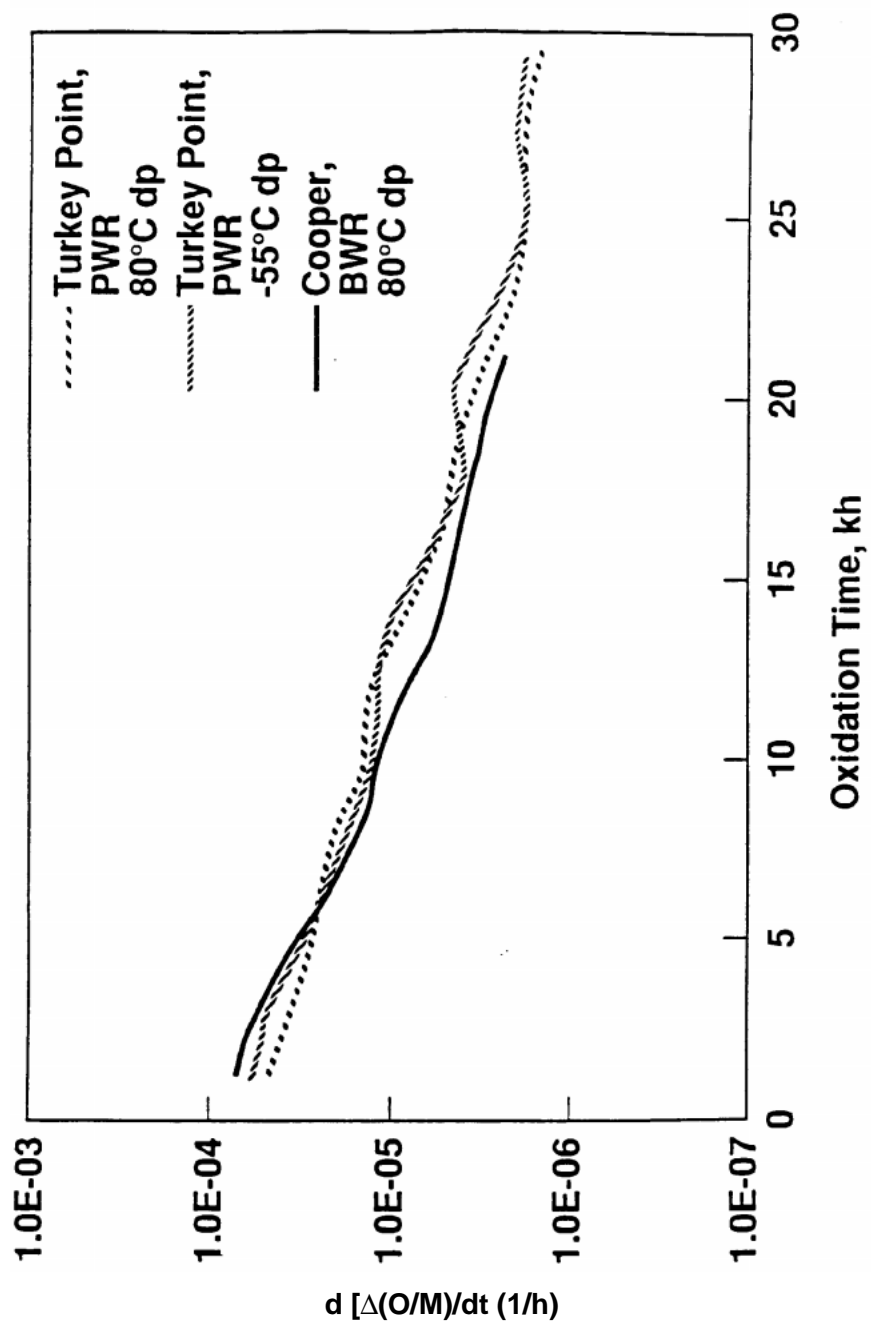


Figure 3.2.1-13 Change in O/M with time, 175°C



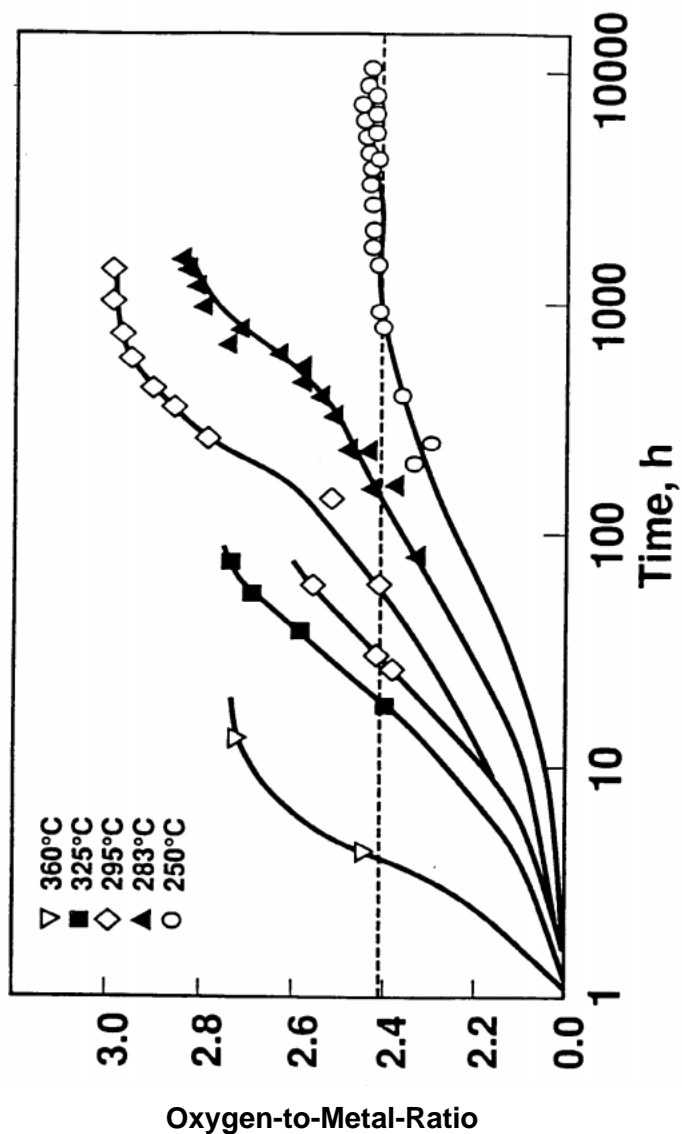


Figure 3.2.1-14 Oxidation of fragments of Turkey Point Fuel

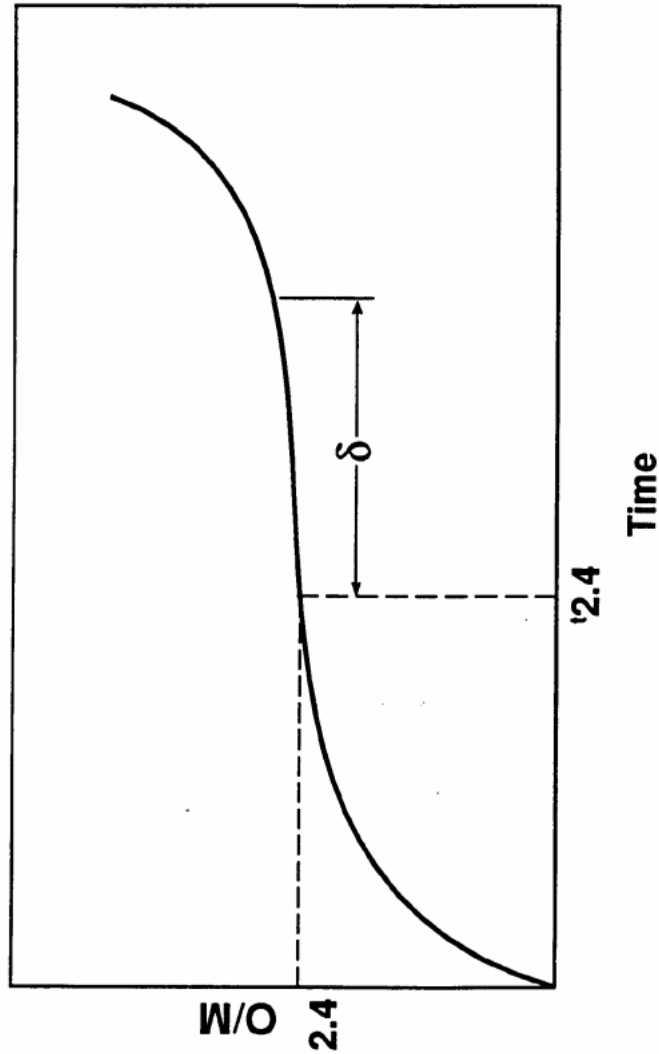


Figure 3.2.1-15 Generalized spent fuel oxidation curve

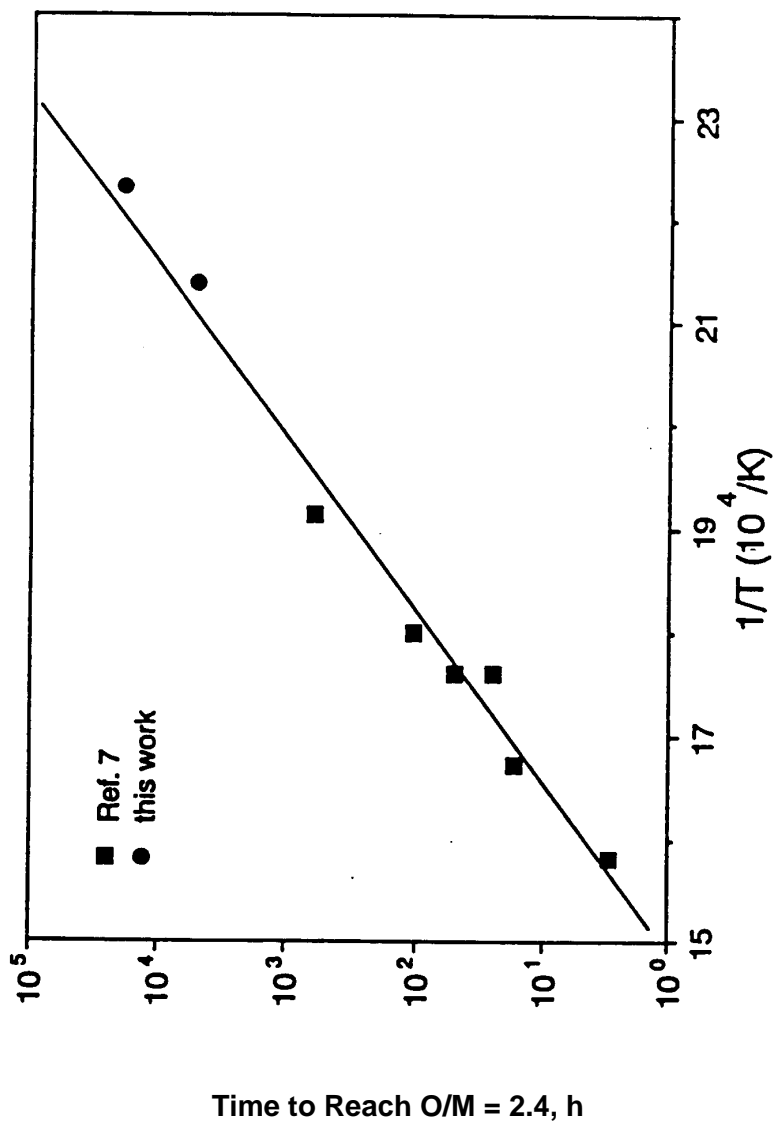


Figure 3.2.1-16

SNTRRE23P.125.NWTRB/10-14/16-92

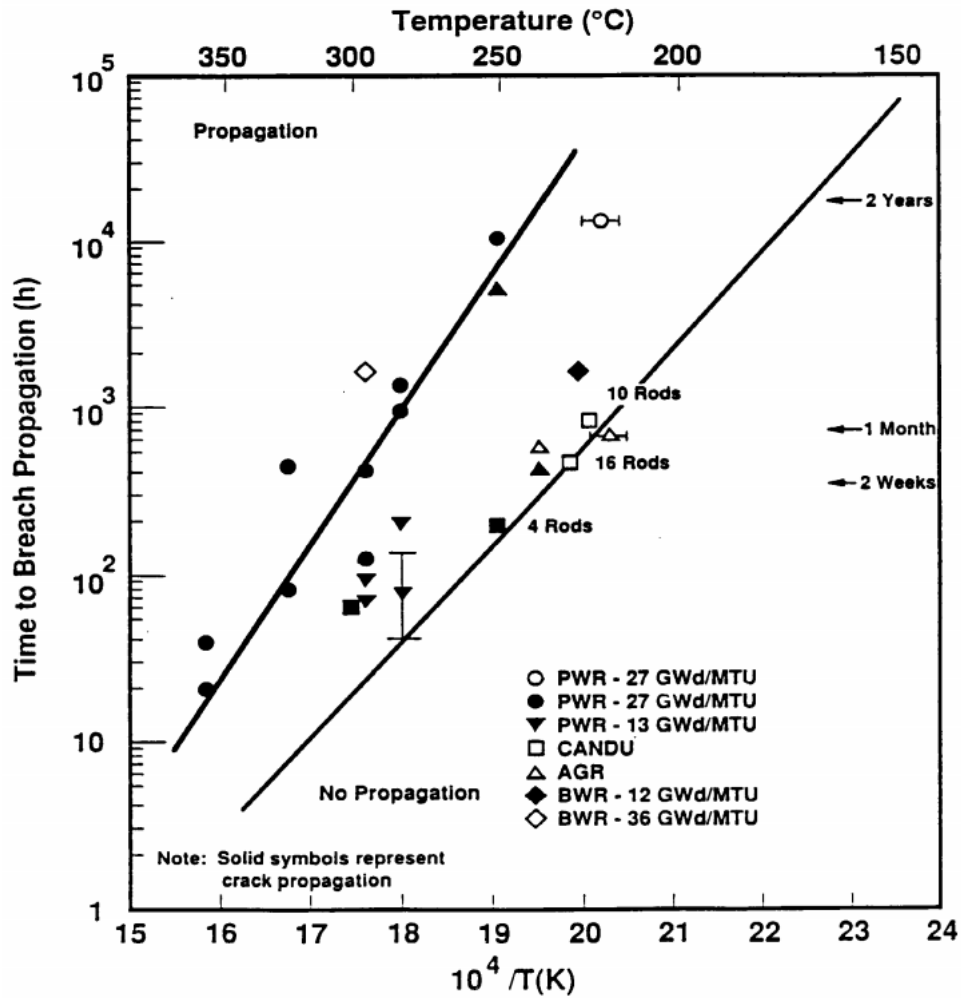


Figure 3.2.1-17 Time required to propagate existing cladding defects

- 1. Spent fuel has different oxidation behavior than unirradiated  $\text{UO}_2$**
- 2. Fuel variability affects oxidation rate in a transitory manner**
- 3. After transient, all tested fuels show similar oxidation behavior**
- 4. No effect of atmospheric moisture**
- 5. Test temperatures too low for oxidation beyond  $\text{UO}_{2.4}$**
- 6. Only  $\text{UO}_2$  and  $\text{U}_4\text{O}_9$  phases found at  $\text{O/M} < 2.4$**
- 7. At  $95^\circ\text{C}$ ,  $>2000$  years to reach plateau**

Figure 3.2.1-18 Preliminary conclusions

1. No tests of high-burnup or Gd-containing fuels
2. Long-term stability of  $\text{UO}_{2.4}$ ·  
Thermodynamics to aid modeling?
3. Oxidation kinetics beyond  $\text{UO}_{2.4}$  (to  $\text{U}_3\text{O}_8$ )
4. Tests on low burnup fuel (12 GWd/MTU) ?
5. Leaching studies from oxidized and  
non-oxidized fuel

Figure 3.2.1-19 Information needs

### 3.2.2 Oxidation Models

#### 3.2.2.1 Summary

This version (1.3) of the *Waste Form Characteristics Report* (WFCR) presents a review of the oxidation-response model that was developed for the two phase transitions:  $\text{UO}_2 \rightarrow \text{U}_4\text{O}_9$  and  $\text{U}_4\text{O}_9 \rightarrow \text{U}_3\text{O}_8$ , and its predictions for the geological repository. Because of the higher potential risk associated with the  $\text{U}_3\text{O}_8$  phase, modeling its phase transformation is emphasized.

In WFCR Version 1.2, the Arrhenius kinetic parameters for both phase transformations were obtained from a set of thermogravimetric-analysis (TGA) experiments of small (200 mg) ATM-105 spent-fuel samples (burnup 27 MWd/kgU). These TGA experiments were conducted at temperatures ranging from 283 to 325°C. That the two phase formation models gave reasonable responses was verified by comparing the model to an independent set of experimental data.

The oven drybath (ODB) experiments used a wide variety of pulverized and spent-fuel fragment sample (5 g); these experiments were conducted at 255°C. It was shown that the oxidation history could be explained by an envelope of various sizes of  $\text{UO}_2$  grains. This review of the kinetic-phase-transformation models and the predictions are presented in Sections 3.2.2.1 through 3.2.2.5.

Sections 3.2.2.6 through 3.2.2.11 presents new material whose focus is the formation of  $\text{U}_3\text{O}_8$ . Although Stout et al. (1993a, 1993b) predicted burnup would be a very important property in spent-fuel oxidation, only recently has Hanson (1998) obtained experimental evidence verifying this theoretical prediction. He showed that the activation energy for the phase transformation  $\text{U}_4\text{O}_9 \rightarrow \text{U}_3\text{O}_8$  varies linearly with burnup. Independent experimental evidence shows that, for burnups greater than 40 MWd/kgU, the  $\text{UO}_2$  grains undergo major restructuring to a much finer and more porous structure.

Several pieces of experimental information were combined in the new theoretical study. First, as  $\text{U}_4\text{O}_9$  forms, the relatively large, unoxidized  $\text{UO}_2$  grains undergo shrinkage cracking, yielding a log normal distribution of  $\text{U}_4\text{O}_9$  grains. Second, the linear activation-energy relation with burnup was also used. Using this approach, half of the TGA and ODB experiment histories were very closely matched. The other set of experiments could not be matched without using unrealistically small  $\text{U}_4\text{O}_9$  grains. Examination (by scanning electron microscopy [SEM] and X-ray fluorescence [XRF]) of some of these questionable samples revealed that a thin layer of what appears to be dehydrated schoepite had formed on the spent fuel. By adjusting the activation energy of some grain fractions downward, all TGA- and ODB-model history curves were within a 5% error of the experimental histories. Such close agreement of the model histories with experimental histories validates the model.

Using reasonable average grain sizes for  $\text{U}_4\text{O}_9$ , the model predicted the volume fractions of  $\text{U}_3\text{O}_8$  formed at 100 and 200°C at burnups of 25, 50, and 75 MWd/kgU. Even though the higher burnup fuels had smaller average grain sizes, the increased activation energy with burnup suppressed  $\text{U}_3\text{O}_8$  formation, even at a higher constant temperature.

#### 3.2.2.2 Introduction

$\text{UO}_2$  spent fuels oxidize to higher uranium oxide phases in an oxygen atmosphere. The oxidation response of spent fuels impacts the radionuclide-release performance in potential repository environments because of two independent functional properties of the higher oxides:

1. Due to geometrical surface area and volume changes that occur as the higher oxides form
2. Due to chemical changes that yield higher dissolution rates of the  $\text{U}_3\text{O}_8$  oxide and the  $\text{UO}_3$  oxide hydrates

To include these known impacts from  $\text{UO}_2$  spent-fuel oxidation for performance assessment (PA) analyses, a model for fuel-oxidation response has been developed.

Model development depends strongly on experimental data obtained from TGA and ODB oxidation testing methods. The modeling approach derives functional forms and uses functional relations consistent with the observed spent-fuel oxidation processes. These functional relations have parametric constants (e.g., the activation energy in the Arrhenius rate expression) that are evaluated by using subsets of the experimental data. The models for spent-fuel oxidation described in the following subsection provide response functions for the elapsed time to higher oxidation phases. These response functions depend on temperature, nominal grain size, and time.

Recent experimental studies have shown that the Arrhenius kinetics are burnup-dependent. The literature shows that, as the concentration of fission products (especially the rare earth isotopes) and the generated actinide products increase with burnup,  $\text{UO}_2$  becomes progressively more difficult to oxidize. Oxidation of the  $\text{UO}_2 \rightarrow \text{U}_4\text{O}_9$  has also shown to be controlled by diffusion of oxygen through the increasingly thicker layer of  $\text{U}_4\text{O}_9$ , with smaller-grained fuels oxidizing faster in accordance to a larger surface area to volume (SA/V) ratio. Thus, the rate of oxidation to higher uranium-oxide forms depends on burnup and the distribution of grain half-sizes. Although idealized, the model development is considered representative of the observed experimental processes that occur in spent-fuel oxidation. With the idealizations, the oxidation-response models for the different phase transformations can be easily applied to provide bounding evaluations and best-estimate values for oxidation impacts of spent-fuel performance in potential repository environments. The two spent-fuel oxidation-phase responses discussed in the following subsections are the  $\text{UO}_2 \rightarrow \text{U}_4\text{O}_9$  phase transformation and the  $\text{U}_4\text{O}_9 \rightarrow \text{U}_3\text{O}_8$  phase transformation.

The  $\text{U}_4\text{O}_9 \rightarrow \text{U}_3\text{O}_8$  phase transformation model used TGA oxidation data to evaluate kinetic parameters as a function of burnup. To partially substantiate the model, the oxidation data were compared to the predictions of the  $\text{U}_4\text{O}_9 \rightarrow \text{U}_3\text{O}_8$  oxidation model. This comparison with ODB data provided preliminary confirmation of the oxidation modeling development that used kinetic parameters evaluated from TGA data.

The updated model discussed in this section has the following new features:

- Activation-energy-dependence on burnup
- Log-normal distributions of grain half-sizes to account for the grain-cracking observed during  $\text{U}_4\text{O}_9$  formation
- The effect of what appears to be dehydrated schoepite formation observed on some experimental samples

At burnups greater than 40 to 45 MWd/kgU, the pellet rim progressively changes physically: the grain sizes get smaller, and takes on a porous cauliflower structure. In the previous version of this report, the bounding calculations were based on Arrhenius kinetics of ATM-105 spent fuel having a burnup of 27 MWd/kgU and larger grain sizes. Using the new information, the new performance predictions are considered much more realistic.



Fuels of sufficiently high burnup that have experienced restructuring in the rim region have much smaller grains, compared to the low-to-intermediate-burnup spent fuels. However, the activation energy for the  $U_4O_9 \rightarrow U_3O_8$  phase transformation varies linearly with burnup. The exponential dependence of this activation energy is orders of magnitude more important in suppressing this phase transformation than is the inversely proportional grain-size dependence in accelerating it.

The improved models, which is based on more recent information that will be presented, yields excellent fits to the TGA and the ODB tests. This agreement gives an extra degree of confidence that predictions of long-term geological repository safety of low- and high-burnup spent fuel are warranted.

Sections 3.2.2.2 through 3.2.2.5 present a review of the previous work; Sections 3.2.2.6 through 3.2.2.11 present more recent information, model enhancements, comparisons with TGA and ODB experiments, and improved predictions for safety of the geological repository.

#### 3.2.2.3 Oxidation Response of $UO_2$ to $U_4O_9$

The first oxidation-phase transition of  $UO_2$  spent fuel produces a  $U_4O_9$  lattice structure with a weight-gain “oxide” of  $UO_{-2.42}$ . Thus, the  $U_4O_9$  phase is not stoichiometric. This  $U_4O_9$  phase-transition time response has an Arrhenius temperature-dependence and a geometric dependence on grain size. At early times, the  $U_4O_9$  phase progresses very rapidly down the grain boundaries of the  $UO_2$  spent fuels. This elapsed time to oxidize grain boundaries is neglected in the following oxidation-response models. The rapid grain boundary oxidation is partly due to fission gas bubbles, which form on grain boundaries in spent fuels during reactor operation. These gas bubbles enhance porosity and decrease density of material in a grain boundary relative to material in an adjacent grain volume.

In addition, the  $U_4O_9$  lattice is more dense (has less specific volume) than that of the initial  $UO_2$  by about 1.5 to 2.0%. This higher density phase promotes grain-boundary cracking and opens grain-boundary pathways for oxygen transport to the surfaces of all the grain volumes in a spent-fuel fragment. The subsequent  $U_4O_9$  oxidation of grain volumes is observed to progress as a  $U_4O_9$  phase front that propagates into each  $UO_2$  grain. Behind this phase front is the  $U_4O_9$  crystal lattice structure with a weight-gain oxide of  $UO_{-2.42}$ . The rate of propagation of the  $U_4O_9$  front was conservatively evaluated as part of the ODB testing (Einziger, et al., 1992; Thomas, et al., 1992).

For a set of spent-fuel samples, experiments measured the position of the  $U_4O_9$ - $UO_2$  oxidation front relative to the grain boundary. Each sample in the set was oxidized for a different duration. These measurements of widths of  $U_4O_9$  oxidation front (relative to the grain boundary) versus oxidation time had an approximate square root time-dependence at constant temperature. The temperature-dependence was assumed to be an Arrhenius exponential function. Using this time- and temperature-dependence, the data in an upper bounding band were used to evaluate parameters  $k$  and  $Q$  in the following equations for the width  $W$  of the  $U_4O_9$  oxidation front

$$W = 2\sqrt{kt} \quad 3.2.2-1$$

where

$t$  = time (hours, h)

$k = k_o \exp(-Q_{49}/RT)$

$k_o = 1.04 \times 10^8 \text{ (}\mu\text{m}^2/\text{h)}$

$Q_{49} = 24.0 \text{ kcal/mole}$  (Arrhenius activation energy for the reaction  
 $\text{UO}_2 \rightarrow \text{U}_4\text{O}_9$ )

$R = 1.986 \text{ cal/mole/}^\circ\text{K}$  (gas constant)

$T$  = temperature (Kelvin)

The time derivative of Eq. 3.2.2-1 gives the rate that the  $\text{U}_4\text{O}_9$  propagates into a grain volume of  $\text{UO}_2$ , which, at constant temperature, is

$$\dot{W} = \sqrt{k/t} \quad 3.2.2-2$$

and which has an initial square root in time singularity. This is typical for surface-film formations that are rate-controlled by diffusion through a film of increasing thickness.

From Eq. 3.2.2-1, the elapsed time for oxidation of  $\text{UO}_2$  grains to  $\text{U}_4\text{O}_9$  can be evaluated by solving for time. Thus, the elapsed time  $t_{2.4}$  to fully oxidize a  $\text{UO}_2$  grain of nominal dimension  $2W_o$  to  $\text{U}_4\text{O}_9$  in atmospheric air at constant temperature  $T$  is

$$t_{2.4} = W_o^2 / (4k_o \exp(-Q_{49}/RT)) \quad 3.2.2-3$$

Table 3.2.2-1 lists the values of  $t_{2.4}$  for different temperatures and different nominal grain sizes.

### 3.2.2 Oxidation Models

Table 3.2.2-1 Elapsed time  $t_{2.4}$  for  $U_4O_9$  [LL980912451021.055]

Phase Transformation of UO <sub>2</sub> for Grain Size				T in C	250	200	150	100	75	50	25
2W <sub>0</sub> And Constant Temperature.				T in K	523.2	473.2	423.2	373.2	348.2	323.2	298.2
W <sub>0</sub> =Grainsize/2	DVU4O9/VUO <sub>2</sub>	DW/W <sub>0</sub>	DW								
10E-6 meters			10E-6 m		t2.4 Times in Hours, One Year = 24*365 = 8760 hours						
5	1	1	5		6.4558E+02	7.4109E+03	1.5144E+05	6.9461E+06	7.1027E+07	1.0407E+09	2.3916E+10
10	1	1	10		2.5823E+03	2.9643E+04	6.0577E+05	2.7784E+07	2.8411E+08	4.1627E+09	9.5663E+10
15	1	1	15		5.8102E+03	6.6698E+04	1.3630E+06	6.2515E+07	6.3924E+08	9.3660E+09	2.1524E+11
20	1	1	20		1.0329E+04	1.1857E+05	2.4231E+06	1.1114E+08	1.1364E+09	1.6651E+10	3.8265E+11
25	1	1	25		1.6139E+04	1.8527E+05	3.7860E+06	1.7365E+08	1.7757E+09	2.6017E+10	5.9789E+11
30	1	1	30		2.3241E+04	2.6679E+05	5.4519E+06	2.5006E+08	2.5570E+09	3.7464E+10	8.6097E+11
35	1	1	35		3.1633E+04	3.6313E+05	7.4206E+06	3.4036E+08	3.4803E+09	5.0993E+10	1.1719E+12
					t2.4 Times in Years						
					7.3696E-02	8.4599E-01	1.7288E+01	7.9293E+02	8.1081E+03	1.1880E+05	2.7301E+06
					2.9478E-01	3.3840E+00	6.9151E+01	3.1717E+03	3.2433E+04	4.7519E+05	1.0920E+07
					6.6326E-01	7.6139E+00	1.5559E+02	7.1364E+03	7.2973E+04	1.0692E+06	2.4571E+07
					1.1791E+00	1.3536E+01	2.7661E+02	1.2687E+04	1.2973E+05	1.9008E+06	4.3682E+07
					1.8424E+00	2.1150E+01	4.3220E+02	1.9823E+04	2.0270E+05	2.9699E+06	6.8253E+07
					2.6530E+00	3.0456E+01	6.2236E+02	2.8546E+04	2.9189E+05	4.2767E+06	9.8284E+07
					3.6111E+00	4.1453E+01	8.4710E+02	3.8854E+04	3.9730E+05	5.8211E+06	1.3378E+08

Parameters: Q<sub>49</sub> = 24,000 cal/ mole, kD = 1.04E + 8 micron<sup>2</sup>/h, R = 1.986 cal/ mole /K

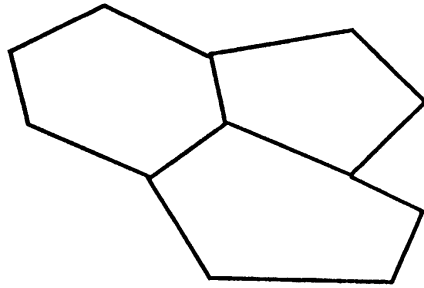
The use of constant temperature for elapsed times is an easy way to conservatively bound the time for full oxidation: pick the highest temperature value in the time interval. For repository evaluations, after the initial heat-up period, the temperatures are expected to be monotonically decreasing. Thus the temperature value when the spent fuel is initially exposed is conservatively high for the shortest elapsed time. To obtain a better approximation for the  $t_{2,4}$  elapsed time, the rate Eq. 3.2.2-2 can be assumed valid for quasi-steady temperature processes. Then the elapsed time  $t_{2,4}$  can be found by integration over the time-dependent temperature history such that  $W$  at  $t_{2,4}$  equals  $W_o$ .

The grain size is the other variable dependence in Eq. 3.2.2-3 used to calculate elapsed times for oxidation of  $UO_2 \rightarrow U_4O_9$ . Samples of spent fuels have a statistical distribution of grain sizes and geometrical shapes. Large samples for oxidation testing give better integration and averaging of grain-size distribution. This averaging process would tend to conceal second-order, or small, effects related to a detailed dependence on the statistical distribution attributes other than the mean, or average, grain size of a sample.

Similarly, the various geometric shapes, from six-sided cubic to many-sided approaching spherical, tend to be averaged over when testing with large samples. In the following, which is considered an effective or “macro” representation for oxidation response, grain-size distribution attributes are reduced to one, the nominal or average dimension of the grains. The nominal grain size will vary from sample to sample and does depend on the approved testing material (ATM) of the sample. Finally, to reduce modeling complexities, the geometric shape of the individual grains is assumed to be cubic; each grain is assumed to be subdivided into six pyramids with square bases. The cubes fill space contiguously and simplify the visualization of an idealized  $U_4O_9$  phase boundary propagating into a pyramidal subdivision of a cubical  $UO_2$  grain.

With the simplification of only nominal grain size and cubic-shaped grains, oxidation response for the volumetric quantity of  $U_4O_9$  at any time will be represented first as a rate and then as a time integral. Figures 3.2.2-1 through 3.2.2-3 provide sketches of the generic approach to create triangular (two-dimensional) spatial subsets and pyramidal (three-dimensional) spatial subsets of  $UO_2$  to  $U_4O_9$  oxidation fronts.

**A set of grain volumes (In cross section)**



**Put a point at the center of each grain, and decompose into a set of pyramids (triangles in cross section).**

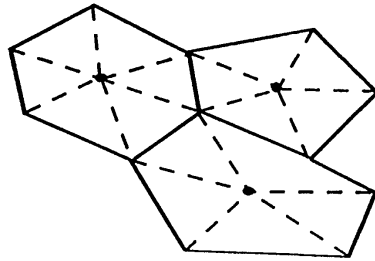


**Figure 3.2.2-1** Grain volume oxidation front: pyramidal volume in an oxidizing grain and its associated physical attributes

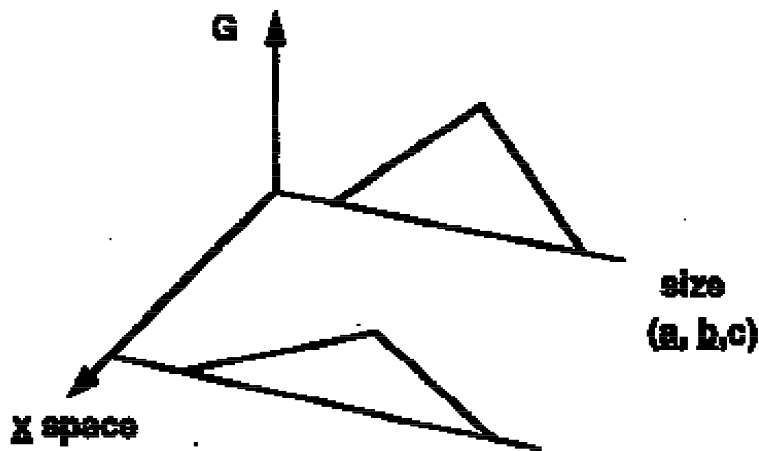


**Figure 3.2.2-2** Density function: probable number of grain pyramids

Large numbers of grain pyramids exist, many of which are of the same size (compact domain set). A size can be identified by attributes (a, b, c), as illustrated. Let  $G(x, t, a, b, c)$  denote the probable number of pyramids of size (a, b, c) in a unit spatial volume of grains about point x at time t.

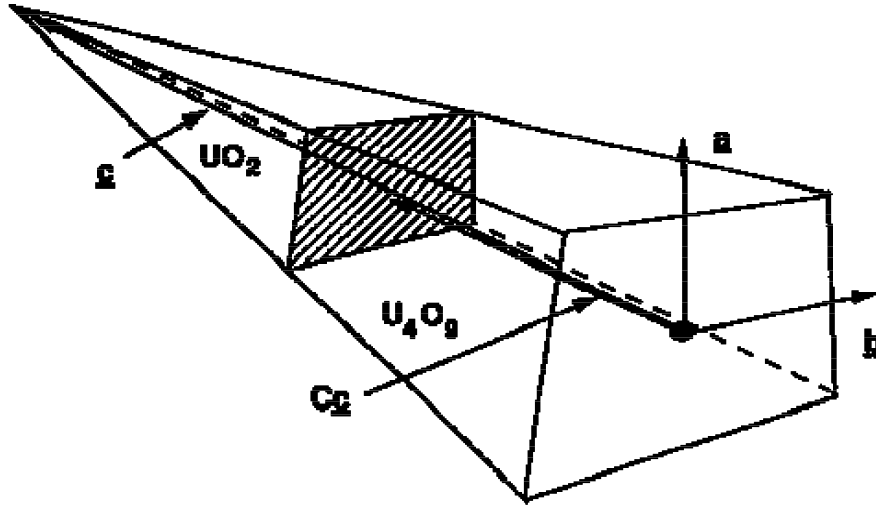


**Figure 3.2.2-3 Grain volume oxidation front: pyramidal volume in an oxidizing grain and its associated physical attributes**

The size attributes of the pyramids shown in Figure 3.2.2-3 are vector sets  $\{\underline{a}, \underline{b}, \underline{c}\}$ . Vectors  $\underline{a}$  and  $\underline{b}$  are the bases vectors of the pyramid, and  $\underline{c}$  is the height vector from a base (face of a cube) to the center of the grain. There are six vector sets per cube. In the case of cubic grains, the length  $W_o$  of vector  $\underline{c}$  is one-half the length of vector  $\underline{a}$  or  $\underline{b}$ .

The rate of oxygen weight gain for a single pyramid is equal to the instantaneous area of the front moving at its frontal velocity along vector  $\underline{c} \times$  the weight of oxygen added to convert  $\text{UO}_2$  to  $\text{U}_4\text{O}_9$  at oxide weight of  $\text{UO}_{2.42}$ . The instantaneous area is linearly reduced in vectors  $\underline{a}$  and  $\underline{b}$  as the front moves along vector  $\underline{c}$ . This area-reduction can be written in terms of a scalar function of time  $C(t)$ , which has a value between zero and one and scales the length of vector  $\underline{c}$  that has been converted to  $\text{U}_4\text{O}_9$  from  $\text{UO}_2$ . When  $C$  equals zero, the pyramid is all  $\text{UO}_2$ ; when  $C$  equals one, the pyramid is all  $\text{U}_4\text{O}_9$ . Thus,  $\underline{c}\dot{C}(t)$  is the current width of the  $\text{U}_4\text{O}_9$  front. At width  $C(t)$ , the reduced length of  $\underline{a}$  and  $\underline{b}$  would be  $\underline{a}(1-C)$  and  $\underline{b}(1-C)$ , respectively. The  $\text{U}_4\text{O}_9$  frontal velocity would be  $\underline{c}\dot{C}(t)$ . From Eq. 3.2.2-2 for  $\dot{W}$ , the function of  $\dot{C}(t)$  is given by

$$\dot{C}(t) = \dot{W}/|\underline{c}| = \sqrt{k/t}/|\underline{c}| \quad 3.2.2-4$$

where  $|\underline{c}|$  is the scalar magnitude of vector  $\underline{c}$  and  $k$  is a function of temperature. The amount of oxygen added per atom of uranium to form the  $\text{UO}_2$  oxide at the points on the  $\text{UO}_2$ -to- $\text{U}_4\text{O}_9$  phase front is chemically known to be



or 0.42 oxygen atoms per each uranium atom. Thus, when the phase boundary is at  $\underline{C}_t$ , the rate that oxygen atoms are added per cubic grain of  $\text{UO}_2$  is

$$[\dot{O}] = 0.42[U]\dot{C}(t)c_{ijk}a_j(1-C(t))b_k(1-C(t)) \quad 3.2.2-6$$

In Eq. 3.2.2.3-6,  $e_{ijk}$  is an alternating tensor used to form the vector dot product of  $\underline{c}$  with the vector cross product of vectors  $\underline{a}(1-C)$  and  $\underline{b}(1-C)$  for the six, pyramidal pieces of a cube;  $[U]$  is the number of uranium atoms per unit volume of the  $UO_2$  spent fuel. To find the change in  $[O]/[U]$  ratio for a partially oxidized sample of  $UO_2$  and  $U_4O_9$ , Eq. 3.2.2.3-6 must be multiplied by the number of grains in the sample and integrated over the time interval during which partial oxidation has occurred. This time interval is less than the value of  $t_{2.4}$  evaluated from Eq. 3.2.2.3. For  $G$  number of grains in the samples, this integration yields the following expression (Stout, et al., 1989).

$$[O]/[U](UO_2 \rightarrow U_{2.42}; t) = 0.42(6Gc_i e_{ijk} a_j b_k (3C(t) - 3C^2(t) + C^3(t)))/3 \quad 3.2.2-7$$

For a sample of  $G$  (total number) cubical grains, this ratio is

$$[O]/[U]V_{UO_2}(G) = 0.42(3C(t) - 3C^2(t) + C^3(t)) \quad 3.2.2-8a$$

where the initial volume of  $UO_2$  is

$$V_{UO_2}(G) = 6Gc_i e_{ijk} a_j b_k / 3 \quad 3.2.2-8b$$

From Eq. 3.2.2-7, the volume amount of  $UO_{2.4}$  formed for a sample of  $G$  grains at time  $t < t_{2.4}$  is

$$V_{UO_{2.4}}(G, t) = 6Gc_i e_{ijk} a_j b_k (3C(t) - 3C^2(t) + C^3(t))/3 \quad 3.2.2-9$$

which is also a parametric function of the temperature history and neglects the small volume decrease ( $\sim 2\%$ ) from the phase transformation. The function  $C(t)$  is the time integration of Eq. 3.2.2.3-4, with  $C(t=0)$  equal to zero, which is

$$C(t) = 2\sqrt{kt}/|\underline{c}| \quad \text{and } C(t) = 1 \text{ for } t \geq t_{2.4} \quad 3.2.2-10$$

where  $k$  is given as a function of temperature in Eq. 3.2.2-1, and  $|\underline{c}|$  is one-half the nominal length of an effective cubic grain. From Eq. 3.2.2-8 and Eq. 3.2.2-9, the volume fraction of a sample of cubic grains that is  $UO_2$  at time  $t$  is given by

$$V_{UO_{2.4}}(G, t)/V_{UO_2}(G) = 3C(t) - 3C^2(t) + C^3(t) \quad 3.2.2-11$$

that, from Eq. 3.2.2-10, depends on grain size and temperature ( $k$  is temperature-dependent).

Eq. 3.2.2-11 can be inverted to find the elapsed time  $t_v$  during which a prescribed volume fraction of  $UO_{2.44}$  has transformed from  $UO_2$  at constant temperature. The inverse is found by adding one to the negative of equation 3.2.2.3-11 to obtain

$$(1 - C(t))^3 = (1 - V_{UO_{2.4}}/V_{UO_2}) \quad 3.2.2-12a$$

Then

$$C(t) = 1 - \left(1 - V_{\text{UO}_{2.4}}/V_{\text{UO}_2}\right)^{1/3} \quad 3.2.2-12b$$

Using equation 3.2.2-1 and 3.2.2-10, the elapsed time  $t_{v2.4}$  for a prescribed volume fraction of  $\text{UO}_{2.4}$  at constant temperature is

$$t_{v2.4} = |c|^{-2} \left(1 - \left(1 - V_{\text{UO}_{2.4}}/V_{\text{UO}_2}\right)^{1/3}\right)^2 / \left(4k_o \exp(-Q_{49}/RT)\right) \quad 3.2.2-13$$

Note that, as the volume fraction of  $\text{UO}_{2.4}$  approaches unity, Eq. 3.2.2-13 becomes the same as Eq. 3.2.2.3-3 because  $W_o$  equals  $|c|$ . Tables 3.2.2.3-2 through 3.2.2.3-4 have elapsed times  $t_{v2.4}$  for 25%, 50%, and 75% volume fractions of  $\text{U}_4\text{O}_9$ .



### 3.2.2 Oxidation Models

Table 3.2.2-2 Elapsed time  $t_{2.4r}$  25%  $U_4O_9$  [LL980912451021.055]

Phase Transformation of UO <sub>2</sub> for Grain Size				T in C	250	200	150	100	75	50	25
2W <sub>o</sub> And Constant Temperature.				T in K	523.2	473.2	423.2	373.2	348.2	323.2	298.2
W <sub>o</sub> =Grainsize/2	DVU4O9/VUO2	DW/W <sub>o</sub>	DW								
10E-6 meters			10E-6 m		tv2.4 Times in Hours, One Year = 24*365 = 8760 hours						
5	0.25	0.091439695	0.457198474		5.3978E+00	6.1964E+01	1.2662E+03	5.8078E+04	5.9387E+05	8.7012E+06	1.9997E+08
10	0.25	0.091439695	0.914396949		2.1591E+01	2.4786E+02	5.0649E+03	2.3231E+05	2.3755E+06	3.4805E+07	7.9986E+08
15	0.25	0.091439695	1.371595423		4.8580E+01	5.5767E+02	1.1396E+04	5.2270E+05	5.3449E+06	7.8311E+07	1.7997E+09
20	0.25	0.091439695	1.828793897		8.6365E+01	9.9142E+02	2.0260E+04	9.2924E+05	9.5020E+06	1.3922E+08	3.1994E+09
25	0.25	0.091439695	2.285992372		1.3494E+02	1.5491E+03	3.1656E+04	1.4519E+06	1.4847E+07	2.1753E+08	4.9991E+09
30	0.25	0.091439695	2.743190846		1.9432E+02	2.2307E+03	4.5584E+04	2.0908E+06	2.1379E+07	3.1324E+08	7.1987E+09
35	0.25	0.091439695	3.20038932		2.6449E+02	3.0362E+03	6.2046E+04	2.8458E+06	2.9100E+07	4.2636E+08	9.7983E+09
					tv2.4 Times in Years						
					6.1619E-04	7.0735E-03	1.4455E-01	6.6299E+00	6.7794E+01	9.9329E+02	2.2827E+04
					2.4647E-03	2.8294E-02	5.7819E-01	2.6519E+01	2.7118E+02	3.9732E+03	9.1308E+04
					5.5457E-03	6.3661E-02	1.3009E+00	5.9669E+01	6.1014E+02	8.9396E+03	2.0544E+05
					9.8590E-03	1.1318E-01	2.3128E+00	1.0608E+02	1.0847E+03	1.5893E+04	3.6523E+05
					1.5405E-02	1.7684E-01	3.6137E+00	1.6575E+02	1.6948E+03	2.4832E+04	5.7068E+05
					2.2183E-02	2.5465E-01	5.2037E+00	2.3868E+02	2.4406E+03	3.5758E+04	8.2177E+05
					3.0193E-02	3.4660E-01	7.0828E+00	3.2486E+02	3.3219E+03	4.8671E+04	1.1185E+06

Parameters: Q<sub>49</sub> = 24,000 cal/ mole, kD = 1.04E + 8 micron<sup>2</sup>/h, R = 1.986 cal/ mole/ K

Table 3.2.2-3 Elapsed time  $t_{2.4}$ , 50%  $U_4O_9$  [LL980912451021.055]

Phase Transformation of UO <sub>2</sub> for Grain Size				T in C	250	200	150	100	75	50	25
2Wo And Constant Temperature.				T in K	523.2	473.2	423.2	373.2	348.2	323.2	298.2
Wo=Grainsize/2	DVU4O9/VUO2	DW/Wo	DW								
10E-6 meters			10E-6 m		tv2.4 Times in Hours, One Year = 24*365 = 8760 hours						
5	0.5	0.206299456	1.031497278		2.7475E+01	3.1540E+02	6.4453E+03	2.9562E+05	3.0229E+06	4.4290E+07	1.0178E+09
10	0.5	0.206299456	2.062994557		1.0990E+02	1.2616E+03	2.5781E+04	1.1825E+06	1.2092E+07	1.7716E+08	4.0714E+09
15	0.5	0.206299456	3.094491835		2.4728E+02	2.8386E+03	5.8007E+04	2.6606E+06	2.7206E+07	3.9861E+08	9.1606E+09
20	0.5	0.206299456	4.125989114		4.3961E+02	5.0464E+03	1.0312E+05	4.7299E+06	4.8366E+07	7.0864E+08	1.6285E+10
25	0.5	0.206299456	5.157486392		6.8688E+02	7.8851E+03	1.6113E+05	7.3905E+06	7.5572E+07	1.1073E+09	2.5446E+10
30	0.5	0.206299456	6.18898367		9.8911E+02	1.1354E+04	2.3203E+05	1.0642E+07	1.0882E+08	1.5944E+09	3.6642E+10
35	0.5	0.206299456	7.220480949		1.3463E+03	1.5455E+04	3.1582E+05	1.4485E+07	1.4812E+08	2.1702E+09	4.9874E+10
					tv2.4 Times in Years						
					3.1365E-03	3.6005E-02	7.3576E-01	3.3747E+01	3.4508E+02	5.0560E+03	1.1619E+05
					1.2546E-02	1.4402E-01	2.9430E+00	1.3499E+02	1.3803E+03	2.0224E+04	4.6477E+05
					2.8228E-02	3.2404E-01	6.6219E+00	3.0372E+02	3.1057E+03	4.5504E+04	1.0457E+06
					5.0183E-02	5.7608E-01	1.1772E+01	5.3995E+02	5.5212E+03	8.0895E+04	1.8591E+06
					7.8411E-02	9.0012E-01	1.8394E+01	8.4367E+02	8.6269E+03	1.2640E+05	2.9048E+06
					1.1291E-01	1.2962E+00	2.6487E+01	1.2149E+03	1.2423E+04	1.8201E+05	4.1829E+06
					1.5369E-01	1.7642E+00	3.6052E+01	1.6536E+03	1.6909E+04	2.4774E+05	5.6934E+06

Parameters: Q<sub>49</sub> = 24,000 cal/mole, kD = 1.04E + 8 micron<sup>2</sup>/h, R = 1.986 cal/mole/K

### 3.2.2 Oxidation Models

Table 3.2.2-4 Elapsed time  $t_{2.4}$  75%  $U_4O_9$  [LL980912451021.055]

Phase Transformation of UO <sub>2</sub> for Grain Size				T in C	250	200	150	100	75	50	25
2W <sub>0</sub> And Constant Temperature.				T in K	523.2	473.2	423.2	373.2	348.2	323.2	298.2
W <sub>0</sub> =Grainsize/2	DVU4O9/VUO2	DW/W <sub>0</sub>	DW								
10E-6 meters			10E-6 m		tv2.4 Times in Hours, One Year = 24*365 = 8760 hours						
5	0.75	0.370039446	1.85019723		8.8398E+01	1.0148E+03	2.0737E+04	9.5112E+05	9.7257E+06	1.4250E+08	3.2748E+09
10	0.75	0.370039446	3.700394459		3.5359E+02	4.0591E+03	8.2947E+04	3.8045E+06	3.8903E+07	5.6999E+08	1.3099E+10
15	0.75	0.370039446	5.550591689		7.9558E+02	9.1329E+03	1.8663E+05	8.5601E+06	8.7531E+07	1.2825E+09	2.9473E+10
20	0.75	0.370039446	7.400788919		1.4144E+03	1.6236E+04	3.3179E+05	1.5218E+07	1.5561E+08	2.2800E+09	5.2396E+10
25	0.75	0.370039446	9.250986149		2.2100E+03	2.5369E+04	5.1842E+05	2.3778E+07	2.4314E+08	3.5624E+09	8.1869E+10
30	0.75	0.370039446	11.10118338		3.1823E+03	3.6531E+04	7.4652E+05	3.4240E+07	3.5013E+08	5.1299E+09	1.1789E+11
35	0.75	0.370039446	12.95138061		4.3315E+03	4.9723E+04	1.0161E+06	4.6605E+07	4.7656E+08	6.9824E+09	1.6046E+11
					tv2.4 Times in Years						
					1.0091E-02	1.1584E-01	2.3672E+00	1.0858E+02	1.1102E+03	1.6267E+04	3.7383E+05
					4.0364E-02	4.6336E-01	9.4688E+00	4.3430E+02	4.4410E+03	6.5067E+04	1.4953E+06
					9.0820E-02	1.0426E+00	2.1305E+01	9.7718E+02	9.9922E+03	1.4640E+05	3.3645E+06
					1.6146E-01	1.8534E+00	3.7875E+01	1.7372E+03	1.7764E+04	2.6027E+05	5.9813E+06
					2.5228E-01	2.8960E+00	5.9180E+01	2.7144E+03	2.7756E+04	4.0667E+05	9.3458E+06
					3.6328E-01	4.1703E+00	8.5220E+01	3.9087E+03	3.9969E+04	5.8561E+05	1.3458E+07
					4.9446E-01	5.6762E+00	1.1599E+02	5.3202E+03	5.4402E+04	7.9707E+05	1.8318E+07

Parameters: Q<sub>49</sub> = 24,000 cal/mole, kD = 1.04E + 8 micron<sup>2</sup>, R = 1.986 cal/mole/K

In summarizing the preceding oxidation model for the phase transition of  $\text{UO}_2$  to  $\text{U}_4\text{O}_9$  (often written as  $\text{UO}_{2.4}$  or  $\text{UO}_{2.42}$ ), Eq. 3.2.2-3 can be evaluated for the elapsed time  $t_{2.4}$  for complete transformation of  $\text{UO}_2$  to  $\text{U}_4\text{O}_9$ . Eq. 3-2-2-10 [for  $C(t)$ ] and Eq. 3.2.2-11 can be evaluated for the volume fraction of  $\text{UO}_{2.4}$  relative to  $\text{UO}_2$  at times  $t$  less than  $t_{2.4}$ . Eq. 3.2.2.3-13 can be evaluated for the time  $t_{v,2.4}$  at which a prescribed fractional volume of  $\text{UO}_{2.4}$  relative to  $\text{UO}_2$  is attained. In each case, the results calculated from these equations depend on grain size  $|c|$  and temperature history  $T$ .

A full comparison of this model with future TGA and ODB oxidation weight-gain data will be provided as part of a model-validation process. Because grain size is a parameter of the model and has a distribution in any sample, a bounding model will most likely be proposed. For now, a nominal value for grain size is recommended to be an estimated average value of the particular spent fuel sample's grain size. The grain size is not a parameter readily known for all commercial spent fuels. A best estimate may be obtainable by a survey of nuclear fuel vendors. Otherwise, the range of grain size in the current ATM could be used as a sparse data set from which to stochastically evaluate the oxidation impact on spent fuel performance in a suitable repository.

### 3.2.2.4 Oxidation Response of $\text{U}_4\text{O}_9$ to $\text{U}_3\text{O}_8$

Following the  $\text{UO}_2$ -to- $\text{U}_4\text{O}_9$ -phase transformation, the second oxidation-phase transition of spent fuels is from  $\text{U}_4\text{O}_9$  to a  $\text{U}_3\text{O}_8$  phase. The transition time to initiate the  $\text{U}_3\text{O}_8$ -phase change has a temperature-dependent delay time. The kinetics of this delay-time response is not understood in detail. It is believed to be related to the elapsed time for diffusion of oxygen into grain volumes and surface adsorption of oxygen onto grain surfaces of the  $\text{U}_4\text{O}_9$ . Hanson (1998) showed that the plateau and the oxidation to  $\text{U}_3\text{O}_8$  have the same activation energies and explained this observation as a restructuring of the crystal lattice. Until  $\text{UO}_2$  is fully converted to the  $\text{U}_4\text{O}_9$  phase, there will be no  $\text{U}_3\text{O}_8$  formation. During the delay-time interval, these diffusion and adsorption processes increase the local spatial concentration of oxygen atoms sufficiently for the  $\text{U}_3\text{O}_8$  oxidation transformation to occur. Early observations indicated that the delay time was relatively monotonic with respect to temperature. That is, the lower constant temperature tests showed longer elapsed times to initiate the transformations of  $\text{U}_3\text{O}_8$  (Einziger, et al., 1992, 1995). The duration of this elapsed time was estimated to be long at low temperatures ( $6 \times 10^7$  yr at  $100^\circ\text{C}$ ).

However, recent TGA test data show variations in the elapsed times for  $\text{U}_3\text{O}_8$  initiation at constant temperature. The elapsed-time duration is the length of time that a plateau exists in the oxygen-to-metal (O/M) weight-gain-time response plots of the test data. The variations in elapsed times are observed for a sequence of TGA tests, which are all at the same constant temperature, on small ( $\sim 200$  mg) spent-fuel fragments from the high-burnup region of the same fuel rod. This suggests that the variability is associated with small spatial differences of the spent-fuel test samples. The current conjecture is that the radial location of a test sample influences the  $\text{U}_3\text{O}_8$  oxidation response. This radial dependence is linked to a well-known "rim" region on the circumference of the pellet where higher  $^{238}\text{U}$  resonance-capture of incoming neutrons occurs. This locally increases the density of plutonium isotopes and correspondingly enriches fissile isotopic density in the rim region ( $\sim 200$   $\mu\text{m}$ ). The consequences of this enriched fissile-density radial gradient is a radial burnup gradient with higher concentrations of fission products and actinides in the rim region relative to the central portion of a pellet. It is hypothesized that the sample-to-sample variations in observed  $\text{U}_3\text{O}_8$ -oxidation response are due to radial chemical compositional variations from the burnup gradient.

Until these variations are understood, no credible model for the plateau delay time to initiate  $\text{U}_3\text{O}_8$ -oxidation response can be analytically represented. In terms of time-response models of oxidation, the neglect of this plateau delay time is conservative. This leads to a modeling assumption that the  $\text{U}_3\text{O}_8$ -oxidation response is initiated at the time the  $\text{U}_4\text{O}_9$  phase transformation is completed. This elapsed time is  $t_{2,4}$  evaluated from Eq. 3.2.2-3.

For times  $t$  greater than  $t_{2,4}$ , the following preliminary model of  $\text{U}_3\text{O}_8$  oxidation response is based on five assumptions:

1. The oxide that forms on the outer surfaces of the  $\text{U}_4\text{O}_9$  grains is essentially  $\text{U}_3\text{O}_8$  phase. ( $\text{U}_3\text{O}_8$  lattice has been identified in the TGA test samples; however, some powders found in the ODB 255°C test samples remain an enigma.)
2. The oxide surface is nonprotective; this follows for a  $\text{U}_3\text{O}_8$  phase because the large (~30%) volume increase of  $\text{U}_3\text{O}_8$  relative to  $\text{U}_4\text{O}_9$  causes the  $\text{U}_3\text{O}_8$  oxide surface to crack and spall, leaving the  $\text{U}_4\text{O}_9$  surface continuously exposed.
3. The  $\text{U}_3\text{O}_8$  boundary proceeds at constant speed into the  $\text{U}_4\text{O}_9$  grain volumes, which is really a consequence of the second assumption.
4. The high temperature data (250°C to 300°C) can be extrapolated to lower temperatures (25°C to 100°C).
5. The phase transition to  $\text{U}_4\text{O}_9$  must be completed before the phase transition to  $\text{U}_3\text{O}_8$  is initiated.

Note that these assumptions make the  $\text{U}_3\text{O}_8$ -oxidation geometric response similar to that of  $\text{U}_4\text{O}_9$  (i.e., an oxidation front that propagates into a grain volume). Thus, Figures 3.2.2-1 through 3.2.2-3 illustrate the frontal propagation, only now the  $\text{U}_3\text{O}_8$  replaces  $\text{U}_4\text{O}_9$ , and  $\text{U}_4\text{O}_9$  replaces  $\text{UO}_2$  of the figures.

Given these five assumptions, the TGA data can be used to provide preliminary estimates of the  $\text{U}_3\text{O}_8$  oxidation response. The data shown in Figure 3.2.2-4 (Einziger, et al., 1995) shows TGA oxidation data at five temperatures for spent-fuel samples from ATM-105. The three higher temperature curves (325°C, 305°C, and 283°C) show that the  $\text{U}_3\text{O}_8$ -oxidation response rate is less than the  $\text{U}_4\text{O}_9$ -oxidation response rate.

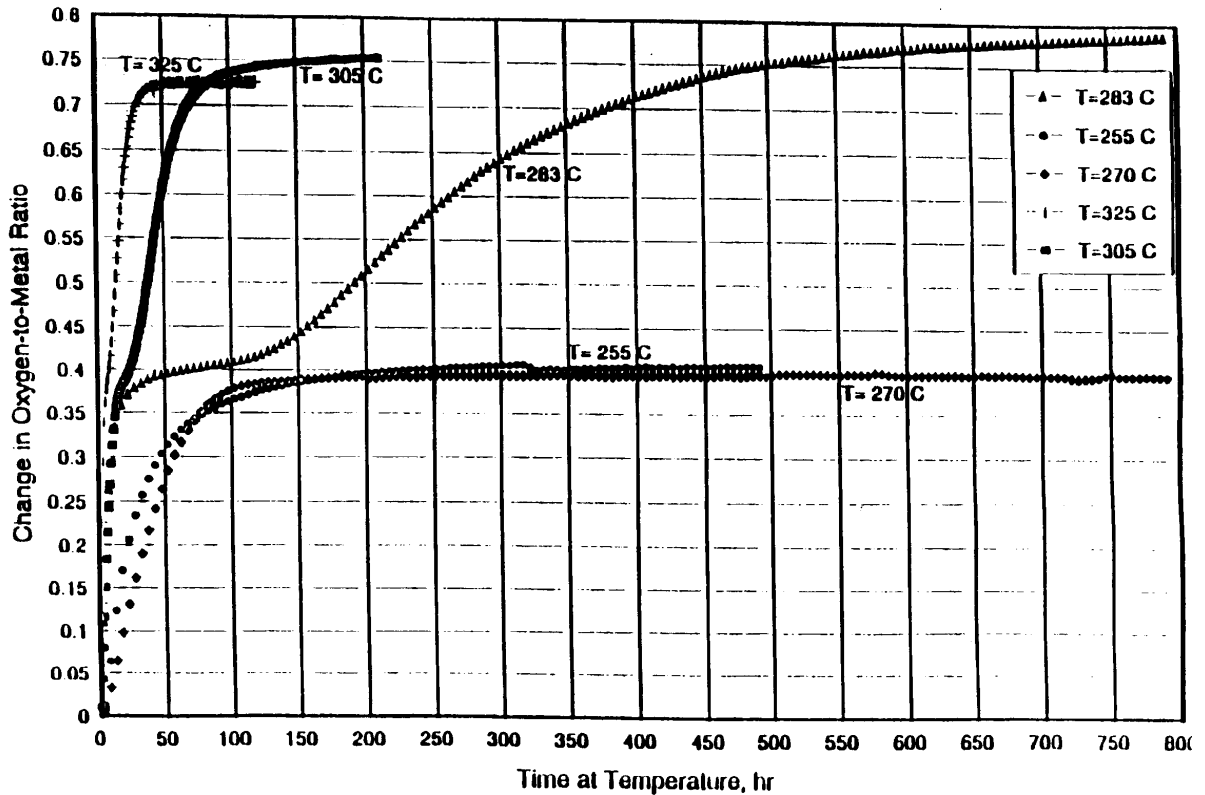


Figure 3.2.2-4 Oxidation of ATM-105 fuel at various temperatures

From these three curves, two methods exist to estimate the  $U_3O_8$ -oxidation rate response. One method is to graphically estimate the early time slopes of these curves as  $U_3O_8$  forms and to use these values to calculate an Arrhenius activation energy. With additional analysis, an estimate for the speed of the  $U_3O_8$  oxidation can be derived. The estimated slope and temperature values for the activation energy were  $(1.65 \times 10^{-2}/h, 598.2 \text{ K})$ ,  $(8.47 \times 10^{-3}/h, 578.2 \text{ K})$ , and  $(1.46 \times 10^{-3}/h, 556.2 \text{ K})$ . The activation energy estimate from these data was 38540 cal/mole.

For this reason, a second method was used to estimate the frontal speed of the  $U_3O_8$  oxidation process. This method used graphic estimates for the elapsed times to full oxidation from the  $U_4O_9$  plateau to a  $U_3O_8$  phase. The elapsed time is the time interval from estimated initiation of  $U_3O_8$  to estimated completion of  $U_3O_8$ , totally converted  $U_4O_9$ . This elapsed time neglects the delay elapsed time of the plateau and is a conservative estimate for the elapsed time to fully oxidize to  $U_3O_8$ . The three values for time intervals and temperatures were (33.33 h, 598.2 K), (106.25 h, 578.2 K), and (425.0 h, 556.2 K). The activation energy from these data was 40057 cal/mole, which is similar to the active energy of the previous method. The samples of spent fuel for these test data were all from ATM-105, which has a nominal grain size of 13  $\mu\text{m}$ . For constant temperature histories, the speed of the  $U_3O_8$  oxidation front was previously assumed constant, hence the frontal speed  $\dot{W}_{38}$  or  $|c|\dot{C}_{38}$  is given by an Arrhenius expression. The rate  $\dot{W}_{38}$  is given by

$$\dot{W}_{38} = k_{38} \exp(-Q_{38}/RT) \quad 3.2.2-14a$$

where  $Q_{38}$  and  $k_{38}$  can be estimated from the ATM-105:

$$\begin{aligned} Q_{38} &= 40057 \text{ cal/mole (Arrhenius activation energy for the reaction } U_4O_9 \rightarrow U_3O_8) \\ k_{38} &= 8.58 \times 10^{13} \text{ } \mu\text{m/h using } |\underline{c}| = 6.5 \text{ } \mu\text{m for ATM-105} \\ R &= 1.986 \text{ cal/mole K} \\ T &= \text{temperature Kelvin} \end{aligned}$$

The  $U_3O_8$  frontal speed  $\dot{W}_{38}$  for any grain size is constant and  $\dot{C}_{38}$  is given by

$$\dot{C}_{38} = \dot{W}_{38} / |\underline{c}| \quad 3.2.2-14b$$

The preceding values for  $k_{38}$  and  $Q_{38}$  are preliminary and will be evaluated again as additional data become available. The preceding activation-energy value is higher than that of unirradiated fuel, but lower than expected when burnup-dependence is used.

The oxidation rate, in terms of  $[\dot{O}]$  to  $[M]$  response for  $U_3O_8$  is analogous to that of Eq. 3.2.2-6 for  $U_4O_9$ , except that the factor for the number of oxygen atoms added per uranium atom changes from 0.42. For the  $U_3O_8$ -oxidation response, which is also not stoichiometric, the oxidation curves plateau around  $UO_{2.75}$ , which chemically implies



Thus, each uranium atom will require, on the average, 0.33 of an oxygen atom to form a  $U_3O_8$  lattice cell at the  $UO_{2.42}$  oxidation front. With this value for oxygen atoms added per uranium atom for  $U_3O_8$ -phase transformation, and the frontal speed of Eq. 3.2.2-14, the rate of  $U_3O_8$  oxidation for a pyramidal section of a cubic grain follows analogously from Eq. 3.2.2-6 as

$$[\dot{O}]/[U](U_4O_9 \rightarrow U_3O_8; t) = 0.33 \dot{C}_{38} c_i e_{ijk} a_j (1 - C_{38}(t)) b_k (1 - C_{38}(t)) \quad 3.2.2-16$$

for times  $t \geq t_{2.4}$  of the  $U_4O_9$  oxidation.

In Eq. 3.2.2-16,  $\dot{C}_{38}$  is constant for a prescribed constant temperature and a nominal grain dimension  $|\underline{c}|$  as given in Eq. 3.2.2-14; i.e.,

$$\dot{C}_{38} = (k_{38} / |\underline{c}|) \exp(-Q_{38} / RT) \quad 3.2.2-17a$$

and  $C_{38}(t)$  is the time integration of  $\dot{C}_{38}$  for  $t > t_{2.4}$ , which, for constant temperature, is

$$C_{38}(t) = (t - t_{2.4}) \dot{C}_{38} \quad \text{for } t_{2.4} < t < tot_{3.8} \quad 3.2.2-17b$$

The time  $tot_{3.8}$  occurs at the time  $C_{38}$  equals unity. It is the total elapsed time from initial exposure of the  $UO_2$  at time  $t$  set to zero for the  $UO_2$  to change fully through the  $U_4O_9$  and  $U_3O_8$  phases. It does not include any estimate of the delay elapsed time of the plateau region

thus, for a model response, it is conservative. Thus,  $tot_{38}$  consists of a  $t_{2.4}$  time and  $t_{3.8}$ ; the former given by Eq. 3.2.2-3 and the latter incremental time from Eq. 3.2.2-17a, when  $C_{38}$  is one, is given by

$$t_{3.8} = |\underline{c}| / (k_{38} \exp(-Q_{38}/RT)) \quad 3.2.2-18a$$

Recall that  $|\underline{c}|$  is  $W_{or}$  half the grain size. Then  $tot_{3.8}$  is

$$tot_{3.8} = t_{2.4} + t_{3.8} \quad 3.2.2-18b$$

Values of elapsed time  $t_{3.8}$  are given in Table 3.2.2-5 for different constant temperature histories and nominal grain sizes.



### 3.2.2 Oxidation Models

**Table 3.2.2-5 Elapsed time  $t_{3.8}$  for  $U_3O_8$  [LL980912451021.055]**

1	Table 3.2.2-5. Elapsed Time, $t_{3.8}$ , for $U_3O_8$				273.2	Parameters: Q38=40057 cal/mole, k38=8.58E+13 micron/h, R=1.986 cal/mole/K					
2	Phase Transformation of $UO_2$ for Grain Size				T in C	250	200	150	100	75	50
3	2Wo And Constant Temperature.				T in K	523.2	473.2	423.2	373.2	348.2	323.2
4	Wo=Grainsize/2	DVU3O8/VUO2	DW/Wo	DW							
5	10E-6 meters			10E-6 m		$t_{3.8}$ Elapsed Times in Hours, One Year = $24 \times 365 = 8760$ hours					
6	5	1	1	5		3.2196E+03	1.8917E+05	2.9103E+07	1.7260E+10	8.3607E+11	7.3817E+13
7	10	1	1	10		6.4393E+03	3.7835E+05	5.8205E+07	3.4520E+10	1.6721E+12	1.4763E+14
8	15	1	1	15		9.6589E+03	5.6752E+05	8.7308E+07	5.1780E+10	2.5082E+12	2.2145E+14
9	20	1	1	20		1.2879E+04	7.5669E+05	1.1641E+08	6.9039E+10	3.3443E+12	2.9527E+14
10	25	1	1	25		1.6098E+04	9.4587E+05	1.4551E+08	8.6299E+10	4.1804E+12	3.6908E+14
11	30	1	1	30		1.9318E+04	1.1350E+06	1.7462E+08	1.0356E+11	5.0164E+12	4.4290E+14
12	35	1	1	35		2.2537E+04	1.3242E+06	2.0372E+08	1.2082E+11	5.8525E+12	5.1672E+14
13											
14						$t_{3.8}$ Elapsed Times in Years					
15											
16						3.68E-01	2.16E+01	3.32E+03	1.97E+06	9.54E+07	8426597454
17						7.35E-01	4.32E+01	6.64E+03	3.94E+06	190883958	1.6853E+10
18						1.10E+00	6.48E+01	9.97E+03	5.91E+06	286325937	2.528E+10
19						1.47E+00	8.64E+01	1.33E+04	7.88E+06	381767916	3.3706E+10
20						1.84E+00	1.08E+02	1.66E+04	9.85E+06	477209896	4.2133E+10
21						2.21E+00	1.30E+02	1.99E+04	1.18E+07	572651875	5.056E+10
22						2.57E+00	1.51E+02	2.33E+04	1.38E+07	668093854	5.8986E+10

Parameters: Q38 = 40,057 cal/mole, k38 = 8.58E+13 micron/h, R = 1.986 cal/mole/K

Given the  $U_3O_8$  frontal speed Eq. 3.2.2-14 and the preceding Eq. 3.2.2-17b for  $C_{38(t)}$ , the  $[O]/[U]$  ratio of a  $U_4O_9$  sample transforming to  $U_3O_8$  is the time integration of Eq. 3.2.2-16, and is analogous to that of Eq. 3.2.2-7, namely

$$[O]/[U](U_4O_9 \rightarrow UO_{2.75}; t) = 0.33(6Gc_i e_{ijk} a_j b_k (3C_{38}(t) - 3C_{38}^2(t) + C_{38}^3(t)/3)) \quad 3.2.2-19$$

for a sample containing  $G$  number of grains.

The  $UO_{2.4}$  volume expressions of Eq. 3.2.2-8b and Eq. 3.2.2-9 are analogs for the  $V_{U3O8}$  expressions, except that the function  $C(t)$  is replaced by  $C_{38(t)}$ . Thus, the volume of  $UO_2$  converted to  $U_3O_8$  for times  $t$  greater than  $t_{2.4}$  is

$$V_{U3O8}(G, t) = 6Gc_i e_{ijk} a_j b_k (3C_{38}(t) - 3C_{38}^2(t) + C_{38}^3(t))/3 \quad 3.2.2-20$$

where the dimensional lengths of grains for vectors  $\underline{c}$ ,  $\underline{a}$ , and  $\underline{b}$  are those of the  $UO_2$  phase. Thus, the volume of  $U_3O_8$  that exists at time  $t$  would be approximately 1.30 times larger than  $V_{U3O8}$  evaluated from Eq. 3.2.2-20.

Finally, the volume ratio relative to the  $UO_2$  phase transformed to  $U_3O_8$  is an analog of Eq. 2.2.2-11, namely

$$V_{U3O8}(G, t)/V_{UO2}(G) = 3C_{38}(t) - 3C_{38}^2(t) + C_{38}^3(t) \quad \text{for } t_{2.4} \leq t \leq t_{3.8} \quad 3.2.2-21$$

and depends on grain size and temperature history of  $\dot{C}_{38}$  and  $C_{38}$  given in Eq. 3.2.2-17a and Eq. 3.2.2-17b.

In a manner similar to that of the elapsed time  $t_{v2.4}$  for a prescribed volume fraction of  $UO_{2.4}$ , Eq. 3.2.2-21 can be inverted to find the elapsed time,  $t_{v3.8}$ , after  $U_3O_8$  initiation to attain a prescribed volume fraction of  $U_3O_8$ . The expression is analogous to that of Eq. 3.2.2-13, except that the speed of the  $U_3O_8$  front is constant, rather than depending on the square root in time. Thus, the expression is

$$t_{v3.8} = |\underline{c}| \left( 1 - \left( 1 - V_{U3O8}/V_{UO2} \right)^{1/3} \right) / \left( k_{38} \exp(-Q_{38}/RT) \right) \quad 3.2.2-22$$

Values for  $t_{v3.8}$  fractional volumes of  $U_3O_8$  at 25%, 50%, and 75%, at different constant temperatures and grain sizes, are given in Tables 3.2.2-6 to 3.2.2-8.

### 3.2.2 Oxidation Models

Table 3.2.2-6 Elapsed time  $t_{3.8}$  25%  $U_3O_8$  [LL980912451021.055]

Phase Transformation of UO <sub>2</sub> for Grain Size				T in C	250	200	150	100	75	50	25
2W <sub>0</sub> And Constant Temperature.				T in K	523.2	473.2	423.2	373.2	348.2	323.2	298.2
W <sub>0</sub> =Grainsize/2	DVU3O8/VUO2	DW/W <sub>0</sub>	DW								
10E-6 meters			10E-6 m		tv3.8 Times in Hours, One Year = 24*365 = 8760 hours						
5	0.25	0.091439695	0.457198474		2.9440E+02	1.7298E+04	2.6611E+06	1.5782E+09	7.6450E+10	6.7498E+12	1.2632E+15
10	0.25	0.091439695	0.914396949		5.8881E+02	3.4596E+04	5.3223E+06	3.1565E+09	1.5290E+11	1.3500E+13	2.5264E+15
15	0.25	0.091439695	1.371595423		8.8321E+02	5.1894E+04	7.9834E+06	4.7347E+09	2.2935E+11	2.0249E+13	3.7897E+15
20	0.25	0.091439695	1.828793897		1.1776E+03	6.9192E+04	1.0645E+07	6.3129E+09	3.0580E+11	2.6999E+13	5.0529E+15
25	0.25	0.091439695	2.285992372		1.4720E+03	8.6490E+04	1.3306E+07	7.8912E+09	3.8225E+11	3.3749E+13	6.3161E+15
30	0.25	0.091439695	2.743190846		1.7664E+03	1.0379E+05	1.5967E+07	9.4694E+09	4.5870E+11	4.0499E+13	7.5793E+15
35	0.25	0.091439695	3.20038932		2.0608E+03	1.2109E+05	1.8628E+07	1.1048E+10	5.3515E+11	4.7249E+13	8.8426E+15
					tv3.8 Times in Years						
					3.3608E-02	1.9747E+00	3.0378E+02	1.8016E+05	8.7272E+06	7.7053E+08	1.4420E+11
					6.7215E-02	3.9493E+00	6.0757E+02	3.6033E+05	1.7454E+07	1.5411E+09	2.8841E+11
					1.0082E-01	5.9240E+00	9.1135E+02	5.4049E+05	2.6182E+07	2.3116E+09	4.3261E+11
					1.3443E-01	7.8986E+00	1.2151E+03	7.2066E+05	3.4909E+07	3.0821E+09	5.7681E+11
					1.6804E-01	9.8733E+00	1.5189E+03	9.0082E+05	4.3636E+07	3.8526E+09	7.2102E+11
					2.0165E-01	1.1848E+01	1.8227E+03	1.0810E+06	5.2363E+07	4.6232E+09	8.6522E+11
					2.3525E-01	1.3823E+01	2.1265E+03	1.2611E+06	6.1090E+07	5.3937E+09	1.0094E+12

Parameters: Q38 = 40,057 cal/mole, k38 = 8.58E+13 micron/h, R = 1.986 cal/mole/K

Table 3.2.2-7 Elapsed time  $t_{3.8}$ , 50%  $U_3O_8$  [LL980912451021.055]

Phase Transformation of UO <sub>2</sub> for Grain Size				T in C	250	200	150	100	75	50	25
2W <sub>0</sub> And Constant Temperature.				T in K	523.2	473.2	423.2	373.2	348.2	323.2	298.2
W <sub>0</sub> =Grainsize/2	DVU3O8/VUO <sub>2</sub>	DW/W <sub>0</sub>	DW								
10E-6 meters			10E-6 m		tv3.8 Times in Hours, One Year = 24*365 = 8760 hours						
5	0.5	0.206299456	1.031497278		6.6421E+02	3.9026E+04	6.0039E+06	3.5607E+09	1.7248E+11	1.5228E+13	2.8500E+15
10	0.5	0.206299456	2.062994557		1.3284E+03	7.8053E+04	1.2008E+07	7.1214E+09	3.4496E+11	3.0457E+13	5.7000E+15
15	0.5	0.206299456	3.094491835		1.9926E+03	1.1708E+05	1.8012E+07	1.0682E+10	5.1744E+11	4.5685E+13	8.5500E+15
20	0.5	0.206299456	4.125989114		2.6568E+03	1.5611E+05	2.4015E+07	1.4243E+10	6.8992E+11	6.0914E+13	1.1400E+16
25	0.5	0.206299456	5.157486392		3.3210E+03	1.9513E+05	3.0019E+07	1.7803E+10	8.6241E+11	7.6142E+13	1.4250E+16
30	0.5	0.206299456	6.18898367		3.9853E+03	2.3416E+05	3.6023E+07	2.1364E+10	1.0349E+12	9.1370E+13	1.7100E+16
35	0.5	0.206299456	7.220480949		4.6495E+03	2.7319E+05	4.2027E+07	2.4925E+10	1.2074E+12	1.0660E+14	1.9950E+16
					tv3.8 Times in Years						
					7.5823E-02	4.4551E+00	6.8537E+02	4.0647E+05	1.9690E+07	1.7384E+09	3.2534E+11
					1.5165E-01	8.9101E+00	1.3707E+03	8.1294E+05	3.9379E+07	3.4768E+09	6.5068E+11
					2.2747E-01	1.3365E+01	2.0561E+03	1.2194E+06	5.9069E+07	5.2152E+09	9.7602E+11
					3.0329E-01	1.7820E+01	2.7415E+03	1.6259E+06	7.8759E+07	6.9536E+09	1.3014E+12
					3.7912E-01	2.2275E+01	3.4269E+03	2.0324E+06	9.8448E+07	8.6920E+09	1.6267E+12
					4.5494E-01	2.6730E+01	4.1122E+03	2.4388E+06	1.1814E+08	1.0430E+10	1.9520E+12
					5.3076E-01	3.1186E+01	4.7976E+03	2.8453E+06	1.3783E+08	1.2169E+10	2.2774E+12

Parameters: Q38 = 40,057 cal/mole, k38 = 8.58E+13 micron/h, R = 1.986 cal/mole/K

### 3.2.2 Oxidation Models

Table 3.2.2-8 Elapsed time <sub>13.8</sub> 75% U<sub>3</sub>O<sub>8</sub> [LL980912451021.055]

Phase Transformation of UO <sub>2</sub> for Grain Size				T in C	250	200	150	100	75	50	25
2Wo And Constant Temperature.				T in K	523.2	473.2	423.2	373.2	348.2	323.2	298.2
Wo=Grainsize/2	DVU3O8/VUO2	DW/Wo	DW								
10E-6 meters			10E-6 m		tv3.8 Times in Hours, One Year = 24*365 = 8760 hours						
5	0.75	0.370039446	1.85019723		1.1914E+03	7.0002E+04	1.0769E+07	6.3868E+09	3.0938E+11	2.7315E+13	5.1120E+15
10	0.75	0.370039446	3.700394459		2.3828E+03	1.4000E+05	2.1538E+07	1.2774E+10	6.1876E+11	5.4630E+13	1.0224E+16
15	0.75	0.370039446	5.550591689		3.5742E+03	2.1001E+05	3.2307E+07	1.9160E+10	9.2814E+11	8.1946E+13	1.5336E+16
20	0.75	0.370039446	7.400788919		4.7656E+03	2.8001E+05	4.3077E+07	2.5547E+10	1.2375E+12	1.0926E+14	2.0448E+16
25	0.75	0.370039446	9.250986149		5.9570E+03	3.5001E+05	5.3846E+07	3.1934E+10	1.5469E+12	1.3658E+14	2.5560E+16
30	0.75	0.370039446	11.10118338		7.1484E+03	4.2001E+05	6.4615E+07	3.8321E+10	1.8563E+12	1.6389E+14	3.0672E+16
35	0.75	0.370039446	12.95138061		8.3398E+03	4.9001E+05	7.5384E+07	4.4708E+10	2.1657E+12	1.9121E+14	3.5784E+16
					tv3.8 Times in Years						
					1.3600E-01	7.9911E+00	1.2294E+03	7.2909E+05	3.5317E+07	3.1182E+09	5.8357E+11
					2.7201E-01	1.5982E+01	2.4587E+03	1.4582E+06	7.0635E+07	6.2363E+09	1.1671E+12
					4.0801E-01	2.3973E+01	3.6881E+03	2.1873E+06	1.0595E+08	9.3545E+09	1.7507E+12
					5.4402E-01	3.1964E+01	4.9174E+03	2.9164E+06	1.4127E+08	1.2473E+10	2.3343E+12
					6.8002E-01	3.9955E+01	6.1468E+03	3.6454E+06	1.7659E+08	1.5591E+10	2.9178E+12
					8.1602E-01	4.7946E+01	7.3761E+03	4.3745E+06	2.1190E+08	1.8709E+10	3.5014E+12
					9.5203E-01	5.5937E+01	8.6055E+03	5.1036E+06	2.4722E+08	2.1827E+10	4.0850E+12

Parameters: Q38 = 40,057 cal/mole, k38 = 8.58E+13 micron/h, R = 1.986 cal/mole/K

The comparison of the elapsed times for full oxidation of  $\text{UO}_2$  to the  $\text{U}_4\text{O}_9$  and  $\text{U}_3\text{O}_8$  phases are presented for  $t_{2.4}$  values in Table 3.2.2-1 and for  $t_{3.8}$  values in Table 3.2.2-5. At lower temperatures ( $T$  less  $100^\circ\text{C}$ ), the  $t_{3.8}$  values are significantly greater than the  $t_{2.4}$  values. It appears that large amounts of  $\text{U}_4\text{O}_9$  will form within thousands of years of exposure at  $\sim 100^\circ\text{C}$  temperatures, whereas it will take hundreds of thousands of years for large amounts of  $\text{U}_3\text{O}_8$  to form at the same temperatures ( $\sim 100^\circ\text{C}$ ).

### 3.2.2.5 Comparison of Model Response to Oven Drybath Data

The confirmation of a model depends primarily on how well it explains existing data and on its potential to explain future experiments. In this case, the  $\text{U}_4\text{O}_9$  and  $\text{U}_3\text{O}_8$  oxidation models based on the kinetic data from the small-sample TGA experiments successfully bounded the ODB data obtained over a larger scale and variety of spent-fuel sample sizes. This comparison confirms the “bounding approximations” of the oxidation-response model.

The kinetic parameters for the reaction  $\text{U}_4\text{O}_9 \rightarrow \text{U}_3\text{O}_8$  obtained from higher-temperature (greater than  $283^\circ\text{C}$ ) TGA measurements were applied to the lower-temperature ( $255^\circ\text{C}$ ) ODB experiments. The TGA tests used very small samples; approximately 200 mg of spent fuel. Compared to the TGA experiments, the ODB experiments accommodated much larger spent-fuel samples that must likely include both edge and center spent-fuel fragments. Thus, the ODB experiments are more representative of integral or averaged spent fuel.

The amounts of  $\text{U}_4\text{O}_9$  to  $\text{U}_3\text{O}_8$  ODB data are limited because these were obtained at  $255^\circ\text{C}$ , at which point the time response of  $\text{UO}_2$  conversion to  $\text{U}_3\text{O}_8$  is much slower. The ODB data have been provided by for the following fuels:

- Turkey Point PWR fuel
- ATM-104
- ATM-105
- ATM-106

These ODB data are additional, independent, experimental measurements for the oxidation of  $\text{U}_4\text{O}_9$  to  $\text{U}_3\text{O}_8$ . The ODB samples had initial  $\Delta(\text{O}/\text{M})$  ratios of 0.0 or 0.42 relative to  $\text{UO}_2$  because some of the samples had been previously oxidized at lower temperatures. Some of the spent-fuel samples used were as-removed fragments, while others were pulverized fragments. The majority of these ODB samples had nominal, grain half-sizes primarily in the range of 3 to 15 microns. When comparing ODB data to the model response that used kinetic parameters from TGA data, it is important to note that there was a wider spectrum of grain half sizes in the ODB samples.

In Figure 3.2.2-5 through Figure 3.2.2-8, the change in the oxygen-to-metal ratio  $\Delta(\text{O}/\text{M})$  is plotted against time (thousands of hours). The  $\Delta(\text{O}/\text{M})$ -versus-time curves represent the cumulative effect of the consecutive reactions:  $\text{UO}_2 \rightarrow \text{U}_4\text{O}_9 \rightarrow \text{U}_3\text{O}_8$ . At the ODB temperature  $T = 255^\circ\text{C}$  (528.2 K), the reaction rate  $k_{v4.9}$  for  $\text{UO}_2 \rightarrow \text{U}_4\text{O}_9$  is  $k_{v4.9} = 1.205 \times 10^{-2} \mu\text{m}^2/\text{hr}$ , and the reaction rate  $k_{v3.8}$  for  $\text{U}_4\text{O}_9 \rightarrow \text{U}_3\text{O}_8$  is  $k_{v3.8} = 3.4414 \times 10^{-4} \mu\text{m}/\text{hr}$ . The front propagation speeds for the respective reactions are given by Eq. 3.2.2-4 and Eq. 3.2.2-14a and Eq. 3.2.2-14b, respectively. A  $\Delta(\text{O}/\text{M})$  of 0.42 represents the complete conversion of  $\text{UO}_2 \rightarrow \text{U}_4\text{O}_9$  (no  $\text{UO}_2$  or  $\text{U}_4\text{O}_9$  assumed to be present), and the time to achieve complete conversion is represented by  $t_{\text{total } 4.9}$ . A  $\Delta(\text{O}/\text{M})$  of 0.75 represents the complete conversion of  $\text{U}_4\text{O}_9 \rightarrow \text{U}_3\text{O}_8$  (no  $\text{UO}_2$  or  $\text{U}_3\text{O}_8$  assumed to be present). Using Eq. 3.2.2-13 and Eq. 3.2.2-22, the cumulative elapsed time for any  $\Delta(\text{O}/\text{M}) > 0.42$  is given by Eq. 3.2.2-18b.

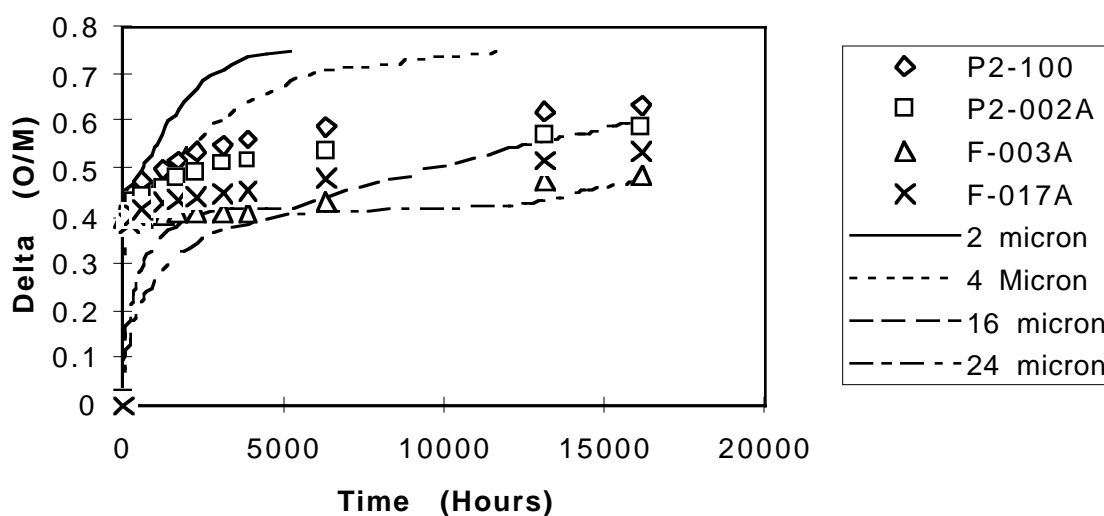


Figure 3.2.2-5  $\Delta(O/M)$  versus time for  $UO_2 \rightarrow U_4O_9 \rightarrow U_3O_8$ : model response and experimental data corresponding to Figure 10 (Turkey Point SNF sample) of Einziger and Hanson (1996) ODB tests conducted at 255°C

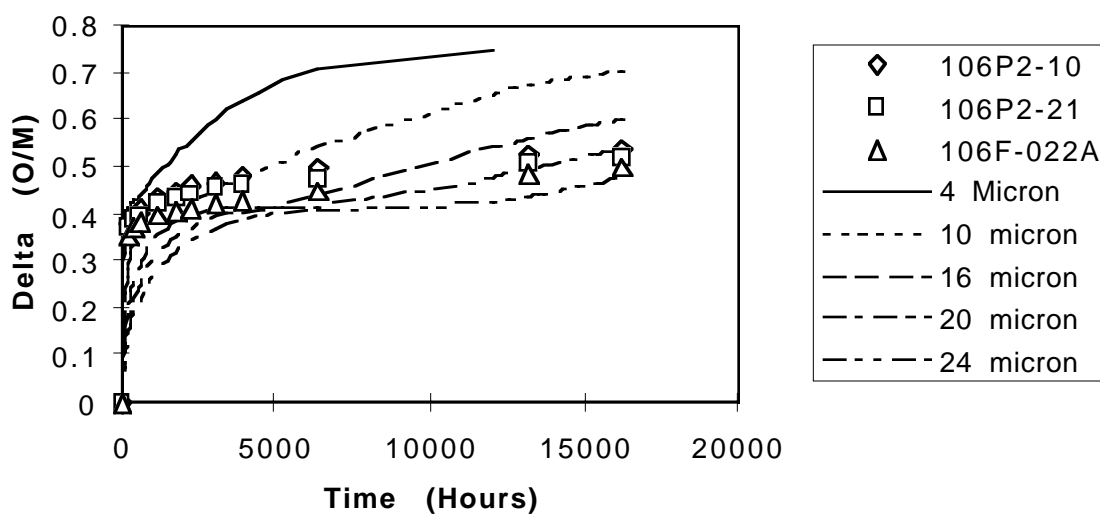


Figure 3.2.2-6  $\Delta(O/M)$  versus time for  $UO_2 \rightarrow U_4O_9 \rightarrow U_3O_8$ : model response and experimental data corresponding to Figure 11 (ATM-106 SNF samples) of Einziger and Hanson (1996) ODB tests conducted at 255°C [LL980912351021.054]

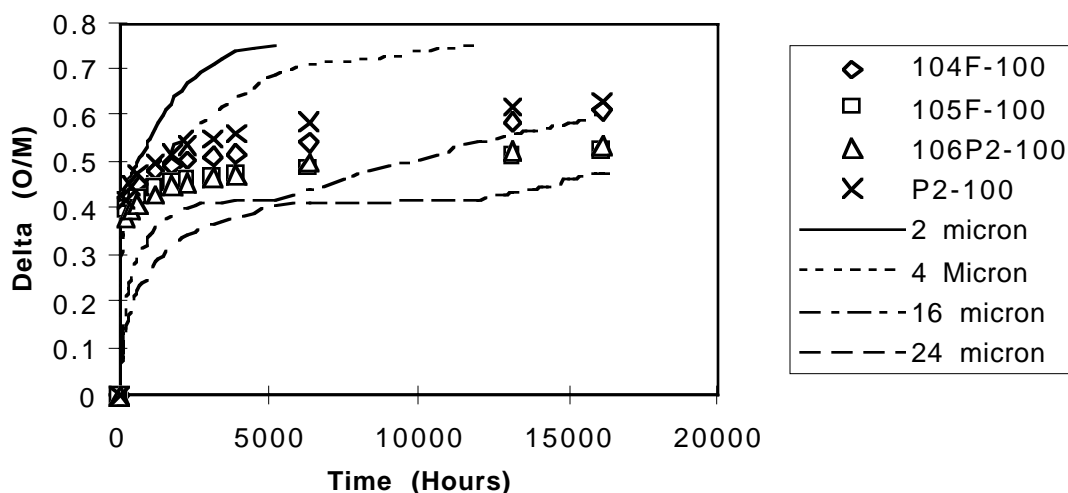


Figure 3.2.2-7  $\Delta(\text{O/M})$  versus time for  $\text{UO}_2 \rightarrow \text{U}_4\text{O}_9 \rightarrow \text{U}_3\text{O}_8$ : model response and experimental data corresponding to Figure 14 (SNF samples) of Einziger and Hanson (1996) ODB tests conducted at 255°C [LL980912351021.054]

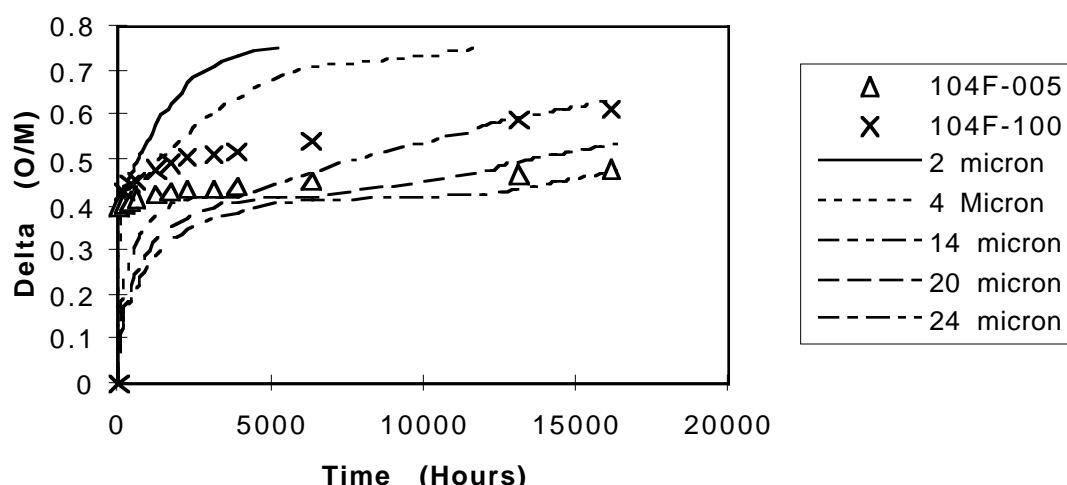


Figure 3.2.2-8  $\Delta(\text{O/M})$  versus time for  $\text{UO}_2 \rightarrow \text{U}_4\text{O}_9 \rightarrow \text{U}_3\text{O}_8$ : model response and experimental data corresponding to Figure 15 (SNF samples, initial  $\Delta(\text{O/M})=0.4$ ) of Einziger and Hanson (1996) ODB tests conducted at 255°C [LL980912351021.054]

In these figures, the experimental ODB  $\Delta(\text{O/M})$ -versus-time results are represented as symbols without lines; the various monosized grain half size  $\Delta(\text{O/M})$ -versus-time curves are represented as continuous lines (solid, dotted, dashed, dot-dash, etc.). At time  $t = 0.0$ , the data have samples that were initially  $\text{UO}_2$  or had been oxidized at lower temperatures to  $\text{U}_4\text{O}_9$ . Some of these figures have both types.

As pointed out previously, the initial  $\text{UO}_2$  grain size determines the time scale required for the complete transformation of  $\text{UO}_2$  to  $\text{U}_4\text{O}_9$ , and the subsequent transformation of  $\text{U}_4\text{O}_9$  to  $\text{U}_3\text{O}_8$ . The  $\Delta(\text{O/M})$ -versus-time curves show that the completion of the  $\text{UO}_2 \rightarrow \text{U}_4\text{O}_9$  reaction



### 3.2.2 Oxidation Models

and the initiation of the  $\text{U}_4\text{O}_9 \rightarrow \text{U}_3\text{O}_8$  reaction require progressively longer times for larger grain half sizes. This model dependence on grain half size becomes quite pronounced for grain half sizes larger than 16 microns.

Figure 3.2.2-5 shows the plots of  $\Delta(\text{O}/\text{M})$  versus time for the experimental samples (P2-100, P2-002A, F-003A, and F-017A) from Turkey Point spent fuel. Figure 3.2.2-6 shows the plots of  $\Delta(\text{O}/\text{M})$  versus time for the ATM 106 samples (106F-022A, 106P2-100, and 106P2-21A). Figure 3.2.2-7 shows similar plots for the spent-fuel samples (104F-100, 106P2-100, 105F-100, P2-100, 106F-022A, and 106P2-21A). These figures show that the ODB experimental data are bounded by an envelope of model  $\Delta(\text{O}/\text{M})$ -versus-time curves for grain half sizes of 2 microns to 24 microns. The grains of the various samples of  $\text{U}_4\text{O}_9$  are distributed over a spectrum of grain sizes, with the very small grains of  $\text{U}_4\text{O}_9$  oxidizing relatively rapidly to form  $\text{U}_3\text{O}_8$  and the larger grains requiring longer times. Three different sets of  $\Delta(\text{O}/\text{M})$ -versus-time plots of oxidizing spent-fuel samples are bounded by the envelope of model curves ranging from 2 microns to 24 microns.

Figure 3.2.2-8 shows the plots of  $\Delta(\text{O}/\text{M})$  versus time for SNF samples (104F-100, 104F-005, and F-003A). Samples 104F-005 and F-003A had an initial  $\Delta(\text{O}/\text{M}) = 0.395$ ; sample 104F-100 had an initial  $\Delta(\text{O}/\text{M}) = 0.0$ . These ODB data are bounded by the envelope of model curves having grain half sizes from 2 microns to 24 microns. The distribution of grain half sizes varies from sample to sample. It appears that most of the ODB data at 255°C can be bounded by an envelope of monosized model-response  $\Delta(\text{O}/\text{M})$ -versus-time curves for grain half sizes of 2 microns to 24 microns.

The kinetics used for the comparison of ODB data with model results were obtained independently from the higher temperature TGA experiments. The ODB experiments used various spent-fuel samples that were obtained from different types of reactors under different operating conditions. All the available ODB data, however, were bounded within a model-response envelope of grain half sizes ranging 2.0 to 24 microns. The results of the model comparison with the ODB data give confidence that the model accounts for the essential features of spent-fuel oxidation (i.e., the response history depends on both the temperature history and initial grain half-sizes).

Table 3.2.2-9 shows the time required, for various grain half sizes, to reach different volume fractions  $V_{\text{U}_3\text{O}_8}/V_{\text{UO}_2} = 0.00, 0.20, 0.40, 0.60, 0.80$ , and 1.00, for a ODB temperature held at 255°C. The time for the volume fraction  $V_{\text{U}_3\text{O}_8}/V_{\text{UO}_2} = 0.00$  represents the time required for the different grain half sizes to undergo the complete conversion of  $\text{UO}_2$  to  $\text{U}_4\text{O}_9$ , given by Eq. 3.2.2-13 for  $V_{\text{U}_4\text{O}_9}/V_{\text{UO}_2} = 1.0$ . The time required for a 5-micron grain half size of  $\text{UO}_2$  to form  $\text{U}_4\text{O}_9$  is 519 hr; the time to convert  $\text{U}_4\text{O}_9$  to  $\text{U}_3\text{O}_8$  is 15,048 hr. However, the time required for a 30-micron grain half size of  $\text{UO}_2$  to form  $\text{U}_4\text{O}_9$  is 18,676 hr; the time to convert  $\text{U}_4\text{O}_9$  to  $\text{U}_3\text{O}_8$  is 105,850 hr.

**Table 3.2.2-9** Total elapsed time (hr) as a function of grain half size to convert  $\text{UO}_2$  to various volume fractions of  $\text{U}_3\text{O}_8$ , assuming temperature of 255°C (528.2 K) [LL980912451021.055]

Grain Size/2 (microns)	$V_{\text{U}_3\text{O}_8}/V_{\text{UO}_2} =$ 0.0	$V_{\text{U}_3\text{O}_8}/V_{\text{UO}_2} =$ 0.2	$V_{\text{U}_3\text{O}_8}/V_{\text{UO}_2} =$ 0.4	$V_{\text{U}_3\text{O}_8}/V_{\text{UO}_2} =$ 0.6	$V_{\text{U}_3\text{O}_8}/V_{\text{UO}_2} =$ 0.8	$V_{\text{U}_3\text{O}_8}/V_{\text{UO}_2} =$ 1.0
3.0	187	812	1552	2481	3806	8904
4.0	332	1165	2152	3391	5158	11955
5.0	519	1560	2794	4343	6551	15048

Grain Size/2 (microns)	$V_{U3O8}/V_{UO2} = 0.0$	$V_{U3O8}/V_{UO2} = 0.2$	$V_{U3O8}/V_{UO2} = 0.4$	$V_{U3O8}/V_{UO2} = 0.6$	$V_{U3O8}/V_{UO2} = 0.8$	$V_{U3O8}/V_{UO2} = 1.0$
6.0	747	1997	3477	5336	7986	18182
7.0	1017	2475	4201	6370	9462	21357
8.0	1328	2994	5968	7446	10980	24574
9.0	1681	3556	5775	8564	12539	27833
10.0	2075	4158	6625	9723	14140	31133
15.0	4669	7794	11493	16141	22766	48256
20.0	8301	12467	17400	23596	32430	66416
30.0	18676	24925	32325	41620	54871	105850

In the next sections, new information will be used to extend the bounding approximations to fitting TGA and drybath experiments by using log-normal grain-size distributions and burnup-dependent activation energies. The primary focus will be the oxidation of  $U_4O_9 \rightarrow U_3O_8$ .

### 3.2.2.6 Model Predictions of Spent-Fuel Oxidation in a Constant 100°C Temperature Environment

The rates of conversion of  $UO_2$  to  $U_4O_9$  and  $U_4O_9$  to  $U_3O_8$  depend exponentially on the inverse absolute temperature ( $1/T$  °K<sup>-1</sup>). Consequently, the rates of conversion are considerably more reduced when the temperature is held fixed at 100°C than they are when the temperature is held at 255°C. At 100 °C, the reaction rate for  $UO_2$  to  $U_4O_9$ ,  $k_{v4.9} = 8.9979E^{-07}$  mm<sup>2</sup>/hr; the reaction rate for  $U_4O_9$  to  $U_3O_8$ ,  $k_{v3.8} = 4.4568E^{-11}$  mm<sup>2</sup>/hr.

Table 3.2.2-10 compares the time required, for various grain half sizes, to reach different volume fractions of  $U_4O_9$  and  $UO_2$ . In contrast, Table 3.2.2-9 shows the results for grain half sizes for which the temperature was held constant at 255°C. Consider the time required to convert  $UO_2$  to  $U_4O_9$  for grain half size of 5 microns: at 100°C, the total conversion time required to convert  $UO_2$  completely to  $U_4O_9$  is 6.9E+06 hr; at 255°C, the conversion time is 519 hr. Consider the time required to convert  $UO_2$  to  $U_4O_9$  for grain half-size of 10 microns: at 100°C, the total conversion time is 3.8E+07 hr; at 255°C the conversion time is 2075 hr.

**Table 3.2.2-10 Total elapsed time (hr) as a function of grain half size to convert  $UO_2$  to various volume fractions of  $U_4O_9$ , assuming temperature of 100°C (373.2K) [LL980912451021.055]**

Grain Size/2 (microns)	$V_{U4O9}/V_{UO2} = 0.0$	$V_{U4O9}/V_{UO2} = 0.2$	$V_{U4O9}/V_{UO2} = 0.4$	$V_{U4O9}/V_{UO2} = 0.6$	$V_{U4O9}/V_{UO2} = 0.8$	$V_{U4O9}/V_{UO2} = 1.0$
3.0	0	1.3E+04	6.1 E+04	1.7E+05	4.3E+05	2.5E+06
4.0	0	2.3E+04	1. 1E+05	3.1E+05	7.7E+05	4.4E+06
5.0	0	3.6E+04	1.7E+05	4.8E+05	1.2E+06	6.9E+06
6.0	0	5.1E+04	2.5E+05	6.9E+05	2.7E+06	2.0E+07
7.0	0	7.0E+04	3.3E+05	9.4E+05	2.3E+06	1.4E+07
8.0	0	9.1E+04	4.4E+05	1.2E+06	3.1 E+06	1.8E+07

### 3.2.2 Oxidation Models

Grain Size/2 (microns)	$V_{U_4O_9}/V_{UO_2} = 0.0$	$V_{U_4O_9}/V_{UO_2} = 0.2$	$V_{U_4O_9}/V_{UO_2} = 0.4$	$V_{U_4O_9}/V_{UO_2} = 0.6$	$V_{U_4O_9}/V_{UO_2} = 0.8$	$V_{U_4O_9}/V_{UO_2} = 1.0$
9.0	0	1.2E+05	5.5E+05	1.6E+06	3.9E+06	2.3E+07
10.0	0	1.4E+05	6.8E+05	1.9E+06	4.8E+06	3.8E+07
15.0	0	3.2E+05	1.5E+06	4.3E+06	1.1 E+07	6.3E+07
20.0	0	5.7E+05	2.7E+06	7.7E+06	1.9E+07	1.1E+08

Table 3.2.2-11 shows the total elapsed time as a function of grain half-size to convert  $UO_2$  to  $U_3O_8$  at 100°C. The conversion time to 100%  $U_3O_8$  is significantly longer for the 100°C as compared to the 255°C (Table. 3.2.2-9). Consider a grain half-size of 5 microns: the complete conversion time at 255°C is 15,048 hr., but the time 100°C is 1.1E10 hr. Consider a grain half-size of 10 microns: the conversion time at 255°C is 31,113 hr., but the conversion time at 100°C is 2.2E11 hr.

**Table 3.2.2-11** Total elapsed time (hr) as a function of grain half size to convert  $UO_2$  to various volume fractions of  $U_3O_8$ , assuming a constant temperature of 100°C (373.2K) [LL980912451021.055]

Grain Size/2 (microns)	$V_{U_3O_8}/V_{UO_2} = 0.0$	$V_{U_3O_8}/V_{UO_2} = 0.25$	$V_{U_3O_8}/V_{UO_2} = 0.50$	$V_{U_3O_8}/V_{UO_2} = 0.75$	$V_{U_3O_8}/V_{UO_2} = 1.0$
4.0	4.445E+06	8.211E+09	1.852E+10	3.322E+10	8.976E+10
5.0	6.946E+06	1.027E+10	2.315E+10	4.152E+10	1.122E+11
6.0	1.000E+07	1.232E+10	2.778E+10	4.983E+10	1.346E+11
7.0	1.361E+07	1.438E+10	3.242E+10	5.813E+10	1.571E+11
8.0	1.778E+07	1.643E+10	3.705E+10	6.644E+10	1.795E+11
9.0	2.251E+07	1.849E+10	4.168E+10	7.475E+10	2.020E+11
10.0	2.778E+07	2.054E+10	4.632E+10	8.306E+10	2.244E+11
11.0	3.362E+07	2.260E+10	5.095E+10	9.137E+10	2.468E+11
12.0	4.001E+07	2.466E+10	5.559E+10	9.967E+10	2.693E+11
13.0	4.696E+07	2.672E+10	6.022E+10	1.080E+11	2.917E+11
14.0	5.446E+07	2.878E+10	6.486E+10	1.163E+11	3.142E+11
15.0	6.251E+07	3.084E+10	6.950E+10	1.246E+11	3.366E+11
16.0	7.113E+07	3.290E+10	7.413E+10	1.329E+11	3.591E+11
17.0	8.030E+07	3.496E+10	7.877E+10	1.412E+11	3.815E+11
18.0	9.002E+07	3.702E+10	8.341E+10	1.495E+11	4.040E+11
19.0	1.003E+08	3.908E+10	8.805E+10	1.579E+11	4.264E+11
20.0	1.111E+08	4.115E+10	9.269E+10	1.662E+11	4.489E+11

#### 3.2.2.7 Chemical and Physical Alteration of Spent Fuel

Depending on the burnup, spent fuel is always chemically, and sometimes physically, altered. Park and Olander (1992) show that the fission products in spent  $UO_2$  can be considered as dopants. The rare earth fission products from the lanthanide series are typically trivalent and form the compound  $(U_{1-z}Ln_z)O_{2+x}$ .  $Gd^{3+}$  does not form extended defects with oxygen interstitial, and it reduces the number of sites that can be occupied by oxygen

interstitials. Consequently, as the number of oxygen vacancies increases, the stability occurs by the formation of Gd-vacancy clusters. In contrast,  $\text{Eu}^{3+}$  forms anion-vacancy clusters. The Gd-like dopants are isolated defects and tend to remain as such until the oxygen interstitial concentration becomes high enough to form a complex dopant cluster. But Eu forms clusters with anions. Eu exists as clusters of 6 other  $\text{Eu}^{3+}$  ions/anion vacancies and is stable at all stoichiometries. These authors believe that the lanthanide dopants whose concentrations are directly proportional to burnup are the major reason why spent fuel is more resistant to oxidation than unirradiated  $\text{UO}_2$ .

Walker et al (1992) point out that the burnup experienced in the rim tends to be about double the average burnup of the pellet itself. They studied five different fuels with average burnups (31.5 to 75 MWd/kgU) and  $^{235}\text{U}$  enrichment ranging from 1.5 to 7.0%. They noted structural changes such as markedly increased porosity with threshold burnups greater or equal to 40-45 MWd/kgU. While the altered shell or rim appeared to be small, it still accounted for 4 to 8% of the total volume. At high burnup, the grain volumes can experience anywhere from 1,000- to 10,000-fold reduction. The irradiated grain sizes can range from 0.4 to 1.0  $\mu\text{m}$ , compared to the unirradiated grains that range from 7 to 30  $\mu\text{m}$ . It appears that, if high burnup were maintained for a long time, the entire fuel cross-section could be affected. At high burnups, Xe and Kr bubbles are formed near the pellet surface and yield a sharp reduction in  $\text{UO}_2$  grain sizes. Near the surface, the local burnup is approximately double that of the average burnup; this region can experience very high temperatures (> 1100-1200°C) in which the thermally active Xe forms micro-bubbles over considerable distances and micro-structural changes. The formation of Pu from neutron absorption of  $^{238}\text{U}$  does not appear to account for the micro-structural changes. Walker et al observed a high concentration of gas bubbles (pores) forming in the rim due to the fission gas products, namely Xe and Kr. Similar observations on the high burnup structure were noted by Lassmann et al. (1995).

Matzke (1992) found that, in the region from the pellet surface to a depth  $d$ , the radial Pu, Np, and Xe concentrations vary exponentially. Pu, U-metal activity, and the Nd/Zr ratio also vary exponentially from approximately 200 mm from the interior to the pellet surface. The altered shell region, of width  $d$  for high burnups 40-60 MWd/kgU, represents 4 to 8% of the total pellet volume. This zone is characterized by very small grains (0.3 to 1.0  $\mu\text{m}$ ) and about 30% porosity. It is also Pu-rich. Matzke postulates that the burnup-dependent fission-gas content is the driving force for the structural changes. At high burnup, the gas pressure from fission gases can be approximately 10,000 bars.  $\text{UO}_2$  is not expected to be subject to radiation-induced amorphism. However, depending on the fuel temperature during burnup, the stresses and deformations on a unit cell can cause grain subdivision. The pores that form will contain Re, As, I, Te, etc., that facilitate rounding the sharp edges of the smaller pieces. Radiation-induced thermal plasticity is known to occur in  $\text{UO}_2$  during fission. This plasticity is proportional to the fission rate. Pronounced plasticity prevents a buildup of very high pressure bubbles; instead, it produces swelling. Because the plasticity is proportional to the fission rate, radiation induced-plasticity is small in light-water reactors (LWRs). Neutron capture of  $^{238}\text{U}$  produces  $^{239}\text{Np}$  and  $^{239}\text{Pu}$ . The fission of  $^{239}\text{Pu}$  results in relatively high yields Pd, Ru, Rh, etc., that do not readily bind with oxygen. The burnup of 40 MWd/kgU appears to be the critical point at which small grains of  $\text{UO}_2$  are formed. At even higher burnups (70 to 80 MWd/kgU), the rim appears to be depleted of Xe and Kr, and the altered  $\text{UO}_2$  structure can extend 1.2 to 2.0 mm into the pellet. Of interest is the fact that the cauliflower structure from high burnup is not observed in the fast-breeder (U,Pu) $\text{O}_2$  reactor because most of the fission gas is readily released.

In a more recent study, Ray et al. (1997) examined the rim effect in very high-burnup spent fuel. The average burnup was 74 MWd/kgU; but, at the pellet surface, the local burnup was approximately 210 MWd/kgU. The original grain sizes that had been 10 to 20  $\mu\text{m}$  were now subdivided into grains ranging from 0.15 to 0.30  $\mu\text{m}$  in the irradiated rim region. The high burnup structure extended 1.65 mm below the surface.

Paraschiv et al. (1997) developed a mathematical formalism for fission-gas release. As for the cases of irradiated spent fuels, long-range diffusion can be required for the cases in which impurities segregate to the moving boundary. In the dissolved state, impurities will retard grain growth through elastic attraction toward the open structure of the grain boundary. It has long been observed that unirradiated  $\text{UO}_2$ , when annealed at high temperatures, has far larger grain sizes than does irradiated  $\text{UO}_2$  annealed at high temperatures (such as those occurring during burnup), apparently because, due to solute segregation, small amounts of metal oxide impurities dominate grain growth.

In summary, when the average burnup exceeds 40-45 MWd/kgU, the region at or near the pellet surface can undergo a drastic physical change. The effective burnup at the rim can be two to three times that of the average burnup. The rim is characterized by a radial distribution of fission and actinide products concentrations that decreases exponentially as one moves toward the center of the pellet. Furthermore, the rim has a very porous, cauliflower structure whose  $\text{UO}_2$  grains undergo significant grain-size reductions. Grains in the unirradiated  $\text{UO}_2$  that had originally been 10 to 20  $\mu\text{m}$  were now subdivided into grains ranging from 0.15 to 0.30  $\mu\text{m}$  in the high burnup rim region.

#### 3.2.2.8 Oxidation Studies of Spent Fuel

$\text{UO}_2$ , which has a cubic fluorite crystalline structure, oxidizes initially by accommodating excess oxygen interstitially. There is some controversy about whether spent fuel “oxidizes” to  $\text{U}_3\text{O}_7$ . Boase and Vandergraf (1977) show that  $\text{UO}_2$  rapidly oxidizes to form a thin film of  $\text{U}_3\text{O}_7$  whose thickness is 22 nm.  $\text{U}_3\text{O}_7$  is found on very fine samples of spent fuel with large surface areas greater than 0.3  $\text{m}^2/\text{g}$ . Further oxidation proceeds by oxygen diffusion through the  $\text{U}_3\text{O}_7$  layer to form  $\text{U}_4\text{O}_9$ . The sequence is thought to be as follows:



$\text{U}_4\text{O}_7$  and  $\text{U}_4\text{O}_9$  phases are essentially cubic fluorite crystalline structures, but the  $\text{U}_4\text{O}_9$  phase lattice is about 0.4% smaller than the  $\text{UO}_2$  crystal. On the other hand,  $\text{U}_3\text{O}_8$  phase is quite different from the basic  $\text{UO}_2$  because there is an increase in volume, as noted by the 30 to 36% decrease in density. Not only can  $\text{U}_3\text{O}_8$  disrupt cladding and spall, but its dissolution rate, as shown by Gray et al. (1993), is two to four times greater than that of  $\text{UO}_2$  and  $\text{U}_3\text{O}_7$  when the rates are normalized to the grain-surface areas.

Choi et al. (1996) argued that various studies in the burnup range 11.7 to 26.7 MWd/kgU reveal much scatter and uncertainty in the induction time and  $\text{U}_3\text{O}_8$  formation. To understand better the oxidation process, they examined SIMFUEL that is  $\text{UO}_2$  and that had been doped with nonradioactive, simulated fission products such as Gd. They doped different SIMFUEL samples to simulate 0, 1.5, 3.0, 4.0, 6.0, or 8.0 atom% burnup. They found that the fraction of  $\text{UO}_2$  oxidized to  $\text{U}_3\text{O}_8$  at a constant temperature of 250°C required progressively larger amounts of time as the dopant concentration increased. These authors postulate that the dissolved solid dopants significantly alter the kinetics of oxidation-to- $\text{U}_3\text{O}_8$  formation. They believe that, for similar  $\text{UO}_2$  grain sizes, the activation energy required for the reaction,  $\text{U}_4\text{O}_9 \rightarrow \text{U}_3\text{O}_8$ , would depend directly on burnup.

Hanson (1998) has shown that the fission product and actinide dopants appear to suppress the onset of oxidation of  $U_4O_9$  to  $U_3O_8$ . The higher concentration of fission products gives a more stable crystalline structure for the fluorite  $UO_2$  and delays the formation of  $U_3O_8$ . Irradiated  $UO_2$  resists oxidation, as evident from the O/M histories. Moderate burnup  $UO_2$  (27 to 30 MWd/kgU) has a very long plateau at which  $U_4O_9$  resists further oxidation to  $U_3O_8$ . This plateau has both a burnup dependency and a grain-size dependency. Lower temperatures and higher burnup fuels resist this transformation to  $U_3O_8$ , whereas unirradiated and low-burnup fuel oxidize to  $U_3O_8$  more rapidly. The formation of  $U_3O_8$  from  $U_4O_9$  in irradiated fuels proceeds very slowly if the temperature is less than 250°C because of the high activation-energy barrier.

McEachern et al. (1997) performed a critical evaluation of the various techniques to measure the kinetics of  $U_3O_8$  formation and to understand the reason behind the considerable disparities in the results. Instead of using the weight-gain experiments, they used X-ray powder diffraction (XRD) to measure the rate of formation of  $U_3O_8$  on the  $UO_2$  surface. Involved are at least two different reactions, seemingly at different temperature ranges:

- $U_3O_8$ -spallation reaction
- Powder-formation reaction

McEachern et al. state there is no theoretical justification for the assumption of linearity in the kinetic reactions when it has been repeatedly shown the oxidation reactions are really sigmoidal. They obtained an average value for the activation energy of approximately 146.5 kJ/mole (35 kcal/mole) for the formation of  $U_3O_8$ , which is the range measured by other investigators.

Harrison et al. (1967) argue that the oxidation of  $UO_2 \rightarrow U_3O_7/U_4O_9 \rightarrow U_3O_8$  is at least a two-stage kinetic reaction. In their experiments, they considered the oxidation of spheres of both natural uranium oxide (mean diameter of 120  $\mu\text{m}$ ) and enriched 93v (93%  $^{235}\text{UO}_2$ ) spheres with mean diameters of 150  $\mu\text{m}$ . The thickness of the  $U_3O_7$  layer was estimated to be less than 100 nm, and the  $U_4O_9$  formation appeared to follow behind the propagating  $U_3O_7$  front. They observed that, based on first-order kinetics, the two-stage kinetic reaction had discontinuous slopes. They found it very difficult to ascribe an exact meaning to the "order" of the reaction. They subjected the 93v pellets to different burnups and observed a dependence on the second-stage activation energies.

Thomas et al. (1993) studied the oxidation of LWR fuel in the burnup range 27-48 MWd/kgU. In this burnup range, 3 to 4.5% of the initial U atoms are involved in fission. At approximately 30 MWd/kgU, there are about 1% Pu and 3% fission products that exist in solid solution. Table 3.2.2-12 is reproduced from the paper by Thomas et al. (1993).

**Table 3.2.2-12 Physical properties of some spent fuels**

Fuel Reactor	ATM-105 Cooper	TP Turkey Point	ATM-104 Calvert Cliffs	ATM-106 Calvert Cliffs
<b>Fuel Type</b>	BWR 7x7	PWR 15x15	PWR 14x14	PWR 14x14
<b>Burnup (MWd/kgU)</b>	28	27	43	48
<b>Fission Gas Release</b>	0.6%	0.3%	1.1%	1.8%
<b>Post Grain Size (<math>\mu\text{m}</math>)</b>	11–15	20–30	10–13	7–15

Oxidation of spent fuel at 175 and 195°C showed  $\text{UO}_2$  oxidized to  $\text{U}_4\text{O}_9$  along grain boundaries and saturated at the O/M levels of 2.40. Thomas et al. (1989) studied 27 MWd/kgU spent fuel by transmission electron microscopy (TEM) and found very small 2-nm gas bubbles and 30-nm solid particles deposited within the  $\text{UO}_2$  and apparent cracks from oxidation of  $\text{UO}_2$  to  $\text{U}_4\text{O}_9$ . Whereas unirradiated  $\text{UO}_2$  oxidized uniformly, the irradiated  $\text{UO}_2$  with the gas bubbles appeared to oxidize preferentially, causing a short circuit in favor of bulk oxygen diffusion. In spent fuel,  $\text{U}_4\text{O}_9$  forms preferentially along grain boundaries, and sharp oxidation fronts were observed.

Einzigler et al. (1991) argued that, thermodynamically,  $\text{UO}_2$  should oxidize completely to  $\text{UO}_3$ . The basic uncertainty is the kinetics of such oxidation. They found that, because the grain-boundary-surface-area-to-volume ratio is inversely proportional to grain size, the 11 to 15 mm Cooper BWR fuel oxidized more rapidly than the larger, 20 to 30  $\mu\text{m}$  Turkey Point PWR fuel. In 12 comparisons with experimental data, the oxidation model by Stout et al. (1989, 1991, 1993a, 1993b, and version 1.2 of this document) clearly show this grain-size dependency on the O/M histories for the consecutive reactions:  $\text{UO}_2 \rightarrow \text{U}_4\text{O}_9$  and  $\text{U}_4\text{O}_9 \rightarrow \text{U}_3\text{O}_8$ . Stout et al. (1993a and 1993b) showed that the stress state for  $\text{UO}_2 \rightarrow \text{U}_4\text{O}_9$  transformation is sufficient to form microcracks; this is even more so the case for the  $\text{U}_4\text{O}_9 \rightarrow \text{U}_3\text{O}_8$  transformation in which  $\text{U}_3\text{O}_8$  spalls.

Experimentally, it is nearly impossible to obtain a monosized distribution of spent-fuel grain sizes. Stout et al. (version 1.2 of this document) showed that the experimental results were bounded in an envelope of monosized particles whose grain half sizes ranged from 4-24  $\mu\text{m}$ . The larger-sized particles oxidized considerably more slowly, and the transformation from  $\text{U}_4\text{O}_9$  to  $\text{U}_3\text{O}_8$  would exhibit a plateau.

With this brief background, it is possible to extend the previous work of Stout et al. (version 1.2 of this document). Previously, a set of monosized  $\text{UO}_2$  grains formed a bounding envelope for the ODB experimental measurements of  $\text{UO}_2 \rightarrow \text{U}_4\text{O}_9 \rightarrow \text{U}_3\text{O}_8$ . This envelope of grain half sizes is appropriate for the phase transformation  $\text{UO}_2 \rightarrow \text{U}_4\text{O}_9$  but not for the next phase transformation,  $\text{U}_4\text{O}_9 \rightarrow \text{U}_3\text{O}_8$ .

The initial grain-size distribution for the phase transformation  $\text{UO}_2 \rightarrow \text{U}_4\text{O}_9$  is not appropriate for the subsequent phase transformation  $\text{U}_4\text{O}_9 \rightarrow \text{U}_3\text{O}_8$  because shrinkage cracks in the  $\text{U}_4\text{O}_9$  alter the original  $\text{UO}_2$  grain-size distribution. Thomas et al. (1991) presented optical micrographs of LWR (ATM-101) spent-fuel fragments showing the pellet rim and the fracture edge of the partial oxidation of  $\text{UO}_2 \rightarrow \text{U}_4\text{O}_9$ . The nominal burnup was 28.4 MWd/kgU, and the initial  $\text{UO}_2$  grain sizes were typically about 15 to 25  $\mu\text{m}$ . However, the micrographs of the  $\text{U}_4\text{O}_9/\text{UO}_2$  (see Thomas et al, 1991, Figure 2) showed a multitude of grain boundary and transverse cracks with a grain-size distribution ranging from 1.5 to 11  $\mu\text{m}$ , with a preponderance of fine grain sizes, and relatively few larger grains (on the order of 8 to 11  $\mu\text{m}$ ). Grain-boundary cracking in the  $\text{U}_4\text{O}_9$  phase is a result, rather than the cause, of the oxidation.

Similarly, Thomas and Einzigler (1992) studied ATM-103 PWR spent-fuel oxidation. The nominal burnup was 30 MWd/kgU, and the post-irradiation average grain size of the  $\text{UO}_2$  was 18.5  $\mu\text{m}$ . They oxidized the spent fuel at a constant temperature of 195°C. In Figure 1 of their report, they presented a series of micrographs taken at 24, 48, 118, and 355 hr. That boundary and transverse cracks yielded progressively finer grains is clearly evident from their micrographs. At 355 hr [ $\Delta(\text{O}/\text{M}) = 0.16$ ], there were grain sizes ranging from 3 to 22  $\mu\text{m}$ . The American Society for Testing and Materials (ASTM) grain size was determined to be 9.6  $\mu\text{m}$ .

## 3.2.2.9 Model Enhancements

The model enhancements for the reaction  $U_4O_9 \rightarrow U_3O_8$  are three-fold:

1. A log-normal distribution for grain sizes are assumed for the  $U_4O_9$ .
2. The activation energy  $Q_{38}$  for the phase transformation  $U_4O_9 \rightarrow U_3O_8$  varies linearly with burnup.
3. Spent-fuel  $U_4O_9$  samples contaminated with what appears to be a dehydrated schoepite film have a lower  $Q_{38}$  than does unhydrated  $U_4O_9$ . (This issue of dehydrated schoepite will be discussed subsequently.)

The basic formulation of the grain and fragment size statistical dependence for the oxidation response model has been presented by Stout et al. (1989, 1991, 1993a, 1993b, and version 1.2 of this document). Fragments are assumed to be composed of pyramidal shapes of varying sizes, in accordance with some probabilistic density function. The integrated response for the oxidation or weight gain history of a heterogeneous sample having some probabilistic density function of grain size distribution was formulated.

A heterogeneous sample of  $U_4O_9$  grains can be viewed as an ensemble of various numbers of monosized grains. For each monosized grain of half size  $c_i$ , assume there are  $N_i$  grains. Let  $P(c_i)$  be the normalized fractional distribution of grains with half-size,  $c_i$ . Let the response history of a monosized  $U_4O_9$  grain of size  $c_i$  be denoted by  $h(t | c_i)$ . Then the average, or expected, value of the history of a heterogeneous sample undergoing oxidation ( $U_4O_9 \rightarrow U_3O_8$ ) is given by

$$h(t) = \sum_i h(t | c_i) P(c_i). \quad 3.2.2-23$$

Remenyi (1974, pp 78-81) showed that, in most circumstances, the grain-size distribution is a log normal with the mean value shifted toward fine grain sizes. This type of distribution will be assumed throughout the remaining portions of Section 3.2.2.

The Arrhenius chemical kinetics are very temperature-sensitive. The rate of  $U_3O_8$  formation is the primary concern in a repository environment. The frontal speed  $\dot{W}_{38}$  (see Eq. 3.2.2-14a) depends on temperature, activation energy, and the distribution of grain half sizes.

By using nonequilibrium thermodynamics, Stout et al (1993b) showed that the phase-transformation, front-rate tensors and mass-transport tensors are burnup-dependent. That is, oxidation rate is suppressed monotonically with increasing concentrations of fission products and actinides. They predicted that the thermodynamic models have a linear burnup dependence. After considerable analyses of numerous TGA and ODB experiments, Hanson (1998) confirmed the conjecture that there is indeed a linear burnup dependence on the activation energy for the reaction  $U_4O_9 \rightarrow U_3O_8$ . He found that, because the dopant fission products are directly proportional to burnup, the activation energy varies approximately as

$$Q_{38} = (Q_{38}^0 + \alpha^* BU) \text{ kJ/mole-}^\circ\text{K} \quad 3.2.2-25$$

where  $Q_{38}^0 = 155 \text{ kJ/mole-}^\circ\text{K}$ , and  $\alpha = 1.2 \text{ kJ/(mole-}^\circ\text{K- MWd/kgU)}$ .

The uncertainty in  $Q_{38}$  is at least 10 to 15 kJ/mole (2.4-3.6 kcal/mole). Larger uncertainties in the fit can be attributed to the radial distribution in the fission and actinide concentrations; the quantity of actinides produced by neutron absorption can vary even for samples of nearly identical burnup. For more details, see Hanson (1998).



Thin films of what appears to be dehydrated schoepite have been found on some TGA and ODB samples. Before conducting the experiments, the spent-fuel samples had been stored at room temperature for a couple of years, and these samples reacted with the water vapor in the air to form thin schoepite films. Those samples with such schoepite films gained weight much more rapidly than did the unhydrated samples. The most plausible explanation is that the schoepite having a fine needle-like structure has a greatly increased effective surface area for oxygen adsorption and thus raises the oxygen potential available to the adjacent grains. These grains behaved as if their respective activation energies were lower than were those of the unhydrated grains.

The model presented in Section, 3.2.2.4, with the modification introduced in Section 3.2.2.9, is sufficiently robust to handle  $U_4O_9$  distributions, burnup-dependent activation energies, and schoepite-modified activation energies.

The enhanced model is compared with experiments from two distinct experiments:

1. Thermogravimetric analysis (TGA), in which small samples (200 mg) were oxidized
2. Oven drybath (ODB) oxidation, in which larger samples (5 g) were used

In the next two subsections, model comparisons with the various experiments will be presented. Because  $U_3O_8$  has a potential, disruptive effect on depository performance, these studies will focus on the conversion of  $U_4O_9 \rightarrow U_3O_8$ .

#### 3.2.2.10 Model Predictions of $U_4O_9 \rightarrow U_3O_8$ with TGA Experiments

It is advantageous to focus on the TGA oxidation experiments because there ought to be much less variability among individual samples (200 mg) than there is with the much larger ODB samples (5g). The present focus is on ATM-105-sample experiments conducted at different temperatures. The ATM-105 samples were stored in hot cells at room temperature for a number of years, and some of them appear to have formed a hydrated phase of dehydrated schoepite on the  $UO_2$ . Using SEM, clear photographic evidence of this hydrated film was found on several samples for both the TGA and the ODB oxidation experiments. The hydrated-surface formation was observed on the TGA samples ATM-105-01 and ATM-105-02 and on the ODB samples TP-P2-100 and 104F-100. This formation was identified on the fines of ATM-105 stored under identical conditions in the same hot cell. It is highly probable that the hydrated formation exists on other samples as well, especially on those that have been stored for extended periods at ambient temperature before being oxidized. Whilenot all the suspected samples were analyzed by SEM, Hanson inferred that those samples that experienced very rapid initial weight gains had this dehydrated schoepite contamination, and the model results appear to have confirmed this hypothesis.

It is assumed that, in the process of forming  $U_4O_9$ , stress cracks will subdivide the original, larger grain-sized  $UO_2$ . Theoretically, the grain sizes have a log-normal grain-size distribution. This distribution was approximated by four grain half-size bins. Four grain half-size bins were chosen to limit the number of adjustable free parameters. An initial set of four representative grain half-size bins and their corresponding fractions were selected, and iteratively improved to give the best fit with the experimental  $\Delta(O/M)$  histories. Note that the  $\Delta(O/M)$  histories of this set of experiments exhibit a linear relation.

Hanson (1998) recorded the axial location in the fuel rod from which the sample came. He performed analyses on these samples to estimate the individual burnup. Even though the ATM-105 samples had a reported average burnup of 31 MWd/kgU in the high-burnup region, Hanson found significant variations in burnup with the ATM-105 samples. These

variations in burnup are presented in Table 3.2.2-13. Because of these variations, it was decided to verify the model against the TGA experiments, taking into account the burnup variation with  $Q_{38}$ .

**Table 3.2.2-13 Burnup estimates of the TGA-104 and TAG-105 200-mg samples**

Sample Identifier	Sample Burnup (MWd/kgU)
105-01	unknown
105-02	unknown
105-03	28.1
105-04	27.5
105-06	31.5
105-10	29.8
105-11	29.6
105-14	28.1
105-15	18.6
105-17	16.7
105-18	16.8
104-01	42.3

**Table 3.2.2-14** lists the sample specimen for samples ATM-105-04 through ATM-105-10, the optimized activation energy  $Q_{38}$ , the four grain half-sizes bins, and their respective fractions. Figures 3.2.2-9 through 3.2.2-12 show the fit of the theoretical histories (solid lines) and the experimental histories (dotted lines). The experimental measurements of  $\Delta(O/M)$  are accurate to 0.01; except for the experimental data scatter, the agreement is excellent. None of the ODB data that was used was regressed or smoothed. The TGA data shown in the figures are averages over a one-hour period; no other smoothing was performed.

**Table 3.2.2-14 TGA nonhydrated samples listing the temperatures at which the experiment was conducted, the optimized  $Q_{38}$ , and the grain half sizes and corresponding fractions**

Sample	T (°C)	$Q_{38}$	$c_1$	$F_1$	$c_2$	$F_2$	$c_3$	$F_3$	$c_4$	$F_4$
105-04	270	182	1.05	0.45	2.00	0.40	5.00	0.10	7.00	0.05
105-06	283	189	1.00	0.39	2.00	0.36	4.00	0.13	7.00	0.12
105-10	305	183	0.90	0.61	2.00	0.29	3.50	0.09	6.40	0.01
105-11	305	185	0.90	0.33	1.70	0.36	4.10	0.15	7.50	0.16
105-14	305	183	1.00	0.35	1.80	0.43	3.30	0.14	6.00	0.08
105-17	305	174	0.35	0.60	0.70	0.25	3.50	0.10	7.00	0.05
104-01	305	194	1.00	0.48	2.00	0.33	4.00	0.13	7.00	0.06

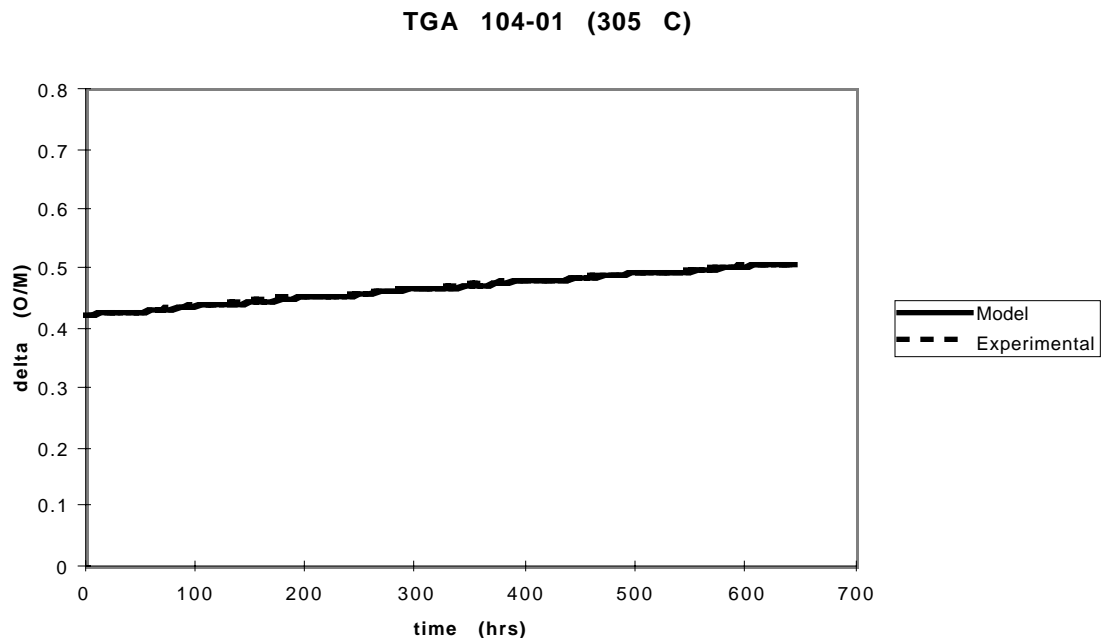


Figure 3.2.2-9  $\Delta$  (O/M) versus time (hr) for the TGA sample ATM-104-01 (305°C)  
[LL980912451021.055]

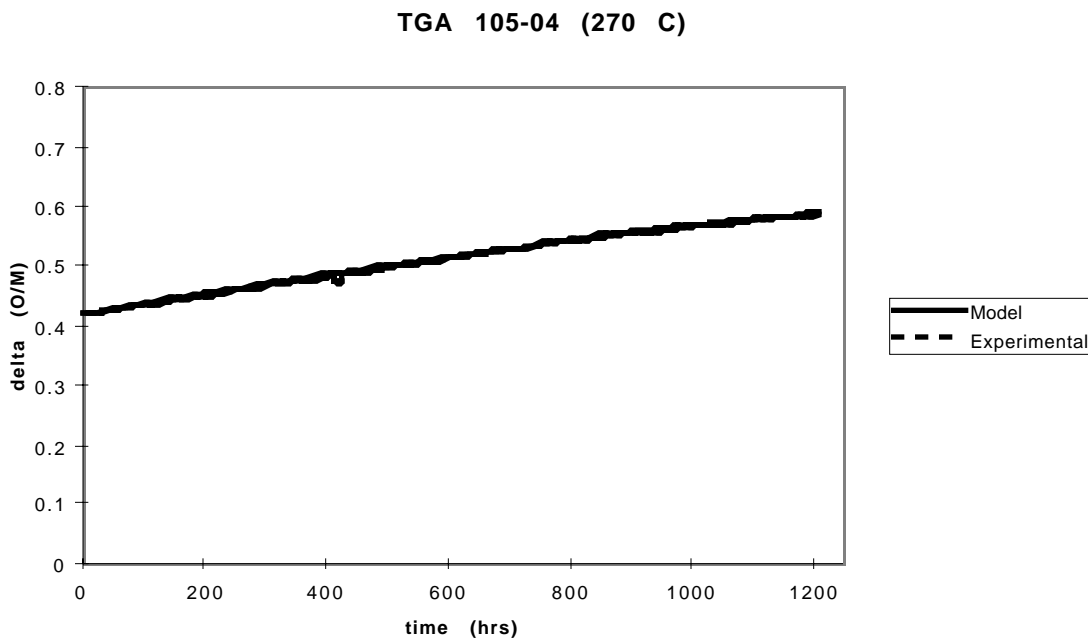
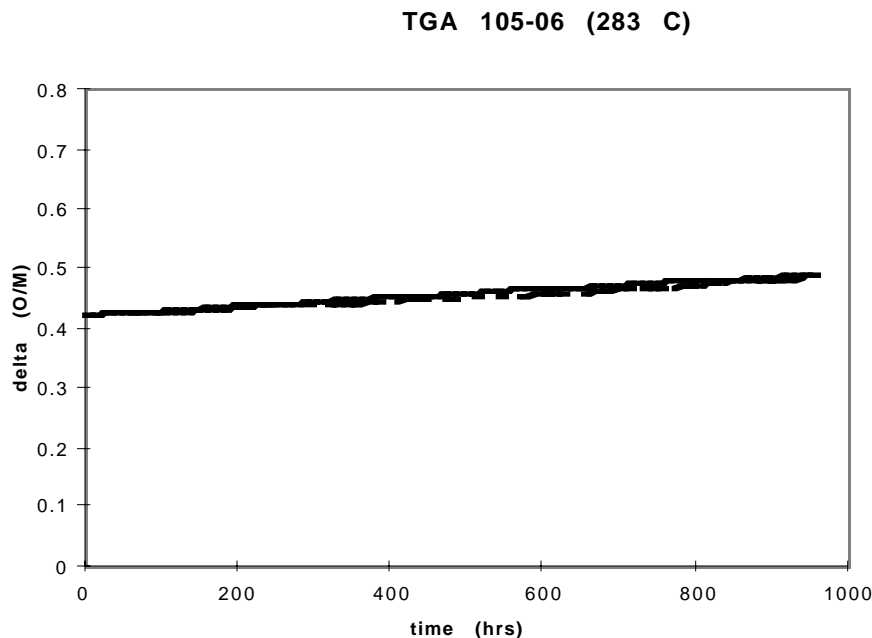
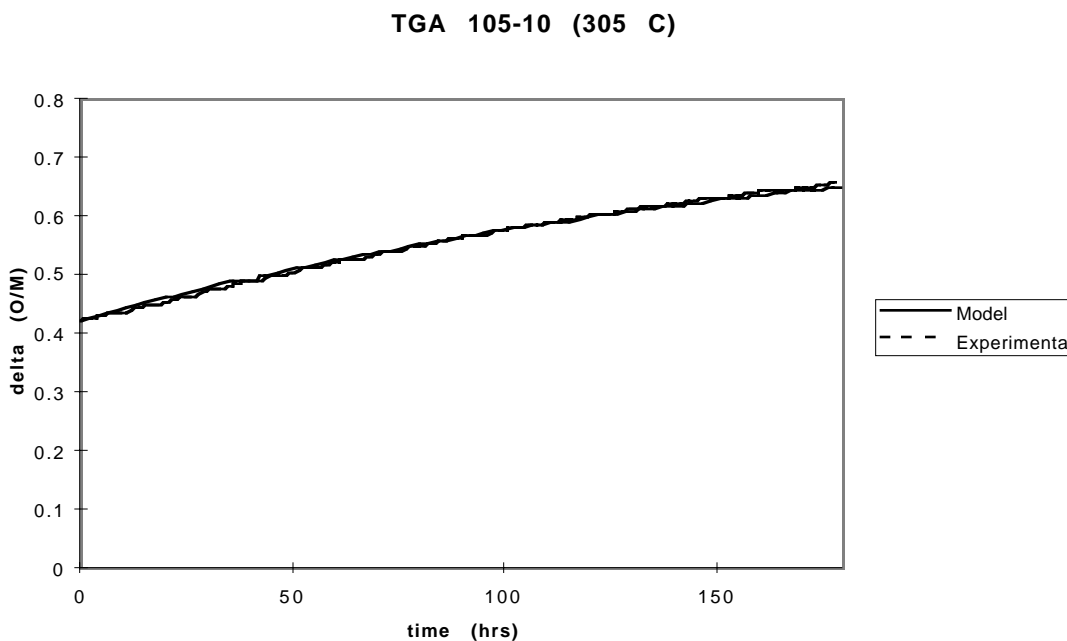


Figure 3.2.2-10  $\Delta$  (O/M) versus time (hr) for the TGA sample ATM-105-04 (270°C)  
[LL980912451021.055]



**Figure 3.2.2-11**  $\Delta(O/M)$  versus time (hr) for the TGA sample ATM-105-06 (283°C)  
[LL980912451021.055]



**Figure 3.2.2-12**  $\Delta(O/M)$  versus time (hr) for the TGA sample ATM-105-10 (305°C)  
[LL980912451021.055]

Other TGA samples (ATM-105-01, ATM-105-02, ATM-105-03, ATM-105-11, ATM-105-14, ATM-105-15, 105-17, and ATM-105-18) appear to exhibit anomalous behavior. These TGA samples did not exhibit a linear relation of  $\Delta(O/M)$  with respect to time. On closer inspection using SEM, Hanson observed that samples ATM-105-01 and ATM-105-02 had formed a thin layer of what appears to be dehydrated schoepite. (It is possible that samples ATM-105-03,

### 3.2.2 Oxidation Models

ATM-105-11, and ATM-105-14 had some hydrated-phase formation, but this has not been confirmed.) Such samples exhibited a nonlinear weight-gain relation early in the experiment but asymptotically leveled off to a more linear relation with time. This behavior could be explained by either of two explanations:

- Somehow the samples had a distribution of very fine grain sizes, some of which could be smaller than  $0.07\text{ }\mu\text{m}$ . This explanation was dismissed because the shrinkage stresses that would occur in the formation of  $\text{U}_4\text{O}_9$  were not believed sufficient to form such small grains.
- The dehydrated schoepite, having a pronounced needle-like structure that greatly increases the effective surface area (the same effect as having smaller grain sizes), acts as a conduit for rapid oxygen transfer initially. After a sufficient amount of  $\text{U}_4\text{O}_9$  had formed and spalled, the remaining unhydrated  $\text{U}_4\text{O}_9$  oxidized more slowly with a nearly linear relation with time. This explanation seems to be the more reasonable scenario, and there is sufficient evidence that this is most plausible.

Samples ATM-105-15, ATM-105-17, and ATM-105-18 all came from the low-burnup (15-20 MWd/kgU), upper end of the same fuel rod as did the other ATM-105 samples. These samples are expected to have experienced very little grain growth because of the lower temperatures corresponding to the lower fission density. It is not clear whether  $\text{U}_3\text{O}_8$  formed concurrently with the  $\text{U}_4\text{O}_9$  phase or if  $\text{U}_3\text{O}_7$  formed instead. Further work on the low-burnup fuels is necessary to determine the cause for the observed difference in oxidation behavior. These samples came from a freshly cut segment of clad fuel, so the presence of the hydrated phase is not expected.

Tables 3.2.2-15 through 3.2.2-18 list the optimized  $Q_{38}$ , grain half sizes and fractions for the four bins for the TGA samples: ATM-105-01, ATM-105-02, ATM-105-03, ATM-105-11, ATM-105-14, ATM-105-17, and ATM-105-18. Figures 3.2.2-13 through 3.2.2-20 show the experimental and model  $\Delta(\text{O}/\text{M})$  histories. The TGA model time histories are in excellent agreement with the experimental measurements for those samples with a thin layer of schoepite. It appears that the  $\text{U}_4\text{O}_9 \rightarrow \text{U}_3\text{O}_8$  kinetic model can indeed account for the presence of schoepite if the activation energies and effective grain sizes were adjusted downward for those bins influenced by the hydrated phase.

**Table 3.2.2-15 TGA-105-01 hydrated sample listing the optimized  $Q_{38}$  for each bin and the corresponding grain half sizes and fractions**

$Q_{38}$	$c_1$	$F_1$	$c_2$	$F_2$	$c_3$	$F_3$	$c_4$	$F_4$
178.5	0.70	0.18						
178.0			1.50	0.30				
169.6					3.70	0.515		
169.6							7.00	0.005

**Table 3.2.2-16 TGA-105-02 hydrated sample listing the optimized  $Q_{38}$  for each bin and the corresponding grain half sizes and fractions**

$Q_{38}$	$c_1$	$F_1$	$c_2$	$F_2$	$c_3$	$F_3$	$c_4$	$F_4$
178.5	0.7	0.18						
178.5			1.50	0.30				
170.0					4.00	0.47		
170.0							6.00	0.05

**Table 3.2.2-17 TGA-105-03 hydrated sample listing the optimized  $Q_{38}$  for each bin and the corresponding grain half sizes and fractions**

$Q_{38}$	$c_1$	$F_1$	$c_2$	$F_2$	$c_3$	$F_3$	$c_4$	$F_4$
159.6	1.00	0.45						
159.6			2.00	0.35				
154.8					4.00	0.15		
154.8							7.00	0.05

**Table 3.2.2-18 TGA-105-18 hydrated sample listing the optimized  $Q_{38}$  for each bin and the corresponding grain half sizes and fractions**

$Q_{38}$	$c_1$	$F_1$	$c_2$	$F_2$	$c_3$	$F_3$	$c_4$	$F_4$
150.4	1.15	0.45						
150.4			2.30	0.35				
160.6					4.00	0.15		
160.6							7.00	0.05

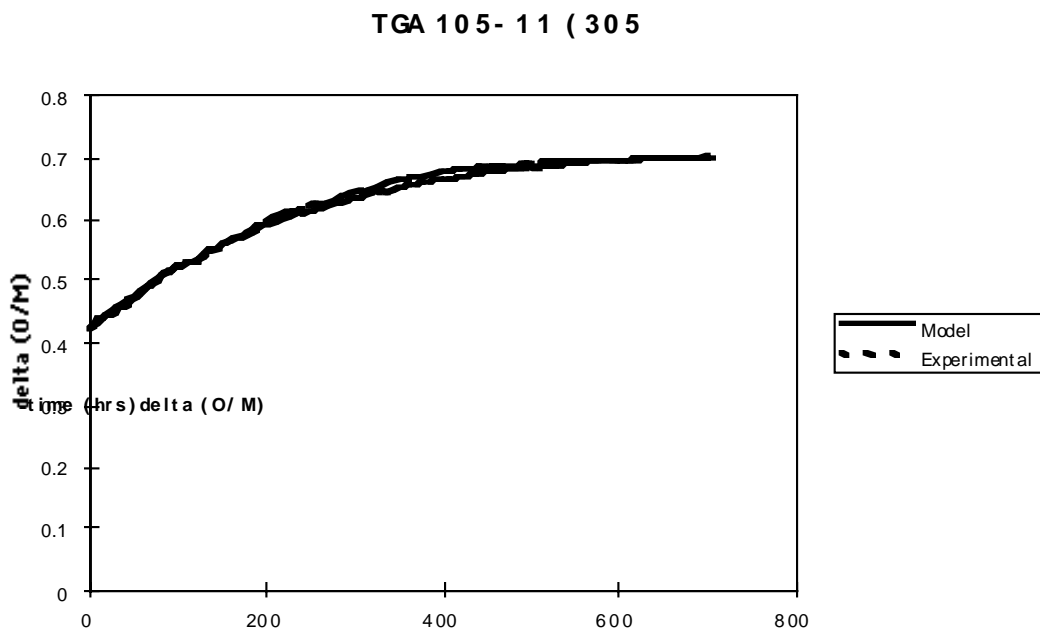


**Figure 3.2.2-13**  $\Delta$  (O/M) versus time (hr) for the TGA sample ATM-105-11 (305°C); some shoebite present [LL980912451021.055]

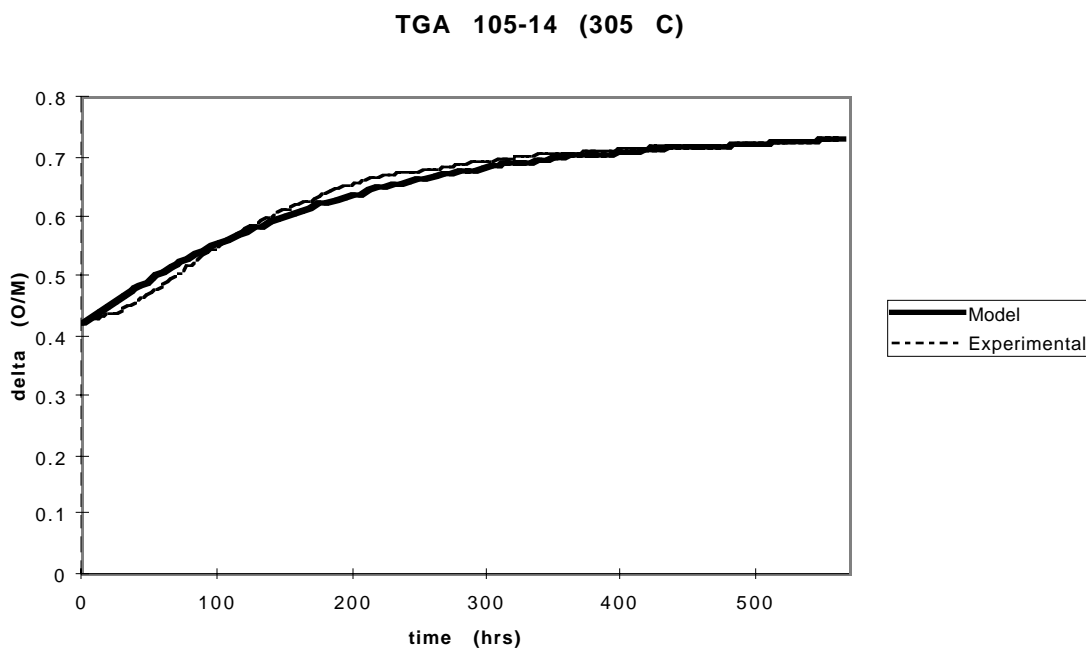


**Figure 3.2.2-14**  $\Delta$  (O/M) versus time (hr) for the TGA sample ATM-105-14 (305°C); some shoebite present [LL980912451021.055]

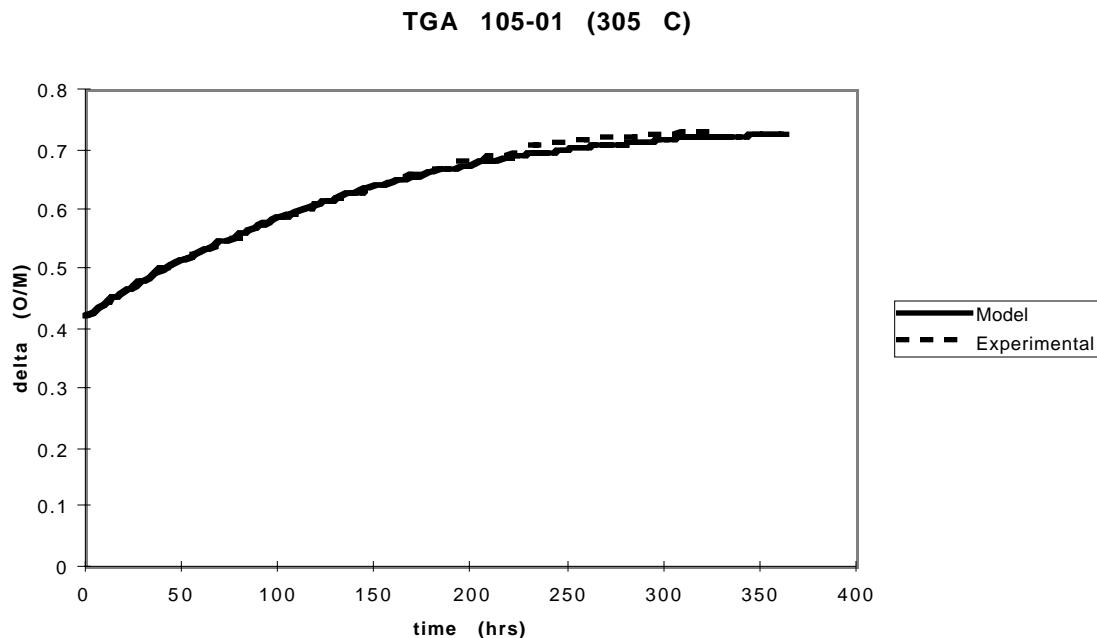


**Figure 3.2.2-15**  $\Delta (O/M)$  versus time (hr) for the TGA sample ATM-105-01 (305°C); shoebite present (Figure 3.2.2-15) [LL980912451021.055]

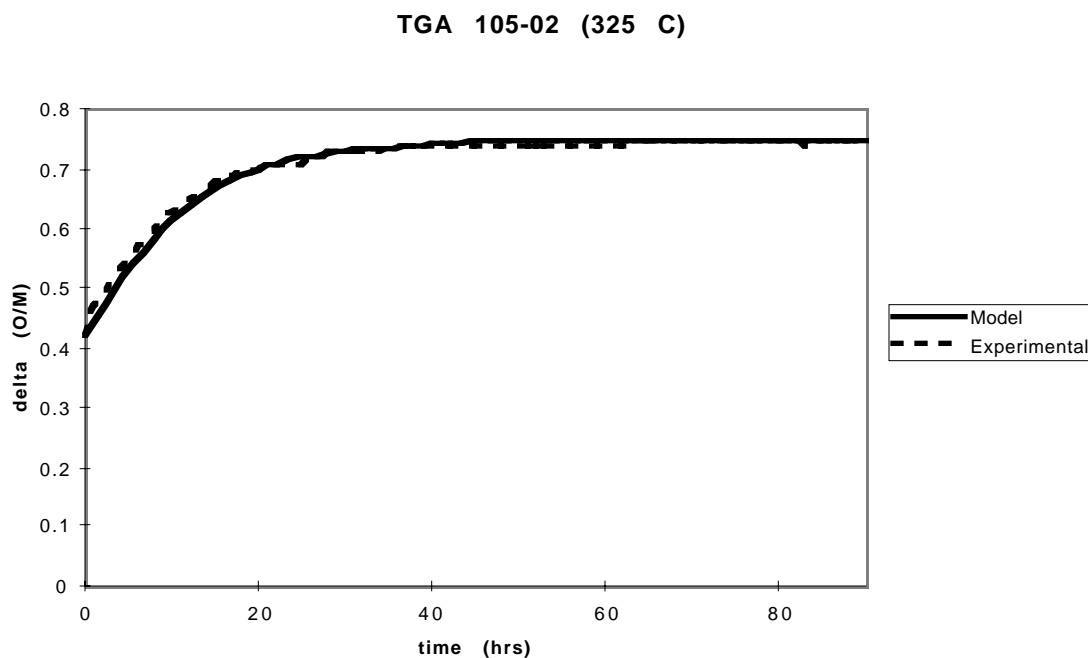


**Figure 3.2.2-16**  $\Delta (O/M)$  versus time (hr) for the TGA sample ATM-105-02 (325°C); shoebite present [LL980912451021.055]



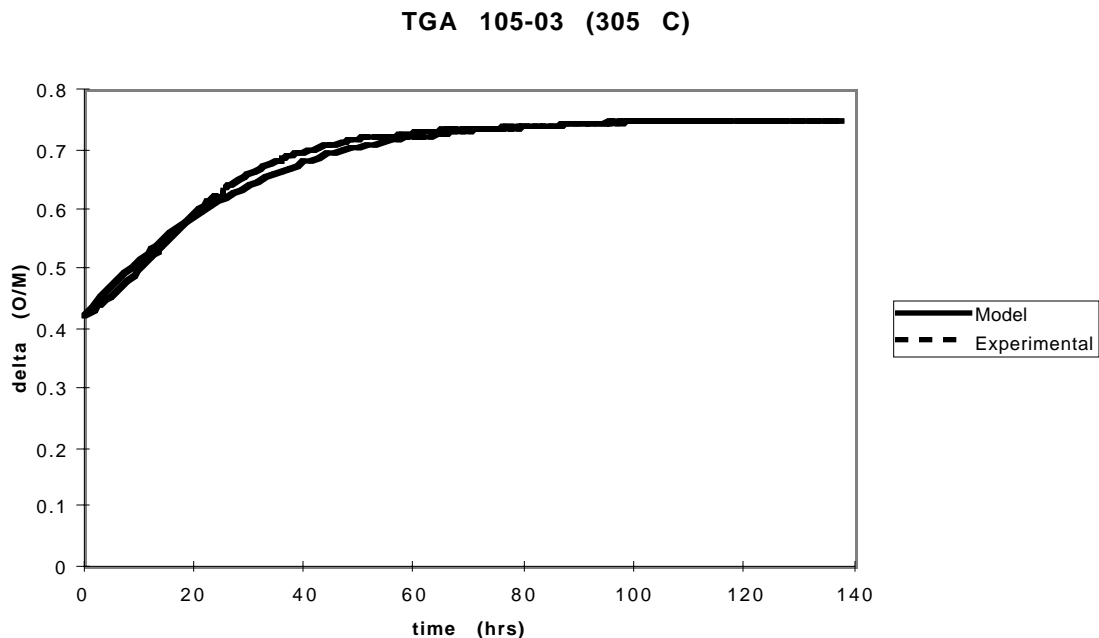


Figure 3.2.2-17  $\Delta$  (O/M) versus time (hr) for the TGA sample ATM-105-03 (305°C); shoepite present [LL980912451021.055]

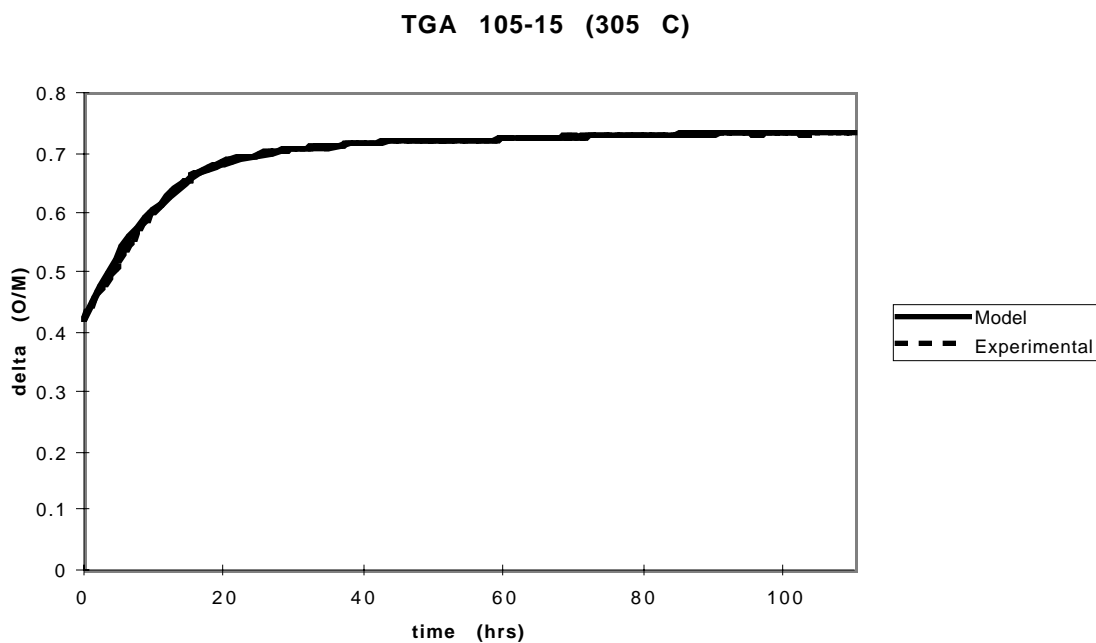
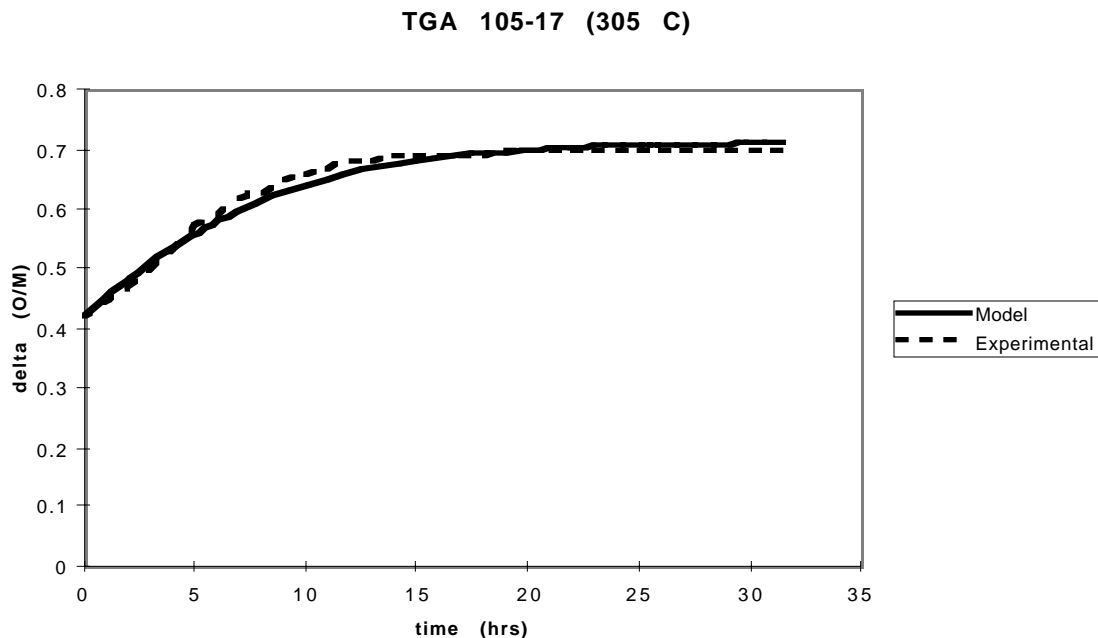
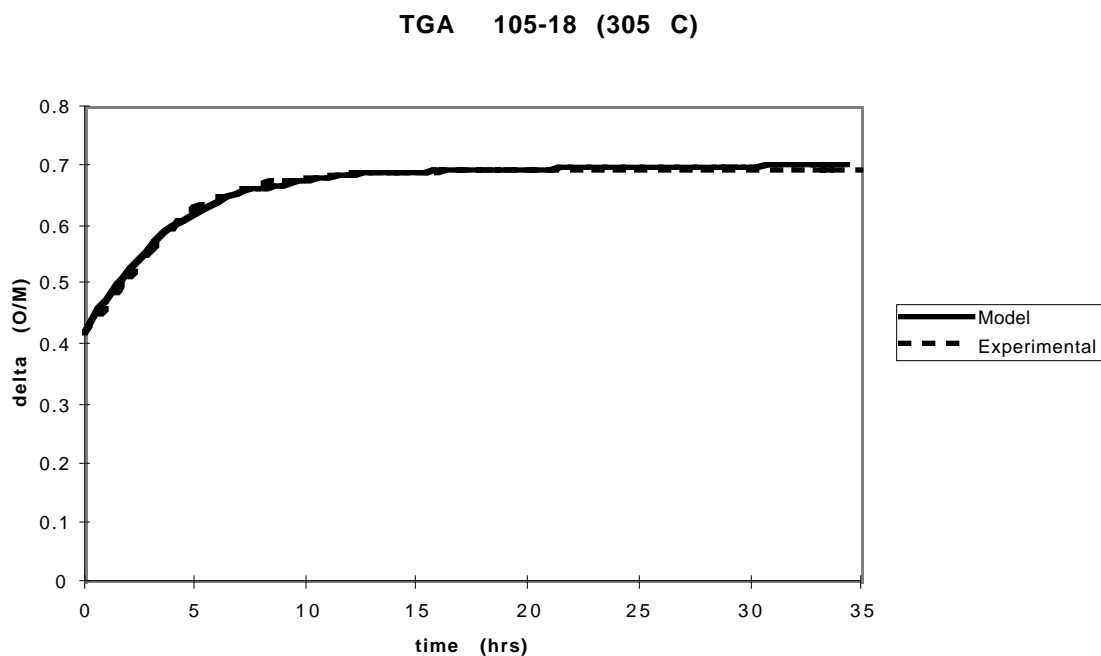


Figure 3.2.2-18  $\Delta$  (O/M) versus time (hr) for the TGA sample ATM-105-15 (305°C); shoepite present [LL980912451021.055]



**Figure 3.2.2-19**  $\Delta$  (O/M) versus time (hr) for the TGA sample ATM-105-17 (305°C); shoebite present [LL980912451021.055]



**Figure 3.2.2-20**  $\Delta$  (O/M) versus time (hr) for the TGA sample ATM-105-18 (305°C); shoebite present [LL980912451021.055]

### 3.2.2.11 Model Predictions of $U_4O_9 \rightarrow U_3O_8$ with Oven Drybath Experiments

The experimental data against which the model was fit were based on the work of Einziger et al. (1995 and 1996) on LWR spent fuel at various burnups and initial  $UO_2$  grain sizes. The test consisted of 11 samples: 7 samples consisted of 5 g of spent-fuel fragments, and the remaining 4 samples consisted of 5 g of crushed fuel fragments.

Two of the seven samples of the uncrushed fragments were prepared from one of each ATM-104 and ATM-105 as-irradiated fuel fragments with no prior oxidation. The third sample was the Turkey Point fuel that had been oxidized at 110°C for 28,868 hr to an O/M of ~2.004. The fourth sample was ATM-106 fragments that had been oxidized at 110°C for 525 hr to an O/M = 2.000. Another set of samples included Turkey Point fuel that had been slightly oxidized at 175°C for 43,945 hr to an O/M = 2.395, an ATM-105 fuel that had been oxidized at 175°C for 34,430 hr to an O/M = 2.422, and an ATM-104 sample that had been oxidized at 175°C for 15,671 hr to an O/M = 2.395. For more details, see Hanson (1998).

For a specific ATM, the pulverized samples (denoted by the suffix P) gained weight more rapidly than did the samples of fragments (denoted by the suffix F). All samples with a -100 designation had been stored at ambient temperature in the hot cell longer than the other samples of the same ATM. These -100 samples were expected to have a greater amount of hydrated-phase formation. This assumption is partially verified by the known presence of the hydrated phase on two of these samples (P2-100 and 104F-100).

Because the starting point for the various samples varied from unoxidized  $UO_2$ , mixtures of  $UO_2$  and  $U_4O_9$ , and completely converted  $U_4O_9$ , all the  $U_4O_9 \rightarrow U_3O_8$  modeling studies presented here adjusted the time when the reaction  $UO_2 \rightarrow U_4O_9$  was complete. Using the O/M measurement at various times, the time for complete conversion of  $UO_2 \rightarrow U_4O_9$  was linearly extrapolated to the estimated time at which  $\Delta(O/M) = 0.42$ . With these caveats, the modeling and experimental studies focused on studying the reaction,  $U_4O_9 \rightarrow U_3O_8$  as a function of time.

The linear relation between activation energy and burnup (Eq. 3.2.2-23) was used for the ODB Turkey Point, ATM-105, ATM-104, and ATM-106 samples in a manner similar to the previously described study with the TGA samples. The optimized fractions and grain half sizes obtained from the TGA fits were used to start the iteration scheme. In the TGA experiments, the O/M histories were obtained at different temperatures; all the ODB samples used for this analysis were conducted at a constant 255°C.

As was the case with the TGA experiments, the ODB data set was fitted in two categories:

- Those experimental samples that each had a nearly uniformly linear weight-gain history
- Those experimental samples that each had a rapid nonlinear initial weight-gain history that tended asymptotically to a linear weight-gain history

The ODB experiments that did exhibit a linear weight-gain history were lumped into two classes:

1. The Turkey Point and ATM-105 experiments had nearly similar burnups (28 and 27 MWd/kgU) and were expected to have similar grain half-size distributions and activation energies.

- The ATM-104 and ATM-106 fuels had burnups of 43 and 48 MWd/kgU, respectively. These higher-burnup spent fuels had smaller starting  $U_4O_9$  grain half sizes because their starting  $UO_2$  grain half sizes were smaller. The ATM-106 fuel is known, however, to have a small amount of a restructured rim.

The optimized grain-size distributions for the nonhydrated Turkey Point and ATM-105 ODB samples are presented in 3.2.2-19, and the resulting comparison of the model fit and the experimental  $\Delta(O/M)$  histories are presented in Figures 3.2.2-21 through 3.2.2-23. The grain-size fractions of the  $U_4O_9$  are reasonable with the photographs published by Thomas et al. (1991).

**Table 3.2.2-19 ODB nonhydrated Turkey Point and ATM-105 samples listing the optimized  $Q_{38}$  for all bins and the corresponding grain half sizes and fractions**

Fuel Sample	$Q_{38}$	Fraction (0.75,2.0) $\mu\text{m}$	Fraction (2.0,8.0) $\mu\text{m}$	Fraction (8.0,14.0) $\mu\text{m}$	Fraction >(14.0) $\mu\text{m}$
TP-F-003A	188.6	0.61	0.28	0.095	0.025
TP-F-017A	188.6	0.26	0.23	0.16	0.14
105F-13A	190.5	0.00	0.20	0.40	0.40

**TP-F-003A**

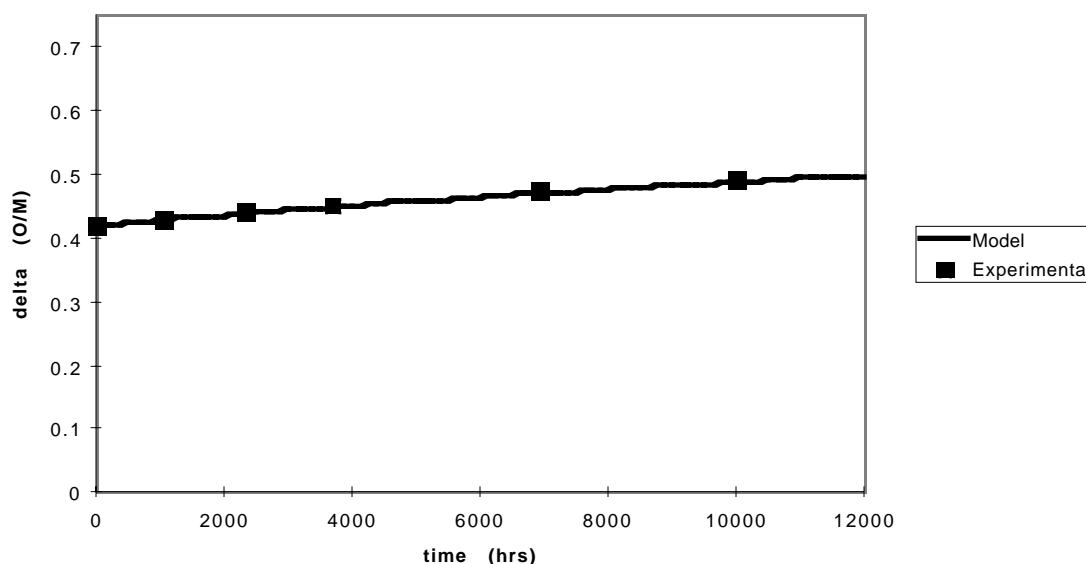


**Figure 3.2.2-21  $\Delta(O/M)$  versus time (hr) for the ODB sample TP-F-003A; nominal burnup, 27 MWd/kgU [LL980912451021.055]**

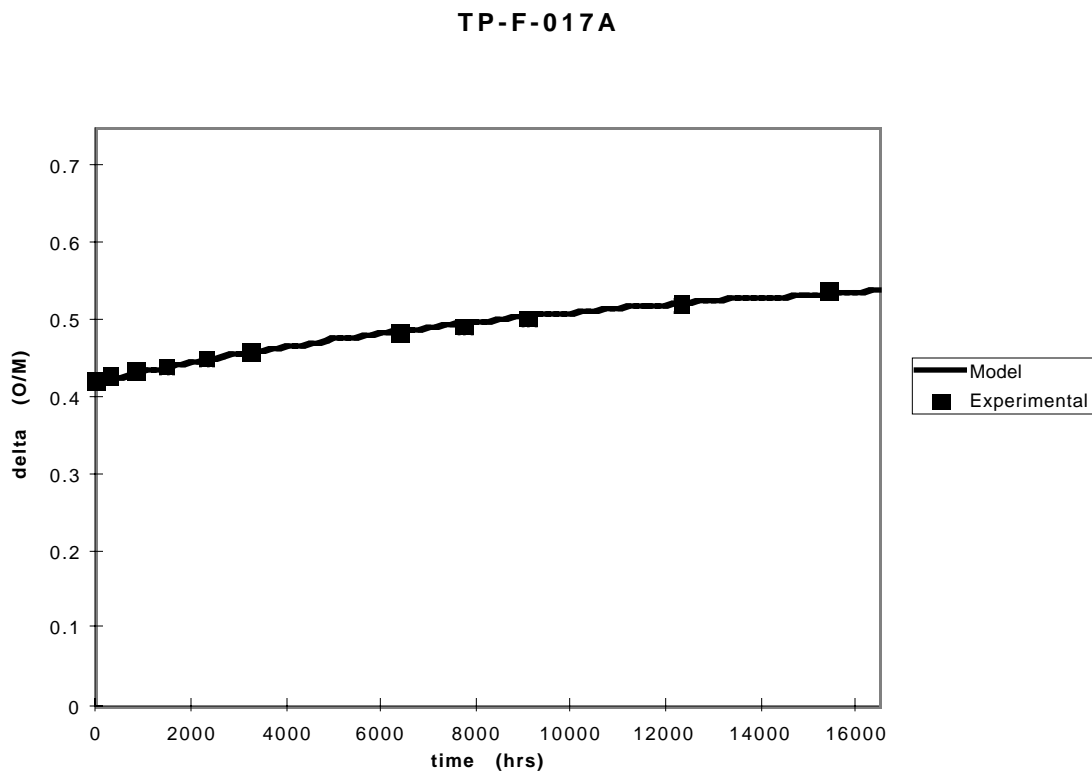


Figure 3.2.2-22  $\Delta$  (O/M) versus time (hr) for the ODB sample TP-F-017A; nominal burnup, 27 MWd/kgU [LL980912451021.055]

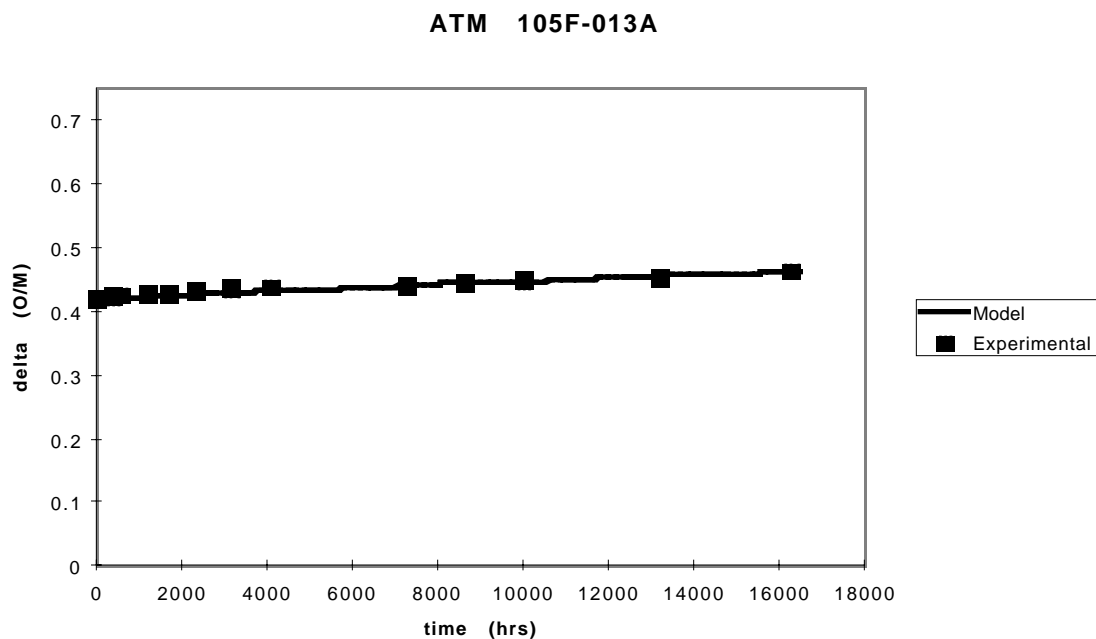


Figure 3.2.2-23  $\Delta$  (O/M) versus time (hr) for the ODB sample ATM-105F-013A; nominal burnup, 28 MWd/kgU [LL980912451021.055]

The higher burnup ATM-104 and ATM-106 fuel samples were an interesting set of experiments to fit. First, if nominal activation energy of 167.4 kJ/mole (40 kcal/mole) were used to fit these samples, the grain half sizes required would have ranged from 2-24  $\mu\text{m}$ . However, as shown in Table 3.2.2-12, which is taken from Thomas et al. (1991), the ATM-104 and ATM-106 spent fuels had unoxidized grain half sizes in the range of 5 to 6.5  $\mu\text{m}$  and 3.5 to 7.5  $\mu\text{m}$ , respectively. Not only do such large grain half sizes exceed that of the unoxidized  $\text{UO}_2$ , but also it would require that no grain subdivision occur in the formation of  $\text{U}_4\text{O}_9$ . This assumption was rejected as unphysical for these two reasons. It is not valid to use a  $Q_{38}$  that was optimized for a spent fuel having a burnup of 27 MWd/kgU for higher burnup spent fuels. The more reasonable approach was to use a burnup-dependent activation energy to account for the differences among the ATM fuels used in the ODB experiments.

The optimization for these higher burnup fuels was constrained to have grain sizes no smaller than 0.1 to 0.25  $\mu\text{m}$ , the size obtained when the rim region undergoes restructuring. Thus, the free parameters of the oxidation reaction  $\text{U}_4\text{O}_9 \rightarrow \text{U}_3\text{O}_8$  are the distribution of the grain half sizes in the bins and the activation energy. It was assumed that these higher burnup fuels with no obvious evidence of hydrated layers could be assigned a uniform activation energy throughout the sample. As pointed out by Hanson (1998), the activation energy has an uncertainty of at least 10 to 15 kJ/mole for the  $\text{U}_4\text{O}_9 \rightarrow \text{U}_3\text{O}_8$  reaction. The optimized grain half-size distributions and activation energies are presented in Table 3.2.2-20 for the ATM-104F-005A, ATM-106F-022A, and ATM-106F-13A samples. The comparison of the model fits and the experimental data are presented in Figures 3.2.2-24 through 3.2.2-26. The extremely fine-grain structure obtained for these samples is not realistic. The samples would have to contain virtually all restructured rim and/or there must be more cracking of the  $\text{U}_4\text{O}_9$  grains. Because all the ODB samples were at 255°C,  $\text{U}_4\text{O}_9$  would be expected to yield similarly sized cracked-grain sizes. An alternative explanation is that these samples contained, at most, 20% restructured rim and also hydrated phase. This would shift the effective grain sizes toward smaller values. At present, much more experimental study is required to confirm such speculations.

**Table 3.2.2-20 ODB nonhydrated ATM-104 and ATM-106 samples listing the optimized  $Q_{38}$  for all bins and the corresponding grain half sizes and fractions**

Fuel Sample	$Q_{38}$	Fraction (0.1–0.25) mm	Fraction (0.25–0.5) mm	Fraction (0.5–1.0) mm
104F-00F5A	201.1	0.74	0.11	0.05
106F-022A	203.2	0.74	0.11	0.05
106F-13A	204.6	0.74	0.11	0.05

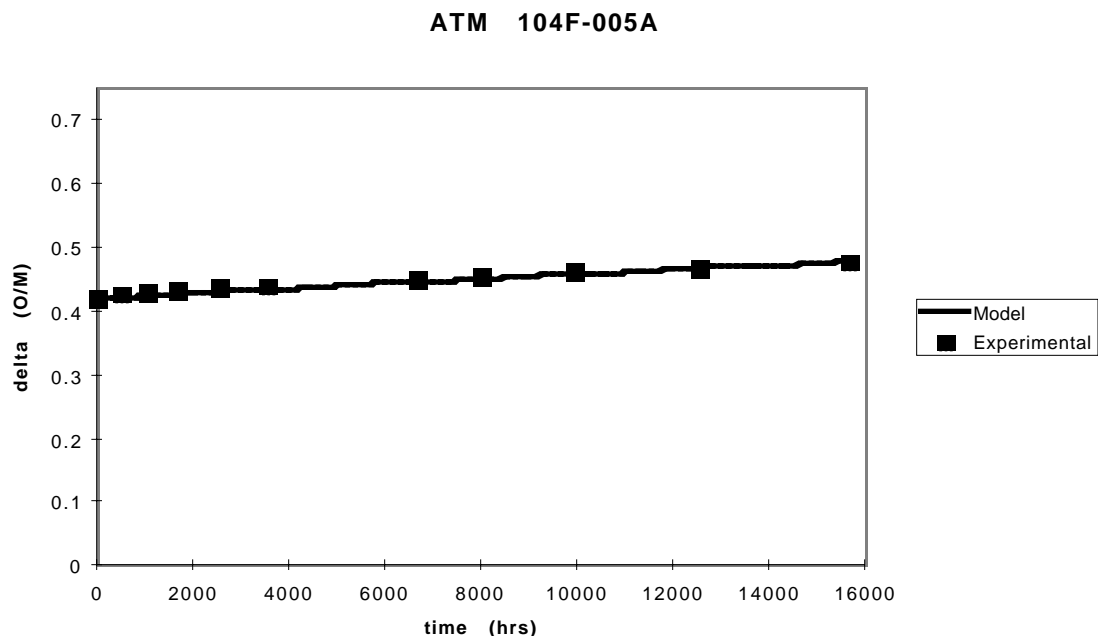


**Figure 3.2.2-24**  $\Delta$  (O/M) versus time (hr) for the ODB sample ATM-104F-005A; nominal burnup, 43 MWd/kgU [LL980912451021.055]

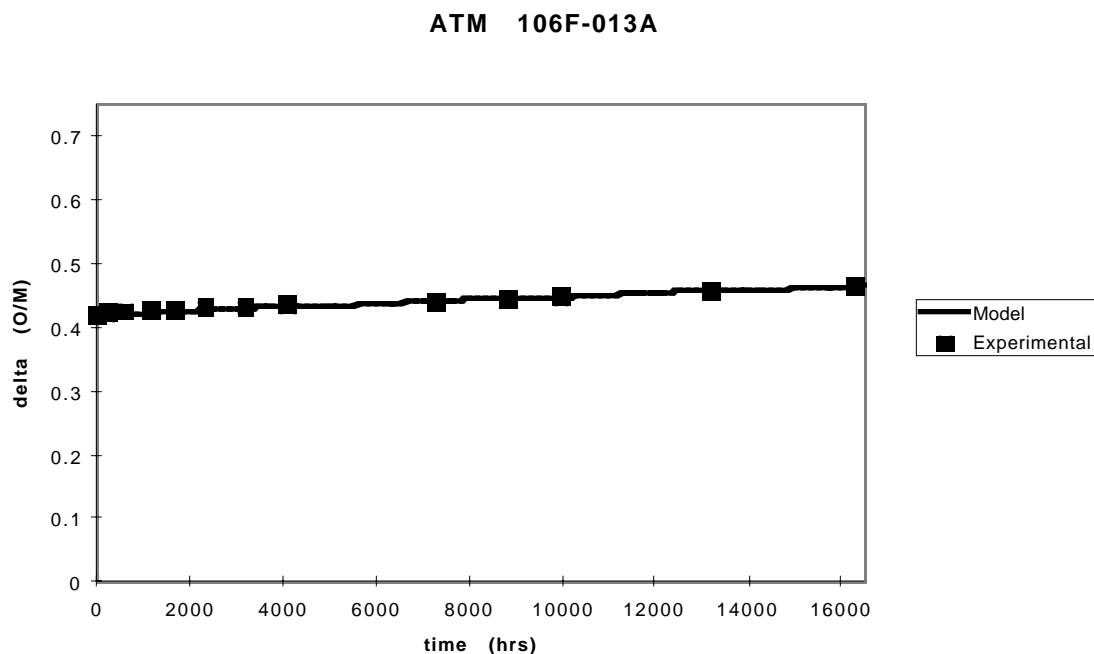


**Figure 3.2.2-25**  $\Delta$  (O/M) versus time (hr) for the ODB sample ATM-106F-013A; nominal burnup, 48 MWd/kgU [LL980912451021.055]

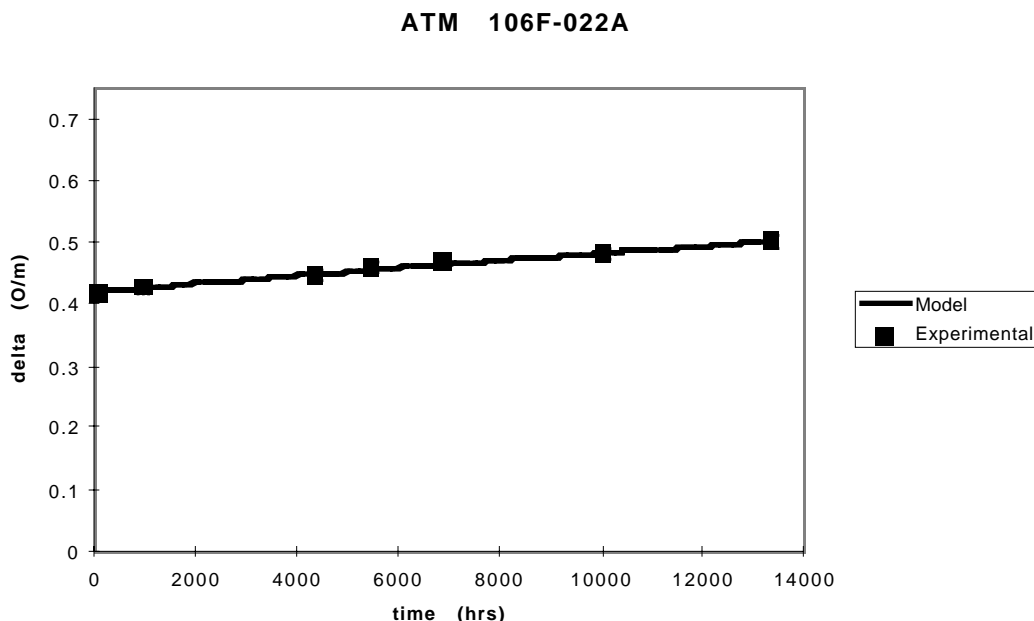


**Figure 3.2.2-26  $\Delta$  (O/M) versus time (hr) for the ODB sample ATM-106F-002A; nominal burnup, 48 MWd/kgU [LL980912451021.055]**

Some ODB experiments involved samples in which schoepite formed a thin layer on the surface of the unoxidized spent fuel and accelerated the weight gain by raising the oxygen potential, giving those grains with schoepite an apparent lower activation energy. As with the TGA experiments that involved hydrated spent fuel, it was assumed that the true sample is a mixture of hydrated  $U_4O_9$  and nonhydrated  $U_4O_9$ .

Table 3.2.2-21 and Table 3.2.2-22 present the results for the ODB experiments with those samples that exhibited a schoepite layer. Table 3.2.2-21 shows the activation energies and grain half-size distributions for the Turkey Point and ATM-105 fuel samples. The comparison of the experimental and model histories for the hydrated Turkey Point and ATM-105 samples is presented in Figures 3.2.2-27 through 3.2.2-29. Table 3.2.2-22 presents the activation energies and grain half-size distributions for the ATM 104 and ATM-106 fuel samples. The comparison of the experimental data and the model fits for the hydrated ATM-104 and ATM-106 fuels is presented in Figures 3.2.2-30 through 3.2.2-32. It must be reiterated that only the TP-P2-100 and 104F-100 samples were examined by SEM and are known to have the dehydrated schoepite. Because of their weight-gain histories, it was conjectured that the ATM-105F-100 and ATM-106-P2-100 samples also have schoepite. The same is true for the samples TP-P2-003A and 106-P2-021A. More study is required to confirm this conjecture.

**Table 3.2.2-21 ODB hydrated Turkey Point and ATM-105 samples listing the optimized  $Q_{38}$  for each bin and the corresponding grain half sizes and fractions**

Sample	Fraction (0.5–1.0) $\mu\text{m}$	Fraction (1.0–2.0) $\mu\text{m}$	Fraction (2.0–4.0) $\mu\text{m}$	Fraction (4.0–8.0) $\mu\text{m}$
TP-P2-003a	0.25	0.30	0.25	0.20
Bin $Q_{38}$	182.4	186.0	196.1	196.1



### 3.2.2 Oxidation Models

Sample	Fraction (0.5–1.0) $\mu\text{m}$	Fraction (1.0–2.0) $\mu\text{m}$	Fraction (2.0–4.0) $\mu\text{m}$	Fraction (4.0–8.0) $\mu\text{m}$
TP-P2-100	0.25	0.30	0.25	0.20
Bin $Q_{38}$	178.8	181.3	183.4	191.1
105F-100	0.25	0.25	0.25	0.25
Bin $Q_{38}$	182.1	190.4	198.0	202.8

Table 3.2.2-22 ODB hydrated ATM-104 and ATM-106 samples listing the optimized  $Q_{38}$  for each bin and the corresponding grain half sizes and fractions

Sample	Fraction (0.15–0.30) $\mu\text{m}$	Fraction (0.30–0.60) $\mu\text{m}$	Fraction (0.60–1.20) $\mu\text{m}$	Fraction (1.20–2.40) $\mu\text{m}$
104F-100	0.30	0.23	0.25	0.22
Bin $Q_{38}$	188.1	195.2	202.1	180.0
106-P2-021A	0.42	0.35	0.10	0.08
Bin $Q_{38}$	186.9	197.1	206.8	224.7
106-P2-100	0.42	0.35	0.10	0.08
Bin $Q_{38}$	182.1	197.1	205.8	218.7

ATM 105F-100

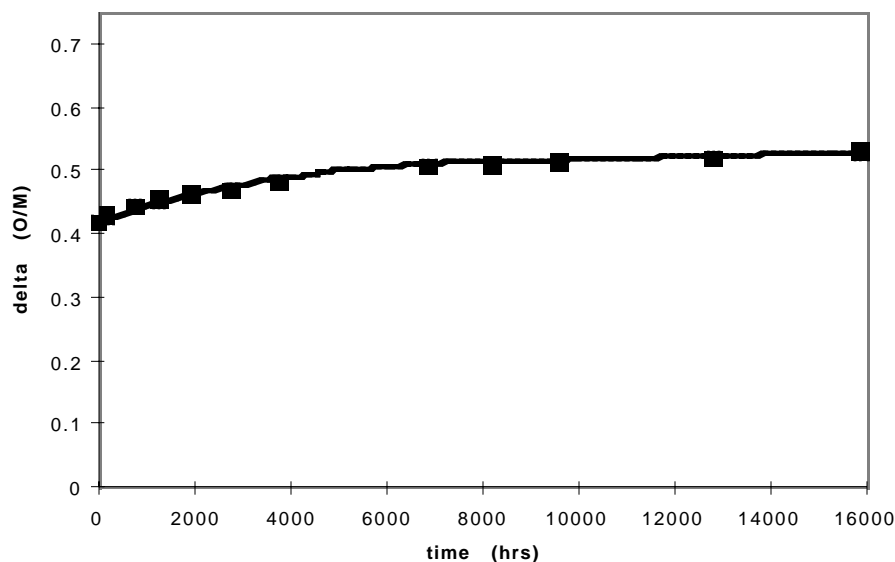


Figure 3.2.2-27  $\Delta$  (O/M) versus time (hr) for the ODB sample ATM-105F-100; nominal burnup, 27 MWd/kgU; shoeplate present [LL980912451021.055]

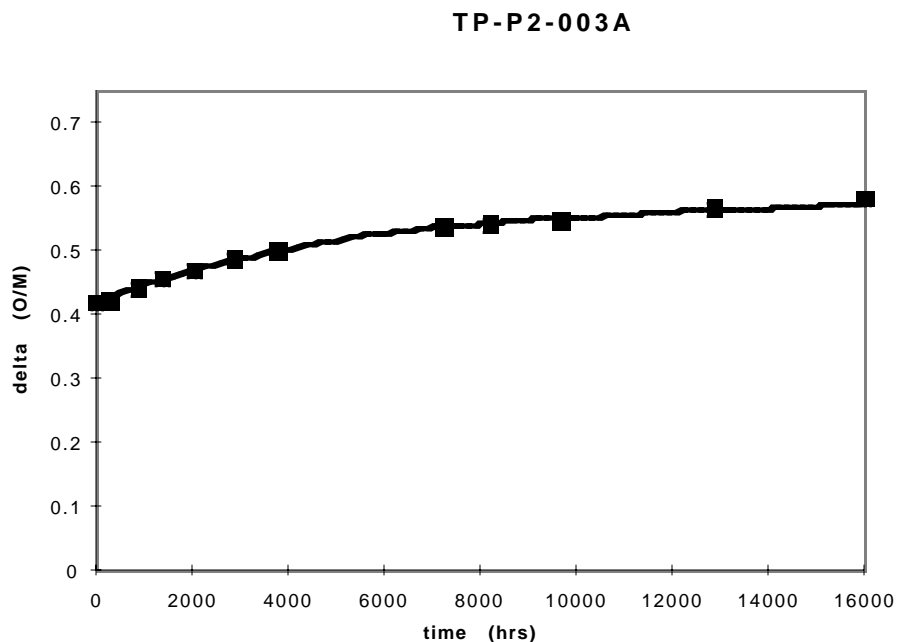


Figure 3.2.2-28  $\Delta$  (O/M) versus time (hr) for the ODB sample TP-P2-003A; nominal burnup, 28 MWd/kgU; shoeplate present [LL980912451021.055]

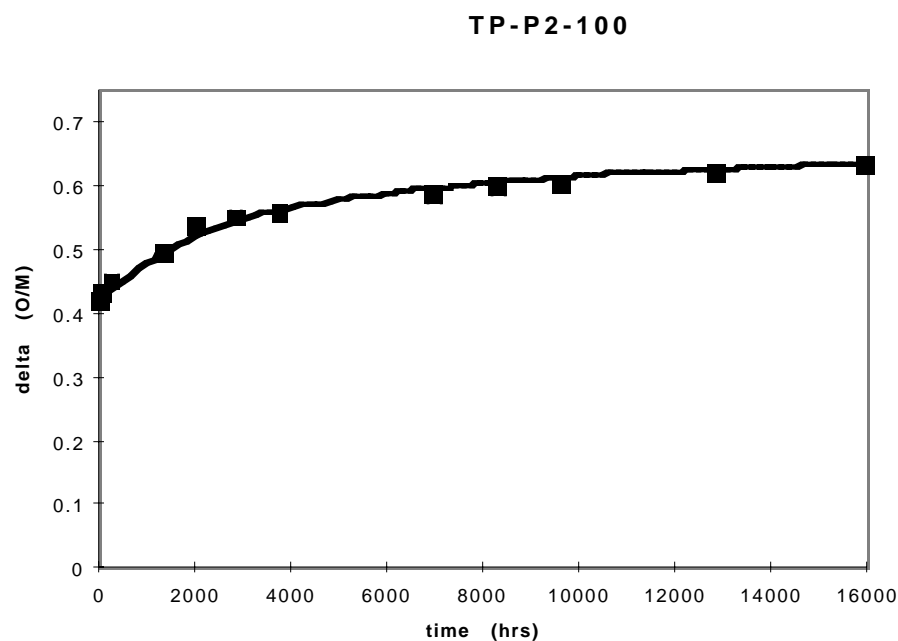


Figure 3.2.2-29  $\Delta$  (O/M) versus time (hr) for the ODB sample TP-P2-100; nominal burnup, 28 MWd/kgU; shoeplate present [LL980912451021.055]

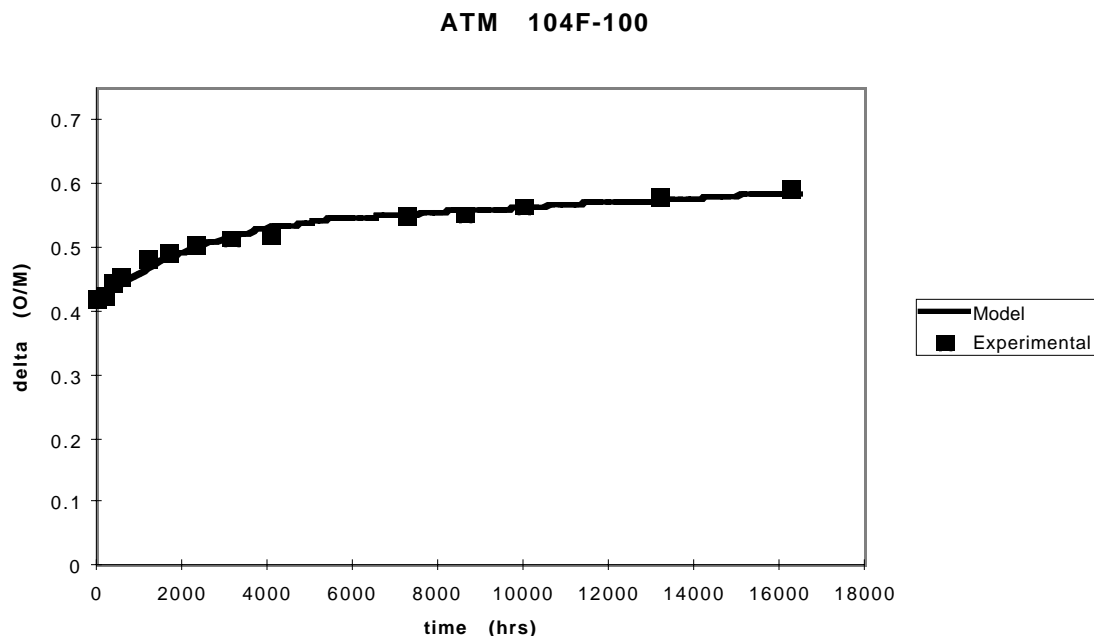


Figure 3.2.2-30  $\Delta$  (O/M) versus time (hr) for the ODB sample ATM-104F-100; nominal burnup, 43 MWd/kgU; shoeplate present [LL980912451021.055]

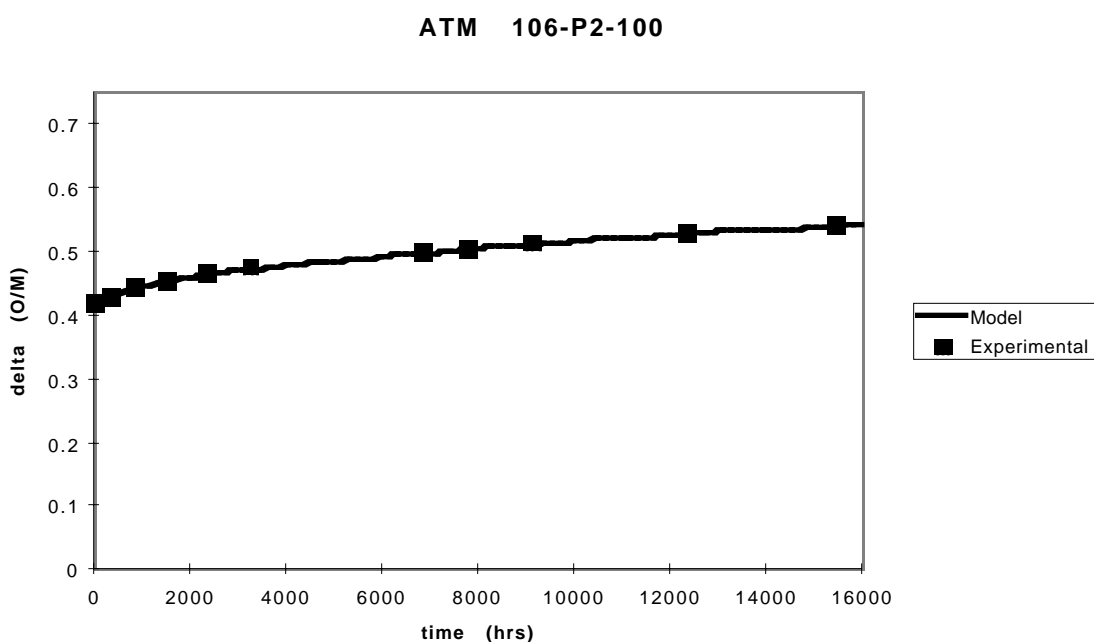
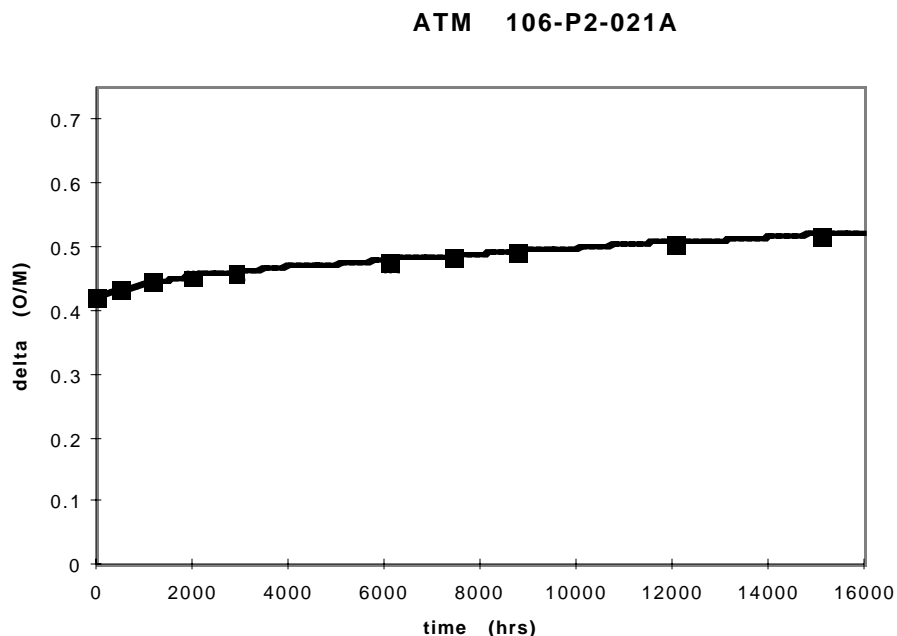


Figure 3.2.2-31  $\Delta$  (O/M) versus time (hr) for the ODB sample ATM-106-P2--100; nominal burnup, 48 MWd/kgU; shoeplate present [LL980912451021.055]



**Figure 3.2.2-32**  $\Delta$  (O/M) versus time (hr) for the ODB sample ATM-106-P2-021A; nominal burnup, 48 MWd/kgU; shoeplate present [LL980912451021.055]

### 3.2.2.12 Discussion of Modeling Comparisons with Experimental $U_4O_9 \rightarrow U_3O_8$ Histories

The frontal speed at which  $U_4O_9 \rightarrow U_3O_8$  is given by Eq. 3.2.2.-14a and Eq. 3.2.2.-14b. This frontal speed depends inversely on the grain half size and exponentially on the activation energy  $Q_{38}$ .

These model calculations had been performed with the uncertainties arising from the grain-size distributions of totally converted  $U_4O_9$ . It was assumed that the grain-size distribution of the cracked  $U_4O_9$  estimated from the paper of Thomas et al. (1991) is valid for totally converted  $U_4O_9$ . This assumption can be verified easily by SEM measurement. A question remains regarding the grain-size distribution at higher burnup that can be easily found by similar experimental techniques.

Hanson (1998) stated there can easily be a 10 to 15-kJ/mole uncertainty in the activation energy  $Q_{38}$ . This activation energy is sensitive to the isotopic composition of the fuel and to the position in the fuel rod because local burnup is not identical to the average burnup.

While some of the fine points of the modeling studies can be debated (with regard to the totally converted  $U_4O_9$  grain-size distribution or to the suitable activation energy), the uncertainties assumed in fitting the model can be easily overcome by additional experimental measurements.

### 3.2.2.13 Environmental Impacts of Oxidation of $UO_2$

Arrhenius chemical kinetics are very temperature-sensitive. Because  $U_3O_8$  formation is the primary concern in a repository environment, the frontal speed depends on temperature and on activation energy. According to Hanson (1998), the activation energy for the reaction  $U_4O_9 \rightarrow U_3O_8$  varies with burnup (see Eq. 3.2.2-25). To obtain a sense of the temperature and activation-energy dependence on the frontal speed  $\dot{w}_{38}$  (see Eq. 3.2.2-14a), Table 3.2.2-23 is

### 3.2.2 Oxidation Models

presented. Instead of expressing the frontal velocities in the units of  $\mu\text{m}/\text{h}$ , these values will be expressed as  $\mu\text{m}/\text{yr}$ . The frontal speed for the very high activation energy 640 kJ/mole was not included because the frontal speed is essentially zero for the temperatures considered.

**Table 3.2.2-23 Frontal speed  $\dot{W}_{38}$  ( $\mu\text{m}/\text{yr}$ ) dependence on temperature and activation energy**

T °K	167.4 (kJ/(mole—°K))	314 (kJ/(mole—°K))	469 (kJ/(mole—°K))
323.2	8.44E-18	1.72E-41	1.62E-66
373.2	3.57E-14	1.09E-34	2.31E-56
528.2	2.69E-07	8.71E-22	4.1880E-37

Rather than using the  $\Delta(\text{O}/\text{M})$  as a dependent variable, using the volume fraction of  $\text{U}_3\text{O}_8$  is more meaningful in a long-term repository for spent fuel. Figure 3.2.2-33 shows the volume-fraction histories for constant temperature 100°C for the phase transformation  $\text{U}_4\text{O}_9 \rightarrow \text{U}_3\text{O}_8$  for three different burnups. It was assumed that a 25-MWd/kgU spent fuel had an average  $\text{U}_4\text{O}_9$  half-grain size of 4.0  $\mu\text{m}$ , the 50 MWd/kgU had an average  $\text{U}_4\text{O}_9$  half-grain size of 0.75  $\mu\text{m}$ , and the 75 MWd/kgU  $\text{U}_4\text{O}_9$  had a half-grain size of 0.25  $\mu\text{m}$ . Figure 3.2.2-37 shows the volume fraction of  $\text{U}_3\text{O}_8$  on a log-time plot in years. Note that, even with progressively smaller average grain half-sizes, the 50 and 75 MWd/kgU burnup fuels require times on the order of  $1\text{E}+12$  and  $1\text{E}+15$  years for complete conversion, even though the average grain sizes become progressively smaller.

**Volume fraction of  $\text{U}_3\text{O}_8$  for med at 100 C vs time**

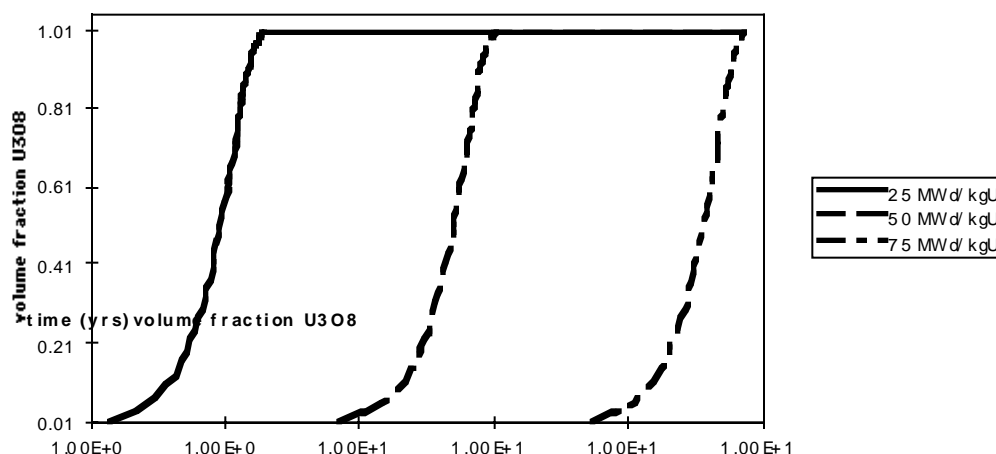


**Figure 3.2.2-33 Volume fraction of  $\text{U}_3\text{O}_8$  formed vs time (yr) at a constant temperature of 100° C at burnups of 25, 50, and 75 MWd/kgU [LL980912451021.055]**

Figure 3.2.2-34 shows the volume-fraction histories for constant temperature 200°C for the phase transformation  $\text{U}_4\text{O}_9 \rightarrow \text{U}_3\text{O}_8$  for three different burnups. It was assumed that a 25 MWd/kgU spent fuel had an average  $\text{U}_4\text{O}_9$  half-grain size of 4.0  $\mu\text{m}$ , the 50 MWd/kgU had an average  $\text{U}_4\text{O}_9$  half-grain size of 0.75  $\mu\text{m}$ , and the 75 MWd/kgU  $\text{U}_4\text{O}_9$  had a half-grain size of

0.25  $\mu\text{m}$ . The lower burnup 25 MWd/kgU fuel oxidizes completely to  $\text{U}_3\text{O}_8$  in 1300 yr; the 50 and 75 MWd/kgU oxidize completely in 500,000 yr and 300 million yr, respectively. However, a simple calculation shows that the low-burnup 25 MWd/kgU burnup fuel would oxidize completely in 335,000 yr if the temperature were at a constant 150°C.

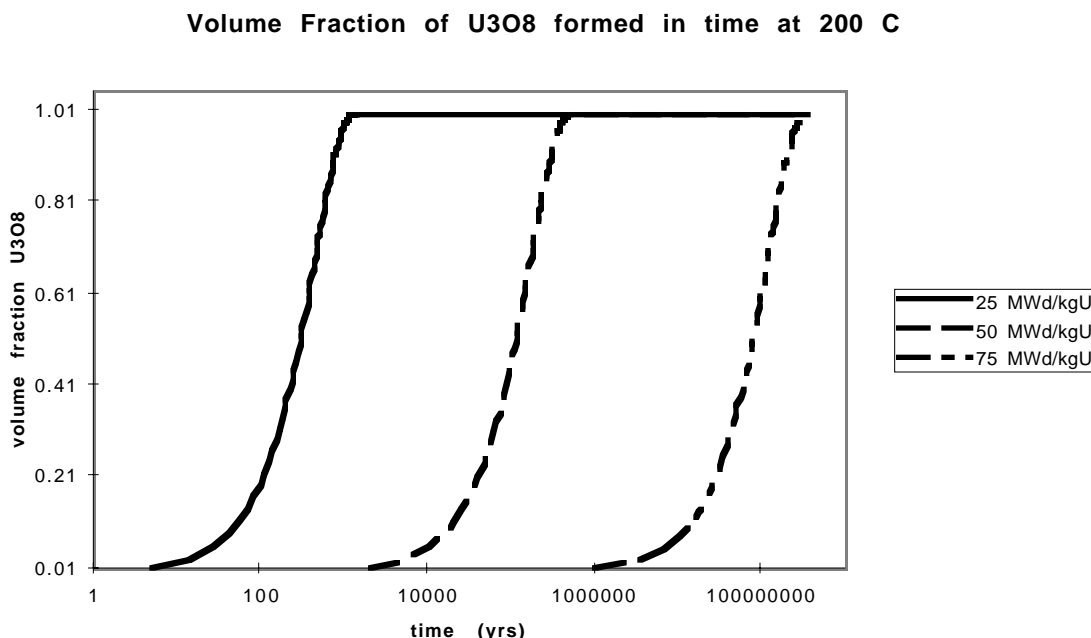


**Figure 3.2.2-34** Volume fraction of  $\text{U}_3\text{O}_8$  formed vs time (yr) at a constant temperature of 200°C at burnups of 25, 50, and 75 MWd/kgU [LL980912451021.055]

Given the presently limited data on the dissolution rates, the dissolution of  $\text{UO}_2$  and  $\text{U}_4\text{O}_9$  appear similar. However, an increase in exposed surface area for potential wetting and dissolution will occur from  $\text{U}_4\text{O}_9$  oxidation. The impact of surface area or grain size on dissolution remains to be evaluated in a release-rate model. Interpretation of dissolution-rate data from flow testing (Gray and Wilson, 1995) indicated that 3 to 14 grain depths may be possible. For pellet fragments having reasonably large grain sizes, the penetration depth is increased by a factor of approximately six times the nominal exterior surface area per grain layer. For unsaturated dissolution/release-rate response, this may not be a conservative estimate of spent-fuel degradation impacts from grain boundary effects.

The impacts of  $\text{U}_3\text{O}_8$  phase are as follows:

- Increased surface area for dissolution is proportional to grain size.
- There is about 30% increase in volume from  $\text{UO}_2$  to  $\text{U}_3\text{O}_8$ .
- $\text{U}_3\text{O}_8$  does not form a protective film on the  $\text{U}_4\text{O}_9$ .

Of these impacts, the first two are considered more significant. The  $\text{U}_3\text{O}_8$  volume increase of ~30% will create significantly larger openings in failed cladding and will, therefore, increase the amount of spent-fuel surface potentially exposed to wetting, compared to that which remains protectively covered by small flaw failures. The small flaw failures of the cladding are due to pressurized creep and/or zirconium hydride mechanisms. The  $\text{U}_3\text{O}_8$  sub-grain particle sizes that result from the  $\text{U}_3\text{O}_8$  spalling and surface fracturing at the  $\text{U}_3\text{O}_8 \rightarrow \text{U}_4\text{O}_9$  oxidation front create several-orders-of-magnitude increases in surface area relative to the nominal grain-sized surface area of  $\text{U}_4\text{O}_9$ . As shown in Tables 3.2.2-5 through

3.2.2-8, the extent of  $U_3O_8$  is significantly delayed for temperature histories less than 100°C. Clearly, it is important to maintain spent-fuel containment for time periods until the local repository temperatures are less than 100°C.

The oxidation-response models discussed in this section provide equations that calculate conservative time estimates for the  $U_4O_9$  and  $U_3O_8$  oxidation-phase transformations. These models are simplistic in form and based on limited experimental data, but are useful for the current stage of design and performance assessment analyses. Updates, refinements, and impacts of these oxidation models will be completed as additional TGA and ODB data become available.

#### 3.2.2.14 References

- Boase, D. G., and T. T. Vandergraf (1977). "The Canadian spent fuel storage canister: some material aspects." *Nucl. Tech.* **32**:60–71. [MOL.19980618.0133]
- Choi, J-W, R. J. McEachern, P. Taylor, and D. D. Wood (1996). "The effects of fission products on the rate of  $U_3O_8$  formation in SIMFUEL oxidized in air at 250°C." *J. Nucl. Mater.* **230**:250–258.
- Einziger, R. E., L. E. Thomas, and B. D. Hanson (1995). *Oxidation of Spent LWR Fuel, FY95 Year-End Report*. (MOL212 and MOL213) Richland, WA: Pacific Northwest National Laboratory. [MOL.19960611.0215]
- Einziger, R. E., L. E. Thomas, H. C. Buchanan, and R. B. Stout (1992). "Oxidation of spent fuel in air at 175 to 195°C." *J. Nucl. Mater.* **190**:53. [MOL.19980213.0585]
- Gray, W. J., and C. N. Wilson (1995). *Spent Fuel Dissolution Studies FY1991 to 1994*. (PNL-10540) Richland, WA: Pacific Northwest Laboratory. [MOL.19960802.0035]
- Gray, W. J., L. E. Thomas, and R. E. Einziger (1993). "Effects of air oxidation on the dissolution rate of LWR spent fuel." In proceedings from Materials Research Society Symposium: Scientific Basis for Nuclear Waste Management XVI. C. G. Interrante and R. T. Pabalan (Eds.) **294**:47. [236035]
- Hanson, B. D. (1998a). "The burnup dependence of light water spent fuel oxidation." Ph.D. Dissertation. Berkeley, CA: University of California at Berkeley. [MOL.19980810.0383]
- Harrison, K. T., C. Padgett, and K. T. Scott (1967). "The kinetics of the oxidation of irradiated uranium oxide spheres in dry air." *J. Nucl. Mater.* **23**:121–138.
- Lassmann, K, C. T. Walker, K. van der Laar, and L. Lindstrom (1995). "Modeling the high burnup  $UO_2$  structure in LWR fuel." *J. Nucl. Mater.* **226**:1–8.
- Matzke, H. (1992). "On the rim effect in high burnup  $UO_2$  LWR fuels." *J. Nucl. Mater.* **189**:141–148.
- McEachern, R. J., J. W. Choi, M. Kolar, W. Long, P. Taylor, and D. D. Wood (1997). "Determination of the activation energy for the formation of  $U_3O_8$  on  $UO_2$ ." *J. Nucl. Mater.* **249**:58–69.
- Paraschiv, M. C, A. Paraschiv, and F. Glodeanu (1997). "On the fission gas release from oxide fuels during normal grain growth." *J. Nucl. Mater.* **246**:223–231.

- Park, K., and D. R. Olander (1992). "Defect models for the oxygen potential of gadolinium and europium doped uranium." *J. Nucl. Mater.* **187**: 89–96.
- Ray, I. L. F., H. Matzke, H. A. Thiele, and M. Kinoshita (1997). "An electron microscopy study of the RIM structure of a  $\text{UO}_2$  fuel with a high burnup of 7.9% FIMA." *J. Nucl. Mater.* **245**:115–123.
- Remenyi, K. (1974). *The theory of grindability and the comminution of binary mixtures*. Budapest, Hungary: Akademiai Kiado.
- Stout, R. B., H. F. Shaw, and R. E. Einziger (1989). *Statistical model for grain boundary and grain volume oxidation kinetics in  $\text{UO}_2$  spent fuel*. (UCRL-100859) Livermore, CA: Lawrence Livermore National Laboratory. [NNA.19891031.0015]
- Stout, R. B., E. J. Kansa, R. E. Einziger, H. C. Buchanan, and L. E. Thomas (1991). "Spent fuel waste form characteristics: Grain and fragment size statistical dependence for oxidation response." In proceedings of Second International Conference on High-Level Radioactive Waste Management. La Grange Park, IL: American Nuclear Society and American Society of Civil Engineers. **1**:103–111. [MOL.19980505.0016]
- Stout, R. B., E. J. Kansa, and A. M. Wijesinghe (1993a). *Kinematics and thermodynamics of non-stoichiometric oxidation phase transitions in spent fuel*. (UCRL-JC-110678) Livermore, CA: Lawrence Livermore National Laboratory. [NNA.19930224.0014]
- Stout, R. B., E. J. Kansa, and A. M. Wijesinghe (1993b). *Kinematics and thermodynamics across a propagating non-stoichiometric oxidation phase front in spent fuel grains*. (UCRL-JC-112823) Livermore, CA: Lawrence Livermore National Laboratory. [NNA.19931029.0077]
- Thomas, L. E., and R. E. Einziger (1992). "Grain Boundary Oxidation of Pressurized-Water Reactor Spent Fuel in Air." *Material Charact.* **28**:149–156. [NNA.19911120.0004]
- Thomas, L. E., R. E. Einziger, and R. Woodley (1989). "Microstructural Examination of Oxidized Spent PWR Fuel by Transmission Electron Microscopy." *J. Nucl. Mat.* **166**:243–251. [NML.880707.0043; NNA.19900709.0482]
- Thomas, L. E., C. E. Beyer, and L. A. Charlot (1992). "Microstructural analysis of LWR spent fuels at high burnup." *J. Nucl. Mat.* **188**:80–89. [MOL.19980326.0383]
- Thomas, L. E., R. E. Einziger, and H. C. Buchannan (1993). "Effect of fission products on air-oxidation of LWR spent fuel." *J. Nucl. Mat.* **201**:310–319.
- Walker, C. T., T. Kamesama, S. Kitajima, and M. Kinoshita (1992). "Concerning the microstructural changes that occur at the surface of  $\text{UO}_2$  pellets on irradiation to high burnup." *J. Nucl. Mater.* **188**: 3–79.



### 3.3 Spent Fuel Fission Gas Release

During irradiation, the fission gases, xenon and krypton, accumulate in the fuel grains. At fuel temperatures from about 1000° to 1600°C, the gas atoms can either diffuse because of the radial temperature gradient to grain boundaries where they form intergranular bubbles or collect in intragranular bubbles that remain immobile unless the temperature exceeds ca. 1600°C. About 20% of the fission gas formed resides in intragranular bubbles at 1400°C. As bubbles accumulate, eventually a pathway to a crack or other free surface will open, releasing the gas. Rapid temperature changes such as occur during reactor shutdown create thermal stresses in the fuel which consequently crack along the bubble-decorated grain boundaries. The extent of fission gas retention by the fuel decreases rapidly as the temperature increases. Fission gas release is significantly less in rods that were at low temperature throughout their reactor residence than in rods that were at higher temperatures. A dependence of gas release on burnup has been shown also.

Given the above general comments, data on the distribution of fission gas release in spent fuel are sparse. However, the available data indicate that most of the fractional fission gas release is below 1%. Furthermore, calculations that predict mean values of fission gas release for fuel irradiated under controlled conditions do not necessarily describe fuels subjected to normal reactor use. Because of the complexity of the fission gas release problem, it is unlikely that sufficient information will be available to predict the process with high reliability. Conservative estimates of fission gas release may be possible by a panel of experts from vendors and researchers. However, should these estimates prove to be limiting, then additional experiments will be required to support the use of fission gas release as an independent variable in the models for gaseous release response, dissolution release response, and cladding failure response of spent fuel that are necessary for performance assessment.

### 3.3.1 Parameters for Fission Gas Release

The Materials Characterization Center has estimated distributions of burnup and fission gas release for the current and projected spent fuel inventories through 2020.<sup>1</sup> This was done both to help assure that the current suite of Approved Testing Materials is representative of the spent fuel inventory and to help define additional spent fuel ATM needs.

From the developed distributions it was concluded that the current ATM's may be considered representative, in terms of fission gas release and burnup, of nearly 100% of the spent fuel inventory discharged through 1988. However, those ATM's may be considered representative of only 61% of the total projected inventory discharged through 2020. That is because 39% of the inventory is projected to have burnup levels in excess of 45 MWd/kgM while none of the ATM's have burnups in excess of 45 MWd/kgM.

Noting that there are no ATM's representative of high burnup spent fuel, it is recommended that the next ATM to be acquired be representative of a modern fuel design (e.g., BWR 8x8 barrier or PWR 17x17) and have the highest possible burnup. It should also have low fission gas release so as to be representative of the large volume of fuel in the low fission gas release/high burnup category of spent fuel. A second ATM to be acquired should have the characteristics of high fission gas release/high burnup to be both representative of the other currently unrepresented category of spent fuel and provide an ATM that would be bounding of the expected spent fuel characteristics.

The current and above-proposed ATM's will be representative of standard design, non-failed LWR spent fuel. Fuel that will still not be represented by ATM's will include stainless steel-clad fuel, fuel that failed either in-reactor or during interim storage, and miscellaneous test and experimental fuel. It is estimated that these two fuel types will account for 2-5% of the total emplacement inventory.

One significant spent fuel classification that is not included in a burnup-fission gas release distribution is fuel that contains a burnable neutron poison. However, the MCC does have an early vintage Gd<sub>2</sub>O<sub>3</sub> burnable poison fuel in its inventory and if a modern high burnup BWR fuel assembly is acquired, modern burnable poison fuel would be part of such an assembly.

---

<sup>1</sup> M. E. Cunningham, et al., "The Impact of Burnup and Fission Gas Release Distributions of the U.S. Spent Fuel Inventory on the Selection of Spent Fuel Test Materials for the U.S. Geological Repository Project," PNL report in preparation, September, 1990.

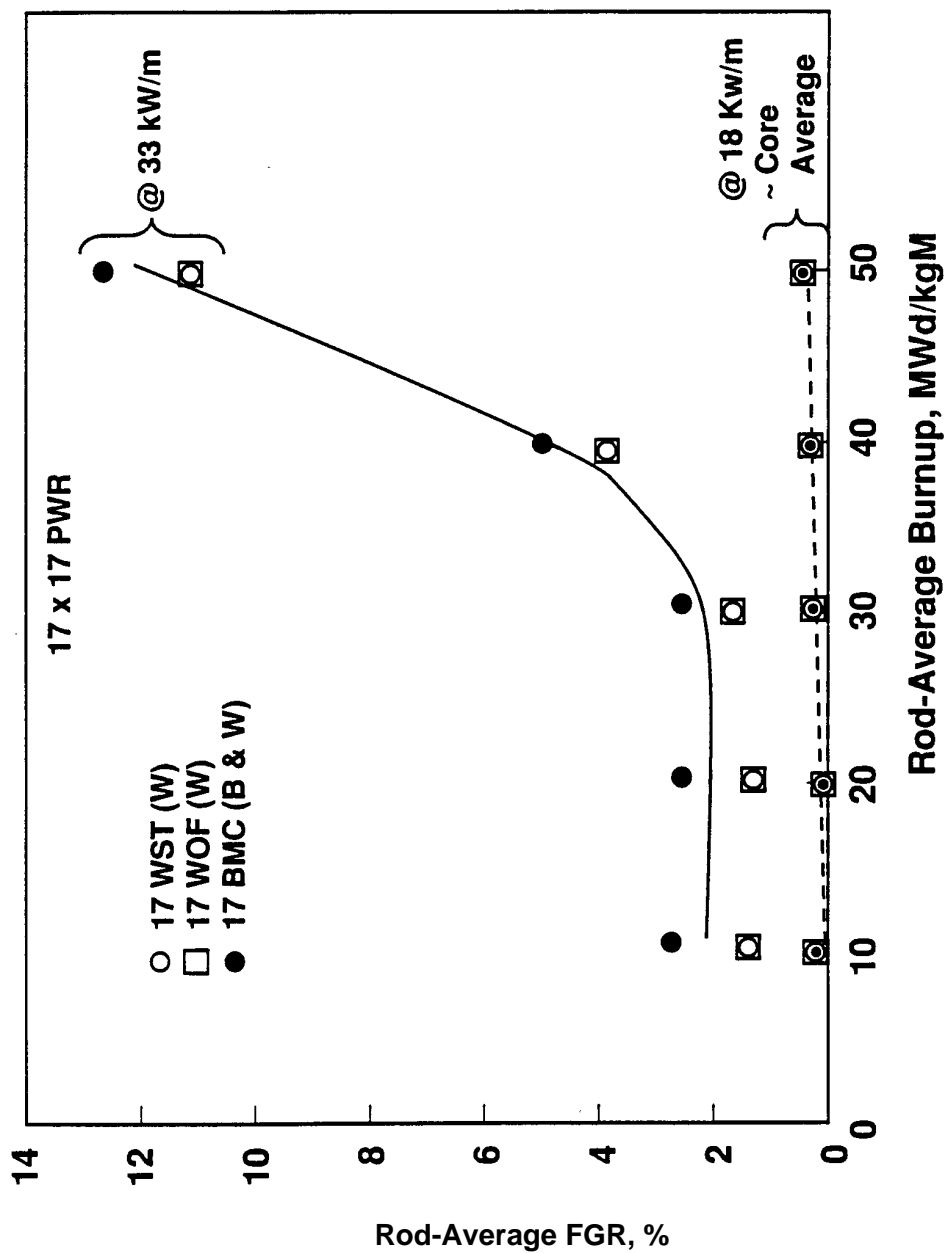


Figure 3.3.1-1 Example of justification for grouping varying rod designs

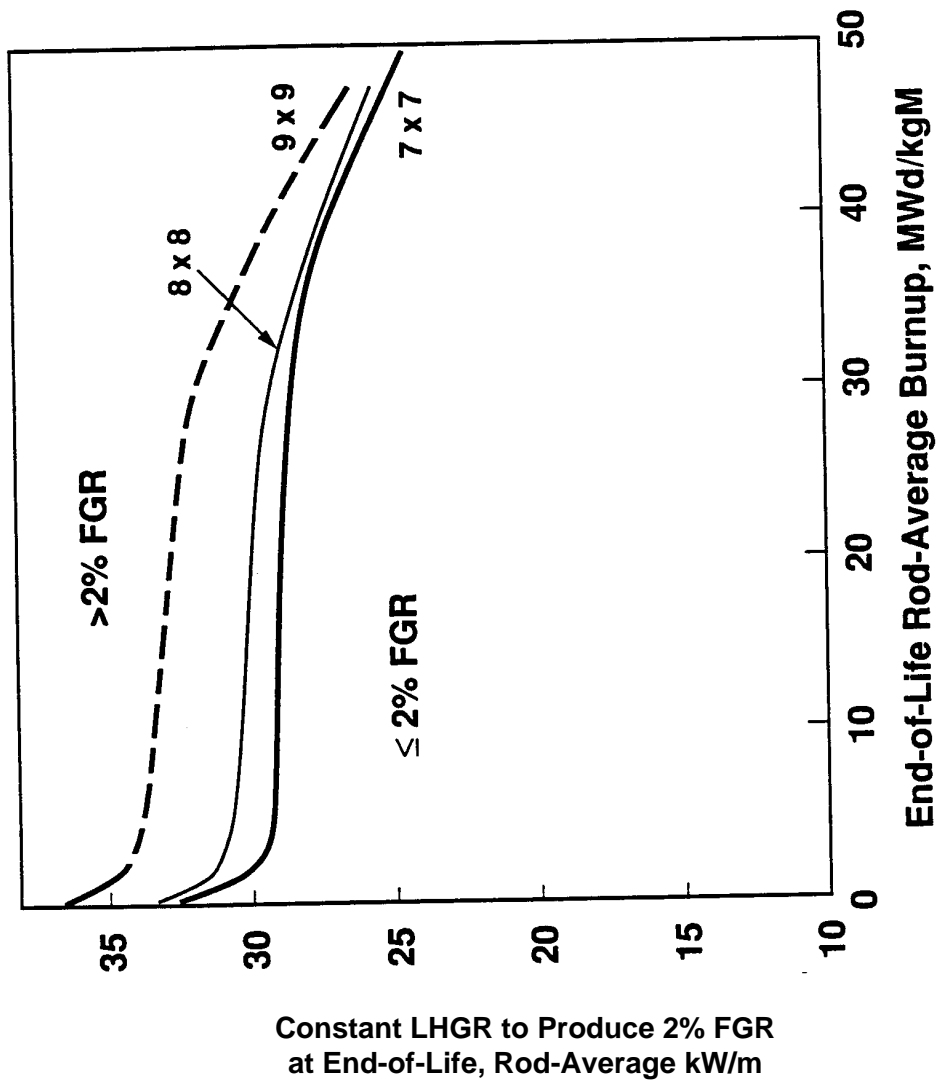


Figure 3.3.1-2 LHGR, burnup, and FGR correlation for BWR rod-types

### 3.3.1 Parameters for Fission Gas Release

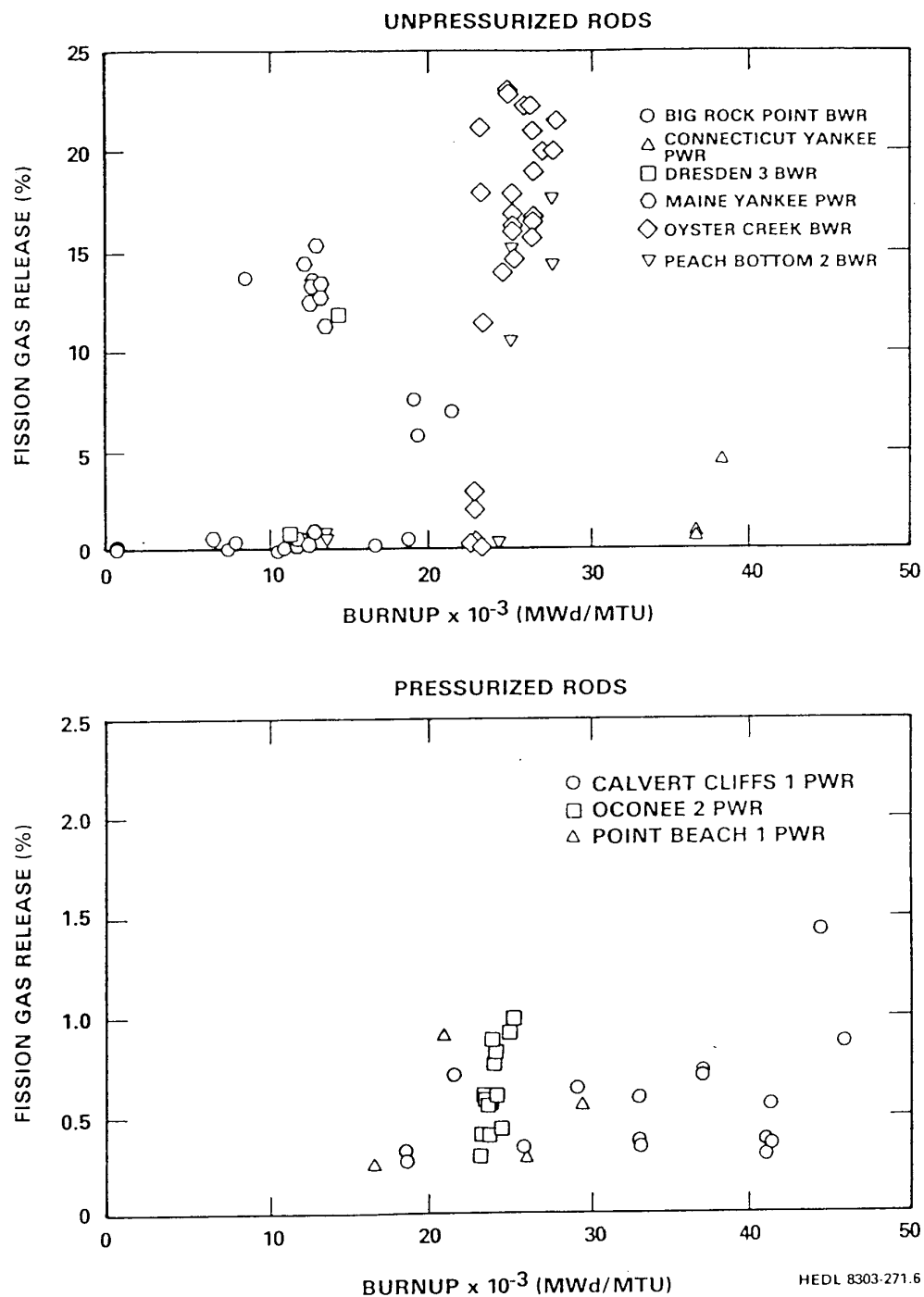


Figure 3.3.1-3 Comparison of fission gas release from unpressurized and pressurized LWR fuel rods<sup>(8)</sup> (Figure 14 from R.E. Woodley, *The Characteristics of Spent LWR Fuel Relevant to its Storage in Geologic Repositories*, HEDL-TME 83-28, October, 1983)

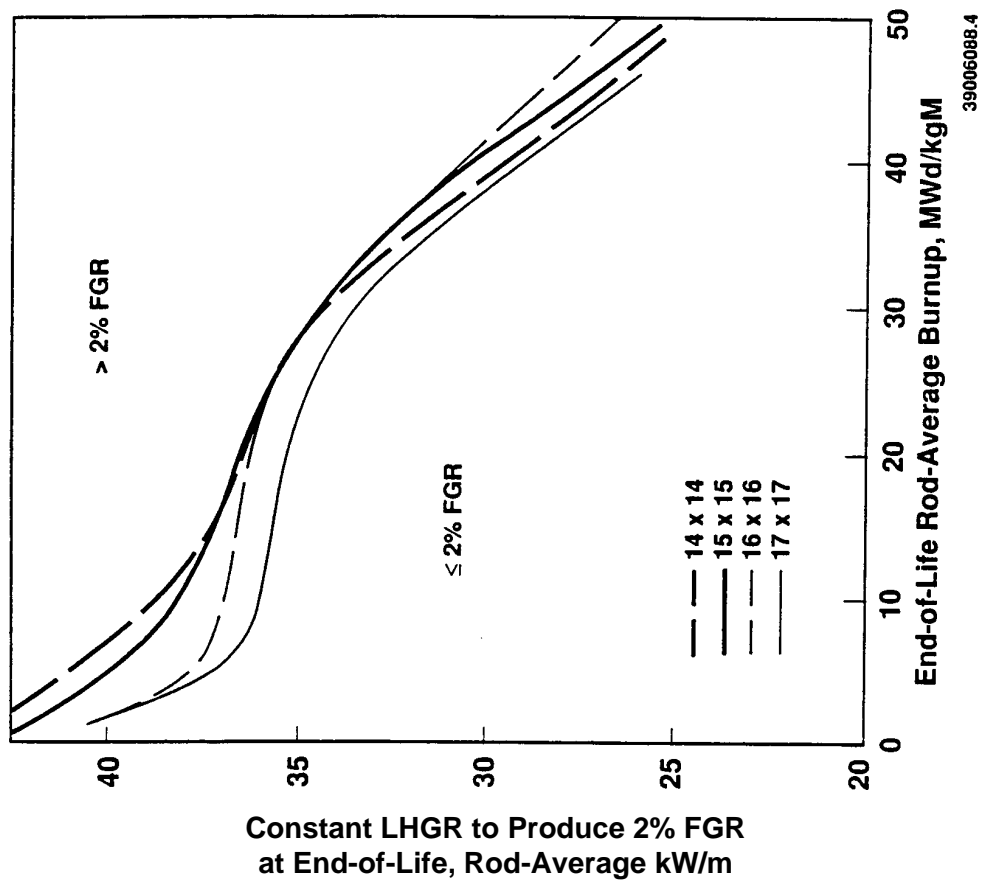


Figure 3.3.1-4 LHGR, burnup, and FGR correlation for PWR rod-types

### 3.3.2 Fission Gas Release Models

Fission gas release has been predicted using a “standard” model, the so-called ANS-5.4 model,<sup>2</sup> as revised by C.E. Beyer of PNL.<sup>3</sup>

Similar fission gas release curves were presented at the “Status and Future Directions of Spent Fuel ATM Acquisition and Characterization” meeting at PNL March 28-29, 1989, by C.E. Beyer of the MCC. These curves were generated using the revised ANS 5.4 Gas Release Model and we have fit these curves to a very simple and easily used equation for burnup  $\geq 20$  MWd/kgM and for gas release  $\leq 60\%$ . This equation is

$$\log_{10}(\text{fractional release}) = \frac{13}{8} \log_{10} (\text{burn - up [MWd/kgM]}) - \frac{4420}{T(K)}$$

We have calculated points at 30 and 40 MWd/kgM and superimposed them on Beyer’s curves to show the agreement. Additional curves for 30, 50, and 60 MWd/kgM calculated using our simple expression are also plotted.

---

<sup>2</sup> “Method for Calculating Fractional Release of Volatile Fission Products from Oxide Fuel,” ANSI/ANS-5.4-1982.

<sup>3</sup> Memo from C.E. Beyer (PNL) to J.C. Voglewede (USNRC), May 24, 1982.

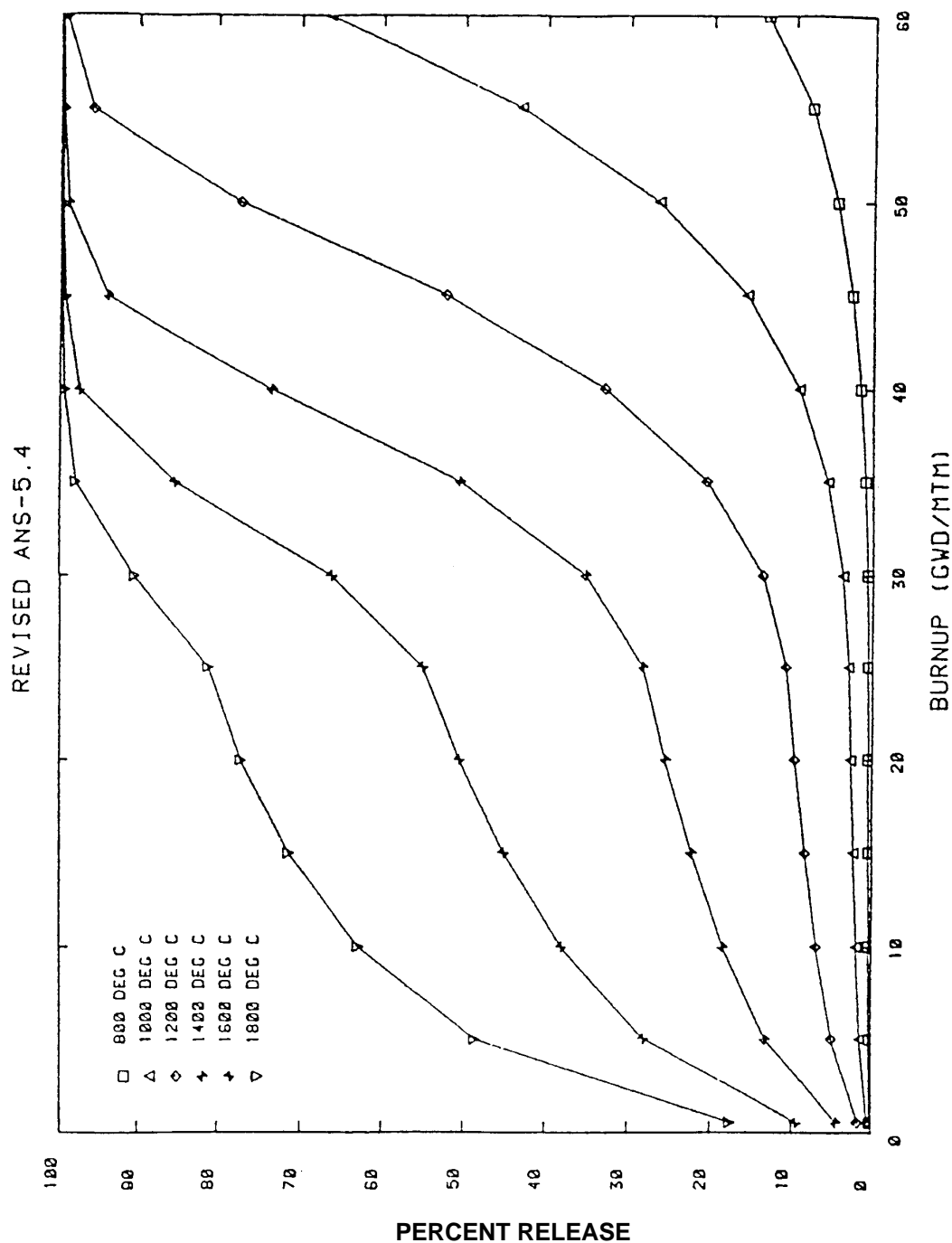
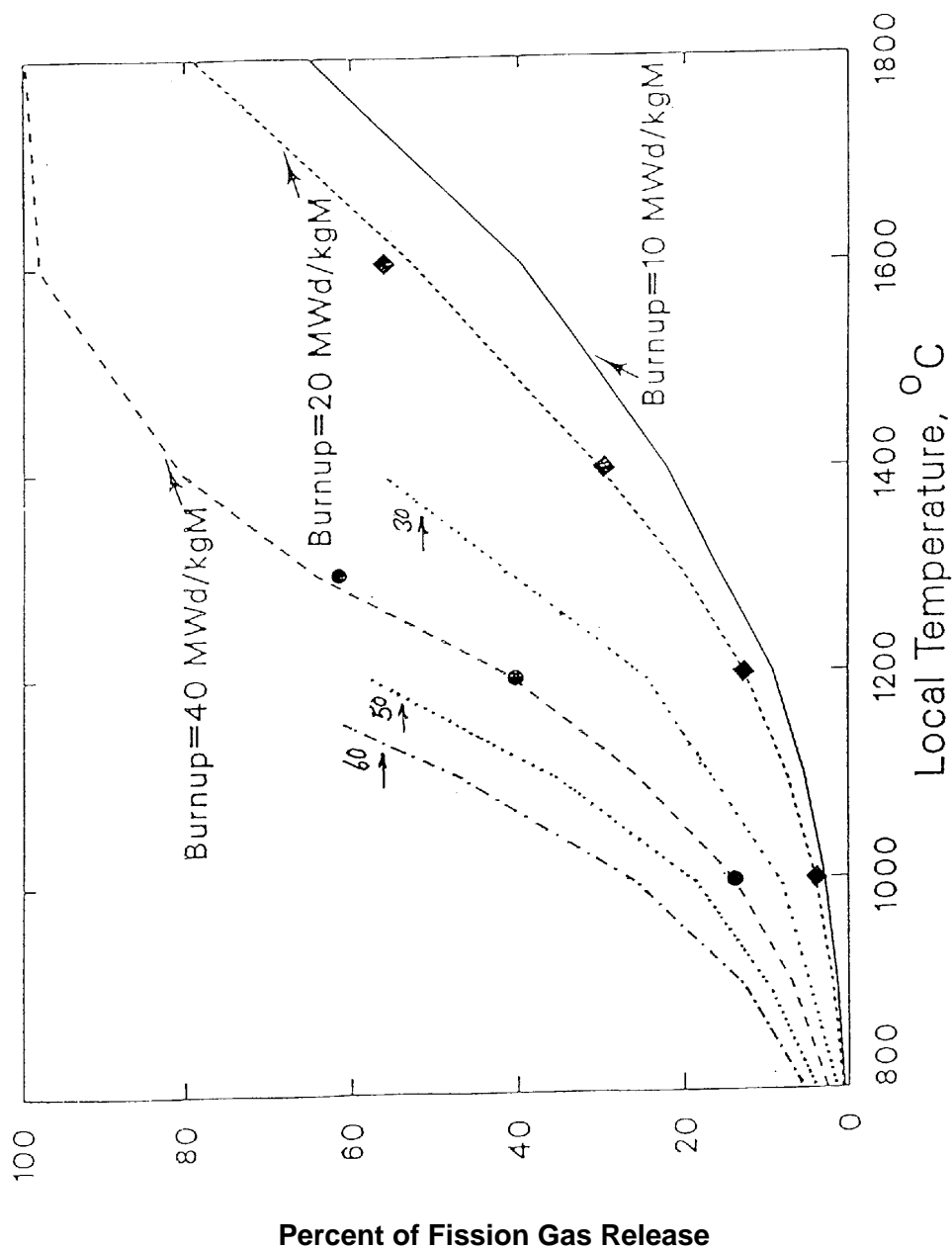


Figure 3.3.2-1 Revised ANS 5.4 model predictions at isothermal temperatures as a function of burnup





**Figure 3.3.2-2** Percent of fission gas release versus local temperature (from C.E. Beyer, in *Status and Future Direction of Spent Fuel ATM Acquisition and Characterization*, meeting in Richland, Washington, March, 1989)

### 3.4 Spent Fuel Dissolution

The dissolution of a waste form and the associated release of the included radionuclides will be limited by two boundary conditions in a geologic repository: (1) in the case of contact with fast moving water, the dissolution rate of the waste form will determine the rate at which radionuclides are released, (2) in the case of contact with slowly moving water (slow relative to the dissolution rate), the rate of release of radionuclides will be determined by their solubility under the prevailing conditions. Thus, in order to assess performance of a repository, both rates of dissolution and solubility limits should be available.

Many researchers have investigated the dissolution of  $\text{UO}_2$ , spent fuel and uraninite (a naturally occurring  $\text{UO}_2$  mineral) in aqueous solutions, under either reducing or oxidizing conditions, and as a function of various other environmental variables. Experimental data on the dissolution rates of  $\text{UO}_2$ , spent fuel and uraninite have been reviewed by Amell and Langmuir,<sup>1</sup> Parks and Pohl,<sup>2</sup> Bruno, et al.,<sup>3</sup> and most recently by Grambow.<sup>4</sup>

Important variables considered in the many investigations were pH, temperature, oxygen fugacity, carbonate/bicarbonate concentrations and other reacting media. The dissolution data are very scattered, and vary as much as six orders of magnitude.<sup>4</sup> The dependence of the dissolution of rates of  $\text{UO}_2$ , spent fuel and uraninite on these variables is not clear because of uncertainties regarding redox chemistry of uranium in solutions and in solid phases, secondary-phase formation, and surface area measurement. In addition, the previous studies were conducted under experimental conditions which were either unconstrained or which simulated complex repositiorial conditions. The results of such studies are difficult to interpret. Several of these researchers have developed equations to correlate dissolution rates as a function of relevant variables.<sup>6</sup> However, none of the rae laws is universal, and inconsistencies or incompatibilities among the proposed laws are common.

The results are equivocal due to the difference in experimental designs, the diverse history of the fuel samples, the formation of secondary phases during the tests, and the complexity of the solution and surface chemistry of  $\text{UO}_2$ . Data indicate that  $\text{UO}_2$  is easily oxidized to  $\text{U}_4\text{O}_9$  and  $\text{U}_3\text{O}_7$  in air<sup>9,10</sup> and can be further oxidized to either  $\text{U}_3\text{O}_8$ <sup>9,10,11</sup> or schoepite,  $\text{UO}_3 \cdot 2\text{H}_2\text{O}$ .<sup>12</sup> The  $\text{UO}_2$  surface oxidation leads to higher leach rates because of higher dissolution rates of  $\text{U}_3\text{O}_7$ ,  $\text{U}_3\text{O}_8$ , or schoepite relative to that of  $\text{UO}_2$  and because of the increase of surface area of the fuels due to surface cracking.

### References

1. A.R. Amell, and D. Langmuir, "Factors Influencing the Solution Rate of Uranium Dioxide Under Conditions Applicable to In-Situ Leaching," Bureau of Mines Open File Report 84-79, U.S. Dept. of Interior, Bureau of Mines (1978).
2. G.A. Parks, and D.C. Pohl, "Hydrothermal Solubility of Uraninite," *Geochim. Cosmochim. Acta*, 52, 863 (1988).
3. J. Bruno, I. Casas, and I. Puigdomenech, "The Kinetics of Dissolution of  $\text{UO}_2(\text{s})$  Under Reducing Conditions," *Radiochim. Acta*, 44/45, 11 (1988).
4. B. Grambow, "Spent Fuel Dissolution and Oxidation. An Evaluation of Literature Data," SKB Technical Report 89-13 (1989).

### 3.4 Spent Fuel Dissolution

---

5. D.E. Grandstaff, "A Kinetic Study of the Dissolution of Uraninite," *Econ. Geo.*, 71, 1493 (1976).
6. W.E. Schortmann, and M.A. DeSesa, "The Kinetics of the Dissolution of Uranium Dioxide in Carbonate-Bicarbonate Solutions," *Proc. 2nd Intern. United National Conf. Peaceful Uses of Atomic Energy*, United Nations, Geneva, 3, 333 (1958).
7. R.L. Pearson and M.E. Wadsworth, "A Kinetic Study of the Dissolution of  $\text{UO}_2$  in Carbonate Solution," *Trans. Metal. Soc. AIME*, 212, 294 (1958).
8. F. Habashi and G.A. Thurston, "Kinetics and Mechanisms of the Dissolution of Uranium Dioxide," *Energ. Nucl.* 14, 238 (1967).
9. S. Aronson, "Oxidation and Corrosion of Uranium Dioxide in Uranium Dioxide: Properties and Nuclear Applications," J. Belle, ed., *U.S. Atomic Energy Comm.*, 377 (1961).
10. R.E. Einziger, "Test Plan for Long-Term, Low-Temperature Oxidation of BWR Spent Fuel," PNL-6427, Pacific Northwest Laboratory (1988).
11. S. Aronson, "Oxidation of  $\text{UO}_2$  in Water Containing Oxygen," *Bettis Tech. Rev.*, Westinghouse Atomic Power Div., Report WAPD-BT-10, 93 (1958).
12. T. Wadsten, "The Oxidation of Polycrystalline Uranium Dioxide in Air at Room Temperature," *T. Nucl. Mat.*, 64, 315 (1977).

## 3.4.1 Parameters for Dissolution

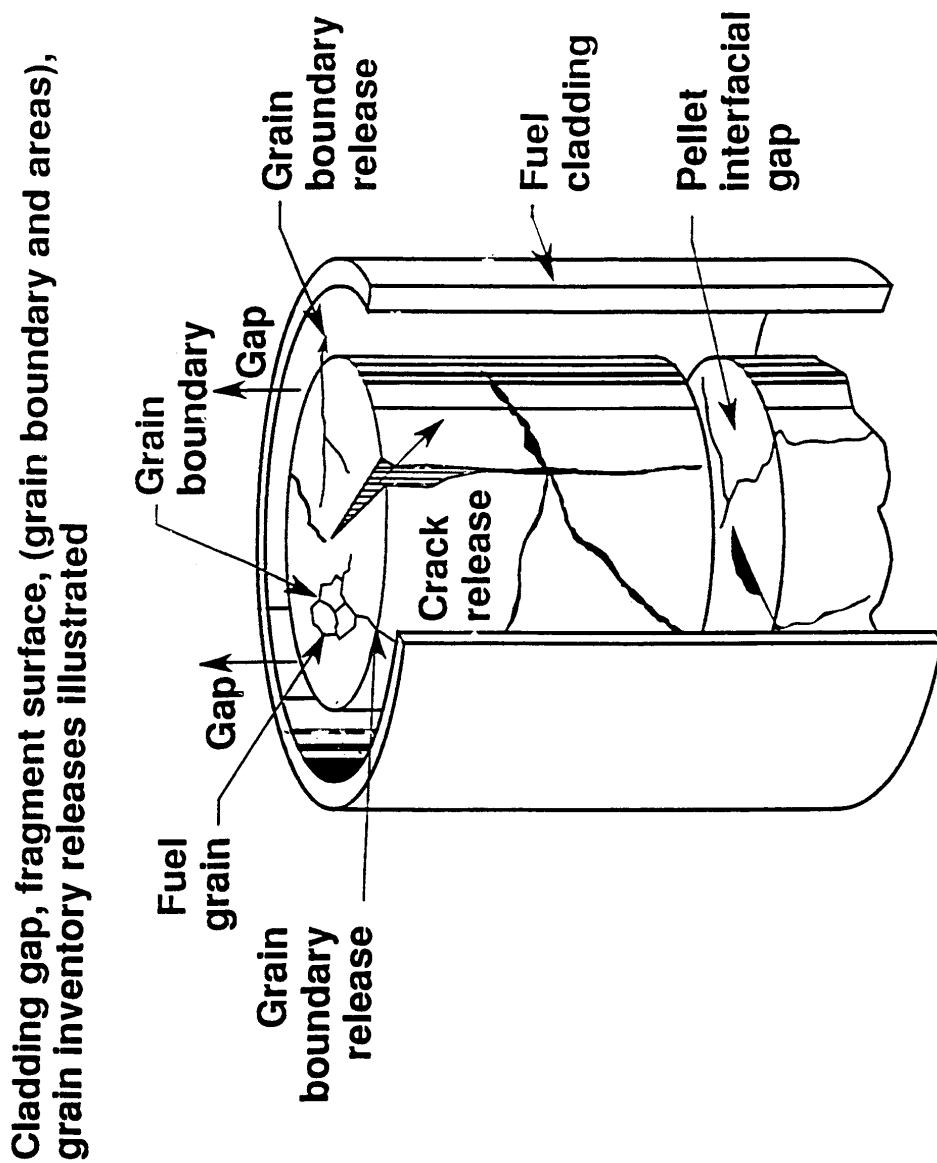
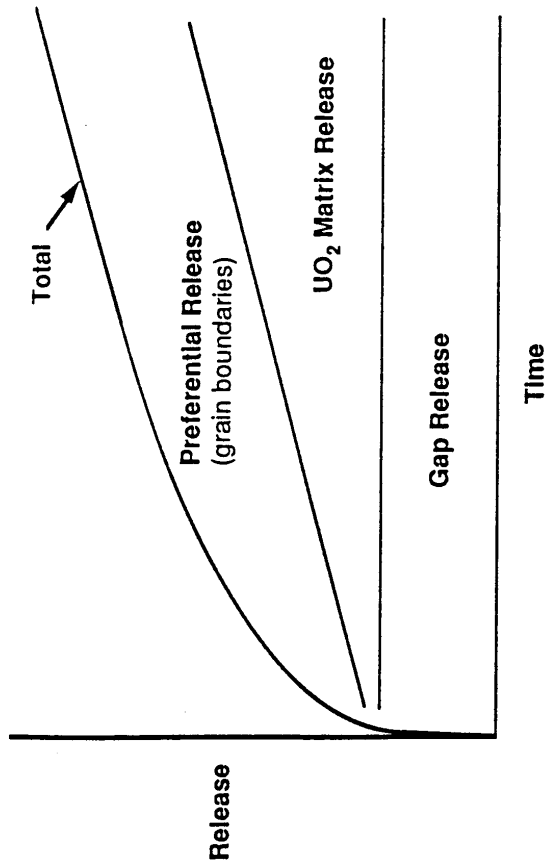


Figure 3.4.1-1 Spent fuel dissolution release rate



- **Rapid release of "gap inventories" with initial water contact (days)**
- **Preferential release from grain boundaries and other sources of radionuclide concentration (years)**
- **Releases are controlled by matrix dissolution after exposed grain boundaries and other sources of radionuclide concentration become depleted** (assuming fuel is not substantially degraded by oxidation)

Figure 3.4.1-2 Soluble radionuclide release

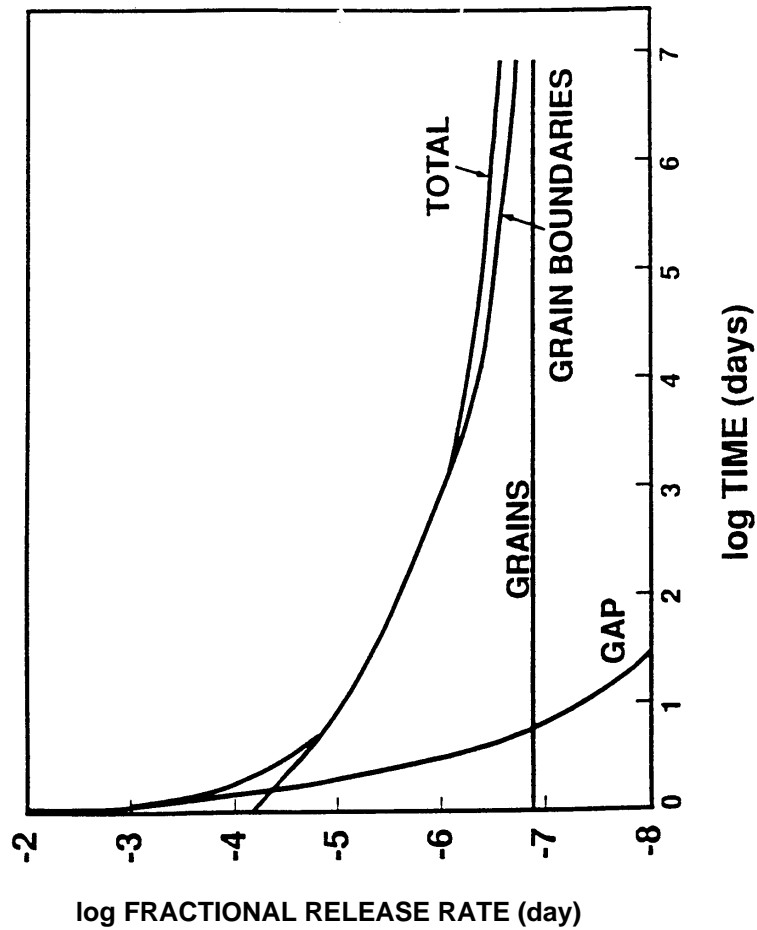


Figure 3.4.1-3 A schematic view of SF dissolution (from L.H. Johnson and D.W. Shoesmith, "Radioactive Waste Forms for the Future," W. Lutze and R.C. Ewing, Eds., Elsevier [1988], p. 686)

#### 3.4.1.1 Dissolution Rates

Recent measurements on both  $\text{UO}_2$  and spent fuel (SF) under comparable conditions have provided dissolution rates for  $\text{UO}_2$  between 25°C and 85°C in waters of various composition and for SF on deionized water (DIW) at 25°C. These experiments were done in equilibrium with air. The results are shown in figures 1 and 2. The rate of dissolution of SF in DIW at 25°C is  $1.2\text{--}1.7 \times 10^{-12} \text{ g cm}^{-2} \text{ sec}^{-1}$  as compared to  $\text{UO}_2$  in DIW at 25°C at  $\sim 5 \times 10^{-12} \text{ g cm}^{-2} \text{ sec}^{-1}$ . Given the great variability in other reported values this is reasonable agreement. In fact, the observed dissolution rate for SF in 25°C is about the same as of  $\text{UO}_2$  in (DIW + Ca + Si), a simulation of ground water.

The measured dissolution rates for  $\text{UO}_2$  and spent fuel allow us to calculate actual times for dissolution. As is evident from figure 3, the overall dissolution rate is greatest at early time and approaches zero as  $t_\infty$  is approached; therefore, we have also calculated the total dissolution time extrapolated from the initial rate,  $t_\infty^1$ . These times calculated for the size distribution in Table I are given in Table II. The actual dissolution rates used are derived from the bottom curve in figure 1. The rate equation used is

$$G(t) (\text{g cm}^{-2} \text{ sec}^{-1}) = 6.43 \times 10^{-9} \exp\left(-\frac{4740}{RT(K)}\right) \quad (5)$$

A model for the dissolution is used in which the dissolution front propagates linearly in time, much like a recently published model for the advance of the oxidation front during oxidation of  $\text{UO}_2$  and spent fuel. This implies that the particle geometry is retained.

We can describe the change in characteristic dimension of a SF particle (a sort of “radius”),  $X$  as follows:

$$X(t) = X_o - \left(\frac{G}{\rho}\right)t$$

where  $X(t)$  = the characteristic dimension as a function of time

- $X_o$  = the original dimension (half of the actual size)
- $t$  = time
- $G$  = dissolution rate per unit area
- $\rho$  = density

The time for complete dissolution of a particle, of original size  $X_o$ , is then  $t_\infty = \frac{X_o \rho}{G}$ .

---

<sup>1</sup> Leider, H.R., et al. “Estimating the Time for Dissolution of Spent Fuel Exposed to Unlimited Water,” LLNL Report UCRL-ID-107289, December, 1991. (See Section 2.1.3.5 for more complete discussion.)

Table 3.4.1.1-1

Approximate Size (cm) $2X_0$	Weight (Volume Fraction)
0.15	0.02
0.25	0.14
0.35	0.29
0.50	0.38
0.70	0.17

Table 3.4.1.1-2

Temperature (°C)	Dissolution Time (years)	
	$t_{\infty}^*$	$t_{\infty}$
25	$8.0 \times 10^3$	$5.5 \times 10^4$
85	$2.2 \times 10^3$	$1.5 \times 10^4$



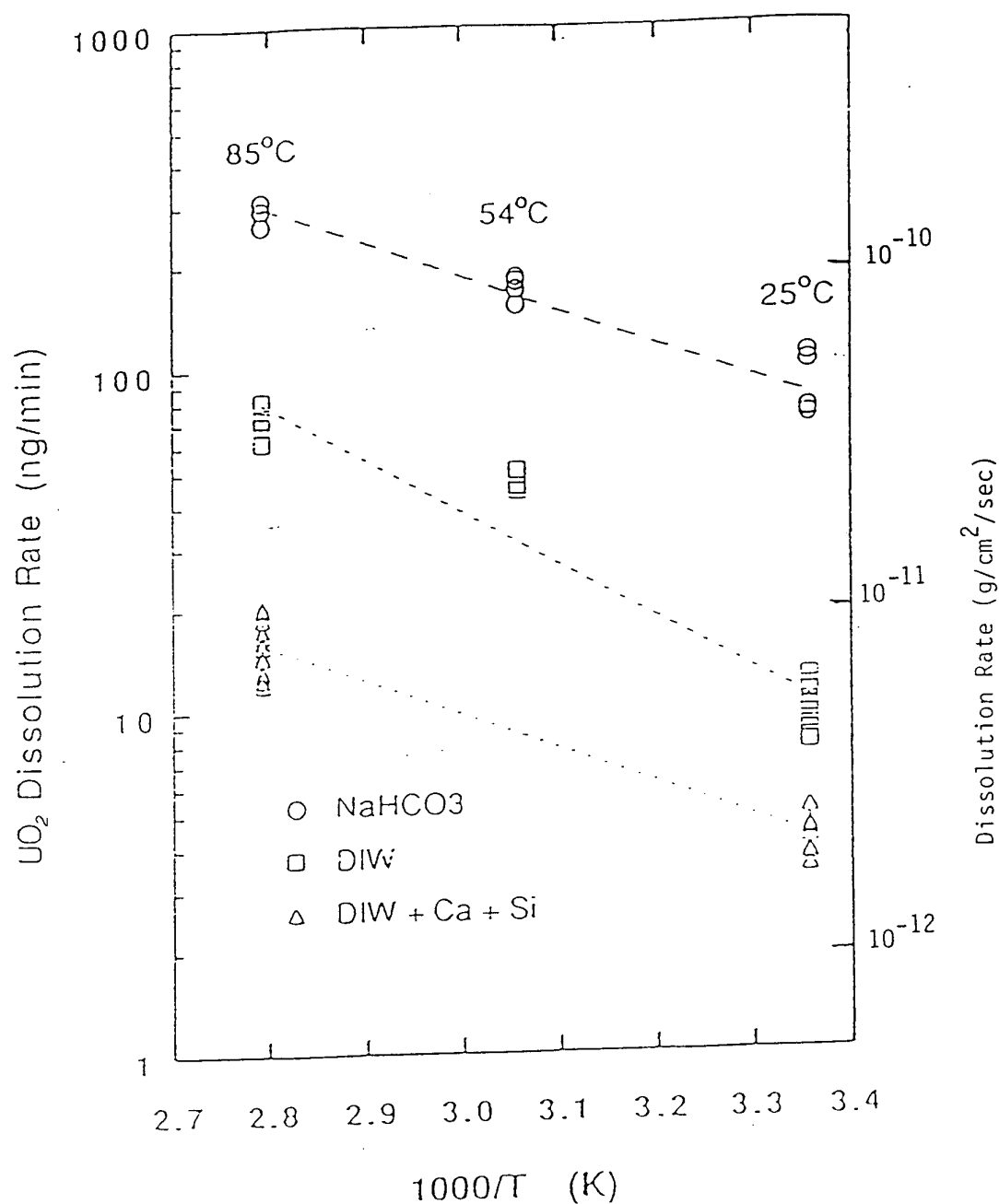


Figure 3.4.1.1-1 (Figure 1 from Gray, W., and Wilson, C., "Effects of Water Composition and Temperature on the Dissolution Rate of  $\text{UO}_2$ ," presented at 1990 Spent Fuel Workshop, Gull Harbor, Manitoba, Canada [1990] NNA.910821.0008)

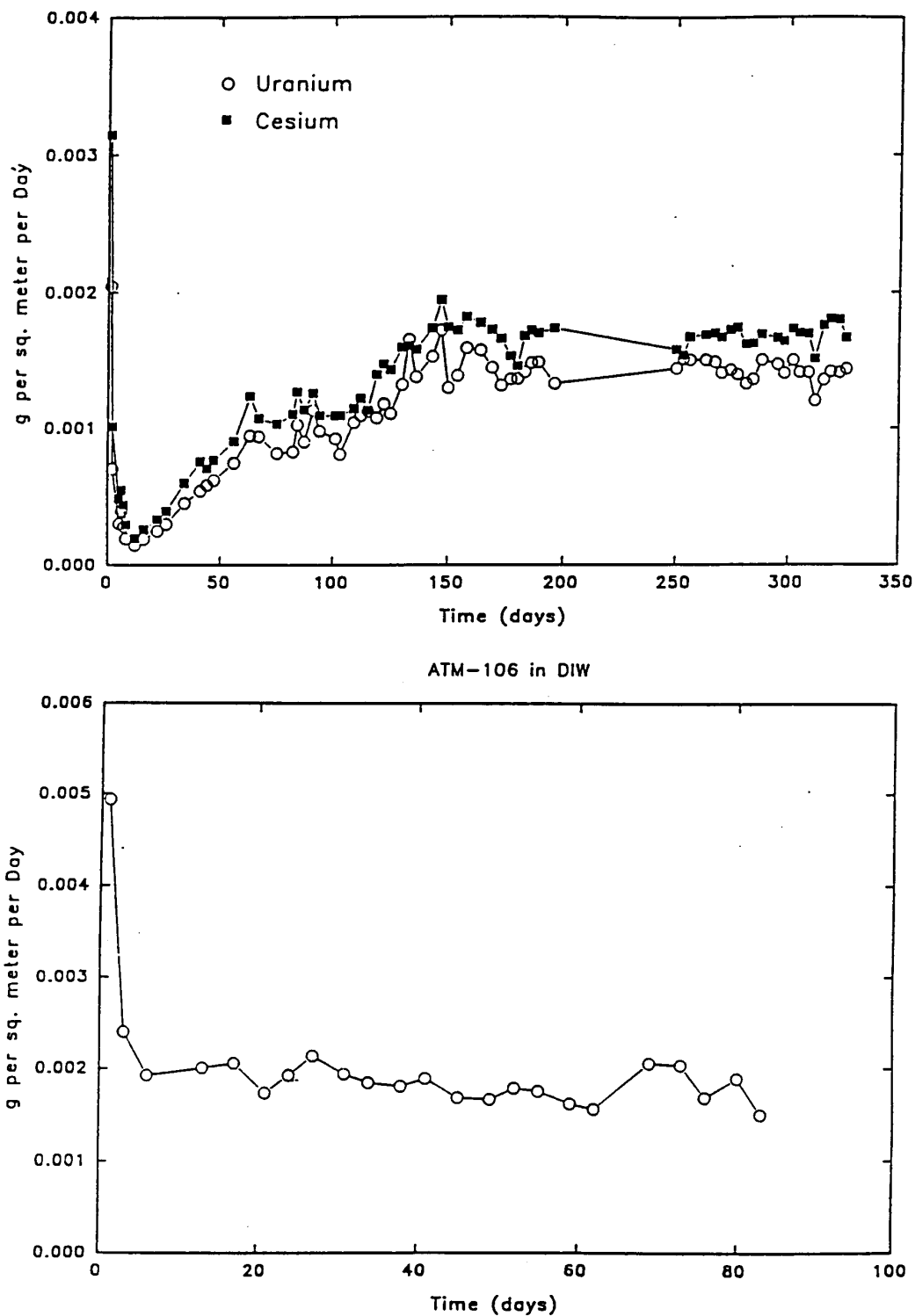


Figure 3.4.1.1-2 (Figure 2 from Gray, W., and Wilson, C., "Spent Fuel Grain Boundary Inventory and Testing the Congruency of  $\text{UO}_2$  Matrix Dissolution of Spent Fuel," presented at 1990 Spent Fuel Workshop, Gull Harbor, Manitoba, Canada [1990] NNA.910821.0009)

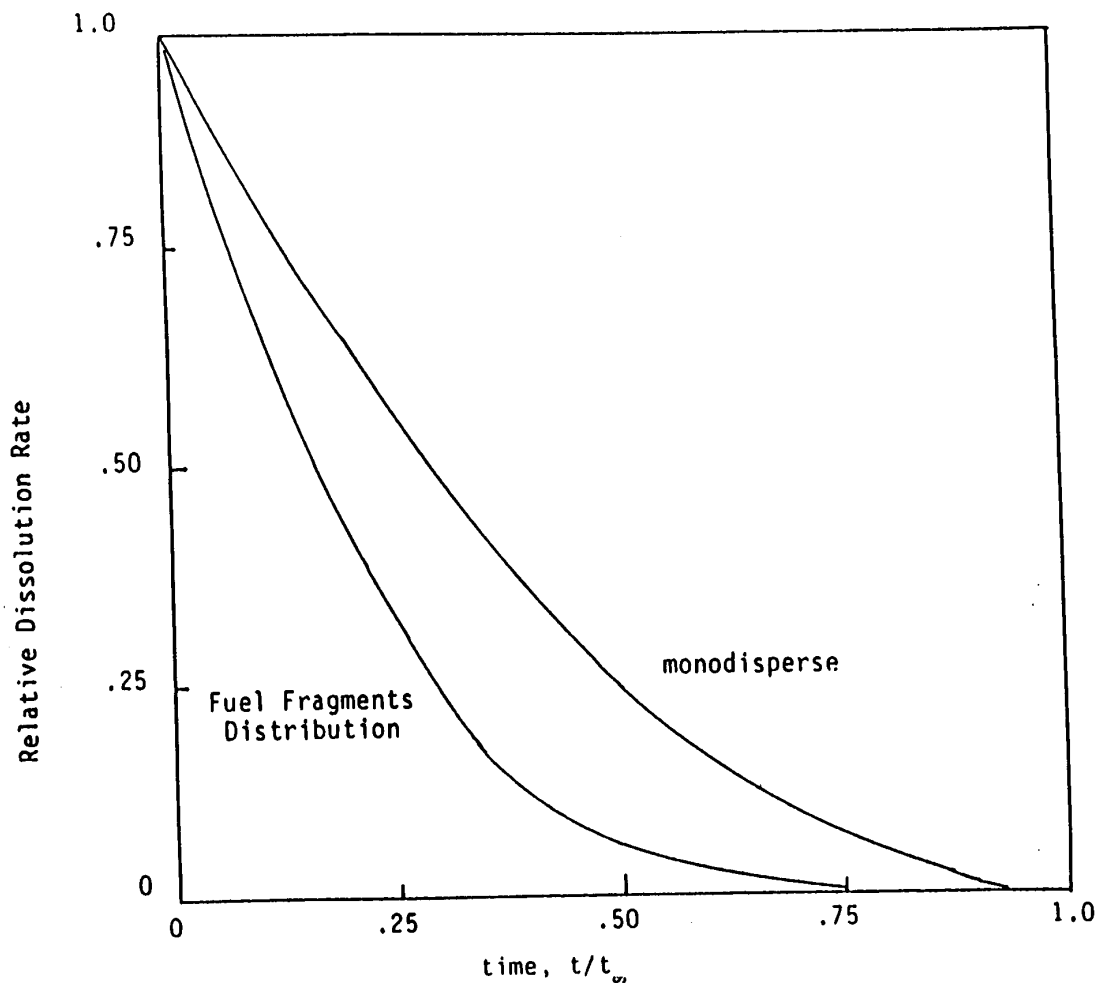


Figure 3.4.1.1-3 Dissolution rate for set of fragments (Figure 3 from Leider, H.R., S.N. Nguyen, R.B. Stout, and H.C. Weed, "Estimating the Time for Dissolution of Spent Fuel Exposed to Unlimited Water," LLNL Report UCRL-ID-107289, December 1991)

Rod Section	Total Weight of Fuel, g	% of Total Sample Weight Retained on Each Sieve Size							
		No. 3-1/2 (5.6 mm or 0.233 in.)	No. 5 (4.00 mm or 0.157 in.)	No. 7 (2.80 mm or 0.111 in.)	No. 10 (2.00 mm or 0.0787 in.)	No. 18 (1.00 mm or 0.0394 in.)	No. 50 (300 $\mu$ m or 0.0117 in.)	Receiver (<300 $\mu$ m or <0.0117 in.)	
205 (1)(a)	243.753	15.98	69.84	12.69	0.71	0.23	0.25	0.31	
385 (1)	225.212	19.88	65.57	13.35	0.71	0.08	0.19	0.22	
305 (2)	253.991	18.66	61.03	15.83	2.20	1.13	0.73	0.42	
3E5 (3)	254.497	18.88	58.28	20.2	1.53	0.44	0.27	0.31	
505 (3)	270.867	23.49	54.95	14.92	0.74	0.38	0.24	0.30	
5D5 (3)	246.704	20.13	64.58	13.61	0.64	0.31	0.32	0.42	
385A (3)	136.598	8.43	70.17	18.97	1.22	0.37	0.33	0.52	
385B (11)	146.223	49.83	45.00	4.52	0	0.07	0.26	0.33	

(a) Number in parentheses indicates the number of whole pellets before size analysis.

**Table 3.4.1.1-3 Particle-size distribution of fuel rods from NRU LOCA Test MT-3 (Rausch 1984) (Table 3.6 from A.E. Van Luik, et al., "Spent Fuel as a Waste Form for Geologic Disposal: Assessment and Recommendations on Data and Modeling Needs," PNL-6329, September 1987)**

### 3.4.1.1 Dissolution Rates

Sieve Number	Sieve Opening, mm	Weight, g	Fraction Retained
3	6.73	0	0
4	4.73	192.883	0.1007
5	4.00	634.765	0.3331
10	2.00	1031.170	0.5384
20	0.841	35.205	0.01838
40	0.420	11.242	0.005869
60	0.250	4.979	0.002599
80	0.177	1.424	0.0007434
100	0.149	1.042	0.0005440
140	0.105	1.204	0.0006286
200	0.074	0.769	0.0004015
200	0.074	0.737	0.0003848

**Table 3.4.1.1-4 Particle-size distribution of fuel fragments from H. B. Robinson Spent Fuel with a Burnup of 28 MWd/kgM (Katayama, Bradley, and Harvey 1980) (Table 3.7 from A.E. Van Luik, et al., "Spent Fuel as a Waste Form for Geologic Disposal: Assessment and Recommendations on Data and Modeling Needs," PNL-6329, September 1987)**

### 3.4.1.2 Solubility Limits

Attached are solubility data developed from two reports:

- 1) C.N. Wilson, "Results from Cycles 1 and 2 of NNWSI Series 2 Dissolution Tests," HEDL-TME85-22, May, 1987.
- 2) C. N. Wilson, "Results from the NNWSI Series 3 Spent Fuel Dissolution Tests," PNL-7170, June, 1990.

The pertinent solubility data taken after "steady-state" was reached are given in Table 1. (See also Section 2.1.3.5 for additional explanation. In cases where several values from different samples with different geometrics and different burnup histories were shown, the most conservative upper value is indicated. Since we don't know the cause of the scatter, it is prudent to assume the worst case, pending a better understanding of the spread in the steady-state solubilities. Where filtered and unfiltered values were available, the filtered data were used because solubility is the information desired.

For slow flow of water over the spent fuel, the solubility can be used to determine the mass of each radionuclide dissolved as a function of time. Given solubilities,  $C$ , a flow rate of water contacting the spent fuel,  $\Phi$ , and a time,  $t$ , over which dissolution occurs, the total amount of any nuclide,  $i$ , dissolved and transported,  $M_i$ , is given by  $M_i = C_i \Phi t$ .

**Table 3.4.1.2-1 Solubility data,  $C_i$**

<u>Species</u>	<u>Upper Limit Steady-State Concentration (<math>\mu\text{g/ml}</math>)</u>	
	<u>25°C</u>	<u>85°C</u>
U	$\leq 5$	$\leq 0.5$
$^{239+240}\text{Pu}$	$\leq 5 \times 10^{-3}$	$\leq 6 \times 10^{-5}$
$^{241}\text{Am}$	$\leq 3 \times 10^{-4}$	$\leq 1.5 \times 10^{-7}$
$^{244}\text{Cm}$	$\leq 1.2 \times 10^{-5}$	$\leq 2.4 \times 10^{-9}$
$^{237}\text{Np}$	$\leq 4 \times 10^{-4}$	$\leq 1.4 \times 10^{-3}$

### 3.4.1.3 Solubility Limiting Phases

#### 3.4.1.3 Solubility Limiting Phases

##### 3.4.1.3.1 Solubility Controls on Radionuclide Concentrations in Solution: Preliminary Results for U, Np, Pu, and Am

Radionuclide concentrations in solution are limited by the precipitation of solids. This is a presentation of calculations of the dissolved concentrations of the radionuclides U, Np, Pu, and Am in equilibrium with potential radionuclide-bearing solids in J-13 water at 25°C. Elemental concentrations vary as a function of solution composition, Eh and pH, among other parameters. To illustrate the potential impact of such variations, the dependence of radionuclide concentrations is solution as well as the identity of the radionuclide-bearing precipitate are calculated as a function of pH. These calculations can be used as a first approximation to estimate potential ranges in radionuclide concentrations in solution.

The chemical composition of J-13 water used in the calculations is given in Table 1. The redox potential of J-13 water was determined by assuming equilibrium with the atmosphere at an oxygen partial pressure of 0.2 bars. At a pH of 7.6, this corresponds to an Eh of 0.77 volts.

Geochemical modeling codes EQ3NR ver. 3245R123, and EQ6 ver. 3245R118, supported by EQLIB version 3245R152 and the thermodynamic data base DATA0.com.R6, were used to make the calculations. All calculations were carried out at 25°C.

**Table 3.4.1.3-1 Average J-13 water anal of LLNL laboratory supply  
(Table 1 from Delany, 1985)**

<b>J-13 Water</b>		
<b>Element</b>	<b>Concentration</b>	
	<b>mg/l</b>	<b>molality (moles/kg)</b>
<b>Li</b>	<b>0.042</b>	<b>6.053E-6</b>
<b>Na</b>	<b>43.9</b>	<b>1.909E-3</b>
<b>K</b>	<b>5.11</b>	<b>1.307E-4</b>
<b>Ca</b>	<b>12.5</b>	<b>3.119E-4</b>
<b>Mg</b>	<b>1.92</b>	<b>7.897E-5</b>
<b>Sr</b>	<b>0.035</b>	<b>3.995E-7</b>
<b>Al</b>	<b>0.012</b>	<b>4.447E-7</b>
<b>Fe</b>	<b>0.006</b>	<b>1.074E-7</b>
<b>Si</b>	<b>27.0</b>	<b>9.613E-4</b>
<b>NO<sub>3</sub></b>	<b>9.6</b>	<b>1.548E-4</b>
<b>F</b>	<b>2.2</b>	<b>1.158E-4</b>
<b>Cl</b>	<b>6.9</b>	<b>1.946E-4</b>
<b>HCO<sub>3</sub></b>	<b>125.3</b>	<b>2.054E-3</b>
<b>SO<sub>4</sub></b>	<b>18.7</b>	<b>1.947E-4</b>
<b>pH</b>	<b>7.6</b>	

Table 3.4.1.3-2 (Tables 2, 3, 4, and 5 from C.J. Bruton, *Solubility Controls on Radionuclide Concentrations in Solution: Preliminary Results for U, Np, Pu, and Am*, LLNL draft report, November, 1990)

Table 2.

U		
Solid	Concentration	
	mg/l	molality (moles/kg)
Haiweeite $\text{Ca}(\text{UO}_2)_2\text{Si}_6\text{O}_{15}\cdot 5\text{H}_2\text{O}$	0.1641E-3	0.6893E-9
Soddyite $(\text{UO}_2)_2\text{SiO}_4\cdot 2\text{H}_2\text{O}$	0.015	0.6096E-7
Sklodowskite $\text{Mg}(\text{H}_3\text{O})_2(\text{UO}_2)_2\cdot (\text{SiO}_4)_2\cdot 4\text{H}_2\text{O}$	11.05	0.4642E-4
$\text{CaUO}_4$	12.59	0.5289E-4
Schoepite $\text{UO}_3\cdot 2\text{H}_2\text{O}$	38.90	0.1634E-3
$\text{UO}_2(\text{OH})_2(\text{beta})$	56.73	0.2383E-3
Uranophane $\text{Ca}(\text{UO}_2)_2(\text{SiO}_3)_2(\text{OH})_2$	142.48	0.5986E-03

Table 3.

Np		
Solid	Concentration	
	mg/l	molality (moles/kg)
$\text{NpO}_2$	0.59	0.2468E-5
$\text{NpO}_2(\text{OH})(\text{am})$	129.39	0.5459E-3
$\text{NaNpO}_2\text{CO}_3\cdot 3.5\text{H}_2\text{O}$	139.99	0.5906E-3
am = amorphous		

Table 4.

Pu		
Solid	Concentration	
	mg/l	molality (moles/kg)
$\text{PuO}_2$	0.39E-6	0.1612E-11
$\text{PuO}_2(\text{OH})_2$	0.015	0.6204E-7
$\text{Pu}(\text{OH})_4$	27.97	0.1146E-3

Table 5.

Am		
Solid	Concentration	
	mg/l	molality (moles/kg)
$\text{AmOHCO}_3$	0.0041	0.1696E-7
$\text{Am}(\text{OH})_3$	8.42	0.3464E-4
$\text{Am}(\text{OH})_3(\text{am})$	158.66	0.6529E-3



### 3.4.1.3 Solubility Limiting Phases

---

**Table 3.4.1.3-3** Phases identified on reacted  $\text{UO}_2$  surface (Table II from J.K. Bates, *Identification of Secondary Phases Formed During Unsaturated Reaction of  $\text{UO}_2$  with EJ-13 Water*, Materials Research Society Symposium proceedings 176:499 (1990))

Phase	Formula	Appearance
Schoepite	$\text{UO}_3 \cdot 2\text{H}_2\text{O}$	Dark yellow crystals
Dehydrated Schoepite	$\text{UO}_3 \cdot 0.8\text{H}_2\text{O}$	Yellow crystals with reflective face
Compreignacite	$\text{K}_2\text{U}_6\text{O}_{19} \cdot 11\text{H}_2\text{O}$	Yellow crystals
Uranophane	$\text{Ca}(\text{UO}_2)_2(\text{SiO}_3)_2(\text{OH})_2 \cdot 5\text{H}_2\text{O}$	Fine white needles
Boltwoodite	$\text{K}(\text{H}_3\text{O})\text{UO}_2(\text{SiO}_4) \cdot n\text{H}_2\text{O}$	Yellow crystals
Sklodowskite	$\text{Mg}(\text{UO}_2)_2(\text{SiO}_3\text{OH})_2 \cdot 5\text{H}_2\text{O}$	Fine needles
Becquerelite	$\text{CaU}_6\text{O}_{19} \cdot 10\text{H}_2\text{O}$	Dark yellow crystals
Fluoropolymer	Not determined	White feathers

## 3.4.2 Spent-Fuel Dissolution Models

### 3.4.2.1 Introduction

This section discusses modeling of the aqueous dissolution and release-rate responses of uranium oxide spent-fuel waste forms. Section 3.4.2.2 describes the development of dissolution-rate function forms. The previous nonequilibrium thermodynamic model for dissolution rate, described in Version 1.2 of the *Waste Form Characterization Report* (WFCR V1.2), has been extended to include surface chemisorption effects. The surface chemisorption phenomenon is represented by the well-known Tempkin isotherm. This extension provides the theoretical basis for function forms used to regress the existing experimental data. A brief discussion is provided for a different function form that would effectively represent radiolysis effects. Additional model development for radiolysis effects is in progress, but is not included in this revision.

In Section 3.4.2.3, numerical regression analyses, using various dissolution-rate functions are discussed. The incorporation of available new data has not changed the previous model significantly. The regression of the existing data to a dissolution-rate model suggested by outside experts has a small R-square value ( $R^2$ ) measure relative to the  $R^2$  of the nonequilibrium thermodynamic model. In Section 3.4.2.4, the development of the aqueous-release-rate model has not been changed; however, it has been used to evaluate film concentrations of radionuclides in the alteration layers based on data from the unsaturated drip tests. This film analysis and values of the film concentrations are discussed in Section 3.4.2.5.

The approach for developing a dissolution-rate model uses concepts from nonequilibrium thermodynamics. The objective is to derive function forms for the dissolution rate that are consistent with quasi-static thermodynamic processes. These function forms will contain thermodynamic chemical potentials of both the solid (spent fuels) and the solution (water chemistries) along with a set of coefficients and parameters that can be evaluated by numerical regression of dissolution-test data. Currently, detailed knowledge is not available for the atomic (mechanistic) steps and the sequence of chemical/electrochemical-reaction steps to describe the dissolution process over the range of spent-fuel inventory, potential water chemistries, and temperatures. The existing approach is to obtain an experimental database (flow-through tests) of dissolution rates for a subset of specific spent fuels approved test material (ATM) over a range of controlled, aggressive water chemistries and temperatures. With a numerical regression algorithm, these data are used to evaluate empirical parameters in a rate law for each specific spent fuel ATM (Gray et al., 1992; Steward and Gray, 1994). The function form of this rate law is a product polynomial of the bulk water chemistry concentrations and temperature (Stumm and Morgan, 1981). This function form has been extended to have an explicit dependence on the thermodynamic properties of the uranium oxide waste form by using fuel-reaction burnup as an aggregate variable for fission product and actinide concentrations.

In addition, the use of bulk concentrations of water chemistry and spent-fuel burnup in the function form for the regression analysis of the dissolution data do not explicitly account for a dependence from possible surface-to-bulk concentration differences due to radiolysis, surface adsorption, and dipole layers. However, some of these shortcomings are effectively addressed, in Section 3.4.2.2, by the phenomena due to surface chemisorption. Several simplifying assumptions are made there.

### 3.4.2 Spent Fuel Dissolution Models

---

The following thermodynamic model uses analysis methods and physical concepts taken primarily from classical mechanics. (Jackson, 1962; Eringen, 1967; Bikerman, 1970; Sedov and Radok, 1972), colloidal foundations (Hunter, 1993), thermodynamics (Gibbs, 1961; Lewis and Randall, 1961; deGroot and Mazur, 1962; Denbigh, 1968; Lupis, 1983), electrochemistry (Bikerman, 1970; Bockris and Reddy, 1970; Antropov, 1972; Pourbaix, 1973), geochemistry (Stumm and Morgan, 1981; Lasaga et al., 1981; Hochella and White, 1990); and surface chemistry (Hayward and Trapnell, 1964; Adamson, 1976; Jaycock and Parfitt, 1981)

The development of a release-rate model is more complex than the development of a dissolution-rate model. The release model includes dissolution rates, precipitation rates, colloidal kinetics, and adsorption rates. At this time, the approach is semi-empirical and depends strongly on the unsaturated testing experiments to provide data and chemical-process models.

The spent-fuel-waste-form dissolution/release-rate responses impact design and performance assessment evaluations and consequences of the substantially complete containment time period (SCCTP) [NRC 10CFR60.113] and the controlled release time period (CTRP) (NRC 10CFR60.113). These two regulatory requirements are coupled because waste-package failures during the SCCTP will potentially expose spent-fuel waste forms to atmospheric conditions in a repository. During this time period, the waste forms may be altered by oxidation and/or water vapor adsorbed to the spent-fuel surface and by dissolution and release of radionuclides from the waste form as a result of wetting by water. In these cases, alteration, hydration and dissolution of the spent-fuel-waste-form lattice-structure will take place. The development of a thermodynamically based dissolution and release model relates to the design requirements, to the subsystem release, and to total system performance assessment (TSPA) model-development needs.

#### 3.4.2.2 Nonequilibrium, Thermodynamic Dissolution-Rate Function Forms

In the following text, thermodynamic internal energy functionals are used to represent the energy responses for a generic solid and a generic liquid. The solid and liquid are assumed to be in contact at an idealized wetted surface. The analysis will assume that the wetted surface has a solid-surface side and liquid-surface side. The wetted surface is a material discontinuity. This surface is also a dissolution front that propagates at an idealized dissolution velocity,  $\underline{V}$ , which, for assumed quasi-steady-state rate processes, will be taken as a constant.

The generic solid will have bulk constituents of typical  $\text{UO}_2$  spent fuel, namely minor concentrations of actinides, fission products, and defects in the bulk lattice structure. For purposes here, and as described elsewhere (Stout, 1996), the bulk lattice is assumed to be nominally that of the  $\text{UO}_2$  lattice structure; however, other oxide phases and adsorbed complexes may exist on and in spatial neighborhoods of the wetted surface. The generic liquid will be represented with a subset of arbitrary initial/bulk constituents, plus two subsets of dissolution products from the solid.

In particular, for the waste form solid with mass density  $\rho$ , let the  $(1 \times I)$  column matrix  $f_s = \{f_{sI}\}$  denote the densities (number per unit volume) of the atomic lattices, other actinide atoms, fission product atoms, and conduction electrons; and, for now, neglect the possible defect structures. The column matrix  $f_s$  is an atomic fraction density, or equivalent to mass fraction densities for the solid. For the liquid, let the  $(1 \times I)$  column matrix  $f_L = \{f_{LI}\}$  denote the densities (number per unit volume) of the aqueous state  $\text{H}_2\text{O}$ ,  $\text{H}_3\text{O}^+$ ,  $\text{OH}^-$  plus the added constituents. During dissolution, the solid constituents will react with the liquid constituents,

although the exact details of these reactions are presently unknown. For purposes of a generic analysis, let the set of products on the solid side of the wetted surface be  $f_{SL}$ , which are created by reactions of general form

$$\underline{A}_S f_S + \underline{B}_S f_L \leftrightarrow \underline{C}_{SL} f_{SL} \quad (3.4.2-1)$$

where  $\underline{A}_S$ ,  $\underline{B}_S$ , and  $\underline{C}_{SL}$  coefficient matrices of the reactions. The set  $\{f_{SL}\}$  represents complexes, compounds, and/or phase-change species on the solid side of the wetted surface. These will also be argument functions in the solid's internal energy functional. Similarly, on the liquid side of the wetted surface, let  $f_{SL}$  denote the set of liquid solution products that are created by reactions of the general form

$$\underline{A}_L f_S + \underline{B}_L f_L \leftrightarrow \underline{C}_{LS} f_{LS} \quad (3.4.2-2)$$

where  $\underline{A}_S$ ,  $\underline{B}_S$ , and  $\underline{C}_S$  are coefficient matrices. In addition to the liquid-solid species set  $\{f_{SL}\}$  created directly from the solid constituents  $f_S$ , there also exists the solid surface constituent set  $\{f_{SL}\}$  that can react to create liquid species. These new species are denoted by a column matrix  $\{f_{SLL}\}$  and are created by reactions of the form

$$\underline{A}_{SL} f_{SL} + \underline{B}_{SL} f_L \leftrightarrow \underline{C}_{LSL} f_{LSL} \quad (3.4.2-3)$$

where  $\underline{A}_{SL}$ ,  $\underline{B}_{SL}$ , and  $\underline{C}_{LSL}$  are coefficient matrices. Thus, the dissolution process creates two species subsets  $\{f_{LS}\}$  and  $\{f_{LSL}\}$  in the liquid, and these concentrations will be included as function arguments of the liquid's internal energy functional.

Each of the constituent densities of the solid and the liquid will be assumed to move with the particle velocity of its spatial neighborhood  $\underline{v}$  plus its intrinsic diffusional velocity  $\underline{v}$  relative to the particle velocity. Thus, the argument variables of the constituent functions  $f_S$ ,  $f_{SL}$ ,  $f_L$ , and  $f_{LSL}$  are the spatial point  $\underline{x}$ , at time  $t$ , and the species associated diffusional velocities  $\underline{v}_S$ ,  $\underline{v}_{SL}$ ,  $\underline{v}_L$ ,  $\underline{v}_{LS}$ , and  $\underline{v}_{LSL}$  respectively. Finally, the thermodynamic internal energy functional also has argument functions for the entropy and the elastic (recoverable) strain tensor. The entropy functions are denoted by  $\eta_s(\underline{x}, t)$  and  $\eta_l(\underline{x}, t)$ , and the strain tensors are denoted by  $\gamma_s(\underline{x}, t)$  and  $\gamma_l(\underline{x}, t)$ , for points  $\underline{x}$  at time  $t$  of the solid and liquid, respectively. Note that entropy and strain are material particle potential functions and do not have diffusional velocities relative to this material particle located at point  $\underline{x}$  with velocity  $\underline{v}(\underline{x}, t)$ . These can be added; however, a later assumption will consider the dissolution process as a chemical reaction that is rate-controlled at the wetted solid-liquid-surface front. Therefore, the diffusion flux terms will be removed for the final dissolution rate model.

In the following, the effect of nonrecoverable deformations with finite, discontinuous strain tensor effects will be neglected. These deformation/strain effects produce stress work at the dissolution front and can be added when their potential import is better understood, as in the oxidation phase change deformation model (Stout et al, 1993a; 1993b).

Using the preceding notation and definitions of functions, the internal energy functional for the solid is defined as

$$\mathcal{E}_S(\eta_S, \gamma_S, \{f_S\}) \equiv \mathcal{E}_S(\eta_S, \gamma_S, f_S, f_{SL}) \quad (3.4.2-4)$$

### 3.4.2 Spent Fuel Dissolution Models

and it is assumed that functional derivatives of  $\varepsilon_s$  exist with respect to each of its argument functions for all times  $t$  and at all points  $\underline{x}$  of the solid body  $\bar{R}_s$  plus its surface  $\partial\bar{R}_s$ . Similarly, the internal energy functional for the liquid is defined as

$$\varepsilon_L(\eta_L, \gamma_L, \{f_L\}) \equiv \varepsilon_L(\eta_L, \gamma_L, f_L, f_{LS}, f_{LSL}) \quad (3.4.2-5)$$

and also that functional derivatives exist for all times  $t$  and at all points  $\underline{x}$  of the liquid body  $\bar{R}_L$  plus its surface  $\partial\bar{R}_L$ . The idealized dissolution front, namely the wetted surface, is simultaneously adjacent to surfaces  $\partial\bar{R}_s$  and  $\partial\bar{R}_L$ , and is notationally written with a single square bracket  $\partial\bar{R}$  that denotes a surface of possible spatial discontinuity for kinematic, mass transport, momentum, stress, and energy relations. The following analysis will provide some details for only the energy conditions across an arbitrary segment  $\partial R$  of  $\partial\bar{R}$  for quasi-static conditions, surrounded by arbitrary subsets  $R_s + \partial R_s$  and  $R_L + \partial R_L$  and  $R_L + \partial R_L$  of the solid and liquid, respectively.

The textbook conservation equation for the rate of energy change of the combined solid and liquid system describes the rate of internal energy change of  $R_s + \partial R$  and  $R_L + \partial R_L$  as equal to the mechanical traction (body force work is neglected) rates. The current–electric rate, plus the heat/flux rates, where the sets of points  $\{\underline{x}\}_s$  on  $\partial R_s$  and points  $\{\underline{x}\}_L$  on  $\partial R_L$  enclose the idealized surface  $\partial R$ , which propagates with the dissolution front velocity,  $\underline{V}$ . In equation form, the energy equation can be written with some shorthand notation as

$$\begin{aligned} & \int_{R_s} d_t \varepsilon_s + \int_{\partial R_s} (\varepsilon_s \underline{n}_s \cdot (\underline{v}_s - \underline{V}) + \Delta_{f_s} \varepsilon_s \underline{n}_s \cdot \{f_s \underline{v}_s\}) + \int_{R_L} d_t \varepsilon_L + \int_{\partial R_L} (\varepsilon_L \underline{n}_L \cdot (\underline{v}_L - \underline{V}) + \Delta_{f_L} \varepsilon_L \underline{n}_L \cdot \{f_L \underline{v}_L\}) \\ &= \int_{\partial R_s} (\underline{\sigma}_s \cdot \underline{v}_s \cdot \underline{n}_s + \underline{h}_s \cdot \underline{n}_s) + \int_{R_s} \underline{J}_s \cdot \underline{E}_s + \dot{H}_s + \int_{\partial R_L} (\underline{\sigma}_L \cdot \underline{v}_L \cdot \underline{n}_L + \underline{h}_L \cdot \underline{n}_L) + \int_{R_L} \underline{J}_L \cdot \underline{E}_L + \dot{H}_L \end{aligned} \quad (3.4.2-6)$$

where the new function symbols are  $\underline{n}_s$  and  $\underline{n}_L$  for the outward normal unit vectors of surfaces  $\partial R_s$  and  $\partial R_L$ , respectively;  $d_t \varepsilon$  denotes total time derivatives;  $\Delta_f \varepsilon$  denotes functional derivatives;  $\{f\underline{v}\}$  denotes the diffusional mass fluxes of constituents of the solid (subscript S) and of liquid (subscript L);  $\underline{\sigma}$  is the stress tensor;  $\underline{h}$  is the heat flux vector;  $H$  is heat generation rate;  $\underline{J}$  is the current vector (flux of charged constituents); and  $\underline{E}$  is the electric field vector, which will have a moving idealized dipole surface due to charges concentrated on  $\partial R_s$  and  $\partial R_L$ . For points  $\underline{x}$  in  $R_s$  and  $R_L$ , the rate and flux volume integrals are regular. However, across moving surfaces  $\partial R_s$  and  $\partial R_L$ , discontinuity conditions may exist for quasi-static internal energy rate changes because of entropy, strain, constituent masses, stress, heat flux, and current–electric–field energy contributions (Jackson, 1962; Eringen, 1967). This is written, again with shorthand notation, for the discontinuity across the surface  $\partial R$  between surfaces  $\partial R_s$  and  $\partial R_L$  as

$$\int_{\partial R} \left( (\Delta_{\eta} \varepsilon \eta + \Delta_{\gamma} \varepsilon \gamma + \Delta_f \varepsilon f) (\underline{v} - \underline{V}) \cdot \underline{n} \right)_s^L + \Delta_f \varepsilon \{f \underline{v}\} \cdot \underline{n}_s^L - \underline{\sigma} \cdot \underline{v} \cdot \underline{n}_s^L - \underline{h} \cdot \underline{n}_s^L + \underline{J} \phi \cdot \underline{n}_s^L = 0 \quad (3.4.2-7)$$

where terms for internal energy discontinuities with particle velocity  $\underline{v}$  minus front velocity  $\underline{V}$  contributions are separated from the diffusional flux velocity  $\underline{v}$  terms and from the energy rate terms from stress, heat flux, and the quasi-static electric current/field work term. The current/field work term is simplified by replacing the electric field vector  $\underline{E}$  with  $-\underline{\nabla} \phi$ , the

gradient of the scalar potential for the charge density, and by assuming that there is no rate or charge changes on the surfaces  $\partial R_s$  and  $\partial R_L$  as the dissolution front  $\partial R$  propagates. This quasi-steady rate assumption for transient-current and charge-rate changes means that any dissolution-rate data measured over short times (seconds to days) may have transient errors and not be true steady-state rates for the imposed, controlled variables. Eq. 3.4.2-7 can be further reduced by assuming that the heat flux vector is continuous across  $\partial R$  and that the internal energy change due to elastic strain is equal to the traction work at the surfaces  $\partial R_s$  and  $\partial R_L$ . Finally the current  $I$  is equal to the flux of charged particles transported across  $\partial R_s$  and  $\partial R_L$ , which can be written as

$$\underline{J}_S = e\{zf\}_S(\underline{v}_S - \underline{V}) + e\{zf\underline{v}\}_S \quad (3.4.2-8)$$

or

$$= e(z_S f_S + z_{SL} f_{SL})(\underline{v}_S - \underline{V}) + e(z_S f_S \underline{v}_S + z_{SL} f_{SL} \underline{v}_{SL})$$

and

$$\underline{J}_L = e\{zf\}_L(\underline{v}_L - \underline{V}) + e\{zf\underline{v}\}_L \quad (3.4.2-9)$$

or

$$= e(z_L f_L + z_{LS} f_{LS} + z_{LSL} f_{LSL})(\underline{v}_L - \underline{V}) + e(z_L f_L \underline{v}_L + z_{LS} f_{LS} \underline{v}_{LS} + z_{LSL} f_{LSL} \underline{v}_{LSL})$$

where the subsets  $\{z\}_S$  and  $\{z\}_L$  are the number of unit charges of magnitude  $e$  (+ for cations and – for electrons and anions) of the associated species subsets  $\{f\}_S$ ,  $\{f\underline{v}\}_S$ ,  $\{f\}_L$ , and  $\{f\underline{v}\}_L$ . Using these assumptions and the shorthand notation of Eq. 3.4.2-8 and Eq. 3.4.2-9, Eq. 3.4.2-7 can be written as an entropy rate expression across an arbitrary subset  $\partial R^+$  of surface  $\partial R$ .

$$\begin{aligned} \int_{\partial R^+} \Delta_\eta \epsilon \eta (\underline{v} - \underline{V}) \cdot \underline{n} \Big|_S^L &= - \int_{\partial R^+} \left( \Delta_f \epsilon f - e\{zf\}\phi \right) (\underline{v} - \underline{V}) \cdot \underline{n} \Big|_S^L \\ &- \int_{\partial R^+} \left( \Delta_f \epsilon \{f\underline{v}\} - e\{zf\underline{v}\}\phi \right) \cdot \underline{n} \Big|_S^L \end{aligned} \quad (3.4.2-10)$$

Equation 3.4.2-10 has an entropy production/dissipation energy term given by the dissolution reaction term moving with essentially nominal velocity  $\underline{V}$  of surface  $\partial R$  and a diffusional mass flux of dissolution product and supply species across surface  $\partial R$ . There are two approaches for developing kinetic (rate) models from Eq. 3.4.2-10: One is the classical Onsager approach that couples rate terms to thermodynamic forces (this is the first regression modeling approach); the second approach is to use the entropy production term across the dissolution surface as the thermodynamic measure for the dissolution propagation velocity. This latter approach results in the classical Butler–Volmer equation, when the Boltzmann configuration form for entropy is used. Both will be formulated in the following. For reasons discussed subsequently, the Butler–Volmer equation provided the better model.

For an Onsager-type model, the kinetics of the surface propagation velocity  $\underline{V}$  and the diffusional flux velocities  $\{f\underline{v}\}$  are thus coupled thermo-electrochemical rate processes, yet are independent kinematic (motion) variables that provide independent contributions to entropy

production. Therefore, a general, nonequilibrium, thermodynamic formulation of dissolution would take the function rate forms  $\{\rho\}(\underline{v}-\underline{V})\cdot\underline{n}$  and  $\{f\underline{v}\}\cdot\underline{n}$ , which are specific mass-dissolution front-velocity terms and diffusion-flux velocity terms as nonequilibrium thermodynamic rate functions for entropy production/dissipation. Corresponding to the rates, there exist the nonequilibrium thermodynamic forces driving the thermo-electrochemical processes toward an equilibrium thermodynamic state. These thermodynamic forces are functional multipliers of the rate functions given in Eq. 3.4.2-10; namely  $((\Delta_f \mathcal{E} - e\{z\}\phi))$ . In terms of the shorthand notation, the coefficients appear to be the same for both rate terms. However, when the stoichiometric equation forms for the reactions of Eq. 3.4.2-1, Eq. 3.4.2-2, and Eq. 3.4.2-3 are formally incorporated, the thermodynamic force functionals describe an independent energy change for chemical reaction kinetics and an independent energy change for diffusional mass-transport kinetics. Using Onsager's concepts to describe nonequilibrium or irreversible thermodynamic processes, the two rate functions are coupled by function or functional coefficients to the two thermodynamic forces of energy kinetics and diffusion mass transport kinetics. Formally these are

$$\{\rho\}(\underline{v}-\underline{V})\cdot\underline{n} = L_{ff}\left[(\Delta_f \mathcal{E} - e\{z\}\phi)\{f\}\right]_{energy} + L_{fv}\left[\Delta_f \mathcal{E} - e\{z\}\phi\right]_{diffusion} \quad (3.4.2-11a)$$

$$\{f\underline{v}\}\cdot\underline{n} = L_{vf}\left[(\Delta_f \mathcal{E} - e\{z\}\phi)\{f\}\right]_{energy} + L_{vv}\left[\Delta_f \mathcal{E} - e\{z\}\phi\right]_{diffusion} \quad (3.4.2-11b)$$

where the four coefficients  $L_{ff}$ ,  $L_{fv}$ ,  $L_{vf}$ , and  $L_{vv}$  (which can be functions of the atomic fraction  $\{f\}$ ) couple the rate functions to the thermodynamic forces. For strictly non-negative entropy production, the Onsager coupling coefficients have symmetry such that, formally,  $L_{vf}$  is equal to  $L_{fv}$ .

Eq. 3.4.2-11a provides an Onsager-type thermodynamic function form that should be evaluated at the dissolution front for the dissolution rate function, which is essentially the dissolution front velocity when the details of the surface particle velocities are neglected. These function forms have internal energy thermodynamic chemical potential functions  $\Delta_f \mathcal{E}_s$  for the solid constituents ( $f=\{f_s, f_{SL}\}$ ) and  $\Delta_f \mathcal{E}_L$  for the waste form liquid constituents ( $f=\{f_s, f_{SL}, f_{LSL}\}$ ) and have parameters related to the surface dipole potential of the dissolution front. For numerical regression analyses in the simplest, ideal cases, particular chemical reactions with some regression parameters could be assumed, and the regression parameters could be evaluated based on the available thermodynamic values and dissolution data sets. For the complex case of spent-fuel waste form dissolution, Eq. 3.4.2-11a was reduced to the following for regression analysis

$$\rho V = L_{ff}\left[\Delta_f \mathcal{E}f - e\{zf\}\phi\right]_L^S \quad (3.4.2-12)$$

which represents the dissolution rate as proportional to the chemical potential energy change of the waste-form solid relative to the liquid; and the Onsager coefficient function  $L_{ff}$  can be represented as a general function of the densities functions  $\{f_S\}$  and  $\{f_L\}$  of the spent-fuel waste form and the liquid.

The second approach also assumes that only the energy-change term of Eq. 3.4.2-10 has the significant contribution to the production of entropy as waste-form solid dissolves into a liquid. Then, from Eq. 3.4.2-10, the entropy term propagating at velocity  $(\underline{v}-\underline{V})$  is set equal to

only the energy term propagating also at velocity  $(\underline{v}-\underline{V})$  (as follows at any arbitrary point on the surface R]:

$$\Delta_{\eta}\epsilon\eta(\underline{v}-\underline{V})\cdot\underline{n}\Big|_S^L = -\left(\Delta_f\epsilon f - e\{zf\}\phi\right)(\underline{v}-\underline{V})\cdot\underline{n}\Big|_S^L \quad (3.4.2-13)$$

The velocity term  $(\underline{v}-\underline{V})\cdot\underline{n}$  is common to both sides of Eq. 3.4.2-13; therefore, the entropy energy change from liquid to solid in Eq. 3.4.2-13 is set equal to the negative chemical potential changes (defined from internal energy) as constituents of the solids that react with and dissolve into the liquid. Thus,

$$\Delta_{\eta}\epsilon\eta\Big|_S^L = -\left(\Delta_f\epsilon f - e\{zf\}\phi\right)\Big|_S^L \quad (3.4.2-14)$$

Using Boltzmann's definition of entropy (Denbigh, 1968), the thermodynamic entropy  $\eta$  can be expressed in terms of a configurational or thermodynamic state probability function  $\Omega$

$$\eta = k \ln \Omega \quad (3.4.2-15)$$

where  $k$  is Boltzmann's constant. Then, Eq. 3.4.2-14 can be rewritten in terms of  $\Omega$  as

$$\Delta_{\eta}\epsilon k \ln \Omega\Big|_S^L = -\left(\Delta_f\epsilon f - e\{zf\}\phi\right)\Big|_S^L \quad (3.4.2-16)$$

If the dissolution process is considered far from equilibrium, the dissolution rate given by the propagation velocity of wetted surface is assumed to be functionally related to the change in the configurational entropy as the solid dissolves into the liquid. From Eq. 3.4.2-16, the ratio of configurational entropy is

$$\Omega_L/\Omega_S = \exp\left[\left(-\left(\Delta_f\epsilon f - e\{zf\}\phi\right)/\Delta_{\eta}\epsilon k\right)\right]\Big|_S^L \quad (3.4.2-17)$$

The simplest form for the quasi-static dissolution response is to assume that the dissolution front velocity is linearly dependent on this configurational entropy ratio. This is the same as assuming that the rate of changing configurational entropy states of a solid into a liquid is related to the dissolution rate. Then, the dissolution rate, in terms of normal velocity and waste-form mass density, is assumed to be of form

$$\begin{aligned} \rho \underline{V} \cdot \underline{n} &= c \Omega_L / \Omega_S \\ &= c \exp\left[\left(-\left(\Delta_f\epsilon f - e\{zf\}\phi\right)/kT\right)\right]\Big|_S^L \end{aligned} \quad (3.4.2-18)$$

where the temperature function  $T$  of classical thermodynamics is substituted for the change of internal energy with respect to changes in entropy, and  $c$  is a parametric constant of the dissolution rate response. Eq. 3.4.2-18 is a form of the Butler-Volmer model (Bockris and Reddy, 1970) used in electrochemical studies of corrosion rates.

In Eq. 3.4.2-12 and Eq. 3.4.2-17, the functional argument of the Onsager model and the Butler-Volmer model is that the internal energy change as a solid surface reacts and dissolves into an adjacent solution. The functional argument includes the chemical potential and electrochemical potential energy contributions for the solid-to-liquid surface reactions. The



chemical potential terms are defined relative to the internal energy  $\Delta_f \epsilon$ , where  $\Delta \epsilon$  is the energy change per unit (atomic or molar) of reacted species in set  $\{f\}$ , and  $f$  denotes the relative amounts of reacted species for members in the set  $\{f\}$ . The relative ratios for the amounts are, in theory, established by the chemical reaction Eq. 3.4.2-1 through Eq. 3.4.2-3. In practice, the chemical reactions are often not stoichiometrically ideal nor well-known (Aagaard and Helgeson, 1982). Furthermore, even the functional forms for the chemical potentials  $\Delta \epsilon$  are not explicitly available in many situations. Similar uncertainties exist for the electrochemical potential term  $e\{zf\}\phi$ , which represents the electric field work at the solid-liquid dipole surface. The magnitude of the dipole charge between the liquid and solid  $\phi_s^L = \phi_L - \phi_s$  is the effective surface charge of the liquid minus the effective surface charge of the solid. Both of these charge fields are complex and depend on the ionic and electronic charges distributions in the liquid and solid, respectively. In particular, the charge distribution in the liquid is nonlinearly dependent on the ionic species in the liquid set  $\{f_L\}$ . These changes can also be spatially distributed in the liquid and adjacent to the solid surface (Antropov, 1972). Thus, selecting chemical and electrochemical functional forms for data regressions is somewhat arbitrary. However, the function variables of the functional forms used in the regression analysis are constrained to be the controlled variables of the experiments performed for dissolution-rate data. These variables are temperature, pH, carbonate, oxygen, and spent-fuel burnup.

Thus, the simplest forms for regression analysis are polynomials in the bulk-controlled concentration variables of the liquid and the spent fuel, and the temperature. Quadratic functions are well known to approximate physical data adequately. They are also easy to differentiate and integrate (Box et. al., 1978; Davies, 1956). Thus, a quadratic function, including cross terms, with parametric coefficients was selected to represent the chemical potential and electrochemical energy functional terms for an Onsager model and an initial or first Butler–Volmer model. In addition to this first Butler–Volmer model (see 3.4.2 Appendix, Eq. A3.4.2-1), a second Butler–Volmer model was selected that had the concentration-dependent chemical-potential terms represented as logarithmic functions of concentrations, which, for small concentrations, is represented in classical thermodynamic texts as

$$\Delta_f \epsilon \equiv \mu_f = \mu_{of} + kT \ln[f] \quad (3.4.2-19)$$

where  $\mu_{of}$  is the chemical potential at standard state conditions and  $[f]$  is species concentration in the aqueous solution or solid.

The logarithmic functions correspond to accepted function representations for both ideal and nonideal solutions often used for both liquids and solids (Antropov, 1972; Lewis and Randall, 1961; Stumm and Morgan, 1981; Lupis, 1983). Because the logarithmic dependence is an exponential argument, the second Butler–Volmer model reduces to a product of concentrations, each raised to a regression parametric power. Thus, Eq. 3.4.2-18 combined with Eq. 3.4.2-19 becomes

$$\rho \underline{V} \cdot \underline{n} = c \exp(-((\mu_{of} + kT \ln[f])f - e\{zf\}\phi)/kT)]_S^L \quad (3.4.2-20)$$

Because  $\exp(\ln[f])=[f]$ , Eq. 3.4.2-2, when combined with the ideal mass balance Eq. 3.4.2-1 through Eq. 3.4.2-3, can be written as

$$\rho \underline{V} \cdot \underline{n} = c(\Pi[f]^N) \exp(-(\mu_{of}f - e\{zf\}\phi)/kT)]_S^L \quad (3.4.2-21)$$

where  $\Pi [f]^N$  is the product of liquid–solid concentrations raised to the power N. This equation can be written in terms of liquid concentration of the water chemistry variables, which, in the current studies, are the hydrogen ion ( $H^+$ ), total carbonate ( $CO_3$ ), and oxygen ( $O_2$ ), with spent fuel burnup (Bu) as an aggregate variable that represents the concentration effects of fission products and actinides. This approach yields the following regression expression for dissolution rate in terms of controlled variables:

$$\rho V \cdot \underline{n} = A[H^+]^{N_H}[CO_3]^{N_C}[O_2]^{N_O}[Bu]^{N_B} \exp(-Q/kT) \quad (3.4.2-22)$$

where Q represents an effective activation energy parameter for the temperature-dependence of dissolution. Eq. 3.4.2-22 has the general character of simple rate laws given in textbooks (e.g., see Stumm and Morgan, 1981, p.90); as discussed in these textbooks, these rate laws are useful in evaluating rate constants and reaction order from given sets of experimental data. In many cases, the dissolution-rate response of a material may not be simple. In this case, a simple rate law with assumed constant parameter values for Q,  $N_H$ ,  $N_C$ ,  $N_O$ , and  $N_B$  that are evaluated by a numerical regression analysis over a set of experimental data would provide a predictive model, but the model would have large error. The measure of relatively large regression model error occurs for small ( $<0.5$ )  $R^2$  values. In these cases, based on analysis of variance, more complex models with cross-term variables and higher-order polynomials are commonly used in numerical regression analysis to obtain larger  $R^2$  values.

As discussed in Section 3.4.2.3, this has been the situation for numerical regression analysis performed over the sets of unirradiated  $UO_2$  and spent-fuel  $UO_2$  dissolution-rate data. One of the simple regression models of Section 3.4.2.3 starts with the familiar form of Eq. 3.4.2-22 and takes the logarithm of each side. For this case, when the parameters Q,  $N_H$ ,  $N_C$ ,  $N_O$ , and  $N_B$  are assumed constants to be evaluated by regression analysis, a linear dissolution model follows with their coefficients being data values from the variable set  $\{1/T, \ln[H^+], \ln[CO_3], \ln[O_2], \ln[Bu]\}$ , which is of the form

$$\ln(\rho V \cdot \underline{n}) = \ln A + Q/kT + N_H \ln[H^+] + N_C \ln[CO_3] + N_O \ln[O_2] + N_B \ln[Bu] \quad (3.4.2-23)$$

This regression model resulted in low  $R^2$  values when Q,  $N_H$ ,  $N_C$ ,  $N_O$ , and  $N_B$  are evaluated. The  $R^2$  value is significantly increased when the regression parameters are assumed functions of the variable set and product cross-terms and higher-order terms of the variable set are included in the regression model. For example, suppose the exponent parameter  $N_C$  of Eq. 3.4.2-22 is represented by the following function form

$$N_C = N_{C_0} + N_{CT}/T + N_{CH} \ln[H^+] + N_{CC} \ln[CO_3] + N_{CO} \ln[O_2] + N_{CB} \ln[Bu] \quad (3.4.2-24)$$

Similar function expressions can be written for exponent parameters  $N_H$ ,  $N_O$ , and  $N_B$ . Substitution of those expressions in Eq. 3.4.2-23 will clearly provide cross-terms (e.g.,  $\ln[CO_3] \cdot \ln[Bu]$ ) for a more complex regression model to fit the sets of dissolution-rate data. As discussed in Section 3.4.2.3, this more-complex regression model results in an improved fit with respect to a larger  $R^2$  value (see Eq. 3.4.2-27).

If development of the dissolution model were left at this point, it could be considered semi-empirical in that cross-terms were included without addressing their physical significance. In addressing this point, it is important to realize that dissolution-model development for a multicomponent solid (spent fuel) in a multicomponent, water-chemistry environment will be more complex than for a single-component solid in a single- or dual-

component water-chemistry environment. Certainly, if a simple physical model with some purported mechanistic basis “fits” the range of data sets available (has a large  $R^2$  value), that simple model should be acceptable. However, if the simple model has a low  $R^2$  value for the available data set, the simple model is normally rejected, irrespective of the purported physical significance, by statisticians as unsuitable for predicting response.

Put concisely, a simple regression model that does not “explain” the available data sets (has small  $R^2$  values) is not generally accepted as a predictive model, any more than is a regression model without some physical basis. Thus, in the ideal situation, development of a model must address both physical basis issues and predictive issues.

At present, the simple model of Eq. 3.4.2-22 has a strong physical basis from nonequilibrium thermodynamics and is similar to function forms proposed in the literature for chemical reactions. However, it does not have high predictive merit unless the exponent parameters are expressed as more general functions, as given by Eq. 3.4.2-24. Thus, physical-basis issues can be addressed by identifying chemical processes or mechanisms that are functionally described by exponent function forms, as given in Eq. 3.4.2-24. One such chemical process or mechanism exists in the form of chemical adsorption on the solid–liquid interface. The surface adsorption mechanism was identified in uraninite dissolution experiments performed by Grandstaff (1976). Grandstaff proposed that the uraninite dissolution-rate dependence on aqueous carbonate concentrations could be explained by using a Langmuir adsorption isotherm. According to Grandstaff, the Langmuir isotherm described the surface coverage as a function of carbonate solution concentration. Grandstaff linearized the Langmuir isotherm at low carbonate concentrations and proposed a linear relationship between surface coverage and concentration. However, at intermediate aqueous concentrations, the Tempkin adsorption isotherm is considered more descriptive of surface adsorption because it is expressed in terms of the thermodynamic chemical potential function (Hayward and Trapnell, 1964, pp. 165 and 176).

The form of the Tempkin adsorption isotherm is very similar to that given in Eq. 3.4.2-24. However, the Tempkin-isotherm-dependent function is the number of active surface sites  $\Theta_i$  for a reaction “i” involving a chemical species subset of  $[f]$  concentrations. An analysis to incorporate the number of active sites  $\Theta_i$  for multicomponent and the multireaction processes has been completed for fixed concentrations  $[f]$  reactions (see Aagaard and Helgeson, 1982). Aagaard and Helgeson showed that it is not expected, nor reasonable to expect, that stoichiometric coefficients in proposed chemical-reaction equations appear in regression analysis of data. The analysis steps to use Eq. 3.4.2-24 as a concentration-dependent exponent in Eq. 3.4.2-23 requires that the derivation of Eq. 3.4.2-14 through Eq. 3.4.2-18 be performed for the case with surface area subsets remaining as a functional dependence. Then the exponents  $N_H$ ,  $N_C$ ,  $N_O$ , and  $N_B$  of Eq. 3.4.2-22 and Eq. 3.4.2-23 would have an explicit linear dependence on the active site number density function  $\Theta_i$ .

For this linear  $\Theta_i$  dependence, the function form for  $N_H$ ,  $N_C$ ,  $N_O$ , and  $N_B$  would have a generalized form of the Tempkin isotherm given by Eq. 3.4.2-24. By substituting these forms into Eq. 3.4.2-23, cross-terms in the logarithmic functions (e.g.,  $\ln[O] \cdot \ln[BU]$ ) appear from the nonequilibrium thermodynamic model and the chemisorption model. Certainly other chemisorption isotherms could be used to derive function forms for regression models of available data. Presently, the use of a generalized Tempkin isotherm is considered consistent with surface complexation of carbonate and hydrogen ionic species of the aqueous solutions to form a change double layer at the surface of a  $UO_2$  solid. In the case of spent fuel, because the  $UO_2$  solid has fission products and actinides, both the number of active sites on the solid and the concentrations of radiolytic aqueous species are functionally dependent on an aggregate

variable such as spent fuel burnup. The problem is sufficiently complex that the explicit dependence of bulk aqueous concentrations and spent-fuel burnup can only be quantified by well-planned and -controlled experiment methods.

The results of regression analysis using these four models—the quadratic-concentration polynomial Onsager model, the first Butler–Volmer model with a quadratic-concentration polynomial, the second Butler–Volmer model (chemisorption-modified) with logarithmic-dependent concentrations, and the simplified chemisorption-modified Butler–Volmer model (Stumm–Morgan form; see Eq. 3.4.2-22) are discussed in Section 3.4.2.3. Each of these models is consistent with nonequilibrium thermodynamics concepts and provides function forms for regression analyses. These models do not contain an explicit dependence on radiolysis effects. Radiolysis effects from spent-fuel radionuclide decay will alter the concentrations of bulk-controlled concentrations in a boundary layer at the liquid–solid interface because of the deposition energy of radiation. The effects of this bulk to boundary-layer concentration are contained in the dissolution-rate data; however, no functional dependence because of radiolysis and these altered concentrations has been completed. Hence, this radiolysis problem remains to be explicitly represented in a functional model. However, because the dissolution data are obtained with radioactive spent fuel, a radiolysis dependence is implicitly contained as the burnup variable in the regression fits of data for each model.

### 3.4.2.3 Regression Fit of Data to Models

#### 3.4.2.3.1 UO<sub>2</sub> and Spent-Fuel Data

Using nonequilibrium thermodynamics, two different function forms were developed to describe the dissolution response of spent-fuel waste forms. Eq. 3.4.2-12 provides a classic Onsager relation for dissolution rate that is linearly related to the energy change of the solid dissolving into a liquid. This is expected to be descriptive of dissolution response close to thermodynamic equilibrium. Eq. 3.4.2-18 provides a classic Butler–Volmer relation for the dissolution rate that is exponentially related to the energy change of the solid dissolving into a liquid. Eq. 3.4.2-12 and Eq. 3.4.2-18 provide a consistent thermodynamic basis for the function forms of dissolution-rate models. Function forms based on both Eq. 3.4.2-12 and Eq. 3.4.2-18 were used for multilinear regression analyses (Davies and Goldsmith, 1972, Chapter 8; Draper and Smith, 1981) over subsets of unirradiated UO<sub>2</sub> and spent-fuel UO<sub>2</sub> dissolution-rate data. Several forms of these models have been examined, and some were included in previous updates and revision of this WFCR and are discussed in Appendix A of this section (Section 3.4.2 Appendix).

The current model has the Butler–Volmer form. By substituting the traditional chemical potentials that include a logarithmic dependence on activities or concentrations for the chemical potential changes in Eq. 3.4.2-18 (also see Eq. 3.4.2-22), the classic chemical kinetic rate law was derived:

$$\text{Rate} = k[A]^a[B]^b[C]^c \dots \exp(E_a/RT) \quad (3.4.2-25)$$

Burnup was also represented as a concentration term, because it is proportional to the aggregated production and concentration of fission products. For regression purposes, Eq. 3.4.2-25 was transformed by taking logarithms of each term and fitting that equation and allowing interaction and quadratic terms indicated by the data to improve the fit. The negative logarithms of the water-chemistry variables were used to be consistent with the standard definition of pH:  $-\log_{10}[H^+]$ .

### 3.4.2 Spent Fuel Dissolution Models

A modest refinement of model 3.4.2.20b in WFCR V1.2 (see Equation A3.4.2-3 in Appendix A) derives from an extensive analysis for performance assessment (PA) (Lawrence Livermore National Laboratory memorandum "Regression Fit of the  $\text{UO}_2$  and  $\text{UO}_2$  Spent-Fuel Matrix Dissolution Data for Use in the PA Model," William O'Connell to Ray Stout, LLYMP9805049, July 31, 1997). This refinement is the accepted intrinsic dissolution model for TSPA-VA at the time Version 1.3 of this report was published and is listed also in Appendix A. This model form includes a linear term of all variables, including the inverse temperature instead of its square and the linear LBU term with minimal loss in the correlation coefficient and adjusted for number of terms in the equation. The linear portion of the model is equivalent to the classic chemical rate law (Eq. 3.4.2-25). Eq. 3.4.2-26 (note base-10 logarithms) represents this current model:

$$\log_{10}(\text{Rate } \text{UO}_2) = a_0 + a_1 \cdot \text{IT} + a_2 \cdot \text{PCO}_3 + a_3 \cdot \text{PO}_2 + a_4 \cdot \text{PH} + a_5 \cdot \text{LBU} + a_6 \cdot \text{PO}_2 \cdot \text{IT} + a_7 \cdot \text{LBU} \cdot \text{IT} + a_8 \cdot \text{LBU} \cdot \text{PCO}_3 + a_9 \cdot \text{LBU} \cdot \text{PO}_2 + a_{10} \cdot \text{LBU} \cdot \text{PH} + a_{11} \cdot \text{PCO}_3^2 \quad (3.4.2.3-2)$$

Table 3.4.2.3-1 lists the coefficients (and their definitions) and the fitting statistics.<sup>1</sup> They are slightly different than those given for the TSPA-VA model in Appendix A because the four additional spent-fuel dissolution data for ATM-106 (30 MWd/kgU) are included. The new ATM-106 data were not available before the TSPA-VA model-acceptance deadline.

**Table 3.4.2-1 Coefficients and fitting statistics for current model**

Term	Coeff. (a <sub>i</sub> )	Standard Error	T-Value	Significance	Term Description
0 1	5.419896	1.253984	4.32	0.0001	Regression Constant
1 IT	-2464.539023	334.080576	-7.38	0.0001	Inverse Temperature (K <sup>-1</sup> )
2 PCO <sub>3</sub>	1.543336	0.415766	3.71	0.0006	[−Log <sub>10</sub> ] of Total Carbonate Conc. (mol/L)
3 PO <sub>2</sub>	-1.706529	0.530258	-3.22	0.0025	[−Log <sub>10</sub> ] of Oxygen Partial Pressure (atm)
4 PH	0.238402	0.056131	4.25	0.0001	[−Log <sub>10</sub> ] of Hydrogen Ion Conc. (mol/L)
5 LBU	-0.591871	0.744152	-0.80	0.4310	[+Log <sub>10</sub> ] of Burnup (MWd/kgM)
6 IT*PO <sub>2</sub>	395.742290	168.814229	2.34	0.0240	
7 IT*LBU	713.604985	186.289045	3.83	0.0004	
8 PCO <sub>3</sub> *LBU	0.158012	0.047410	3.33	0.0018	→2nd Order Interactions
9 PO <sub>2</sub> *LBU	0.163853	0.053389	3.07	0.0038	

<sup>1</sup> For the regression fit to this model, all 53 runs from Tables 2.1.3.5-4 and 4a in Section 2.1.3.5 were used. Because unirradiated  $\text{UO}_2$  represents zero or no burnup, logarithmic values of zero  $\text{UO}_2$  burnup used in this model would produce infinitely negative values for the terms in the regression fit of such data, and could not be allowed. For this reason, a value of 1 MWd/kgM ( $\log_{10}(1)=0$ ) was substituted for the burnup of  $\text{UO}_2$  in the regression data set for this model. Nominal initial pH values were used for the  $\text{UO}_2$  data, following the same approach used for the tabulated pHs of the spent-fuel data.

Term	Coeff. (a.)	Standard Error	T-Value	Significance	Term Description
10 PH*LBU	-0.264657	0.049583	-5.34	0.0001	
11 PCO3**2	-0.346206	0.076765	-4.51	0.0001	→Quadratic

No. cases = 53

 $R^2 = 0.8687$ 

RMS Error = 0.2223

Resid. df = 41

 $R^2\text{-adj.} = 0.8335$ 

Cond. No. = 199.3

The standard error provides, in the same units as the estimate, a measure of the uncertainty of the coefficient estimate. The fourth and fifth columns provide statistics related to the test of the hypothesis that the coefficient being estimated is zero. A high significance value indicates there is reason to believe that the coefficient is zero; thus, the term can be dropped from the model. Conversely, the closer to zero the significance value in the fifth column, the more important the term.

The table footnotes provide statistics to help assess the fit:

- The number of cases or runs are given.
- The residual degrees of freedom (cases less the number of terms in the model) are provided.
- The correlation coefficients  $R^2$  and adjusted  $R^2$  are numbers that indicate how well the fitted values produced by the model are correlated with the actual response values. An  $R^2$  value is always between zero and one. An adjusted  $R^2$  value (which is adjusted for the number of terms in the model) is less than  $R^2$ , but it is the better of the two for selecting the model with the most significant terms. The closer a value is to one, the better the fit. The best model is usually the one that maximizes both the  $R^2$  and adjusted  $R^2$  values.
- The root mean square (RMS) error is a measure, in the units of the fit, of the response variability that is not explained by the fit.
- The condition number can vary from one, which indicates a perfectly mathematical orthogonal experimental design, to infinity, which indicates a model containing singularities.

This model is the best representation of the existing data for PA purposes. It has a relatively high correlation coefficient; it is based on chemical and physical principles; and it is stable when used to extrapolate to variable values outside the original data space. This model, like the others, should be used only at alkaline conditions and not be used at acidic conditions (i.e., less than pH = 7, which is a chemically different regime).

Figure 3.4.2-1, Figure 3.4.2-2, and Figure 3.4.2-3 show the model (Eq. 3.4.2-20) calculations at aggressive conditions, using the coefficients in Table 3.4.2-1. Each of these three figures depicts conditions at a different pH, at 0.02 M total carbonate; the data are extrapolated beyond the currently available dissolution data to a burnup of 70 MWd/kgM and 100°C. Figure 3.4.2-1 is at a pH of 7. Figure 3.4.2-2 and Figure 3.4.2-3 are similar, but at pH = 8 and pH = 10, respectively. All figures are at atmospheric oxygen partial pressure. Figure 3.4.2-4 shows model results at aggressive "J-13-like" conditions, which means a pH of 7.7, total carbonate of 0.002 M, but including no calcium or silicate precipitating components. Calculations at even 0.30 atm oxygen, imitating radiolysis effects, show only a modest increase in dissolution rates.

### 3.4.2 Spent Fuel Dissolution Models

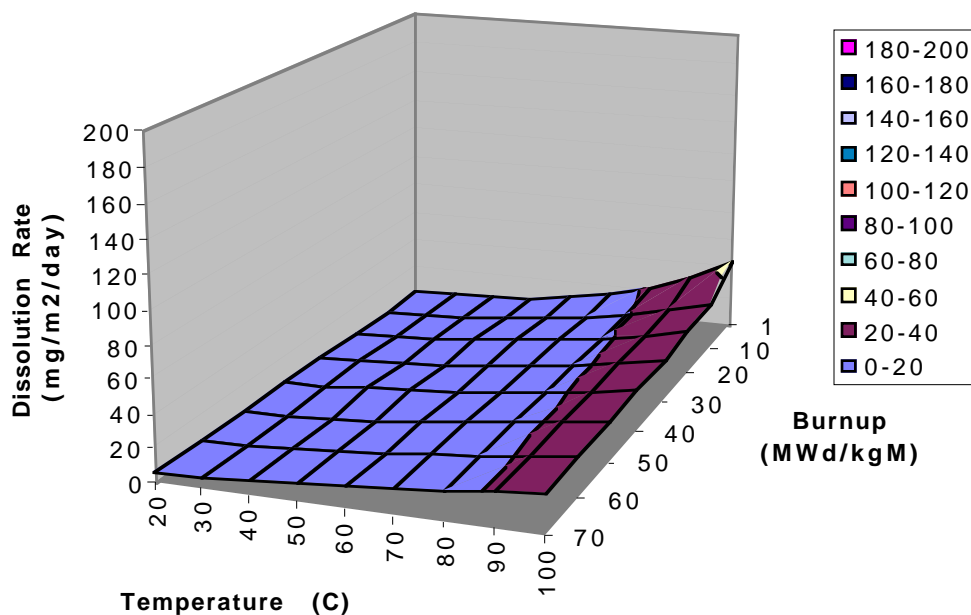


Figure 3.4.2-1 Dissolution rate at pH = 7, atmospheric oxygen, and 0.02M total carbonate [LL980912251031.053]

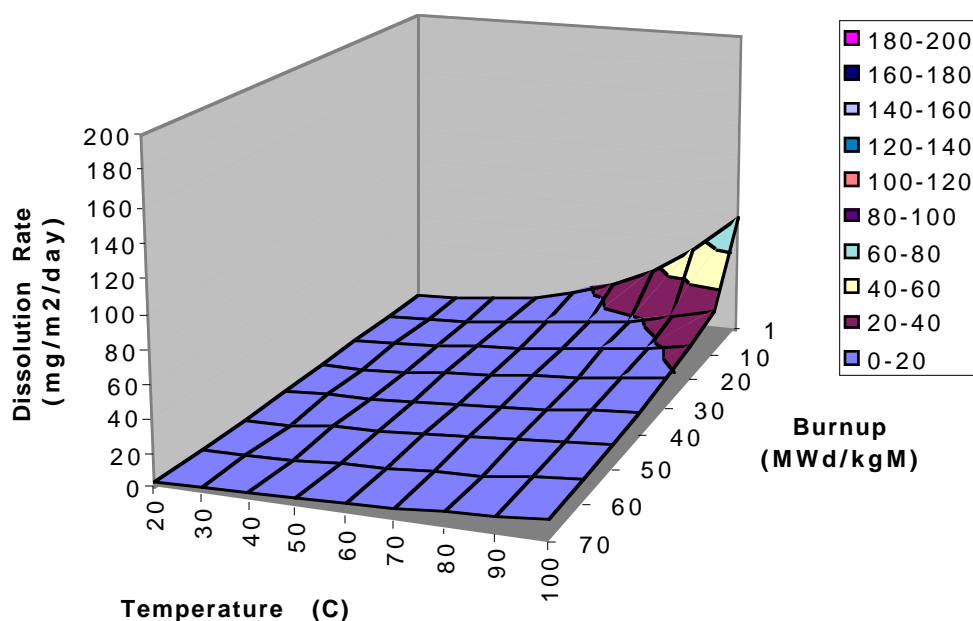


Figure 3.4.2-2 Dissolution rate at pH = 8, atmospheric oxygen, and 0.02M total carbonate [LL980912251031.053]

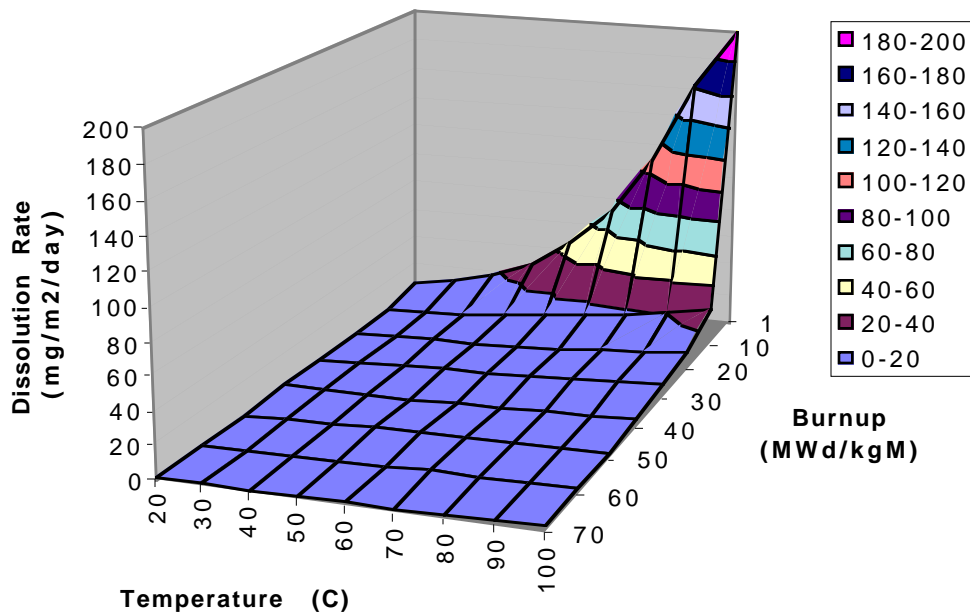


Figure 3.4.2-3 Dissolution rate at pH = 10, atmospheric oxygen, and 0.02M total carbonate [LL980912251031.053]

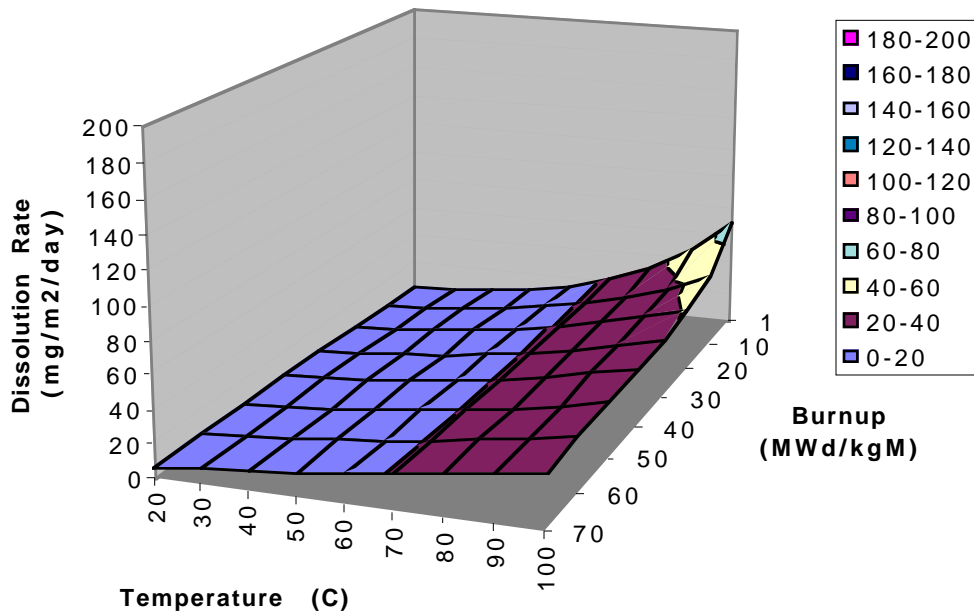


Figure 3.4.2-4 Dissolution rate at J-13 conditions of pH = 7.7 and 0.002M carbonate [LL980912251031.053]



### 3.4.2 Spent Fuel Dissolution Models

#### 3.4.2.3.2 U<sub>3</sub>O<sub>8</sub> Data

For the higher oxide data shown in Table 2.1.3.5-5, only the 14 U<sub>3</sub>O<sub>8</sub> dissolution rate data were modeled. Because the UO<sub>3</sub>·H<sub>2</sub>O dissolved so rapidly, their dissolution rates are estimates or minima and not appropriate for modeling. As with the UO<sub>2</sub> and spent-fuel dissolution data, different approaches to U<sub>3</sub>O<sub>8</sub> dissolution modeling are being explored. Here the classic, observed chemical kinetic rate law was used (Eq. 3.4.2-25).

Model parameters are presented, based on the pHs of the original carbonate solutions before contact with the samples, as used previously for the UO<sub>2</sub> and spent-fuel data. The pHs of the fresh-carbonate-leaching solutions are probably more representative of the pH at the sample than the pH of the leachate-analysis sample that has been exposed to dissolved CO<sub>2</sub> from the air.

Using the pHs of the prepared carbonate solutions given in the Table 2.1.3.5-5, the following equation is obtained from regression analysis: U<sub>3</sub>O<sub>8</sub> (carbonate soln. pHs):

$$\log_{10}(\text{Rate})\{\text{mgU}/\text{m}^2\cdot\text{day}\} = a_0 + a_1 \cdot \text{PCO}_3 + a_2 \cdot \text{PHC} - a_3 \cdot \text{IT} \quad (3.4.2-27)$$

with the coefficients and regression statistics shown in Table 3.4.2-2.

**Table 3.4.2-2 Linear-dissolution model for U<sub>3</sub>O<sub>8</sub> at atmospheric oxygen**

	Term	1. Coefficient (a <sub>i</sub> )	2. Standard Error	3. T-Value	4. Significance
0	1	7.950863	1.433419	—	—
1	IT	-1333.106149	337.537767	-3.95	0.0027
2	PCO <sub>3</sub>	-0.649162	0.084716	-7.66	0.0001
3	PHC	-0.106466	0.094032	-1.13	0.2840

No. cases = 14

R<sup>2</sup> = 0.8757

RMS Error = 0.2924

Resid. df = 10

R<sup>2</sup>-adj. = 0.8384

Cond. No. = 44.47

As with the earlier UO<sub>2</sub> and spent-fuel dissolution data, the pH did not have much effect on the model; however, carbonate concentration—not temperature—had the strongest effect on the U<sub>3</sub>O<sub>8</sub> dissolution rate. The temperature had half the effect of carbonate concentration on the uranium-dissolution rate. The pH was only about one-sixth as effective as carbonate concentration in explaining the changes in U<sub>3</sub>O<sub>8</sub> dissolution rates. Leaving out the pH term had a negligible effect on the other regression coefficients and was absorbed in the constant: U<sub>3</sub>O<sub>8</sub> (carbonate soln. pHs):

$$\log_{10}(\text{Rate})\{\text{mgU}/\text{m}^2\cdot\text{day}\} = a_0 + a_1 \cdot \log_{10}[\text{CO}_3] - a_2 \cdot \text{IT} \quad (3.4.2-28)$$

with the coefficients and regression statistics shown in Table 3.4.2-3.

**Table 3.4.2-3 Linear-dissolution model for U<sub>3</sub>O<sub>8</sub> at atmospheric oxygen without pH**

	Term	1. Coefficient (a <sub>i</sub> )	2. Standard Error	3. T-Value	4. Significance
0	1	6.925056	1.124932	—	—
1	IT	-1307.384093	341.061156	-3.83	0.0028
2	PCO <sub>3</sub>	-0.648615	0.085794	-7.56	0.0001

No. cases = 14

R<sup>2</sup> = 0.8598

RMS Error = 0.2961

Resid. df = 11

R<sup>2</sup>-adj. = 0.8343

Cond. No. = 33.53

All three variables (i.e., temperature, pH, and carbonate concentration) show significant interaction. A five-term equation, with a correlation coefficient of 0.95, that includes a constant, the three possible interaction terms, and a quadratic pH term (all nonlinear) improves the fit significantly. However, this equation is not suitable as a model because of its high degree of nonlinearity and its propensity to predict unrealistic dissolution rates outside the existing data space.

#### **3.4.2.4 Aqueous-Release-Rate Response for Spent Fuels**

This subsection discusses models for the aqueous release of radionuclides from spent fuel. In the following text, the modeling will address quasi-steady-rate responses only and, for the most part, will provide bounding estimates for the concentrations of radionuclides in the quantity of water flowing past the wetted spent-fuel surface. For purposes here, the release rate for a particular radionuclide species is defined as the aqueous concentration of the radionuclide (mass/volume of liquid) multiplied by the flow rate of the liquid (volume of liquid/unit time). The concentration will have additive components of “in-solution” and colloidal masses.

The release-rate response of radionuclides from spent fuels is complex. The release rate depends functionally on the following:

- Volume flow rate of the contacting water
- Intrinsic dissolution rate due to the chemistry of the water wetting the spent fuel
- History and current values of environmental variables surrounding and adjacent to the spent fuel
- Precipitation and colloidal kinetics of dissolved spent fuel in the adjacent water
- Adsorption kinetics of radionuclides on available surfaces
- Existing oxidation phase/alteration state of the spent fuel

Relating to these functional dependencies, Section 3.4.2.3 described a model for the intrinsic dissolution rate for a prescribed subset of aggressive water chemistries, environmental variables of explicit temperature and implicit spent-fuel radiation field, and a limited subset of different  $\text{UO}_2$  spent fuels. This dissolution model had function forms derived from nonequilibrium thermodynamics, and parameters of the function forms were evaluated by regression analyses over subsets of experimental dissolution-rate data. The dissolution rate is a fundamental component of the release rate because the dissolution rate provides a bounding estimate for the concentrations of the high-soluble radionuclides for a thick-film quantity of water flowing past a wetted spent-fuel surface. This statement will be substantiated in subsequent discussion. The other functional dependencies of the release-rate response are not well represented or isolated by available models or available experimental data. It is for this reason that a bounding approach is being used to develop a model of release-rate response.

The mass-balance equation is the basis of the following release-rate model for radionuclides being transported in water from a mass (or volume) of wetted spent fuel. The mass-balance equation, as written here, will initially contain expressions for all the functional dependencies discussed previously. However, because detailed models for each of these functional dependencies are not known, bounding approximations will be assumed to simplify and uncouple expressions in the mass-balance equations for the restricted conditions of quasi-steady-rate responses. This approach to model development will provide equations

### 3.4.2 Spent Fuel Dissolution Models

with parameters that can be evaluated from the available, but limited, experimental data obtained from the fully saturated testing and from the unsaturated testing performed on spent fuels.

The mass-balance equation, as written below, describes the time rate of change of a generic radionuclide in an arbitrary volume of fluid  $V_F$  with fluid-flow surface  $A_F$ . The fluid has an arbitrary (space  $\underline{x}$  and time  $t$  dependent) velocity field  $\underline{v}(\underline{x}, t)$  in contact with spent-fuel surfaces  $A_S$  and adsorption surfaces  $A_A$ . The concentration of a generic “in-solution” radionuclide is denoted by a density distribution function  $C(\underline{x}, t, \underline{v}_C)$ , where  $\underline{x}$ ,  $t$ , and  $\underline{v}_C$  are space, time, and diffusional velocity variables. The units of  $C$  are mass per unit fluid volume per unit diffusional velocity. The in-solution radionuclide denotes ionic, atomic, or molecular components with dimensions less than a few nanometers. If a particular in-solution concentration is to be denoted, the elemental symbol (or isotope symbol) will be enclosed in square brackets (e.g., the in-solution concentration of uranium is  $[U]$ ).

The colloidal radionuclide concentration is more complex and is generically denoted by  $K(\underline{x}, t, \underline{v}_K, \underline{a}, r)$ , where  $K$  is the density-distribution function for the number of colloids at point  $\underline{x}$  and time  $t$  with diffusional velocity  $\underline{v}_K$ , effective area and orientation  $\underline{a}$ , and effective areal radionuclide density per unit area on area  $\underline{a}$  of radionuclide  $r$ . For reasons of notational simplicity, it is assumed that only radionuclide colloids form and that each colloidal species comprises only one radionuclide elemental species. Thus, by assumption, no pseudo-colloidal kinetics are represented in the following analyses, and colloids with multiple radionuclide species on area  $\underline{a}$  are assumed not to form. These assumptions of no pseudo-colloids and no multispecies colloids are consistent with the limited test data. If additional data or new interpretations of existing data are advanced, these modeling assumptions can be readily revisited. The use of subspecies variables  $\underline{v}_C$ ,  $\underline{v}_K$ ,  $\underline{a}$ , and  $r$  to denote physical attributes of a particular subset for diffusion velocities and for generic colloids is notationally cumbersome. However, the notational scheme will be simplified as the model development progresses to reflect experimentally measured concentrations by integration over the domains of attributes variables  $\underline{v}_C$ ,  $\underline{v}_K$ ,  $\underline{a}$ , and  $r$ . These domains are considered broad number sets and are denoted by curly brackets (i.e.,  $\{\underline{v}_C\}$ ,  $\{\underline{v}_K\}$ ,  $\{\underline{a}\}$ , and  $\{r\}$ ). For example, the colloidal concentration of a generic radionuclide at a given diffusion velocity  $\underline{v}_K$  is given by the integration of the density distribution  $K$  times the two attributes variables over their attribute domains. This is denoted in different ways, depending on the context of the discussion:

$$K_v(\underline{x}, t, \underline{v}_K) \equiv \overline{a r K} \equiv \int_{\{\underline{a}\}} \int_{\{r\}} \underline{a} r K(\underline{x}, t, \underline{v}_K, \underline{a}, r) d\underline{a} dr \quad (3.4.2-29)$$

Similarly, the in-solution concentration of a generic species for all diffusional velocities is given by the integration of density distribution  $C$  times the diffusional velocity attribute over its domain

$$\overline{C}(\underline{x}, t) \equiv \int_{\{\underline{v}_C\}} C(\underline{x}, t, \underline{v}_C) d\underline{v}_C \quad (3.4.2-30)$$

Likewise, the colloidal concentration of a generic species for all generic diffusional species is given by the integration

$$\overline{K}(\underline{x}, t) \equiv \int_{\{\underline{v}_K\}} K_v(\underline{x}, t, \underline{v}_K) d\underline{v}_K \quad (3.4.2-31)$$

From the last two equations, the averaged diffusional velocities for in-solution and colloidal concentrations  $\bar{v}_C$  and  $\bar{v}_K$  are defined from the following expressions

$$\bar{v}_C \bar{C} \equiv \overline{v_C C} \equiv \int_{\{v_C\}} v_C C(x, t, v_C) dv_C \quad (3.4.2-32)$$

and

$$\bar{v}_K \bar{K} \equiv \overline{v_K K} \equiv \int_{\{v_K\}} v_K K(x, t, v_K) dv_K \quad (3.4.2-33)$$

In the preceding, the radionuclide-decay / growth, exponential-time responses are implicitly imbedded in the inventory terms. For short-term analysis of experiments, these decay / growth responses can be neglected in the following.

Using the preceding notation for concentrations, the aggregate, mass-balance equation for an arbitrary generic radionuclide can be written as

$$\begin{aligned} & \int_{V_F} \partial_t \bar{C} + \partial_t \bar{K} dV_F + \int_{A_F} (v_F + \bar{v}_C) \cdot \underline{n}_F \bar{C} + (v_F + \bar{v}_K) \cdot \underline{n}_F \bar{K} dA_F \\ &= \int_{A_S} \rho_C v_S \cdot \underline{n}_S + \bar{v}_K \cdot \underline{n}_S \bar{K} dA_S - \int_{A_P} \bar{v}_C \cdot \underline{n}_P \bar{C} + \bar{v}_K \cdot \underline{n}_P \bar{K} dA_P \\ &- \int_{A_K} \bar{v}_C \cdot \underline{n}_K \bar{C} + \bar{v}_K \cdot \underline{n}_K \bar{K} dA_K - \int_{A_A} \bar{v}_C \cdot \underline{n}_A \bar{C} + \bar{v}_K \cdot \underline{n}_A \bar{K} dA_A \end{aligned} \quad (3.4.2-34)$$

which is a statement that the time rate of change for the total concentration in fluid volume  $V_F$  occurs from fluid concentrations transported through a fluid-flow boundary  $A_F$  with outward directed normal  $\underline{n}_F$ , from the congruent dissolution at velocity  $v_S$  of spent-fuel surface  $A_S$  with inward directed normal  $\underline{n}_S$  for generic species  $C$  where the solid has fractional mass density  $\rho_C$  for species  $C$ , from aggregated colloidal spallation and formation  $\bar{K}$  at the spent fuel surface area  $A_S$ , from precipitation kinetics of the in-solution and colloidal concentrations transported to all accessible precipitate surfaces  $A_P$  with outward directed normal  $\underline{n}_P$ , from interchange colloidal kinetics of the in-solution and colloidal concentrations transported to all accessible colloidal surfaces  $A_K$  with outward directed normal  $\underline{n}_K$ , and, finally, from all adsorption kinetics for both in-solution and colloidal concentrations transported to all accessible adsorption surfaces  $A_A$  with outward directed normal  $\underline{n}_A$ .

In the aggregate measure of total concentration, the interchange kinetics terms would determine the relative components rate values for the in-solution concentration  $\bar{C}$  and the colloidal concentration  $\bar{K}$ . However, the value of the total concentration, in-solution plus colloidal, would remain invariant with respect to all models for interchange kinetics. Thus, only the dissolution rate, the precipitation rate, and the adsorption rate integral terms add and/or subtract mass from the total concentration when represented as an aggregate measure of in-solution and colloidal components.

### 3.4.2 Spent Fuel Dissolution Models

When spent fuel is present and dissolving into solution under quasi-steady conditions, it is reasonable to assume that any precipitation- and adsorption-rate processes will be positive in the sense these processes will be subtracting mass from the solution. Given this assumption, it can be seen from Eq. 3.4.2-34 that a bounding model for the total concentration of a radionuclide in solution is provided by neglecting the precipitation and adsorption kinetic terms because these would subtract mass from the total concentration. Of course, for the highly soluble fission-product radionuclides and for cases of significantly high fluid-flow rates, the precipitation integral would be zero. Furthermore, the highly soluble radionuclides, for a bounding model, is assumed not to form colloidal species. Thus, Eq. 3.4.2-34 for a quasi-static-rate state will have bounding release-rate terms that depend on the areas of fluid flow  $A_F$  and spent fuel dissolution  $A_S$  only and would reduce to

$$\int_{A_F} (\bar{v}_F + \bar{v}_C) \cdot \underline{n}_F \bar{C} dA_F = \int_{A_S} \rho_C \underline{v}_S \cdot \underline{n}_S dA_S \quad (3.4.2-35)$$

Eq. 3.4.2-35 can be area-integrated over an inlet-fluid boundary  $A_F$  in and an outlet fluid boundary  $A_F$  out and for flows that have fluid velocities significantly greater than the diffusional velocities. The quasi-steady change in concentration between the inlet and outlet fluid boundaries becomes

$$\bar{C}_{out} - \bar{C}_{in} = 1/Q_F \int_{A_S} \rho_C \underline{v}_S \cdot \underline{n}_S dA_S \quad (3.4.2-36)$$

where the volumetric flow rate  $Q_F$  is defined as

$$Q_F \equiv \int_{A_F} \underline{v}_F \cdot \underline{n}_F dA_F \quad (3.4.2-37)$$

For quasi-steady flows,  $Q_F$  has the same value at the inlet and outlet areas.

Eq. 3.4.2-36 is used to evaluate the dissolution rate and/or the dissolution velocity  $\underline{v}_S$  for the flow-through testing experiments when solid area  $A_S$  is assumed not to evolve in time. In these tests, the flow rate  $Q_F$  is controlled, the dissolution area is measured, and the water chemistry is prescribed at the inlet surface. Thus,  $\underline{v}_S$  can be evaluated for the prescribed set of testing conditions for which the precipitation, colloidal, and adsorption terms do not have contributions.

For these same conditions, the release-rate concentration for fluid flowing over exposed spent fuel in a waste package can be modeled by integrating Eq. 3.4.2-35 in a slightly different manner. For this integration, consider a uniformity thick film of fluid flowing on an arbitrary wetted path  $\ell(\underline{x})$  of exposed spent-fuel surface in a waste package. For a film thickness of  $h$  and an arbitrary film width  $w$  that also wets a width of fuel  $w$ , the change in averaged concentration of the film as the fluids flows from a point  $\underline{x}$  to neighboring point  $\underline{x} + d\underline{x}$  on wetted path  $\ell(\underline{x})$  is

$$\frac{\partial}{\partial \underline{x}} \bar{C}(\underline{x}) \underline{v}_F \cdot \underline{n}_F hw d\underline{x} = \rho_C \underline{v}_S \cdot \underline{n}_S w d\ell \quad (3.4.2-38)$$

In Eq. 3.4.2-38, the area  $A_F$  of the fluid flow is film thickness  $\times$  film width ( $hw$ ), and the dissolution area  $A_S$  is film width  $w \times$  the wetted path length ( $w d\ell$ ). This is ideally valid; however, from observation of dissolution samples and in interpretation of flow-through samples, it has been conjectured that the exposed surface is enhanced by the rapid

dissolution along grain boundaries up to a depth of three to five grain boundaries. Therefore, an empirical factor multiplied by the dissolution area should be applied. This factor would have a dependence on grain size; based on flow-through tests (Gray and Wilson, 1995), a value of four is recommended. A generic parameter  $\delta_s$  will be used for a value of this empirical factor in the following. The integration of Eq. 3.4.2-38 between arbitrary points  $\underline{x}_{in}$  to  $\underline{x}_{out}$  with a corresponding path length of  $\ell(\underline{x}_{out}) - \ell(\underline{x}_{in})$  is

$$\bar{C}(\underline{x}_{out}) - \bar{C}(\underline{x}_{in}) = \left( (\rho_C \underline{v}_S \cdot \underline{n}_S \delta_s w) / (\underline{v}_F \cdot \underline{n}_F h w) \right) (\ell(\underline{x}_{out}) - \ell(\underline{x}_{in})) \quad (3.4.2-39)$$

Equation 3.4.2-39 evaluates the change in concentration as fluid flows past and dissolves spent fuel with a wetted contact length of  $\ell(\underline{x}_{out}) - \ell(\underline{x}_{in})$ . For waste packages with horizontally emplaced fuel rods, the contact length would be the crack opening of the failed rods in a radial direction. For those cases that may be conjectured in which the generic radionuclide concentration evaluated by Eq. 3.4.2-39 exceeds a solubility limit, it is recommended that the outlet concentration be limited such that

$$\bar{C}(\underline{x}_{out}) \leq C_{\text{solubility limit}} \quad (3.4.2-40)$$

A colloidal-release-concentration expression that is an analog to Eq. 3.4.2-39 exists for the case of colloidal spallation and formation adjacent to the surface  $A_s$ . It is given by

$$\bar{K}(\underline{x}_{out}) - \bar{K}(\underline{x}_{in}) = \left( (\underline{v}_K \cdot \underline{n}_S \bar{K} w) / (\underline{v}_F \cdot \underline{n}_F h w) \right) (\ell(\underline{x}_{out}) - \ell(\underline{x}_{in})) \quad (3.4.2-41)$$

In some conjectured situations, there is a potential for a fixed volume  $V_F$  of fluid to be in constant contact with spent fuel. This situation corresponds to the fully saturated tests on spent fuels performed by Wilson (1990) and possibly in the alteration layer of the unsaturated tests (Finn et al., 1997). In these Wilson tests, the highly soluble fission-product radionuclides did not appear to exceed solubility limits. However, the actinide radionuclides did attain constant total concentration values, which, for release rate modeling purposes, will be taken as effective release concentrations and generically denoted as  $C_{erc}$  obtained from fully saturated test by Wilson (1990) are for in-solution plus colloidal concentration. For most cases, the colloidal components were small. For a quasi-steady-rate analysis of these tests, Eq. 3.4.2-34 reduces to

$$\begin{aligned} \int_{V_F} \partial_t \bar{C} + \partial_t \bar{K} dV_F &= \int_{A_S} \rho_C \underline{v}_S \cdot \underline{n}_S + \underline{v}_K \underline{n}_S \bar{K} dA_S \\ - \int_{A_P} \underline{v}_C \cdot \underline{n}_P \bar{C} + \underline{v}_K \cdot \underline{n}_P \bar{K} dA_P &- \int_{A_K} \underline{v}_K \cdot \underline{n}_K \bar{C} + \underline{v}_K \cdot \underline{n}_K \bar{K} dA_K \end{aligned} \quad (3.4.2-42)$$

where surface adsorption is assumed to be zero for this quasi-steady rate analysis. For highly soluble fission products, no colloidal and no precipitation kinetic is assumed, and for constant area of spent fuel  $A_s$  the rate of change in radionuclide concentration is a constant that depends proportionally on the dissolution rate; thus,

$$\bar{C}(t) = \frac{1}{V_F} \int_{V_F} \bar{C}(\underline{x}, t) dV_F = (\rho_C \underline{v}_S \cdot \underline{n}_S A_s / V_F) t \quad (3.4.2-43)$$

### 3.4.2 Spent Fuel Dissolution Models

where the initial concentration at time zero is taken as zero. In applications, the surface area  $A_s$  should be multiplied by the empirical  $\delta_s$  parameter to have a bounding model.

For actinide radionuclides, where precipitation and some colloidal kinetics are occurring, Eq. 3.4.2-42 requires additional assumptions to constrain and formulate a model. From the experimental data (Wilson, 1990), the total concentration of  $(\bar{C} + \bar{K})$  attains an effective release concentration  $C_{erc}$ ; thus, the value of the concentration-rate integral over fluid volume  $V_F$  (first integral expression in Eq. 3.4.2-42) after this time is zero, and

$$\bar{C}(t) + \bar{K}(t) = C_{erc} \text{ for } t \geq t_{erc} \quad (3.4.2-44)$$

where  $t_{erc}$  is the time determined from experimental data when the total concentration  $(\bar{C} + \bar{K})$  is less than  $C_{erc}$ . Based on results of experiments (Wilson, 1990), the time interval  $(0, t_{erc})$  is on the order of days or weeks for these fuel-area-to-water-volume ratios; thus, the value of  $t_{erc}$  can, for most cases, be set to zero. This is bounding because, for times  $t$  less than  $t_{erc}$ , the total concentrations  $\bar{C} + \bar{K}$  is less than  $C_{erc}$ .

From Eq. 3.4.2-42, the preceding experimentally based assumption that the left-side term for concentration changes is zero means that the sum of terms on the right is also zero. Thus, for quasi-steady rates and fixed fluid volumes, the rate of spent-fuel dissolution and colloidal spalling is equal to the rate of precipitation and colloidal kinetics. Although it has not been explicitly stated previously, it will be assumed that the dissolution process is such that the spent-fuel radionuclides of the spent fuel dissolve directly to in-solution concentrations and add to only  $\bar{C}$  at the surface of the spent fuel. To maintain quasi-steady constant  $\bar{C}$ , the precipitation and colloidal kinetic terms on neighboring surfaces  $A_P$  and  $A_K$  must balance this dissolution rate; thus

$$\int_{A_P} \underline{v}_C \cdot \underline{n}_P \bar{C} dA_P + \int_{A_K} \underline{v}_K \cdot \underline{n}_K \bar{C} dA_K = \int_{A_S} \rho_C \underline{v}_S dA_S \quad (3.4.2-45)$$

Similarly, the rate of aggregated colloidal interchanges to surfaces  $A_P$  and  $A_K$  must balance the spallation and formation rate of aggregated colloidal increase. Thus,

$$\int_{A_P} \underline{v}_K \cdot \underline{n}_P \bar{K} dA_P + \int_{A_K} \underline{v}_K \cdot \underline{n}_K \bar{K} dA_K = \int_{A_S} \underline{v}_K \cdot \underline{n}_S \bar{K} dA_S \quad (3.4.2-46)$$

Without additional microscopic details, the precipitation and colloidal surface kinetic rates on surfaces  $A_P$  and  $A_K$  in Eq. 3.4.2-45 and Eq. 3.4.2-46 cannot be partitioned into separate components of the dissolution-rate concentration from surface  $A_S$ . Nonetheless, for quasi-steady state release-rate processes, these equations do show that, for fixed fluid-volume processes, the concentrations of both in-solution species  $\bar{C}$  and aggregated colloidal species  $\bar{K}$  are constants for quasi-static rate processes. Quasi-static rate processes are attainable in a short period of elapsed time when the fluid volume  $V_F$  wetting the spent-fuel surface is small in thickness relative to a length-scale metric of the spent-fuel surface. Hence, for thin film flows or stagnated thin-wetting films, dissolution on surface  $A_S$  potentially would be immediately followed by precipitation and colloidal kinetic processes in the wetted film adjacent to a spent-fuel surface  $A_S$ . This will be assumed case for the analysis

in the following paragraphs. This analysis will result in a bounding model for the release-rate measurements performed in the unsaturated / drip testing on spent fuels that are briefly discussed in the following paragraph.

The unsaturated / drip test is a closed-vessel, 100% humidity experiment. The closed vessel contains fragments of spent fuel placed in a Zircaloy™ tube; an equilibrated, J-13 water is dripped onto the spent-fuel surface. During the first couple of years, the drips flowed over a visually unaltered spent-fuel surface. Release rates were measured for the total in-solution and colloidal concentrations that were transported to an outlet basin of the vessel. These concentrations also include the mass contribution that was adsorbed onto the surface of the outlet vessel. This total concentration is the measured release rate for the drips flowing past the mass of spent fuel in the Zircaloy™ tube. The concentrations are being measured approximately every two to three months for the high-drip-rate tests and slightly less often for the low-drip-rate tests. After approximately a year and a half to two years, a visible layer of alteration products was observed on the spent-fuel surface. These alteration products were precipitates containing fission products and actinide isotopes, not all of which have been fully identified. The alteration layer is highly porous and appears somewhat as a fibrous mat of precipitation species that adhere to the wetted spent-fuel surface.

The following simplified analysis and model of these unsaturated / drip tests has several assumptions. For the first assumption, which covers the transient time period of approximately two years during which the surface visually appears unaltered, the release-rate concentration will be assumed to be given by Eq. 3.4.2-11 and Eq. 3.4.2-13 for the in-solution and colloidal concentrations, respectively. This is considered a transient period. However, a two-year time increment is small when compared to many thousands of years for a repository time period. Thus, the averaging of experimental release data for this time period would be an approximate way to provide nominal data for this initial, short-period, transient time period before the alteration layers form on the spent-fuel surface. The detailed analysis to evaluate the path length  $\ell(\underline{x}_{\text{out}}) - \ell(\underline{x}_{\text{in}})$  and to estimate consistent rate parameters from the high- and low-drip-rate tests has not been completed. This data evaluation requires some additional assumptions. For example, it appears that the high-drip-rate test had sufficient flow rate to pool around the spent-fuel surface in the Zircaloy™ tube. Thus, the high-drip-rate water remained in contact with the spent fuel longer (had a long residence-time interval) than did the low-drip-rate water. Concentrations estimated from the high-drip-rate would then be the bounding concentrations for release rates, independent of the path length and the flow rate. However, for lower drip rates, estimates of the path length and fluid-flow rates can be used to reduce the release concentrations. For example, it can be seen from Eq. 3.4.2-39 that, for high-flow rates ( $\underline{v}_F \cdot \underline{n}_F \cdot hw$ ), the release concentration is reduced. Note, however, that the release rate, which is concentration multiplied by flow rate, depends only on the dissolution rate and the path length. This initial unaltered surface-dissolution / release rate is also enhanced due to rapid release from gap- and grain-boundary radionuclide inventories. The use of the high-drip release data thus would incorporate approximately some nonhomogeneous spatial radionuclide densities into this transient release rate.

Following the transient-release-rate period, the spent-fuel surface is assumed to be altered, and a dense mat of precipitated products is assumed to be adhered to the spent-fuel surface. The porosity of this altered layer is assumed to be fully saturated with water, and the dissolution process is assumed to be actively reacting at the spent fuel surface  $A_s$ . This dissolution process beneath the alteration layer is assumed to be a quasi-steady-rate process in a stagnate (nonflowing) thin film of water. Thus, the concentrations of the in-solution and



### 3.4.2 Spent Fuel Dissolution Models

colloidal components are assumed to attain constant values within the alteration layer. Therefore, Eq. 3.4.2-44 for the total concentrations  $C_{erc}$  is assumed to be valid for the radionuclides in the water of the porous altered layer.

Next, the dripping water is assumed to flow on the exterior surface of the alteration layer, and transport of in-solution and colloidal radionuclides is assumed to occur by mass transport from the alteration layer into the moving drip of water flowing over the alteration layer. In the linear case of intersurface mass transfer, the rate of diffusion exchange (or with slight surface-to-surface fluid mixing) is represented as proportional to the difference between the concentration of the water in the alteration layer and the concentration of the water in the flowing film (or drip, in this case). The equation for this transport process is similar to that of Eq. 3.4.2-38, except that the right side is replaced with the diffusional exchange term, resulting in

$$\frac{\partial}{\partial \underline{x}} \bar{C}(\underline{x}) \underline{v}_F \cdot \underline{n}_F h w d \underline{x} = \lambda_C (\bar{C}_{film} - \bar{C}(\underline{x})) w d \ell \quad (3.4.2-47)$$

where  $\lambda_C$  is a mass-transfer coefficient to be evaluated from data of the high- and low-flow-rate saturated-drip tests. For quasi-steady rates, Eq. 3.4.2-47 can be integrated to

$$\bar{C}(\underline{x}_{out}) = \bar{C}_{film} (1 - \exp(-\Lambda_C (\ell(\underline{x}_{out}) - \ell(\underline{x}_{in})))) \quad (3.4.2-48)$$

where  $\Lambda_C$  is  $\lambda_C w / (\underline{v}_F \cdot \underline{n}_F h w)$ , and the concentration at the inlet point  $\underline{x}_{in}$  is assumed to be zero. Similarly, Eq. 3.4.2-41 for colloidal concentrations can be reformulated analogously, and the aggregated colloidal concentration transferred from the altered surface to the fluid is

$$\bar{K}(\underline{x})_{out} = \bar{K}_{film} (1 - \exp(-\Lambda_K (\ell(\underline{x}_{out}) - \ell(\underline{x}_{in})))) \quad (3.4.2-49)$$

where  $\bar{K}_{film}$  is the aggregate concentration of colloidal species in the water of the porous altered layer, and  $\Lambda_K$  is a transfer coefficient to be evaluated from the high- and low-saturated-drip data. The term  $\Lambda_K$  has the parameter  $\lambda_K$  and flow rate incorporated into it as  $\lambda_K w / (\underline{v}_F \cdot \underline{n}_F h w)$  and is similar to  $\Lambda_C$ .

The parameters  $\bar{C}_{film}$  and  $\bar{K}_{film}$  in Eq. 3.4.2-48 and Eq. 3.4.2-49 will be estimated with release-concentration data from the high-drip-rate tests. In the high-drip-rate tests, the water was observed to remain in contact with the altered layer on the fragments and to pool around the spent-fuel surface. Therefore, the residence-time interval of the water contact on the porous alteration layer is assumed to be sufficiently long that the concentrations of  $\bar{C}$  and  $\bar{K}$  of the water become equal to the concentrations  $\bar{C}_{film}$  and  $\bar{K}_{film}$  in the porous layer. A long residence-time interval is functionally equivalent to a long path-length interval in terms of the water concentrations becoming equal to the film concentrations, as expressed in Eq. 3.4.2-48 and Eq. 3.4.2-49. To defensibly evaluate the film concentration values, this assumption needs to be substantiated. Future experiments are planned to provide better estimates of the in-solution and colloidal concentrations parameters. For now, the available data of the high-drip-rate tests can be used to provide preliminary estimates of release concentrations.

For cases where the flow is in contact with the altered layer for shorter time intervals or, equivalently, shorter path lengths, then the concentration at the outlet point  $\underline{x}_{out}$  will be reduced. To calculate the reductions in concentrations with Eq. 3.4.2-48 and Eq. 3.4.2-49,

values for parameters  $\Lambda_c$  and  $\Lambda_k$  are required. In some cases, the release-concentration data from the low-drip-rate test can be used to estimate values of  $\Lambda_c$  and  $\Lambda_k$  for different radionuclides. This approach uses experimental data to provide release-concentration estimates for cases in which, in a horizontally emplaced waste package, the path-length interval is conjectured to be short (e.g., when cladding failure flaws are expected to be represented as narrow cracks along the axis of spent fuel rods).

The preceding, simplified release models for in-solution and colloidal concentrations have parameters that can be estimated from the limited data now becoming available from the unsaturated test methods. The observations and measurements of colloidal concentrations have greatly added to the complexity of developing waste-form release concentrations and release rates. The colloidal contributions to total concentration means that the release-concentration constraint imposed by idealized solubility limits is not strictly conservative. Of course, once the areal-size classes of colloids are established and validated, it may be possible to design filtration beds or adsorption materials to reduce the colloidal concentration near the waste package; solubility limits would then be applicable. This remains to be evaluated.

Finally, the alteration rate of spent fuel, in the preceding model of an altered layer, is assumed to progress at the rate of the dissolution velocity  $\underline{v}_s$ . Thus, the alteration life time of a spent-fuel fragment is roughly its half-size dimension divided by the magnitude of  $\underline{v}_s$ . Hence, the altered layer is assumed to continue to increase in thickness until all of the fuel particle is transformed into precipitation and colloidal alteration products. Subsequent to this alteration life-time interval, it will be assumed that the release concentrations from the fully altered spent-fuel fragments will be long path-length limited to the  $\bar{C}_{\text{film}}$  and  $\bar{K}_{\text{film}}$  concentrations for a time interval whose span is limited by the inventory of the radionuclide. For short path lengths of fluid flow, the release concentrations would be reduced with values calculated from Eq. 3.4.2-48 and Eq. 3.4.2-49. This means that, although the dissolution-rate process is assumed to be essentially congruent, the release concentrations and release-rate concentrations are not necessarily a congruent process with respect to the initial inventory of the radionuclides. This should pose no problem for the fission-product releases. The releases of fissile isotopes, released and remaining in the altered spent fuel, should be evaluated with respect to the history of their concentration over time.

### 3.4.2.5 Release-Rate Model and Preliminary Analysis of Radionuclide Release in Unsaturated Drip Tests

#### 3.4.2.5.1 Introduction

The focus of this modeling work is on the combined processes of oxidation, dissolution, and redeposition that take place when spent fuel is simultaneously exposed to air and to small amounts of groundwater. The concurrent incorporation of all of these processes distinguishes the *spent-fuel-release models for unsaturated conditions* presented in Section 3.4.2.5 from the *forward-dissolution-rate models for spent fuel* presented in Section 3.4.2.3 (Steward and Gray, 1994)

In the forward-dissolution rate models, the amount of oxygen is limited to that dissolved in water, the amount of flowing water is substantial, and the dissolved products become unavailable for participation in subsequent processes because of the high water-flow rates that rapidly transport dissolved products away from the site of reaction. The parameters of the unsaturated-release-rate models presented here are obtained by analyzing laboratory data from unsaturated, spent-fuel-release drip tests conducted at Argonne National

### 3.4.2 Spent Fuel Dissolution Models

---

Laboratory (Finn et al., 1994a, 1994b, 1995; Bates et al., 1995; personal correspondence, "Yucca Mountain Nuclear Waste Management Program Project Data Transmittal from the Unsaturated Spent Fuel Testing Task at the Argonne National Laboratory to the Waste Form Characterization Task at the Lawrence Livermore National Laboratory," LLYMP9808079, P.A. Finn, Argonne National Laboratory, to Ananda Wijesinghe, Lawrence Livermore National Laboratory, July 1997, MOL.19980820.0204).

In contrast, the basic kinetic-dissolution-rate parameter of the spent-fuel forward-dissolution-rate model is obtained from laboratory flow-through tests conducted under dissolution-rate-limited saturate- flow conditions at high water-flow rates (Steward and Gray, 1994). The unsaturated-release-rate models presented here have been developed to analyze and extract the minimum number of parameters that could represent the experimentally observed releases in drip tests. No attempt has been made to provide a detailed predictive capability based on more fundamental thermodynamic and kinetic properties of the underlying chemical species and reactions. Because the unsaturated-release-rate models incorporate dissolution as one of the active processes, detailed prediction of release rates from fundamental considerations will require, as one of the many required thermodynamic and kinetic parameters, use of the forward-dissolution rate of spent fuel obtained from saturated flow through dissolution tests. Furthermore, because secondary mineral phases are formed and redeposited from solution during spent fuel dissolution under unsaturated conditions at low flow rates, the release rates under these conditions are generally smaller by orders of magnitude than the are release rates predicted by a forward-dissolution-rate model for saturated high flow-rate conditions.

#### 3.4.2.5.1.1 *Physical Transport Phenomena*

The conceptual model for spent-fuel release under unsaturated low-flow-rate conditions divides the region occupied by the fuel fragments into two parts: a drip-water contact zone and a condensed vapor-water contact zone. In the drip-water zone, droplets of water intermittently drip onto the fuel fragments. When the small droplets contact the fuel fragments, they collect in patches of water on the surface and spread out into a thin film of water covering the fuel surface. In addition, localized patches grow in thickness as attached droplets until capillary forces are exceeded, at which point they drain along the surfaces of the fuel fragments in intermittent rivulets. Thus, most of this water quickly flows away from the collection of fuel fragments in rivulets while a small part of the water remains trapped by surface tension at the surfaces of contact between fuel fragments. The void space between fuel fragments that is not occupied by the flowing and/or trapped drip water at any instant is assumed to be occupied by air saturated with water vapor. Thus, the surface of the fuel fragment in this region is contacted by a film of condensed water vapor when it is not in contact with drip water.

In the vapor zone, which is not directly contacted by the dripping water, the fuel fragments exist in an atmosphere saturated by water vapor. The water vapor is assumed to condense on the surface of the fuel fragments to form a thin film of water that covers the entire external surface of each fuel fragment. Surface patches of water may also grow in thickness and coalesce into larger droplets on the surfaces of the fuel fragments that drain away as rivulets, in the same manner as in the drip zone but at a much slower rate.

The liquid film in the vapor-contact regions is assumed to flow under gravity along the surfaces of the fuel fragments. The rate of solution drainage will depend on the film thickness and drop size and on the combined action of surface tension, viscous, and gravitational

forces. A pool of drained water is always assumed to exist in the neighborhood of the fuel fragments; thus, there is always sufficient water to saturate the void spaces. Consequently, the rate of condensation of water on the fuel fragments is assumed to be exactly equal to the rate of drainage of water from the condensed vapor film, and the process is in a steady state with respect to the evaporation and condensation of water vapor and drainage of liquid water.

In the areas contacted by the drip water, the rapidity of drainage of the drops will not permit sufficient time for the chemical reactions of dissolution to act to any significant extent with the intermittent falling droplets. Instead, the significant processes will be the mixing of the drip water with the existing vapor-film water and the mechanical entrainment of colloidal particles from the contacted surface into the droplets as they drain away from the fuel fragments (Finn et al., 1994b). The degree of entrainment of the colloidal particles is likely to be much more significant in the drip region than in the vapor region because the drip water volume is locally much greater and faster flowing than is the water vapor-water film. When each drop has rapidly drained away, the dissolution process reverts to that of a vapor test. In essence, the drip-region behaves in a manner similar to that of the vapor region with the addition of short periods of rapid transport and liquid mixing that coincide with the release of a drop onto the fuel fragments. In this model of release under unsaturated-drip conditions, the differences in chemistry will become evident primarily in the change in chemistry of the residual liquid film along the path of passage of the drip water.

In both regions, the water in the films will react with the fuel fragments and will diffuse into their interiors. However, unlike the surfaces exposed only to water vapor, the surfaces contacted by the dripping water will also be affected by reactions with chemical components dissolved in the original groundwater. Some of the reactants will dissolve and diffuse back into the water film so that the film will consist of a solution of water and dissolution products.

#### *Chemical Transformation Phenomena*

The chemical reactions between the fuel and the water contacting the fuel fragments transform the fuel-fragment surfaces through a sequence of chemical transformations involving the following:

1. Oxidation to more soluble phases
2. Dissolution and removal of the oxidized phases
3. Precipitation of secondary mineral phases from solution
4. Sorption of colloidal matter in the solution phase
5. Redissolution of the secondary mineral phases
6. Reprecipitation as other alteration mineral phases

These complex transformations occur not only at the nominal exposed surface of the altering fuel fragment, but also to some distance into the interior of fuel fragment along grain boundaries that dissolve preferentially. The paragenetic sequences observed in both natural and experimental systems follow the general trend of uranium dioxide  $\Rightarrow$  uranyl oxide hydrates  $\Rightarrow$  alkali- and alkali-earth uranyl oxide hydrates  $\Rightarrow$  uranyl silicates  $\Rightarrow$  alkali- and alkaline-earth uranyl silicates + palygorskite clay. The specific mineral-phase sequence usually observed is uranium dioxide  $\Rightarrow$  dehydrated schoepite compregnacite + becquerelite  $\Rightarrow$  soddyite  $\Rightarrow$  boltwoodite + uranophane + palygorskite clay (Wronkiewicz, 1977).

### 3.4.2 Spent Fuel Dissolution Models

Observation of the mineral transformations that take place in the drip tests indicate that the dissolved minerals in the incoming groundwater would affect only the surfaces directly contacted by the drip water; this effect is significant only at relatively high flow rates that bring substantial amounts of these dissolved minerals. The dominant mineral phases observed in these tests over approximately 3.5 yr are given in the order in which they form in Table 3.4.2.5-1 (Finn et al., 1995; Bates et al., 1995; personal correspondence, "Yucca Mountain Nuclear Waste Management Program Project Data Transmittal from the Unsaturated Spent Fuel Testing Task at the Argonne National Laboratory to the Waste Form Characterization Task at the Lawrence Livermore National Laboratory," P.A. Finn, Argonne National Laboratory, to Ananda Wijesinghe, Lawrence Livermore National Laboratory, July 1997). The alkali- and alkaline-earth uranyl silicates represent the long-term solubility-limiting phases for uranium in these tests and in natural uranium deposits in natural oxidizing systems. From this table, one can see that the mineral transformations that occur under vapor test (condensed vapor–water flow only) and low-drip test (condensed vapor–water and low-drip water-flow rate) conditions are similar over the entire time period; however, they are significantly different from those of the high-drip test (condensed vapor–water and high-drip water-flow rate), particularly at late times. Accordingly, the assumption that the same mineral phases form over the entire time period in vapor and low-drip conditions may be used to simplify and consolidate the analysis models for these two conditions.

**Table 3.4.2-4 Spent-fuel transformation mineral phases in vapor and drip tests**

	Dominant Mineral Phases in Vapor and Drip Tests		
	Vapor Test	Low-Drip Test	High-Drip Test
1	Spent fuel (UO <sub>2</sub> )	Spent fuel (UO <sub>2</sub> )	Spent fuel (UO <sub>2</sub> )
2	Higher oxides	Higher oxides	Higher oxides
3	Schoepite	Schoepite	Schoepite
4			Compreignacite bequerelite
5			Soddyite
6			Boltwoodite

#### 3.4.2.5.2 Interpretive Mathematical Model

A mathematical model was developed by the Argonne National Laboratory to analyze the laboratory vapor and drip tests conducted on two standard spent fuels (ATM-103, ATM-106). The water used for these tests was J-13 well water equilibrated with tuffaceous rock from the Yucca Mountain potential repository site. As previously stated, this model is not intended to enable detailed predictions of the radionuclide releases as a function of the chemistry of the groundwater and the temperature of the environment. Instead, it was developed for the limited purpose of extracting the radionuclide concentrations released as a function of the drip-water rate for the given groundwater composition and temperature, while allowing for the formation of secondary minerals under unsaturated low-flow-rate conditions.

The experimental configuration adopted in the drip tests for evaluating radionuclide release from spent fuels under unsaturated hydrologic conditions is shown in Figure 3.4.2-5. In these tests, the experimental test condition was the same for the drip test and the vapor test except that, in the drip test, the drip groundwater had a different chemical composition

than did the initial water used in the vapor test. The interpretation of the drip tests is more complicated than the interpretation of the vapor tests because of the uncertainty regarding the spatial distribution of the drop water and the area of contact between the drop water with the spent-fuel fragments. A similar uncertainty would exist in application to a repository, in that the spatial extent of the drip water contact zone would have to be estimated.

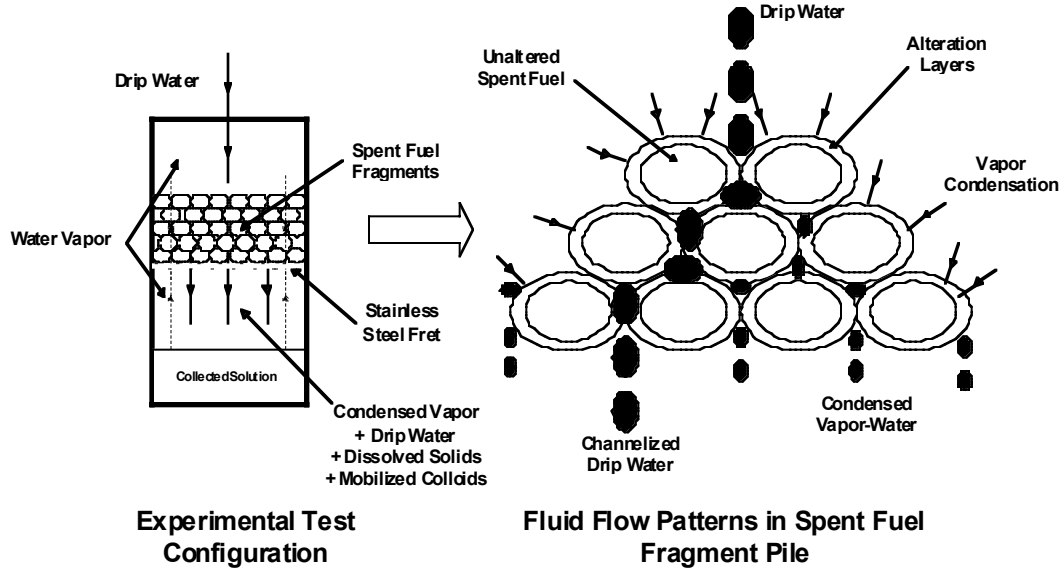


Figure 3.4.2-5 Experimental conditions for unsaturated drip tests

### 3.4.2.5.3 The Mass-Balance Equations

Using the notation developed in Section 3.4.2.4, the mass-balance equation for an arbitrary generic radionuclide in-solution species can be written as

$$\begin{aligned} \int_{V_F} \frac{\partial \bar{C}}{\partial t} dV_F + \int_{A_F} (\underline{v}_F + \underline{v}_{CF}) \cdot \underline{n}_F \bar{C} dA_F = \int_{A_S} \rho_{CS} \underline{v}_{CS} \cdot \underline{n}_S dA_S \\ - \int_{A_P} \underline{v}_{CP} \cdot \underline{n}_P \bar{C} dA_P + \int_{V_F} \mu_{CK} dV_F - \int_{A_A} \underline{v}_{CA} \cdot \underline{n}_A \bar{C} dA_A, \end{aligned} \quad (3.4.2-50)$$

where, the first term represents the rate of species mass accumulation in the fluid phase, the second term represents the net rate of efflux of the species across the transport surface  $A_F$ , the third term is the rate of species mass dissolving into the fluid phase, the fourth term is the rate of precipitation of species mass, the fifth term is the rate of transfer of mass between the in-solution dissolved species and the suspended-colloid phase expressed as an integral over the volume of the fluid phase, and the sixth term is the rate of adsorption of species mass on the solid surfaces exposed to the fluid phase. Likewise, the mass balance equation for the suspended-colloid species is given by the equation

### 3.4.2 Spent Fuel Dissolution Models

$$\int_{V_F} \frac{\partial \bar{K}}{\partial t} dV_F + \int_{A_F} (\underline{v}_F + \underline{v}_{KF}) \cdot \underline{n}_F \bar{K} dA_F = \int_{A_S} \rho_{CS} \underline{v}_{KS} \cdot \underline{n}_S dA_S$$

$$\int_{A_P} \underline{v}_{KP} \cdot \underline{n}_P \bar{K} dA_P - \int_{V_F} \underline{\mu}_{CK} dV_F - \int_{A_A} \underline{v}_{KA} \cdot \underline{n}_A \bar{K} dA_A, \quad (3.4.2-51)$$

where, the terms are directly analogous to the corresponding terms in the mass-balance equation for the dissolved in-solution species in the fluid phase. The third term is now interpreted to be the mass of colloidal particles released by the solid surfaces, while the precipitation and adsorption terms retain the conventional interpretations. Because the mass transfers between the in-solution and suspended-colloid species are equal, the fifth term is represented as the negative of the corresponding term in the in-solution species mass-balance equation. This mass transfer is the result of precipitation and adsorption of material from the in-solution material in the fluid phase onto the solid surfaces of the suspended colloid" and the dissolution and release of the material from the suspended colloids into the fluid phase. This term will be a sink of mass for the in-solution material if precipitation and adsorption exceed the rate of material dissolution and desorption from the suspended-colloidal particles; the term will be a source of mass if the reverse is true. Accordingly, a constitutive relation that reflects this two-way mass transfer may be written for the specific mass transfer term as

$$\mu_{CK}(t) \equiv \lambda_K \bar{K} - \lambda_C \bar{K} \frac{\bar{C}}{\rho_{CS}} \quad (3.4.2-52a)$$

$$= \lambda_K \bar{K} \left( 1 - \frac{\bar{C}}{C_{Km}} \right) \quad (3.4.2-52b)$$

where

$$C_{Km}(t) \equiv \frac{\lambda_K}{\lambda_C} \rho_{CS} \quad (3.4.2-53)$$

and  $\lambda_C$  and  $\lambda_K$  are the kinetic rate coefficients (1/day) for mass transfer from the fluid phase to the suspended colloids (due to precipitation and sorption) and from the suspended colloids to the fluid phase (due to dissolution and desorption), respectively.

The magnitude of the concentration  $C_{Km}$ , a parameter defined for convenience, may or may not exceed the in-solution species concentration  $\bar{C}$ . Therefore, this constitutive equation accommodates net mass transfer in either direction between the solution and colloidal phases. All of these material properties vary with changes in the materials' chemical compositions with time. Because the total surface area of the colloidal particles on which precipitation and sorption occur from solution is proportional to the number density of colloidal particles, and hence to the colloid mass concentration, the second term on the left side of Eq. 3.4.2-52a contains the product of the colloid mass concentration  $\bar{K}$  and the in-solution species concentration  $\bar{C}$ . Therefore, at low in-solution and colloid concentrations, this term will be small compared to the first term on the left side. Also, if the in-solution concentration  $\bar{C}$  is equal to  $C_{Km}$ , the left side of Eq. 3.4.2-52a/b will be zero, and there will be no net mass transfer between the in-solution and the suspended-colloid phases.

Eq. 3.4.2-50 and Eq. 3.4.2-51 can be expressed in the following, simpler lumped-parameter form by assuming that the variables are spatially uniform and that diffusive transport in the fluid phase can be neglected

$$V_F \frac{\partial \bar{C}}{\partial t} + v_F A_F \bar{C} = r_C A_S \left( 1 - \frac{\bar{C}}{C_{\max}} \right) + V_F \lambda_F \bar{K} \left( 1 - \frac{\bar{C}}{C_{Km}} \right), \quad (3.4.2-54)$$

$$V_F \frac{\partial \bar{K}}{\partial t} + v_F A_F \bar{K} = r_K A_S \left( 1 - \frac{\bar{K}}{K_{\max}} \right) - V_F \lambda_F \bar{K} \left( 1 - \frac{\bar{C}}{C_{Km}} \right). \quad (3.4.2-55)$$

In the two preceding equations, it has been assumed that no radioactive species existing in the spent-fuel are present in the incoming groundwater. Furthermore, the rate of mass dissolution from noncolloidal solid surfaces for in-solution species and the rate of colloid mass release from no-colloidal solid surfaces for the suspended-colloids have been defined by the expressions

$$r_C(t) = \rho_{CS} v_{CS}, \quad (3.4.2-56)$$

$$r_K(t) = \rho_{KS} v_{KS}. \quad (3.4.2-57)$$

In addition, equilibrium mass concentrations in the absence of convective and diffusive mass transport and mass transfer between in-solution and suspended-colloid species has been defined by

$$C_{\max}(t) \equiv \frac{r_C A_S}{v_{CP} A_P + v_{CA} A_A}, \quad (3.4.2-58)$$

$$K_{\max}(t) \equiv \frac{r_K A_S}{v_{KP} A_P + v_{KA} A_A}, \quad (3.4.2-59)$$

where the time dependence of these two parameters is explicitly shown to emphasize that all parameters appearing in these definitions vary as the chemical compositions of the materials change with time. Upon solving Eq. 3.4.2-54 and Eq. 3.4.2-55 for the in-solution and suspended-colloid mass concentrations, the total mass released  $\Delta M$  in an increment of time  $\Delta t$  can be computed from the general expression

$$\Delta M \equiv v_F A_F \bar{C}_T \Delta t. \quad (3.4.2-60)$$

where the total concentration  $\bar{C}_T$  of both in-solution and suspended colloidal species is defined by

$$\bar{C}_T \equiv (\bar{C} + \bar{K}). \quad (3.4.2-61)$$



### 3.4.2 Spent Fuel Dissolution Models

---

#### 3.4.2.5.4 Limiting Solutions

Useful limiting solutions can be derived from the preceding equations for certain limiting conditions that may be realized in experimental and field conditions. Several limiting solutions applicable to the unsaturated drip tests are developed in the following text. The first approximation made is to neglect the term that represents the precipitation and sorption of in-solution species mass on the colloid particles because this is a term of second-order of smallness in magnitude and is dominated by precipitation and sorption on the spent-fuel surfaces. Accordingly, Eq. 3.4.2-54 and Eq. 3.4.2-55 reduce to

$$V_F \frac{\partial \bar{C}}{\partial t} + v_F A_F \bar{C} = r_C A_S \left( 1 - \frac{\bar{C}}{C_{\max}} \right) + V_F \lambda_F \bar{K} , \quad (3.4.2-62)$$

$$V_F \frac{\partial \bar{K}}{\partial t} + v_F A_F \bar{K} = r_K A_S \left( 1 - \frac{\bar{K}}{K_{\max}} \right) - V_F \lambda_K \bar{K} . \quad (3.4.2-63)$$

#### 3.4.2.5.5 Pseudo-Steady-State Conditions

Very useful and tractable pseudo-steady solutions to these equations can be obtained if the convective velocities are sufficiently large for the transport terms (second terms) on the right sides of Eq. 3.4.2-62 and Eq. 3.4.2-63 to be much larger than the mass accumulation terms (first term) given by the time derivatives of the concentrations. Neglecting the time derivatives and solving the resulting two simultaneous algebraic equations for the in-solution and colloid-species mass concentrations gives the results

$$\bar{C} = \frac{r_C A_S + V_F \lambda_K \bar{K}}{[r_C A_S + v_F A_F C_{\max}]} C_{\max} , \quad (3.4.2-64)$$

and

$$\bar{K} = \frac{r_K A_S}{[r_K A_S + (v_F A_F + V_F \lambda_K) K_{\max}]} K_{\max} . \quad (3.4.2-65)$$

It important to recognize that, although subject to the pseudo-steady assumption, these expressions are valid for arbitrary in-solution and suspended colloid species mass concentrations in the fluid phase that may be sufficiently high for secondary phases to form and precipitate out of solution.

#### 3.4.2.5.6 Transport-Limited, Pseudo-Steady Conditions

The pseudo-steady solutions given by Eq. 3.4.2-64 and Eq. 3.4.2-65 can be further specialized for two limiting conditions with respect to the flow rate. For low water-flow rates, such as those encountered in certain *unsaturated drip tests*, Eq. 3.4.2-64 yields, for the suspended colloid concentration,

$$\bar{K} \approx K_{\max} , \quad (3.4.2-66a)$$

provided that the water flow rates are sufficiently small to satisfy

$$v_F A_F K_{\max} \ll r_K A_S , \quad (3.4.2-66b)$$

and the kinetic coefficient  $\lambda_K$  for mass transfer between the in-solution species and the suspended colloid satisfies

$$V_F \lambda_K K_{\max} \ll r_K A_S . \quad (3.4.2-66c)$$

Similarly, Eq. 3.4.2-65 yields, for the in-solution species mass concentration,

$$\bar{C} \approx C_{\max} , \quad (3.4.2-67a)$$

provided that the water-flow rates are sufficiently small to satisfy

$$v_F A_F C_{\max} \ll r_K A_S , \quad (3.4.2-67b)$$

and the kinetic coefficient  $\lambda_K$  for mass transfer between the in-solution species and the suspended colloid satisfies Eq. 3.4.2-66c.

The incremental mass released in a time  $\Delta t$  is now obtained by substituting the above results in Eq. 3.4.2-60

$$\Delta M \approx v_F A_F (C_{\max} + K_{\max}) \Delta t . \quad (3.4.2-68)$$

Under these very slow flow-rate *transport-limited conditions*, the colloid and in-solution-species concentrations are approximately equal to their equilibrium-mass concentrations  $K_{\max}$  and  $C_{\max}$  that are attained for equilibrium between the processes of dissolution/ colloidal-mass release from the spent-fuel surfaces and precipitation/ adsorption of the in-solution and suspended colloids from solution. These equilibrium-mass concentrations include the effects of all chemical interactions with the spent fuel and the water and, therefore, can be directly compared with the elemental solubilities previously used in total system performance assessment to bound the radioactive species mass releases.

#### 3.4.2.5.7 Dissolution and Colloidal Particle Release-Limited, Pseudo-Steady Conditions

For the opposite limit of high flow-rate *dissolution and colloid release-rate limited conditions*, Eq. 3.4.2-64 and Eq. 3.4.2-65 give

$$\bar{K} \approx \frac{r_K A_S}{v_F A_F} , \quad (3.4.2-69a)$$

provided that the water flow rates are sufficiently small to satisfy

$$v_F A_F K_{\max} \gg r_K A_S , \quad (3.4.2-69b)$$

and the kinetic coefficient  $\lambda_K$  for mass transfer between the in-solution species and the suspended colloid satisfies

$$v_F A_F K_{\max} \gg V_F \lambda_K K_{\max} . \quad (3.4.2-69c)$$

### 3.4.2 Spent Fuel Dissolution Models

---

Similarly, for this limiting condition, Eq. 3.4.2-65 yields for the in-solution species mass concentration

$$\bar{C} \approx \frac{r_C A_S}{v_F A_F}, \quad (3.4.2-70a)$$

provided that the water flow rates are large to satisfy

$$v_F A_V C_{\max} \gg r_C A_S, \quad (3.4.2-70b)$$

and the kinetic coefficient  $\lambda_K$  for mass transfer between the in-solution species and the suspended colloid satisfies Eq. 3.4.2-69c. The incremental mass  $\Delta M$  released in a time  $\Delta t$  given by Eq. 3.4.2-60 reduces to the form

$$\Delta M \approx (r_C + r_K) A_S \Delta t. \quad (3.4.2-71)$$

Because  $C_{\max}$  and  $K_{\max}$  are absent in these equations for  $\bar{C}$  and  $\bar{K}$ , no phenomena associated with the precipitation and sorption of secondary minerals are represented by these equations. These results are applicable to high flow-rate *flow-through dissolution tests*.

#### 3.4.2.5.8 Total Mass Release Rate for Separate Drip and Vapor Zones

The expressions developed in the preceding text for the in-solution and suspended-colloid species-mass concentrations under low-flow-rate and high-flow-rate conditions can be applied to repository and laboratory release-rate tests by separately identifying the drip-water contact and the condensed vapor-water contact zones in each case and applying the appropriate limiting equations to each zone. If the drip-water-contact-zone volume (and area) fraction is defined by  $f_d$ , the total mass  $\Delta M^a$  released from the vapor and drip zones in a given time increment  $\Delta t$  is given by

$$\Delta M \equiv (1 - f_d) A_F v_{Fv} (\bar{C}_v + \bar{K}_v) \Delta t + f_d A_F v_{Fd} (\bar{C}_d + \bar{K}_d) \Delta t \quad (3.4.2-72)$$

where the vapor-zone concentrations and drip-zone concentrations, separately identified by the subscripts  $v$  and  $d$ . They are given by Eq. 3.4.2-64 and Eq. 3.4.2-65, respectively, in the general case, provided the parameters are separately labeled with these subscripts and are evaluated separately for each zone.

The general expression for mass release given by Eq. 3.4.2-72 may be applied to unsaturated and saturated tests (by appropriately choosing the volume/area fraction  $f_d$ ) and to low flow-rate and high flow-rate conditions. For interpreting the drip tests, the drip-zone liquid-flow velocity can be expressed more conveniently in terms of the condensed vapor-water flow velocity  $v_{Fv}$  and the drip-water-volume flow rate  $q_d$  the equation

$$v_{Fd} \equiv v_{Fv} + q_d / (A_F f_d). \quad (3.4.2-73)$$

In summary, for conditions in which advective transport is sufficiently large for the advective mass transport to dominate the rate of mass accumulation in the liquid phase, the general expressions Eq. 3.4.2-64 and Eq. 3.4.2-65 give the variation of the in-solution and suspended-colloid film-mass concentrations with fluid flow rate while including the dissolution of spent fuel, formation of alteration products, and dissolution of the alteration

products. Only two time-varying constitutive properties appear in each equation for each of the in-solution and colloidal film-mass concentrations of a particular chemical element (i.e., the effective rate of dissolution/colloid release and the equilibrium film-mass concentration). Therefore, in interpreting mass-release data from drip tests using this interpretive model, the task is to determine the condensed vapor–water circulation rate  $v_{Fv}$ , the effective dissolution rates  $r_{Cd}$ ,  $r_{Cv}$  and  $r_K$ ,  $r_{Kv}$ , and the equilibrium film-mass concentrations  $C_{maxd}$ ,  $C_{maxv}$  and  $K_{maxd}$ ,  $K_{maxv}$  given the drip-water flow rate  $q$ , the incremental mass released  $M$  in the time increment  $t$ , the total transport surface area  $A_F$  (i.e., the total fuel-fragment surface area), and the drip-zone area fraction  $f_d$ . For an experiment that involves as many as 10 measured chemical elements, this is a feasible, but formidable, challenge.

#### 3.4.2.5.9 Total Mass Release Under Advective Transport-Limited Conditions

If the water flow rate is sufficiently low for the advective transport of mass to be the mechanism limiting mass release, Eq. 3.4.2-72 for the mass released simplifies to the form

$$\Delta M \equiv (1 - f_d) A_F v_{Fv} (C_{maxv} + K_{maxv}) \Delta t + f_d A_F v_{Fd} (C_{maxd} + K_{maxd}) \Delta t \quad (3.4.2-74)$$

that is independent of the effective rates of dissolution and is a function only of the equilibrium film-mass concentrations. This approximation is valid if the flow velocities is sufficiently small that Eq. 3.4.2-66b, Eq. 3.4.2-66c, and Eq. 3.4.2-67b are satisfied.

The mass released can be expressed in an even more convenient form if it is assumed that, for the flow rates satisfying Eq. 3.4.2-66b, Eq. 3.4.2-66c, and Eq. 3.4.2-67b, *the alteration products being formed are essentially the same in the vapor zone and in the drip zone*. Under this assumption, the equilibrium in-solution and colloidal film-mass concentrations would be the same in the drip zone and in the vapor zone, and Eq. 3.4.2-74 simplifies to the form

$$\Delta M \equiv (A_F v_{Fv} + q_d) (C_{max} + K_{max}) \Delta t \quad (3.4.2-75)$$

where, the separate subscripts for the drip and vapor zones have been dropped from the symbols for the equilibrium in-solution and colloidal film-mass concentrations.

Therefore, in interpreting mass-release data from drip tests using this advective, transport-limited, approximate model, the task is to determine the condensed vapor–water circulation rate  $v_{Fv}$ , the total equilibrium in-solution and colloidal film-mass concentration  $C_{Tmax} \equiv (C_{max} + K_{max})$ , given the drip-water flow rate  $q_d$ , the incremental mass releases  $M$  in the time increment  $t$ , and the transport surface area  $A_F$  (i.e., the total fuel-fragment surface area). Note that, in this approximation, *it is not necessary to independently specify the transport surface-area fraction  $f_d$*  because of the assumption that the same chemical transformations occur in the drip and vapor zones. When compared to the full interpretive model for mass release given by Eq. 3.4.2-73, the number of parameters that must be determined from the drip-test data is much smaller in this approximate model. These parameters are the single value of the condensed vapor–water circulation rate  $v_{Fv}$  and the total equilibrium film-mass concentration  $C_{Tmax}$  for each radionuclide at each measurement time.

#### 3.4.2.5.10 Mass Release Under Reaction-Rate–Limited Drip Zone and Advective Transport-Limited Vapor Zone

If the water drip rate is sufficiently high, and mass release is reaction-rate limited in the drip zone and advective transport-limited in the vapor zone, Eq. 3.4.2-72 for the mass released simplifies to the form

$$\Delta M \equiv (1 - f_d) A_F v_{Fv} (C_{\max v} + K_{\max v}) \Delta t + f_d A_F (r_{Cd} + r_{Kd}) \Delta t \quad (3.4.2-76)$$

that is independent of the equilibrium film-mass concentrations in the drip zone and the effective rates of dissolution and colloid release in the vapor zone. It is a function only of the total effective rate of dissolution and colloid release  $r_{Td} \equiv (r_{Cd} + r_{Kd})$  in the drip zone and of the total equilibrium in-solution and colloid mass concentration  $C_{T\max v} \equiv (C_{\max v} + K_{\max v})$  in the vapor zone. This approximation is valid if the flow velocities in the drip and vapor zones are such that conditions in Eq. 3.4.2-69b, Eq. 3.4.2-69c, and Eq. 3.4.2-50b are satisfied in the drip zone while conditions in Eq. 3.4.2-66b, Eq. 3.4.2-66c, and Eq. 3.4.2-67b are satisfied in the vapor zone. Further, if the flow domain is completely saturated, by setting  $f_d=1$ , one can eliminate the first term on the left side of Eq. 3.4.2-76 and recover the expression applicable to saturated high flow-rate flow-through dissolution tests. Under these circumstances, it is also likely that no alteration products would be formed, and the effective dissolution rate is the dissolution rate for the spent fuel itself.

#### 3.4.2.5.11 Numerical Methodology for Determining Release-Rate Model Parameters from Unsaturated Drip-Test Data

The release rate model presented in the preceding section (Section 3.4.2.4) was used to extract data from the unsaturated drip tests performed at the Argonne National Laboratory. In these tests, two standard fuel types (ATM-103 and ATM-106) were tested at three levels of drip rate in zero-drip, low-drip, and high-drip –rate drip tests. The method adopted to fit the data was to assume that the effective dissolution rates and equilibrium film-mass concentrations defined as model parameters in the unsaturated release-rate model varied with fuel type, released chemical element, experimental time, and drip rate. Even though the effect of drip rate on mass transport was explicitly represented in the model, additional dependence of these two constitutive parameters on drip rate (through effects of dissolved chemicals present in the incoming drip water) was recognized because different types of alteration minerals were formed in the later stages of these experiments. As shown in Table 3.4.2-4, the high drip-rate tests, in particular, showed the formation of boltwoodite as the dominant mineral at long times, whereas schoepite was the predominant mineral formed in the vapor and low-drip tests. These differences in long time response were particularly important because the response at long times, and possible emergence of these minerals as stable end states, are of greater relevance to repository performance than the responses at short times.

By substituting for the in-solution and colloidal-mass concentrations from Eq. 3.4.2-64 and Eq. 3.4.2-65 in the general expression for total incremental mass release given by Eq. 3.4.2-72, one obtains an expression for the incremental mass release  $\Delta M_i^{\alpha\beta}$  of a chemical element  $\alpha$  in flow-rate test (where  $\beta=1$  for a vapor test,  $\beta=2$  for a low-flow-rate drip test, and  $\beta=3$  for a high-flow-rate drip test) during the time interval  $\Delta t_i^\beta$ . Because the same secondary phases were observed during the measurement period in the vapor and low-drip tests and estimates showed that the flow rates were sufficiently small, these two sets of data were analyzed together using Eq. 3.4.2-75 for the incremental mass release. Because the high-drip test exhibited secondary mineral phases that were different from those observed in the vapor and low-drip tests, it was analyzed separately using only the condensed vapor–water flow rate derived from the combined vapor- and low-drip–test analysis. For the high-drip-rate analysis, Eq. 3.4.2-72 was used. Furthermore, because the void spaces were observed to be fully saturated with water in the high-drip test,  $f_d = 1$  was assumed. Therefore, for these test conditions,

$$\Delta M_i^{\alpha\beta} \approx (A_F^\beta v_{Fv}^\beta + q_{di}^\beta) C_{T \max i}^\alpha \Delta t_i \quad (3.4.2-77)$$

for the vapor (=1) and low-drip (=2) tests and

$$\Delta M_i^{\alpha\beta} \approx \left( \frac{r_{Ci}^\alpha A_{Sdi} C_{\max di}^\alpha}{r_{Ci}^\alpha A_{Sdi} + (A_F v_{Fv} + q_{di}) C_{\max di}^\alpha} + \frac{r_{Ki}^\alpha A_{Sdi} K_{\max di}^\alpha}{r_{Ki}^\alpha A_{Sdi} + (A_F v_{Fv} q_{di}) K_{\max di}^\alpha} \right) (A_F v_{Fv} + q_{di}) \Delta t_i \quad (3.4.2-78)$$

for the high-drip ( $\beta=3$ ) test. In the high-drip test, estimates do not clearly indicate that the low-flow-rate assumptions can be invoked to simplify the preceding expression. If the low-flow-rate assumptions can be invoked, Eq. 3.4.2-78 simplifies to the same form as Eq. 3.4.2-77.

The data-fitting task is to find, given the measured values of the previously identified known parameters, the set of unknown parameters. The general method adopted was to minimize, with respect to the values of the unknown parameters, the square error between the experimentally measured mass release and the mass release predicted by the preceding expression summed over all chemical elements, measurement times, and tests. That is, minimize the error  $E$  defined by

$$E(Z) \equiv \frac{1}{2} \sum_{\beta} \sum_{\alpha} \sum_i (\Delta M_i^{\alpha\beta} |_{\text{predicted}} - \Delta M_i^{\alpha\beta} |_{\text{measured}})^2 \quad (3.4.2-79)$$

with respect to each member  $Z_n$  of the set of unknown parameters by setting

$$\frac{dE}{dZ_n} = \left\{ \sum_{\beta} \sum_{\alpha} \sum_i (\Delta M_i^{\alpha\beta} |_{\text{predicted}} - \Delta M_i^{\alpha\beta} |_{\text{measured}}) \frac{d(\Delta M_i^{\alpha\beta} |_{\text{predicted}})}{dZ_n} \right\} = 0. \quad (3.4.2-80)$$

This procedure yields a set of  $n$  coupled, nonlinear algebraic equations that were solved for the  $n$  unknowns by a suitable iterative method (e.g., Newton-Raphson, sub-space projection/iteration methods). A computer program was developed within the Microsoft Excel 97 spreadsheet program for this purpose.

Generally, the number of distinct measurements must equal or exceed the number of unknown parameters for a solution to the problem to be obtained. If the effective rates of dissolution/release and the equilibrium in-solution and colloidal film-mass concentrations were allowed to vary with time and remain different in the vapor, low-drip, and high-drip tests, the number of measurements available was not sufficient to determine all of the unknown parameters. Furthermore, the greater the number of measurements above the minimum required, the more reliable and accurate are the fitted parameters. For these reasons, it was decided to verify the applicability and adopt the approximate model (given by Eq. 3.4.2-77 for advective transport-limited conditions) and the additional assumption of equal-equilibrium film-mass transfer concentrations in the vapor and low-drip tests. The high-drip test, in which the alteration products were different from those observed in the vapor and low-drip tests, was excluded from this first step of the parameter-fitting procedure. That is, the vapor test and low-drip test data were used to determine the vapor-water circulation rate and the time-varying equilibrium film-mass coefficients for each chemical element at each experimental measurement time. The equations solved for the total equilibrium film-mass concentrations, obtained by substituting Eq. 3.4.2-77 in Eq. 3.4.2-80, are given by

$$\sum_{\beta} (\Delta M_i^{\alpha\beta} |_{predicted} - \Delta M_i^{\alpha\beta} |_{measured}) q_{di}^{\beta} \Delta t_i^{\beta} = 0 . \quad (3.4.2-81)$$

Similarly, the equation for the vapor–water recirculation rate  $v_{Fv}$  is given by

$$\sum_{\beta} \sum_{\alpha} \sum_i (\Delta M_i^{\alpha\beta} |_{predicted} - \Delta M_i^{\alpha\beta} |_{measured}) A_F^{\beta} C_{\max i}^{\alpha} \Delta t_i^{\beta} = 0 . \quad (3.4.2-82)$$

These nonlinear algebraic equations were simultaneously solved for the constant value of the condensed vapor–water recirculation rate and the unknown total equilibrium film-mass concentrations at each measurement time.

#### 3.4.2.5.12 Release-Rate Model Parameters for Unsaturated, Low-Flow–Rate Conditions with Secondary Phase Formation

This subsection presents the constitutive parameters fitted to the release rate model for unsaturated, low-flow conditions that accounts for the formation of alteration mineral products. The approximate model for mass release given by Eq. 3.4.2-75 was used to analyze the vapor and low-drip test data. This model is valid when the release rate is limited by advective transport and the alteration minerals formed in the vapor and drip zones are of the same composition and have the same equilibrium film-mass concentrations. The condensed vapor–water flow rate determined from this analysis was then used to determine the total film concentrations in the high-drip test because the condensed vapor–water flow rate is primarily a function of the temperature at which the test is performed.

The equilibrium-mass concentrations and vapor-recirculation velocities that were fitted to the vapor and low-drip test data are given in Table 3.4.2-5 and Table 3.4.26. These values are plotted against time in Figure 3.4.2-6 and Figure 3.4.2-7 for ATM-103 and ATM-106 fuels, respectively. The first important aspect of these results is that all equilibrium film-mass concentrations decrease in value with increasing time by many orders of magnitude. This is important because it implies that the formation of alteration products reduces radionuclide release far below initial levels. The second important feature is that the equilibrium film-mass concentrations appear to approach constant values at long times. This is important because constant long-term values would imply that stable alteration minerals are being formed. The calculated equilibrium film-mass concentrations indicate that the mass releases are not congruent, although dissolution of spent fuel itself may be congruent. Finally, the differences in the relative magnitudes of the equilibrium film-mass concentrations for different chemical elements cannot be explained solely on the basis of their pure element solubilities, further underscoring the importance of preferential substitutional incorporation of elements in alteration minerals.

Table 3.4.2-5 Equilibrium film-mass concentrations fitted to ATM-103 spent-fuel vapor and low-drip test data using the advective transport-limited approximate model; fitted vapor–water recirculation velocity = 2.666E-06 cm/d [LL980912251031.053]

All ATM-103 Tests: Fitted Equilibrium Total Mass Concentrations g/mL									
Time Interval	Pu	U	Cs	Tc	Sr	Mo	Am	Np	I
	0.00E+00	0.00E+00	0.00E+00	0.00E+00	0.00E+00	0.00E+00	0.00E+00	0.00E+00	0.00E+00
1	5.343E-07	1.599E-05	5.349E-08	1.700E-07	2.899E-13	1.317E-07	1.216E-06	8.333E-08	2.117E-04
2	1.201E-08	1.499E-06	4.263E-09	1.171E-08	4.701E-09	2.899E-08	2.279E-09	6.481E-10	1.560E-07
3	7.979E-10	1.397E-07	1.920E-10	2.514E-09	3.032E-10	1.853E-09	3.873E-10	8.059E-11	1.168E-07
4	1.531E-11	2.937E-07	5.126E-10	3.969E-08	6.121E-10	4.832E-10	9.704E-11	3.835E-12	6.983E-08
5	4.456E-12	1.814E-09	2.463E-11	8.203E-10	8.284E-10	1.464E-09	3.030E-12	1.054E-12	1.262E-08
6	2.605E-11	5.536E-09	2.219E-10	1.112E-08	2.160E-09	2.704E-10	7.932E-12	6.361E-12	7.155E-09
7	3.386E-12	4.963E-09	3.132E-10	3.407E-09	6.617E-10	8.341E-11	1.579E-11	2.692E-12	2.201E-09

ATM103: Fitted Film Mass Concentrations

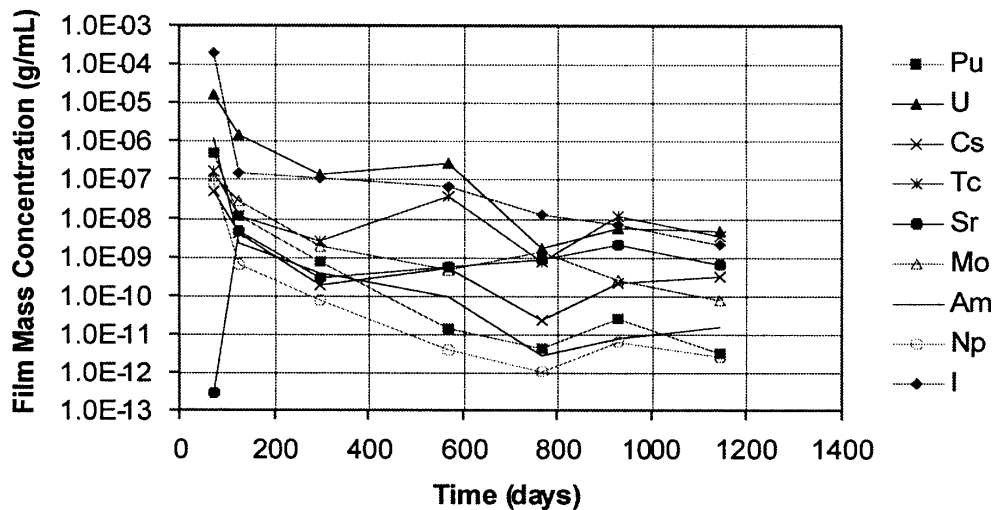


Figure 3.4.2-6 Equilibrium total film-mass concentration fitted to ATM-106 spent-fuel-vapor test and low-drip-test data using the advective transport-limited approximate model [LL980912251031.053]



### 3.4.2 Spent Fuel Dissolution Models

Table 3.4.2-6 Equilibrium film-mass concentrations fitted to ATM-106 spent-fuel vapor and low-drip-test data using the advective transport-limited approximate model; fitted vapor–water recirculation velocity =  $2.014\text{E-}5$  cm/d [LL980912251031.053]

All ATM-106 Tests: Fitted Equilibrium Total Mass Concentrations g/mL									
Time Interval	Pu	U	Cs	Tc	Sr	Mo	Am	Np	I
	0.00E+00	0.00E+00	0.00E+00	0.00E+00	0.00E+00	0.00E+00	0.00E+00	0.00E+00	0.00E+00
1	4.366E-07	6.025E-05	1.515E-10	2.662E-07	1.445E-10	2.330E-07	3.632E-07	1.067E-07	6.026E-04
2	4.959E-09	1.014E-06	1.822E-09	2.901E-09	1.245E-08	1.705E-07	6.001E-10	5.934E-10	1.585E-06
3	7.444E-11	3.065E-08	4.400E-10	6.844E-10	5.952E-10	2.421E-08	8.322E-11	1.950E-11	1.826E-06
4	2.992E-11	4.625E-08	8.306E-10	1.771E-08	7.612E-09	1.888E-09	5.797E-12	3.734E-11	4.080E-07
5	5.811E-12	4.886E-10	1.454E-10	7.647E-10	1.140E-09	2.181E-09	1.190E-12	1.104E-12	3.349E-08
6	3.758E-12	9.465E-10	1.097E-09	5.164E-09	3.411E-10	1.373E-10	2.504E-12	3.514E-13	4.013E-08
7	1.915E-07	2.704E-05	1.128E-07	2.024E-09	1.334E-10	5.248E-11	4.468E-08	1.349E-08	1.508E-08

### ATM106: Fitted Film Mass Concentrations

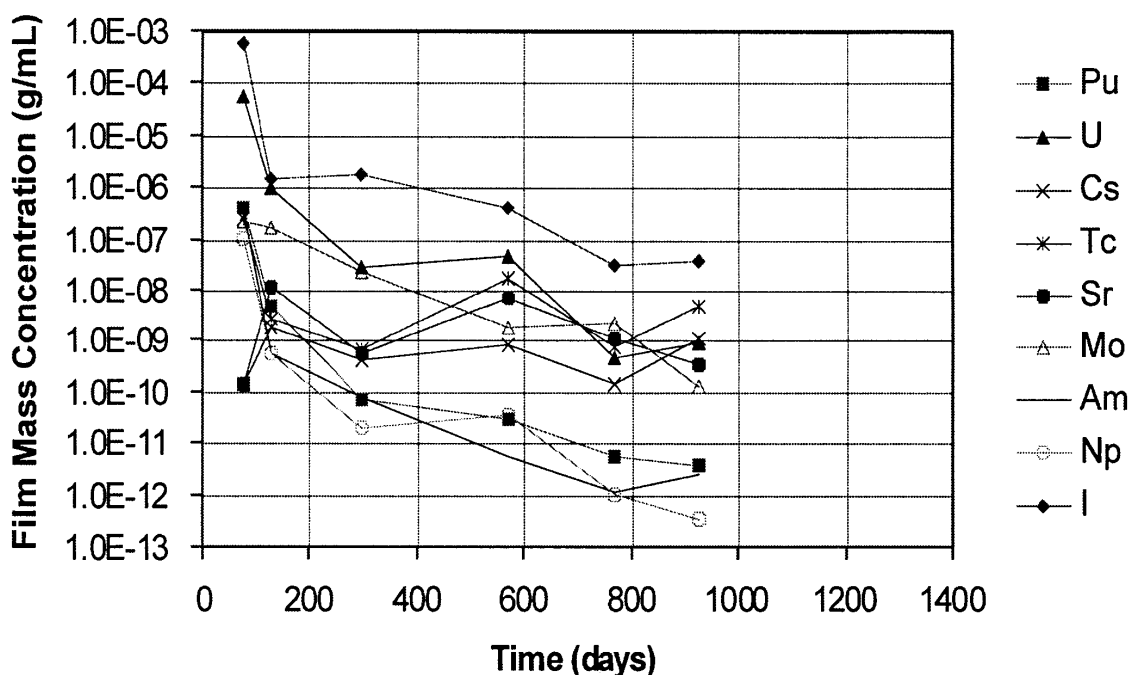


Figure 3.4.2-7 Equilibrium total film-mass concentration fitted to ATM-106 spent-fuel vapor test and low-drip test data using the advective transport-limited approximate model [LL980912251031.053]

### 3.4.2.5.13 Comparison of Equilibrium Mass Concentrations Against TSPA Recommended Solubility Limits

An important aspect of the equilibrium film-mass concentrations presented here is that, in the advective transport-limited analysis model, they are the actual film-mass concentrations of the chemical elements and, therefore, can be compared directly against the pure-element solubilities previously recommended in *Total System Performance Assessment—1995: An Evaluation of the Potential Yucca Mountain Repository* (TSPA—1995; CRWMS M&O, 1995) for bounding the radionuclide mass releases from spent fuel. The long-term equilibrium film-mass concentrations and the TSPA-1995 recommended average, minimum, and maximum solubilities are given in Table 3.4.2-7 and are plotted in Figure 3.4.2-8 for comparison. It can be seen immediately that the equilibrium film-mass concentrations are many orders of magnitude smaller than the average recommended TSPA-1995 values and are often many orders of magnitude smaller than the minimum solubilities recommended in TSPA-1995. Thus, the formation of alteration minerals under unsaturated, slow-flow conditions appears to reduce the release of radionuclides into the flowing groundwater by many orders of magnitude. If these preliminary results from analyzing the unsaturated drip test data can be confirmed, on detailed examination, as correct, they hold highly significant, favorable implications for repository performance.

**Table 3.4.2-7 Comparison of long-term equilibrium film-mass concentrations fitted to spent-fuel vapor and low-drip test data against TSPA (1995) recommended solubility limits [LL980912251031.053]**

Equilibrium Concentration or Solubility Limit (g/mL)	Pu	U	Cs	Tc	Am	Np
ATM-103 Equilib.Conc@ 925 days	2.605E-11	5.536E-09	2.219E-10	8.203E-10	3.030E-12	1.054E-12
ATM-106 Equilib.Conc@ 926 days	5.811E-12	4.886E-10	1.454E-10	7.647E-10	1.190E-12	1.104E-12
TSPA 1995 - Solubility Average	1.200E-07	7.600E-06	3.900E-04	1.000E-04	1.200E-07	3.400E-05
TSPA 1995 - Solubility Minimum	2.400E-09	2.400E-09	1.200E-06	3.500E-08	2.400E-11	1.200E-06
TSPA 1995 - Solubility Maximum	2.400E-07	2.400E-03	2.100E-03	9.900E-01	2.400E-07	2.400E-03

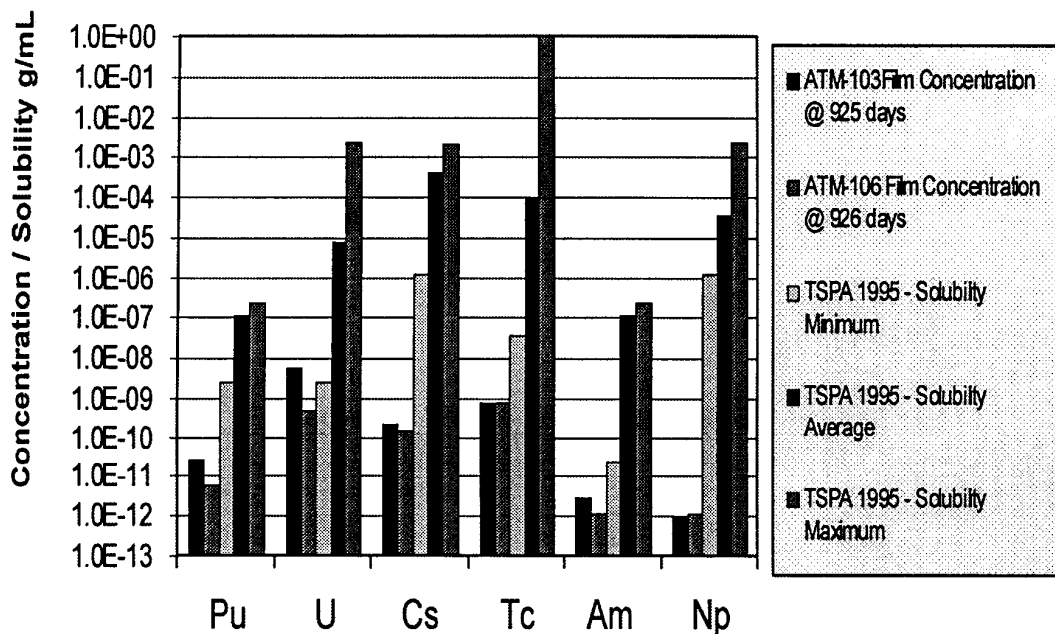


Figure 3.4.2-8 Comparison of long-term equilibrium film-mass concentrations fitted to spent-fuel vapor and low-drip test data against TSPA (1995) recommended solubility limits (Neptunium solubility reduced by two orders of magnitude in TSPA-VA [1997]) [LL980912251031.053]

#### 3.4.2.6 References

- Aagaard, P., and H. C. Helgeson (1982). "Thermodynamic and Kinetic Constraints on Reaction Rates Among Minerals and Aqueous Solutions. I. Theoretical Considerations." *Am. J. Sci.* **282**:237–285. [HQS.19880517.2373]
- Adamson, A. (1976). *Physical Chemistry of Surfaces*, 3rd Ed. New York, NY: John Wiley & Sons.
- Antropov, L. I. (1972). *Theoretical Electrochemistry*. Moscow, Russia: Mir Publishers, Moscow.
- Bates, J. K., Bourcier, W. L., Finn, P. A., Stout, R. B. (1995). "Reaction Progress Pathways for Glass and Spent Fuel Under Unsaturated Conditions," In proceedings of Sixth Annual International Conference on High-Level Radioactive Waste Management. Las Vegas, NV: April 30–May 5, 1995. pp. 600–602. [MOL.19951219.0074]
- Bikerman, J. J. (1970). *Physical Surfaces*. New York, NY: Academic Press.
- Bockris, J. O., and A. K. Reddy (1970). *Modern Electrochemistry*, Vols. 1 & 2. New York, NY: Plenum Press.
- Box, G. E. P., W. G. Hunter, and J. S. Hunter (1978). *Statistics for Experimenters: An Introduction to Design, Data Analysis, and Model Building*. New York, NY: John Wiley & Sons.
- CRWMS M&O (1995). *Total System Performance Assessment—1995: An Evaluation of the Potential Yucca Mountain Repository*. (B00000000-01717-2200-00136, Rev. 01) Las Vegas, NV: Civilian Radioactive Waste Management System Management and Operating Contractor: TRW Environmental Safety Systems, Inc.

- Davies, O. L. (Ed.) (1956). *The Design and Analysis of Industrial Experiments*. London, UK: ICI by Longman.
- Davies, O. L. and P. L. Goldsmith (Eds.) (1972). *Statistical Methods in Research and Production*. New York, NY: Hafner.
- deGroot, S. R., and P. Mazur (1962). *Non-equilibrium Thermodynamics*. Amsterdam, The Netherlands: North Holland, Amsterdam.
- Denbigh, K. (1968). *The Principles of Chemical Equilibrium*. Cambridge, UK: University Press.
- Draper, N., and H. Smith (1981). *Applied Regression Analysis*, 2nd Ed. New York, NY: John Wiley & Sons. [231231]
- Eringen, A. C. (1967). *Mechanics of Continua*. New York, NY: John Wiley & Sons.
- Finn, P. A., J. C. Hoh, S. F. Wolf, M. Surchik, E. C. Buck, and J. K. Bates (1997). Spent Fuel Reaction: The Behavior of the  $\epsilon$ -phase Over 3.1 Years." In proceedings from Scientific Basis for Nuclear Waste Management XX, Mat. Res. Soc. Symp. **465**:527–534. [MOL.19970121.0095]
- Finn, P. A., J. C. Hoh, S. F. Wolf, S. A. Slater, and J. K. Bates (1995). "The Release of Uranium, Plutonium, Cesium, Strontium, Technetium, and Iodine from Spent Fuel Under Unsaturated Conditions." In proceedings from Migration '95: Fifth International Conference on Chemistry and Migration Behavior of Actinides and Fission Products in the Geosphere. Saint-Malo, France: September 10–15, 1995. [238155]
- Finn, P. A., J. K. Bates, J. C. Hoh, J. W. Emery, L. D. Hafenrichter, E. C. Buck, and M. Gong (1994a). "Elements Present in Leach Solutions From Unsaturated Spent Fuel Tests." In proceedings from Materials Research Society Symposia. **333**:399–407. [238007]
- Finn, P. A., E. C. Buck, M. Gong, J. C. Hoh, J. W. Emery, L. D. Hafenrichter, and J. K. Bates (1994b). "Colloidal Products and Actinide Species in Leachate from Spent Nuclear Fuel." *Radiochim. Acta*. **66/67**:189–195. [238493]
- Gibbs, J. W. (1961). *The Scientific Papers of J. Willard Gibbs*. Vols. 1 & 2. New York, NY: Dover Pub.
- Grandstaff, D. E. (1976). "A Kinetic Study of the Dissolution of Uraninite." *Econ. Geo.* **71**:1493. [NNA.19911025.0061]
- Gray, W. J., H. R. Leider, and S. A. Steward (1992). "Parametric study of LWR spent fuel dissolution kinetics." *J. Nucl. Mater.* **190**:46–52. [MOL.19960613.0037]
- Gray, W. J., and C. N. Wilson (1995). *Spent Fuel Dissolution Studies, FY1991 to 1994*. (PNL-10540) Richland, WA: Pacific Northwest National Laboratory. [MOL.19960802.0045]
- Hayward, D. O., and B. M. W. Trapnell (1964). *Chemisorption* (2nd Ed.). London, UK: Butterworths.
- Hochella, M. F., and A. F. White (Eds.) (1990). *Reviews in Mineralogy*, Vol. 23. Mineral-Water Interface Geochemistry, Mineral. Soc. of America. Washington, DC.
- Hunter, R. J. (1993). *Foundations of Colloid Science*. Oxford, UK: Clarendon Press.
- Jackson, J. D. (1962). *Classical Electrodynamics*. New York, NY: John Wiley & Sons.

### 3.4.2 Spent Fuel Dissolution Models

---

- Jaycock, M. J., and G. D. Parfitt (1981). *Chemistry of Interfaces*. New York, NY: Halsted.
- Lasaga, A. C., R. A. Berner, G. W. Fisher, D. E. Anderson, and R. J. Kirkpatrick (1981). *Kinetics of Geo-chemical Processes*, Vol. 8. A. C. Lasaga and R. J. Kirkpatrick (Eds.). Washington, DC: Mineral. Soc. of America.
- Lewis, G. N., and M. Randall (1961). *Thermodynamics*. New York, NY: McGraw-Hill.
- Lupis, C. H. P. (1983). *Chemical Thermodynamics of Materials*. New York, NY: North-Holland.
- Pourbaix, M. (1973). *Lectures on Electrochemical Corrosion*. New York, NY: Plenum Press.
- Sedov, L. I., and J. R. M. Radok (1972). *A Course in Continuum Mechanics, Vol. II Physical Foundations and Formulations of Problems*. Gröningen, The Netherlands: Wolters-Noordhoff Pub.
- Steward, S. A., and W. J. Gray (1994). "Comparison of Uranium Dissolution Rates from Spent Fuel and Uranium Dioxide," In proceedings of the Fifth Annual International High-Level Radioactive Waste Management (IHLRWM) Conference. Las Vegas, NV: May 22–26, 1994. 4:2602–2608. (Also UCRL-JC-115355 for Lawrence Livermore National Laboratory, Livermore, CA.) [NNA.19940524.0024]
- Stout, R. B. (1996). "Nonequilibrium Thermodynamical Model for Spent Fuel Dissolution Rate." In proceedings of Seventh Annual International High-Level Radioactive Waste Management (IHLRWM) Conference. Las Vegas, NV: April 1996. pp. 393–396. (Also UCRL-JC-122737 for Lawrence Livermore National Laboratory, Livermore, CA.) [233230]
- Stout, R. B., E. J. Kansa, and A. M. Wijesinghe (1993a). *Kinematics and Thermodynamics of Non-stoichiometric Oxidation Phase Transformation in Spent Fuel*. (UCRL-JC-110678) Livermore, CA: Lawrence Livermore National Laboratory. [NNA.19930224.0014]
- Stout, R. B., E. J. Kansa, and A. M. Wijesinghe (1993b). *Kinematics and Thermodynamics Across a Propagating Non-stoichiometric Oxidation Phase Front in Spent Fuel Grains*. (UCRL-JC-112821) Livermore, CA: Lawrence Livermore National Laboratory. [NNA.19930323.0053]
- Stumm, W., and J. J. Morgan (1981). *Aquatic Chemistry: An Introduction Emphasizing Chemical Equilibria in Natural Waters*. New York, NY: John Wiley & Sons. [208448]
- Wilson, C. N. (1990). *Results from NNWSI Series 3 Spent Fuel Dissolution Tests*. (PNL-7170) Richland, WA: Pacific Northwest National Laboratory. [200816]
- Wronkiewicz, D. J., E. C. Buck, and J. K. Bates (1997). "Grain Boundary Corrosion and Alteration Phase Formation During the Oxidative Dissolution of UO<sub>2</sub> pellets." In proceedings from Material Research Society Symposium. 465:519. [MOL.19971217.0011]

## Section 3.4.2 Appendix

### Description of Previous or Alternative Intrinsic Dissolution Models

#### A.3.4.2.1 Previous Significant Models

The initial data-modeling efforts to represent available  $\text{UO}_2$  and spent-fuel dissolution data used simplified equations based on the Onsager-type thermodynamic function forms of Equations 3.4.2-11 and 3.4.2-12. The data sets consisted of macroscopic measurements of dissolution rates and the controlled, independent variables, temperature, and bulk solution chemistry, which consisted of total carbonate, dissolved oxygen, and hydrogen ion concentrations. Therefore,  $L_{ff}$  was initially represented by a product of solution chemical concentrations  $\times$  an exponential energy term,  $\exp(-Q/RT)$ , to include the temperature dependence. The solid potential energy  $\mu_{ss}$  was represented by a constant and a coefficient  $\times$  the burnup. The liquid or solid chemical potential energy for a concentration  $C_i$ ,  $\mu(C_i)$  was represented by  $\mu_0 + RT\ln\{\gamma C_i\}$ . The solid-liquid chemical potential energy-change term  $\mu_s - \mu_l$  was the difference of these representations. Thus, the dissolution rate was represented essentially as  $L_{ff}(\mu_s - \mu_l)$ .

Several polynomial variations for the forms of  $L_{ff}$ ,  $\mu_s$  and  $\mu_l$  were explored. Nonlinear regression analysis was used with these forms. These models all produced substantial differences compared with the measured dissolution rates. Because these models consisted of many products of the polynomial terms from  $L_{ff}(\mu_s - \mu_l)$ , a simple quadratic polynomial was selected as a close approximation of the model. A polynomial is much easier to analyze using multilinear regression. All of the regression fits of these polynomial, Onsager-type models resulted in low correlation coefficients. Furthermore, these dissolution models often predicted negative dissolution rates. For these reasons, only results with the regression analyses with the two Butler-Volmer expressions are provided as representative dissolution rate models over the available data sets.

The test data for dissolution response is best represented by Equation 3.4.2-18, which has the form of the Butler-Volmer equation used in the correlation of corrosion and electrochemical-rate data. The normal derivation of the Butler-Volmer equation assumes that the electrochemical processes are near thermodynamic equilibrium. In the preceding approach, thermodynamic nonequilibrium was assumed for the dissolution process. Also, the functional form to relate the dissolution velocity to the ratio of nonequilibrium configurational entropy was assumed.

Rather than regress on the exponential function in the Butler-Volmer equation, the natural logarithm of the dissolution rate [ $\text{mg}/(\text{m}^2\cdot\text{day})$ ] was used as the fitted response. The chemical and electrochemical potentials of the exponential function of the first Butler-Volmer model were represented as a polynomial in the bulk concentration and burnup variables. Burnup was also represented as a concentration term because it is proportional to the aggregated production and concentration of fission products. This approach also eliminated the possibility of a model yielding negative dissolution rates. The initial regressions used a

### 3.4.2 Appendix

full, 21-term quadratic polynomial of 5 variables.<sup>2</sup> A third-order term with burnup, oxygen concentration, and inverse temperature was included to better represent the apparent effects of radiolysis. The equation with the smallest root-mean-square error and largest correlation coefficient ( $r^2 = 0.91$ ) was a 13-term model:

$$\ln(\text{Rate UO}_2) = a_0 + a_1 \cdot \text{BU} + a_2 \cdot \text{IT} + a_3 \cdot \text{CO}_3 + a_4 \cdot \text{O}_2 + a_5 \cdot \text{H} + a_6 \cdot \text{BU} \cdot \text{IT} + a_7 \cdot \text{BU} \cdot \text{O}_2 + a_8 \cdot \text{BU} \cdot \text{H} + a_9 \cdot \text{CO}_3 \cdot \text{O}_2 + a_{10} \cdot \text{CO}_3^2 + a_{11} \cdot \text{O}_2^2 + a_{12} \cdot \text{BU} \cdot \text{O}_2 \cdot \text{IT} \quad (\text{A3.4.2-1})$$

with the following:

**Table A3.4.2-1 Coefficients, term descriptions, and regression statistics for 13-term model**

Term	Coefficient ( $a_i$ )	Std. Error	T-Value	Significance	Term Description
0 1	13.848639	1.534127	9.03	0.0001	Regression Constant
1 BU	-0.479226	0.082894	-5.78	0.0001	Burnup (MWd/kg)
2 IT	-4536.815865	480.481755	-9.44	0.0001	Inverse Temperature ( $\text{K}^{-1}$ )
3 CO3	823.431331	132.396019	6.22	0.0001	Total Carbonate Concentration (mol/L)
4 O2	50.158103	12.594141	3.98	0.0004	Oxygen Partial Pressure (atm)
5 H	-1.148737E+08	2.398216E+07	-4.79	0.0001	Hydrogen Ion Concentration (mol/L)
6 BU*IT	147.090980	26.299886	5.59	0.0001	→2nd Order Interaction
7 BU*O2	1.794646	0.550020	3.26	0.0028	
8 BU*H	6.120887E+06	1.12358E+06	5.45	0.0001	
9 CO3*O2	204.202747	86.865356	2.35	0.0255	
10 CO3**2	-38928.713074	6393.94265	-6.09	0.0001	→Quadratic
11 O2**2	-206.190757	59.419902	-3.47	0.0016	
12 BU*O2*IT	-614.563609	172.992767	-3.55	0.0013	→3rd Order Interaction

No. cases = 43

R-sq. = 0.9114

RMS Error = 0.4787

Resid. df = 30

R-sq-adj. = 0.8759

Cond. No. = 118.3

This first Butler–Volmer–type model describes some features of the chemical dissolution processes far from thermodynamic equilibrium and provides a reasonably good fit to the available data. However, the model is nonlinear because the Butler–Volmer model’s energy

<sup>2</sup> The dissolution data used for this regression analysis with the first Butler–Volmer model were the 42 combined flow-through tests of  $\text{UO}_2$  and spent fuel (ATM-103) in Table 2.1.3.5-4 of Section 2.1.3.5 plus the one dissolution rate of  $7 \text{ mg} \cdot \text{m}^{-2} \cdot \text{d}^{-1}$  for ATM-105 (burnup of 31 MWd/kgM also reported in that section).

change term is in the exponent and contains quadratic terms. Depending on the terms and coefficients in the model, extrapolation outside the measured, independent variable space could cause large prediction errors and should be used with caution.

A second Butler–Volmer model also was examined. By substituting the traditional chemical potentials that include a logarithmic dependence on activities or concentrations for the chemical potential changes in equation 3.4.2.2-18, the classic chemical kinetic rate law was derived:

$$\text{Rate} = k[A]^a[B]^b[C]^c \dots \exp(E_a/RT) \quad (\text{A3.4.2-2})$$

Because it is proportional to the aggregated production and concentration of fission products, burnup was also represented as a concentration term. For regression purposes, Eq. A3.4.2-2 was transformed by taking logarithms of each term and fitting that equation. That approach was used here, but allowing interaction and quadratic terms to improve the fit. The resulting model was (note base-10 logarithms)

$$\log_{10}(\text{Rate } \text{UO}_2) = a_2 + a_1 \cdot \text{PCO3} + a_2 \cdot \text{PO2} + a_3 \cdot \text{PH} + a_4 \cdot \text{PO2} \cdot \text{IT} + a_5 \cdot \text{LBU} \cdot \text{IT} + a_6 \cdot \text{LBU} \cdot \text{PCO3} + a_7 \cdot \text{LBU} \cdot \text{PO2} + a_8 \cdot \text{LBU} \cdot \text{PH} + a_9 \cdot \text{IT}^2 + a_{10} \cdot \text{PCO3}^2 \quad (\text{A3.4.2-3})$$

with the coefficients and regression statistics given in Table A3.4.2-2.

A modest refinement of model 3.4.2.20b in Version 1.2 of the *Waste Form Characterization Report* (WFCR V1.2) (see Eq. A3.4.2-3) derives from an extensive analysis of by William O’Connell (Lawrence Livermore National Laboratory memorandum “Regression Fit of the  $\text{UO}_2$  and  $\text{UO}_2$  Spent-Fuel Matrix Dissolution Data for Use in the PA Model,” William O’Connell to Ray Stout, LLYMP9805049, July 31, 1997). This refinement was the currently accepted intrinsic dissolution model for total system performance assessment—viability assessment (TSPA-VA) at the time this version of this report was published. This model form includes a linear term of all variables, including the inverse temperature instead of its square and the linear LBU term with minimal loss in the correlation coefficient and adjusted for the number of terms in the equation. The linear portion of the model is equivalent to the classic chemical rate law (Eq. A3.4.2-2). Equation A3.4.2-4 (note base-10 logarithms) represents this current model:

$$\log_{10}(\text{Rate } \text{UO}_2) = a_0 + a_1 \cdot \text{IT} + a_2 \cdot \text{PCO3} + a_3 \cdot \text{PO2} + a_4 \cdot \text{PH} + a_5 \cdot \text{LBU} + a_6 \cdot \text{PO2} \cdot \text{IT} + a_7 \cdot \text{LBU} \cdot \text{IT} + a_8 \cdot \text{LBU} \cdot \text{PCO3} + a_9 \cdot \text{LBU} \cdot \text{PO2} + a_{10} \cdot \text{LBU} \cdot \text{PH} + a_{11} \cdot \text{PCO3}^2 \quad (\text{A3.4.2-4})$$

The coefficients and fitting statistics are in Table A3.4.2-3.



Table A3.4.2-2 Coefficients and regression statistics for Eq. A3.4.2-2

Term	Coefficient (a <sub>i</sub> )	Std. Error	T-Value	Significance	Term Description
0 1	1.161868	0.803471	1.45	0.1564	Regression Constant
1 PC03	1.547418	0.434866	3.56	0.0010	[−Log10] of Total Carbonate Conc. (mol/L)
2 PO2	−1.672304	0.565034	−2.96	0.0053	[−Log10] of Oxygen Partial Pressure (atm)
3 PH	0.260294	0.053553	4.86	0.0001	[−Log10] of Hydrogen Ion Conc. (mol/L)
4 IT*PO2	384.146973	179.898661	2.14	0.0392	Inverse Temperature (K <sup>−1</sup> )  →2nd Order Interaction
5 IT*LBU	584.818339	123.912588	4.72	0.0001	[Log10] of Burnup (MWd/kgM)  →2nd Order Interaction
6 PCO3*LBU	0.147972	0.050678	2.92	0.0059	→2nd Order Interaction
7 PO2*LBU	0.174971	0.056308	3.11	0.0036	
8 PH*LBU	−0.285106	0.043195	−6.60	0.0001	
9 IT**2	−3.727218E+05	52092.019943	−7.16	0.0001	→Quadratic
10 PCO3**2	−0.345209	0.080324	−4.30	0.0001	

No. cases = 49

R-sq. = 0.8649

RMS Error = 0.2309

Resid. df = 38

R-sq-adj. = 0.8293

Cond. No. = 147.9

Table A3.4.2-3 Coefficients and fitting statistics for Eq. A3.4.2-4

Term	Coefficient (a <sub>i</sub> )	Std. Error	T-Value	Significance	Term Description
0 1	5.299561	1.321560	4.01	0.0003	Regression Constant
1 IT	-2441.512949	352.342615	-6.93	0.0001	Inverse Temperature (K <sup>-1</sup> )
2 PCO3	1.588315	0.437626	3.63	0.0010	[-Log10] of Total Carbonate Conc. (mol/L)
3 PO2	-1.649281	0.567653	-2.91	0.0053	[-Log10] of Oxygen Partial Pressure (atm)
4 PH	0.237613	0.058783	4.04	0.0001	[-Log10] of Hydrogen Ion Conc. (mol/L)
5 LBU	-0.756673	0.808096	-0.94	0.3552	[+Log10] of Burnup (MWd/kgM)
6 IT*PO2	377.413900	180.831077	2.09	0.0438	
7 IT*LBU	731.867389	202.871969	3.61	0.0009	
8 PCO3*LBU	0.157908	0.052016	3.04	0.0044	→2nd Order Interactions
9 PO2*LBU	0.172391	0.056724	3.04	0.0043	
10 PH*LBU	-0.255023	0.053269	-4.79	0.0001	
11 PCO3**2	-0.354358	0.080776	-4.39	0.0001	→Quadratic

No. cases = 49

R-sq. = 0.8668

RMS Error = 0.2323

Resid. df = 37

R-sq-adj. = 0.8272

Cond. No. = 193.5

The simple form of the rate law corresponding to Eq. 3.4.2.2-22 and Eq. 3.4.2.2-23 and to Eq. A3.4.2-2 in this appendix is:

$$\text{Rate (mg/(m}^2\cdot\text{day))} = 7.269 \cdot 10^4 \cdot [\text{O}_2]^{0.38} \cdot [\text{CO}_3]^{0.16} \cdot [\text{H}]^{-0.04} \cdot [\text{BU}]^{-0.13} \cdot \exp(-5382/\text{RT})$$

$$R^2 = 0.61$$

(A3.4.2-5)

The combined effects of spent-fuel burnup with the water chemistry variables is clear from a comparison of the R-squares of Eq. A3.4.2-4 and Eq. A3.4.2-5. The interaction of temperature and oxygen concentration may be caused by radiolysis. The quadratic carbonate term may result from surface coverage effects of carbonate species.

#### A.3.4.2.2 Proposed Model from Expert Elicitation

During the first series of expert-panel-elicitation meetings, an alternative spent-fuel intrinsic-dissolution model was proposed (Geomatrix, 1998). The proposed model was

$$\text{Rate} = k \cdot [\text{O}_2]^{0.7} \cdot [\text{CO}_3]^{0.45} \cdot \exp(-Q/\text{RT})$$

(A3.4.2-6)

The exponents of the oxygen and carbonate concentrations were fixed and based on a compilation (Tait, 1997) of single variable experiments by authors at several laboratories. Spent fuel and UO<sub>2</sub> were considered to have similar dissolution rates (i.e., burnup is not a factor).

This model was fit to the same 49 data points given in Tables 2.1.3.5-4 and 2.1.3.5-4a and used in the earlier models discussed Section A.3.4.2.1 of this appendix. The results are

$$\text{Rate (mg/(m}^2\cdot\text{day))} = 4.3172 \cdot 10^6 \cdot [\text{O}_2]^{0.7} \cdot [\text{CO}_3]^{0.45} \cdot \exp(-5760.9/\text{RT}) \quad R^2 = 0.23 \quad (\text{A3.4.2-7})$$

This is a poor result, and the correlation coefficient is very similar to using only the most significant variable, temperature, in the fit

$$\text{Rate (mg/(m}^2\cdot\text{day))} = 2.0497 \cdot 10^4 \cdot \exp(-5541.3/\text{RT}) \quad R^2 = 0.24 \quad (\text{A3.4.2-8})$$

By determining the coefficient and exponents directly from a regression fit of the data with the same terms as in equation A3.4.2-6, the following equation was obtained:

$$\text{Rate (mg/(m}^2\cdot\text{day))} = 1.928 \cdot 10^5 \cdot [\text{O}_2]^{0.35} \cdot [\text{CO}_3]^{0.15} \cdot \exp(-5627/\text{RT}) \quad R^2 = 0.57, \quad (\text{A3.4.2-9})$$

which provides a much better fit but significantly different exponents on the oxygen and carbonate terms. The R-square of Eq. A3.4.2-9 is only slightly less than the full simple-rate law in Eq. A3.4.2-5 because of the small effect of pH and the fact that burnup exhibits its importance in the interaction or cross-terms.

#### A.3.4.2.3 References

- Geomatrix Consultants, Inc. (1998). *Waste Form Degradation and Radionuclide Mobilization Expert Elicitation Project*. K. J. Coppersmith and R.C. Perlman (Eds.) San Francisco, CA: produced under DE-AC O8-91RW00134 for U. S. Department of Energy.
- Tait, J. C. ,and J. L. Luht (1997). *Dissolution Rates of Uranium from Unirradiated UO<sub>2</sub> and Uranium and Radionuclides from Used CANDU Fuel Using the Single-Pass Flow-Through Apparatus*. (06819-REP-01200-0006 R00) Atomic Energy of Canada, Limited, Whiteshell Laboratories, and Ontario Hydro.

### 3.5 Glass Dissolution

Hydrolysis of Si-O bonds by water initiates glass dissolution and causes the formation of a hydrous reacted layer. Elements released during hydrolysis diffuse outwards into solution while the hydrous altered layer re-polymerizes. The overall rate of reaction appears to be controlled by the rate of dissolution of the re-polymerized hydrous surface layer. Secondary phases consisted of elements present in the leachate and elements released from the glass precipitate from solution or segregate from amorphous material on the glass surface. These alteration layers do not appear to provide a transport barrier.

Current models for glass dissolution combine a rate equation derived from irreversible thermodynamics with reaction path computer codes that account for solution speciation and precipitation of solids. Although these models account for the major features observed in short-term dissolution tests of waste glasses, there remain uncertainties when extrapolating these models to long time periods. The most critical of these uncertainties is that of the nature of the chemical process which determines the long-term dissolution rate of the glass.

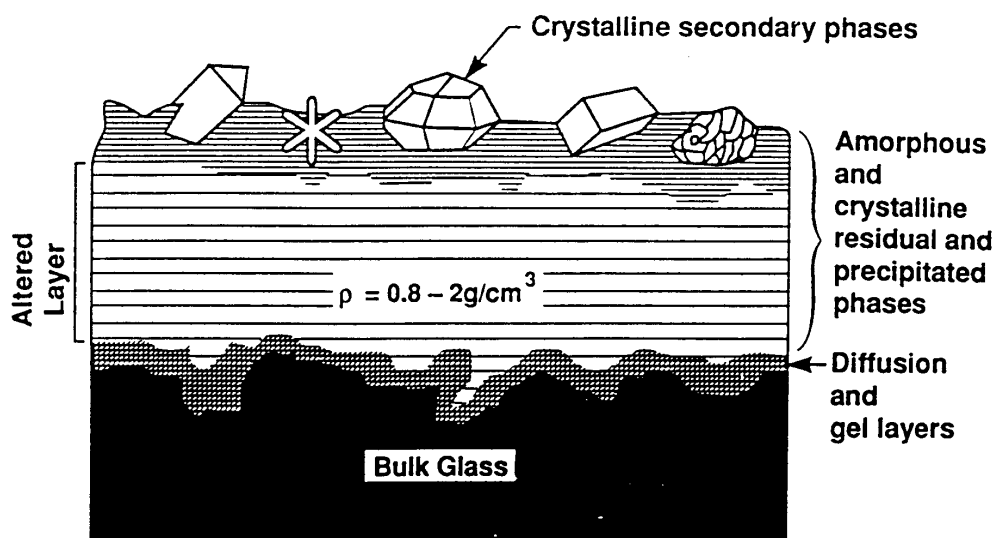


Figure 3.5-1 Features observed on reacted glass surfaces

### 3.5.1 Experimental Parameters for Glass Dissolution

#### 3.5.1.1 Introduction

The goal of the Yucca Mountain Site Characterization Project (YMP) glass task has been to develop a mechanistic model that predicts an alteration/dissolution rate for a glass under localized conditions (i.e., for any spot on the glass, a packet of water with some composition and temperature will cause the glass to react at some rate and to produce some set of alteration products). Integration of this localized process would provide the overall behavior of the glass waste form on a repository scale. For the glass-reaction model, parameters such as surface area/volume (SA/V) ratio and  $f$  (fraction of Si in precipitates discussed subsequently) are not input parameters but derived parameters based on the fundamental mechanisms incorporated in the model. However, this amount of detail will not be appropriate for YMP performance assessment (PA) models. Simplification of the model is necessary for it to be interfaced into present PA codes. The simplified model described here is meant to be a first step in making this connection.

The topic of this section is experimental parameters; however, to provide a context in which to place the parameters, this section also includes a succinct summary of the fundamental rate equations in the model. With this discussion, the proper use and the effective limitations of the present model and model parameters can be understood.

#### 3.5.1.2 Rate Equation for Simplified Glass-Dissolution Model

Because the glass-alteration rate changes as the solution composition changes, it is necessary to closely couple the evolving solution composition with glass dissolution. The rate of glass dissolution depends on the concentrations of all the elements in solution that are present in the surface gel layer of the dissolving glass and on the solution pH. However, some simplifications can be made. Experimental and modeling work on borosilicate glass to date show that the two most important solution compositional parameters to be considered for predicting radionuclide release rates from glass are pH and dissolved silica concentration (temperature and reactive glass surface area must also be known). Thus, the feedback of solution composition to glass dissolution rate can be restricted by regressing experimental rate data of these two parameters. Following are the equations and parameters needed to calculate conservative release rates of radionuclides from glass with this simplified model. Also included are suggestions on further simplifying the model to make it appropriate for input into a first-cut, comprehensive PA model of a repository.

Long-term dissolution models for borosilicate glass employ a rate equation consistent with transition state theory. A simplified rate equation is given as

$$R = s k \left[ 1 - \left( \frac{Q}{K} \right)^\sigma \right] + sr_i \quad (3.5.1-1)$$

where

- R = alteration rate of glass (g/yr)
- s = surface area of reactive glass (m<sup>2</sup>)
- k = glass surface alteration rate constant (g/m<sup>2</sup>/yr), a function of temperature and pH of the solution
- Q = concentration of dissolved silica (g/m<sup>3</sup> water)
- K = solubility constant for borosilicate glass; here it equals the solubility of amorphous silica (g/m<sup>3</sup> water)
- σ = experimentally determined constant
- r<sub>l</sub> = long-term dissolution rate (under "silica saturated" conditions in units of g/m<sup>2</sup>/yr)

To calculate radionuclide release rates from glass, each of these parameters must be known or estimated. At present, the value of σ is not well determined, based on the available experimental data. The value of σ is therefore set to one in this model. Suggested values for each of the other parameters are discussed in subsequent text.

### 3.5.1.3 Parameters for Simplified Glass Dissolution Model

#### Surface Area, s

As the molten glass cools in the melter, it undergoes fracturing. Estimates for the increase in glass surface area due to fracturing range from 2 to 100 times the uncracked surface area. A reasonable average value to use for the extent of fracturing is 25 (Baxter, 1983). The initial total glass surface area per waste package A<sub>o</sub> comprises a nominal area per glass log, the number of glass logs per package n and a cracking factor, which is a multiplier on the nominal area (≥1, typically around 25).

$$A_o = 25 \bullet n \bullet 2\pi r_o^2 \left( 1 + \frac{L_o}{r_o} \right) \quad (3.5.1-2)$$

where

- A<sub>o</sub> = total glass surface area (m<sup>2</sup>)
- r<sub>o</sub> = radius of the glass log
- L<sub>o</sub> = length of the glass log
- n = number of glass logs per waste package

The glass log is assumed to be the same cylindrical shape with a constant length to radius ratio L<sub>o</sub>/r<sub>o</sub> during the dissolution process. Assuming the glass retains a constant density throughout alteration, then

$$A_1 = A_o \left( \frac{M_1}{M_o} \right)^{\frac{2}{3}} \quad (3.5.1-3)$$

### 3.5.1 Experimental Parameters for Glass Dissolution

where

$A_1$  = surface area after dissolution,  $m^2$

$A_o$  = initial surface area,  $m^2$

$M_1$  = glass mass after dissolution, kg

$M_o$  = initial glass mass, kg

In the bathtub-water-contact mode, the total surface area of the glass log is in contact with water when the container is filled. For the flow-through mode, only a fraction of surface contacts water. The wetted area depends on the groundwater flow rate. It is assumed the wetted area remains the same for a given water influx  $q$  until the total glass surface area decreases to less than the initial wetted area because of glass dissolution. Then the wetted area equals the total area until the glass completely dissolved.

#### Rate Constant, $k$

The rate constant  $k$  has been measured over a range of pH and temperature conditions. Table 3.5.1-1 and Figure 3.5.1-1 show the values of  $k$  in units of  $g/m^2/day$  from flow-through experiments by Knauss et al. (1990) for an analog, SRL-165 glass composition. The data are plotted in Figure 3.5.1-1, and the following regression relations are obtained:

$$k = 365 \times 10^m \text{ (g/m}^2\text{/yr)} \quad (3.5.1-4a)$$

where  $m$  is the higher value of the following two equations:

$$m = 8.632 - \frac{2600}{T + 273} - 0.65pH \quad (3.5.1-4b)$$

$$m = 7.268 - \frac{4550}{T + 273} + 0.50pH \quad (3.5.1-4c)$$

and where  $T$  = solution temperature ( $^{\circ}C$ ).

**Table 3.5.1-1**  $\log_{10}$  glass dissolution rate in  $g/m^2/day$   
(from Knauss et al., 1990) [LL980710651021.049]

pH	T = 25°C	T = 50°C	T = 70°C
1	-1.25	0.02	0.51
2	-1.73	-0.68	-0.18
3	-2.21	-1.38	-0.87
4	-2.69	-2.08	-1.56
5	-3.17	-2.78	-2.25
6	—	—	-2.94
7	-4.53	-3.43	-2.30
8	-4.02	-2.92	-1.90
9	-3.51	-2.41	-1.50
10	-3.00	-1.90	-1.10
12	-1.98	-0.88	-0.30

*Solution Chemistry, Q and K*

The major effect of groundwater chemistry on the glass-dissolution rate (other than pH) is the concentration of dissolved silica. In this simple model,  $Q$  equals the concentration of dissolved silica in the water contacting the glass. The chemistry of the groundwater in the vicinity of the potential repository will likely be dominated by the host rocks (Wilder, 1997); the silica concentration is therefore expected to be close to cristobalite saturation at the ambient temperature. Cristobalite is a common constituent of the host rocks at Yucca Mountain. Table 3.5.1-2 lists concentrations of silica in equilibrium with cristobalite at temperatures from 0 to 150°C from the thermodynamic database SUPCRT92 (Johnson et al., 1992)

" $K$ " in Eq. 3.5.1-1 for the waste glass is assumed equal to the equilibrium constant for amorphous silica in this simple model.  $K$  actually varies as a function of glass composition; for most waste glass compositions, the experimentally determined value of  $K$  is of the same general magnitude but less than the value of  $K$  for amorphous silica. This simplification therefore gives conservative estimates. Table 3.5.1-2 lists values of  $\log_{10}K$  (in molality) for temperatures from 0 to 150°C. As an example, at 60°C,  $Q/K = 10^{-3.02} / 10^{-2.43} = 0.26$ . The term  $(1-Q/K) = (1-0.26)$  or 0.74. Thus, the glass reaction rate is about 74% of the rate under silica-free conditions.

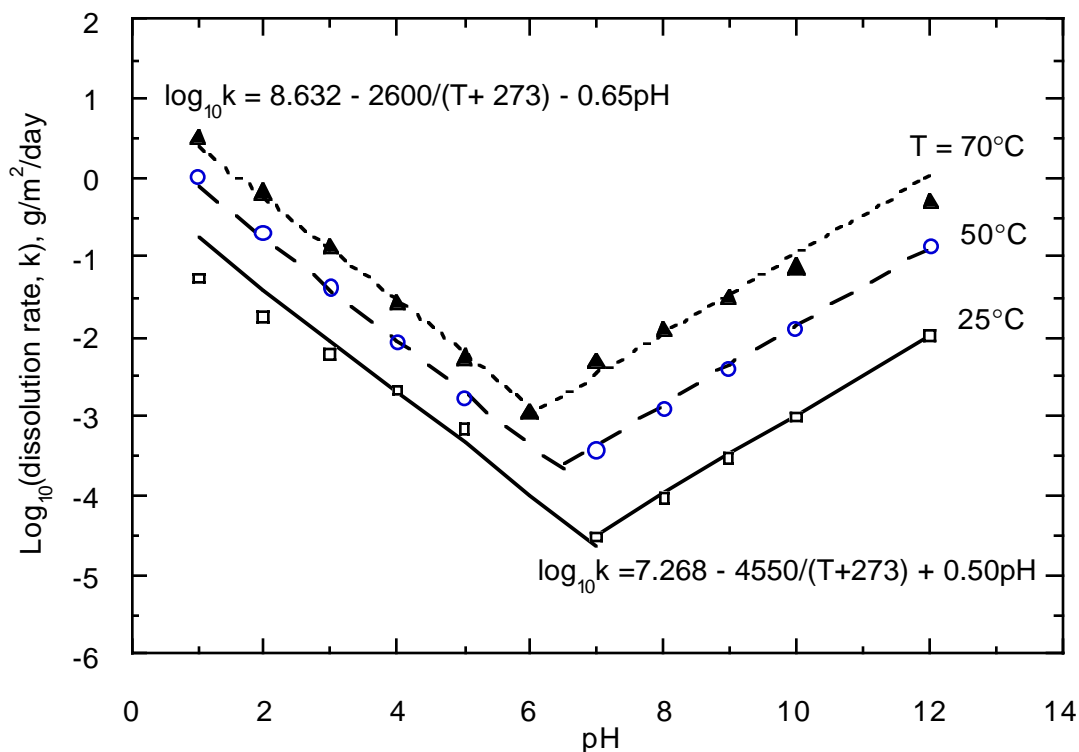


**Figure 3.5.1-1**  $\log_{10}$  (dissolution rate,  $\text{g/m}^2/\text{day}$ ) versus solution pH from Knauss et al. (1990)



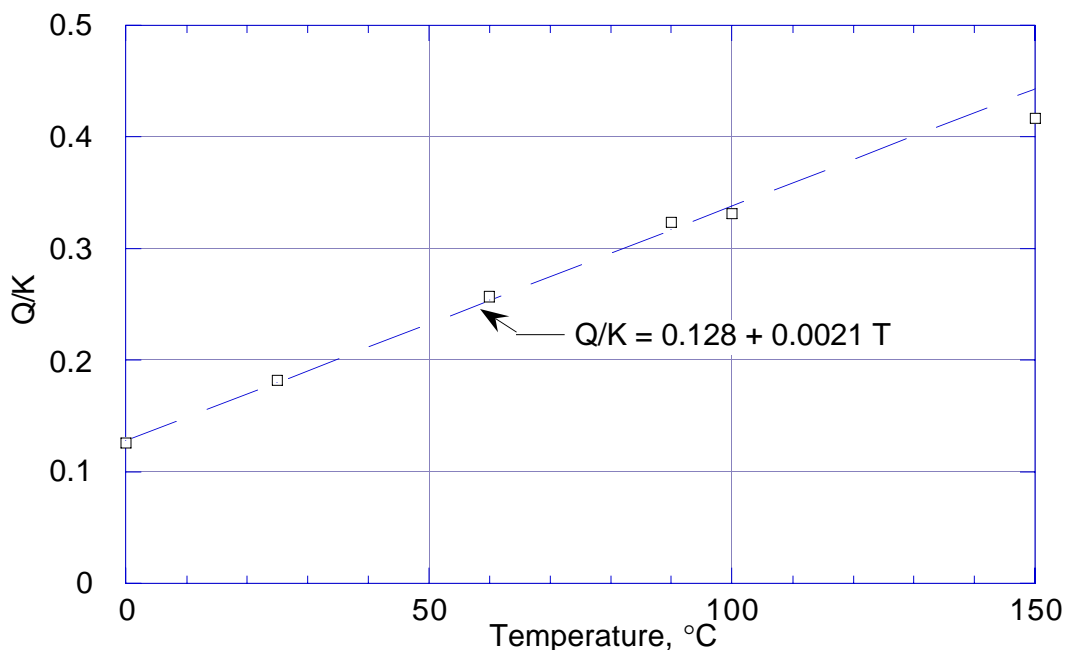
### 3.5.1 Experimental Parameters for Glass Dissolution

Figure 3.5.1-2 shows the relation between  $Q/K$  and temperature. For a temperature between 0 and 100°C, the relation can be expressed as:

$$\frac{Q}{K} = 0.128 + 0.0021T \quad (3.5.1-5)$$

**Table 3.5.1-2 Cristobalite and amorphous silica solubilities**  
(from Johnson et al., 1992) ( $\log_{10}$  [molality])

T°C =	0	25	60	90	100	150
Cristobalite	-3.89	-3.45	-3.02	-2.75	-2.68	-2.36
Amorphous Silica	-2.99	-2.71	-2.43	-2.26	-2.20	-1.98



**Figure 3.5.1-2 Relation between  $Q/K$  and temperature**

#### *Solution pH*

Experimental studies of tuff-water interactions have shown that reacted J-13 water maintains a pH slightly higher than neutral (Knauss et al., 1987). For anticipated repository conditions, a slightly alkaline pH of about 8 is recommended as a substitute for the lack of a more rigorous calculation of groundwater chemistry. This pH value should be used to estimate rate constants for glass dissolution from Table 3.5.1-1 (it should also be consistent with any data for solubility-limited radionuclide concentrations that are also highly dependent on pH). Note, however, that glass-dissolution rates and radionuclide-release rates

are very sensitive to pH, and nothing more than a qualitative estimate of release rates is possible without a more rigorous treatment of solution chemistry in the repository performance assessment model.

#### *Temperature Dependence of Glass Dissolution Rate*

Experiments have shown that glass-dissolution rates follow the Arrhenius relation  $\text{rate} \propto e^{-E/RT}$ , where R is the gas constant, T is temperature (Kelvin) and the activation energy (E) is about 20 kcal/mole. This corresponds roughly to dissolution rate increasing by a factor of 2 for a 10° rise in temperature. This simple rule can be used to describe the effect of temperature on glass-dissolution rate if the data in Table 3.5.1-1 cannot be explicitly used.

#### *Radionuclide Content of Glass*

Table 3.5.1--3 lists anticipated radionuclide contents for SRL glasses. More information on glass compositions is provided in Section 2.2.1 of this report. Conservative estimates for release rates for radionuclides from the glass waste form are given by multiplying the glass-dissolution rate (R) by the weight fraction of radionuclide in the glass from Table 3.5.1-3.

**Table 3.5.1-3     Radioisotope content per high-level waste (HLW) container for borosilicate glass from the Savannah River Site (from Table 6.14 of Version 1.2 of the Waste Form Characteristics Report) [LL980710651021.049]**

Isotope	g/canister	Isotope	g/canister
U-234	.549e1	Tc-99	.182e3
U-235	.727e2	Pd-107	.286e2
U-236	.174e2	Sn-126	.156e2
U-238	.312e5	Cs-135	.863e2
Np-237	.126e2	Cs-137	.499e3
Pu-238	.867e2	Ce-143	.401e3
Pu-239	.208e3	Ce-144	.309e1
Pu-240	.381e2	Nd-144	.411e3
Pu-241	.162e2	Pm-147	.261e2
Pu-242	.321e1	Sm-147	.877e2
Am-241	.321e1	Sm-148	.192e2
Cm-244	.132e1	Sm-149	.742e1
Se-79	.243e1	Sm-151	.941e1
Rb-87	.996e1	Eu-154	.229e1
Sr-90	.343e3	Eu-155	.102e1
Zr-93	.444e3		

Contents in grams of each isotope

Mass of glass in each canister is 1682 kilograms.

Only elements with more than 1 gram per canister are reported here.

### 3.5.1 Experimental Parameters for Glass Dissolution

---

#### 3.5.1.4 Example Calculation

What is the rate of release of  $^{235}\text{U}$  from one canister of glass at  $70^\circ\text{C}$  in cristobalite-saturated groundwater of  $\text{pH} = 8$ ? The rate constant for glass dissolution at  $70^\circ\text{C}$  and  $\text{pH} = 8$  is  $10^{-1.9} \text{ g/m}^2/\text{day}$ . The affinity term  $(1-Q/K)$  has a value of  $(1-10^{-2.93}/10^{-2.37})$  or 0.72. The bulk dissolution rate of glass is therefore  $0.0091 \text{ g/m}^2/\text{day}$ . Surface area for one canister is  $125 \text{ m}^2$ ; thus, the total rate of glass dissolution is  $1.13 \text{ g/day/canister}$ . Predicted  $^{235}\text{U}$  content of SRL waste glass is  $72.78 \text{ g/canister}$ . Total weight of glass in a canister is  $1682 \text{ kg}$ ; thus, the weight fraction of  $^{235}\text{U}$  is  $4.3 \times 10^{-5}$ . Release rate of  $^{235}\text{U}$  is therefore  $1.13 \times 4.3 \times 10^{-5} = 4.89 \times 10^{-5} \text{ g/day}$  or  $.018 \text{ g/year}$ .

Further simplification of the model can be achieved by the following:

- Assume constant  $\text{pH}$  of 8 and cristobalite saturation of the groundwater.
- Use Table 3.5.1-1 to provide the rate constant as a function of temperature at  $\text{pH} = 8$ .
- Use Table 3.5.1-2 to provide the factor that accounts for the lowering of glass-dissolution rate due to dissolved silica. (This provides a simple function of glass-dissolution rate with temperature and no other variables need to be considered.)

#### 3.5.1.5 Limitations of the Simplified Model

This simplified treatment of estimating glass-dissolution rates provides conservative estimates for release rates of radionuclides. It ignores solubility limits of some radioactive species (such as the actinides) and instead uses the conservative assumption that the radionuclides will be released no faster than the breakdown of the glass structure. This is consistent with the measured rates of diffusion of actinides in the glass, which are negligible under repository temperatures. Experiments have shown that, during glass corrosion, the actinides are commonly included in alteration phases at the surface of the glass either as minor components of other phases or as phases made up predominantly of actinides. No credit for this process is taken in this simple glass-dissolution model. To perform accurate estimates of solubility-limited release rates, one needs detailed information on water chemistry (e.g.,  $\text{pH}$ ,  $\text{Eh}$ ), which demands a much more complex PA model that explicitly accounts for coupled chemical interactions among all the repository materials (e.g., spent fuel, glass, metals).

This simple model also ignores all solution chemistry other than  $\text{pH}$  and silica concentration of the leachate. It is known from a variety of experiments that species such as dissolved  $\text{Mg}$  and  $\text{Fe}$  can change glass-dissolution rates by as many as several orders of magnitude.  $\text{Mg}$  decreases the rate;  $\text{Fe}$  increases the rate. Effects such as these are not accounted for in this model. Because these effects have not yet been quantified, it is currently impossible to include them in PA models of any level of complexity.

Also ignored is vapor-phase alteration of the glass. If a canister containing glass is breached, and humid air reaches the glass, the glass will react and form a thick alteration rind composed of hydrated glass and secondary phases. The durability of this material with respect to later contact with liquid water may be much greater or much less than the durability of unaltered glass. This effect is not accounted for here.

#### 3.5.1.6 Incorporation of Simplified Glass Model into Performance-Assessment Models

Much of the information presented in this section was developed by O'Connell et al. (1997). That document includes a more complete derivation of the equations used to predict borosilicate glass dissolution in the performance assessment code.

Three more pieces of information are needed to incorporate a simple glass-dissolution model into the current PA model:

1. A functional relation between the amount of silica released into solution and the amount that remains in solid alteration phases and layers
2. A functional relation between the pH and the amount of glass dissolved
3. Estimates of long-term rates determined from experimental data

This information is necessary to apply the glass model to the range of hydrologic conditions, from bathtub to flow-through mode, using a single model. The fraction of silica released to solution is needed to compute the silica concentration in the evolving leachate. The pH is needed to compute the reaction-rate constant for the glass during reaction progress.

#### 3.5.1.6.1 Silica Distribution Between Alteration Phases and Solution

The relation between the amount of silica released to solution and the amount tied up in secondary phases depends on the composition of the glass, the temperature, the pH, the composition of the starting solution, and probably other factors.

As the glass dissolves, secondary phases begin to precipitate. The types of phases that form depend on the glass composition. These phases lower the concentration of dissolved silica. The exact phases that will precipitate for a given glass in a given fluid composition cannot presently be predicted. Data from experiments is used to identify the phases.

In spite of these complexities, it is generally true that, given enough time, the solution in any closed-system test approaches the condition in which the amount of silica released from the glass equals the amount taken up in alteration phases. This is referred to as the “silica-saturated” or “long-term” dissolution rate. This is the slowest rate at which glasses are known to react. Because high SA/V test conditions act to accelerate the test, high SA/V conditions generally show behavior where “f” (the ratio of total released silica in the alteration phases to silica in solution) approaches one (silica is almost entirely in the alteration phases). Under these conditions, the PA model should predict that the glass will react at the long-term rate (see discussion of long-term rates in Section 3.5.1.6.3).

The plot in Figure 3.5.1-3 (from Delage et al., 1992) shows the silica fraction trapped in alteration layers versus silica concentration in solution. The relation is one that shows an increasing fraction of silica trapped in the alteration layer with increasing SA/V ratio. In terms of the extent of reaction, this is consistent with the higher SA/V tests being more advanced and, therefore, having both higher silica concentrations in solution and higher values of “f” as the tests approach silica saturation. Unfortunately, the test conditions and raw data from which this plot was made were not provided in Delage et al., so no more interpretation is possible.

The simple linear trend reported in the paper by Delage et al. should not be overinterpreted. The tests are for a very restricted range of experimental conditions, in distilled water, and over a very narrow range of SA/V conditions. This simple trend cannot be reliably extrapolated to more complex conditions where fluid composition depends on materials other than glass, and the history of glass reaction is not known because most of the initial pH increase is due to ion exchange of the outermost few microns of glass surface. After this zone is depleted of alkali, there will be a reduction in the rate of pH increase. In a repository with variable hydrologic regimes, evolving input fluid composition, variable

### 3.5.1 Experimental Parameters for Glass Dissolution

---

temperature, and other more complex conditions, a simple linear trend between Si concentration in solution and “f” is not expected.

Some data on the value of “f” for Savannah River glasses are available. For example, data for the SRL-202 glass based on closed system tests at SA/V ratios of 10, 2000, and 20,000 m<sup>-1</sup> give “f” values of 0.42, 0.54, and 0.98, respectively, after about 1 to 2 yr reaction. SRL-202 is currently the target glass composition to be produced by the defense waste-processing facility (DWPF).

Based on the preceding discussion, it is recommended that the current PA model use a simple relationship between SA/V and “f” for the SRL-202 glass using the data in the preceding paragraph (or Figure 3.5.1-3). However, the numerous conditions and limitations discussed indicate that, although the relation provides what is a correct trend, the absolute magnitude of the value of “f” at a particular value of SA/V is only an estimate. This is perhaps an adequate approximation for this initial glass-dissolution model. If the application is limited to an SRL-202 glass at near-neutral to weakly alkaline pHs, the results are probably correct in a semi-quantitative sense. More experimental work and analysis of existing data are needed to better define whether any simple relation exists between SA/V and “f.”

#### 3.5.1.6.2 pH versus Extent of Reaction

As glasses dissolve in closed-system tests, the pH of the leachant solution increases because of two effects:

1. Ion exchange between cations in the glass and H<sup>+</sup> in solution
2. Bulk glass dissolution

Precipitation of secondary phases tends to lower the pH. For most glasses, a near-neutral, unbuffered pH solution will quickly rise to pHs of between 9 and 11, depending on the alkali content of the glass (Na, Li, K) and the SA/V ratio of the test. The higher the SA/V ratio, the higher the pH. The pH of the leachant quickly reaches a limiting (steady state) and nearly constant value. For tests at approximately 100°C, this plateau is reached in a few days to a few weeks.

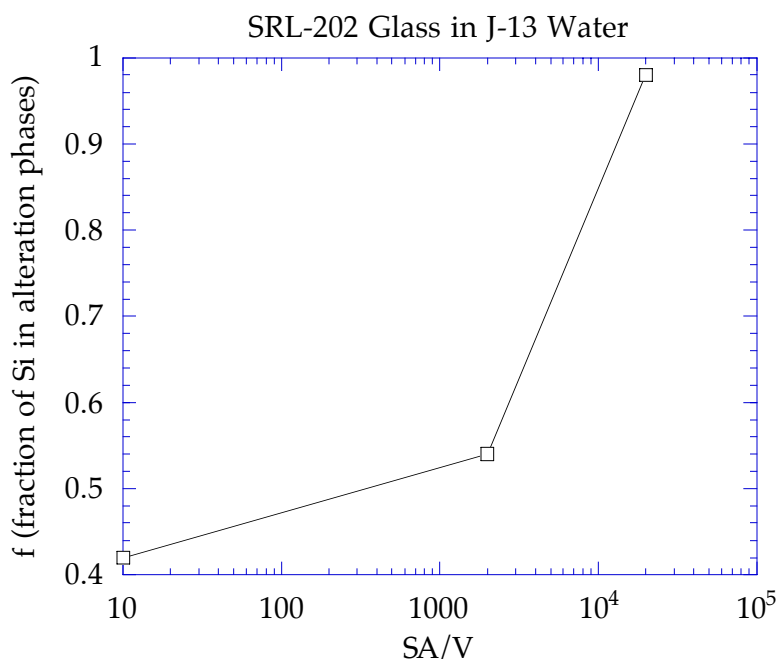


**Figure 3.5.1-3** Experimental data for fraction of silica released from glass that is incorporated into alteration layer, as a function of SA/V ratio of the test [LL980710651021.049]

This pH effect is not important in flow-through tests. The very low effective SA/V ratios of these tests cause the ion-exchange effect to be much less effective in modifying the solution pH.

An additional factor to be considered is that the solution entering the glass canister will have some initial pH and pH-buffering capacity that will be greater than the buffering capacity of the distilled water used in most of the test results. This buffer capacity will oppose pH changes because of glass dissolution and ion exchange. The change in pH will be a complex function of the flow rate, buffer capacity of the fluid, and alkali content of the glass; there is also no simple relation obvious from test results.

The dominant effect in this complex situation will most likely be the ion-exchange capacity of the glass. If one assumes the other factors are negligible, the pH that the solution will reach can be interpreted as a simple function of SA/V ratio. At high SA/V, the pH will increase to some higher constant value; at low SA/V (below about  $0.01\text{m}^{-1}$ ), the pH will not change at all.

It is impossible to consider all these effects in the current PA model. Therefore, the following simplified approach is recommended. Data for the steady-state pH for closed system tests of SRL-202 glass at  $90^\circ\text{C}$  are as shown in Table 3.5.1-4 (see also Figure 3.5.1-4).

**Table 3.5.1-4 Steady state pH vs. SA/V ratio of test**

Surface-Area-to-Volume Ratio (m <sup>-1</sup> )	Steady-State pH
10	9.0
2000	10.5
20,000	12.0

For bathtub-type hydrologic scenarios, a reasonable value for the solution pH can be estimated directly from the relation between pH and SA/V in Table 3.5.1-4. For flow-through and intermediate hydrologic scenarios, the situation is more difficult because the ion-exchange process, which is the dominant mechanism causing the pH to rise, takes place early in the glass-water reaction. The initial packets of reacting fluids will carry away the alkalis as high pH solutions. Later fluids will contact alkali-depleted glass, which will not have nearly as great an effect on the pH of the solution. Again, because a rigorous analysis is not possible in the PA code (although it is currently something that can be done in the glass submodel), the extension of the SA/V vs. pH relationship to the extreme end member of essentially SA/V=0 for flow-through conditions, where the pH will be equal to the initial pH, is recommended. A curve regressed to these data will provide a reasonable value of the pH of the reacting fluid for any given effective SA/V ratio of the system.

#### 3.5.1.6.3 Estimate of Long-Term Reaction Rate

Experimental data show that, even when the solution is saturated with silica after a long period of time, there is still a long-term dissolution rate for several glass compositions. Because a mechanistic model does not exist that can predict the variation of the long-term rates with environmental parameters, an averaged experimental value must be used.

Table 3.5.1-5 lists measured long-term (silica saturation) dissolution rates for several glass compositions. The SRL-202 glass is the current, most likely composition for glasses to be produced at DWPF and should be used for estimating glass behavior at the YMP site. Based on the data in this table, a value of 0.002 g glass/m<sup>2</sup>/day for the long-term (silica saturated) rate for SRL-202 glass is recommended for a temperature of 30°C.

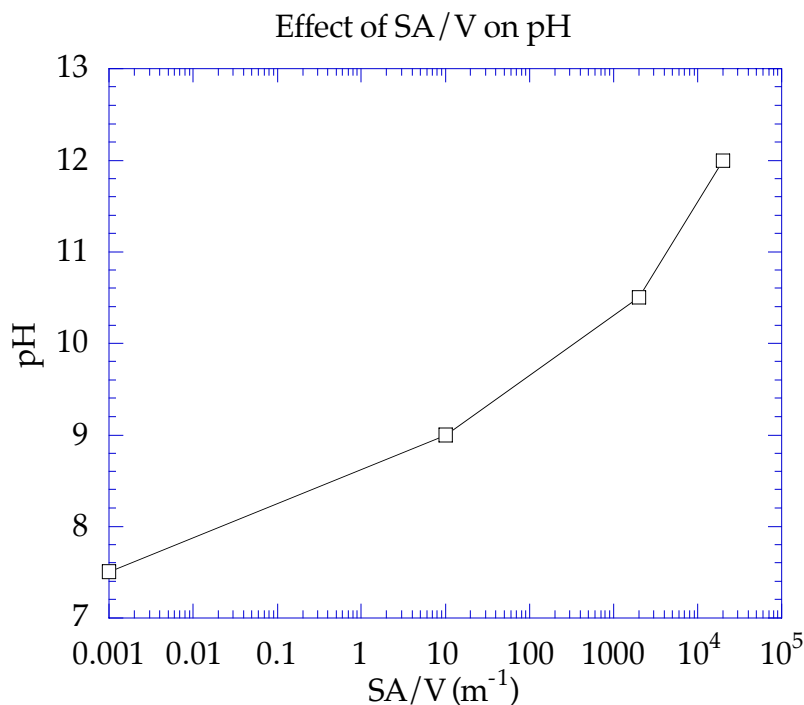


**Figure 3.5.1-4 Steady state pH vs. SA/V ratio of test**

For other temperatures, the same temperature-dependency relation for the long-term rate is assumed for the saturation rate. That is,

$$k_{long} \cong 2.5 \times 10^{\delta} \text{ g} / \text{m}^2 / \text{yr} \quad (3.5.1-6a)$$

$$\delta = 12 - \frac{4550}{T + 273} \quad (3.5.1-6b)$$

Note that here,  $k_{long}$  is identical to  $r_1$  in Eq. 3.5.1-1. More experimental data are needed to improve these numbers.

Clearly, a simplified model of glass dissolution will have numerous conditions and limitations that will make it unable to predict accurate behavior outside a clearly defined and restricted set of conditions. A single mechanistic model that covers the range of hydrologic conditions, from flow-through to bathtub-type scenarios, does not currently exist. However, by making several simplifying assumptions, a simple model based on mechanistic glass-dissolution reaction has been developed and can be used to predict closed-system (bathtub) type conditions and flow-through test conditions with some ability to model hydrologic conditions between those two end-member scenarios.



### 3.5.1 Experimental Parameters for Glass Dissolution

Table 3.5.1-5 Forward and saturation rates for HLW glasses [LL980710651021.049]

Glass/Leachant	SA/V (m <sup>-1</sup> )	Forward Rate	Saturation Rate	Reference
<b>Static Tests</b>				
PNL 76-68/DIW	2,000	1.6	0.08 <sup>a</sup>	A
SRL 165/DIW	2,000	0.80	0.024 <sup>a</sup>	A
EMS-11/DIW	2,000	0.083	0.0016 <sup>a</sup>	A
JSS-A/DIW	10 <sup>b</sup>	1.5	0.0025	B
PNL 76-68/DIW	10 <sup>b</sup>	1.8	0.0075	B
SRL 131/DIW	10 <sup>b</sup>	3.0	0.033	B
SRL 131/J-13 <sup>c</sup>	10	0.14	—	C
SRL 131/J-13	2,000	0.24	0.021	C
SRL 131/J-13	20,000	0.84	0.053	C
SRL 202/J-13	10	0.10		C
SRL 202/J-13	2,000	0.025	0.0016	C
SRL 202/J-13	20,000	0.04	0.0025	C
R7T7/DIW	5	4.9 (100°C)	—	D
R7T7/DIW	50		0.0083	E
R7T7/Volvic <sup>d</sup>	50		0.0133	E
R7T7/DIW	400		0.0045	E
R7T7/Volvic	400		0.025	E
R7T7/Volvic	2,000		0.0006	E
R7T7/Volvic	8,000		0.0006	E
R7T7/Volvic	20,000		<0.0001	E
MW/DIW	1,320	1.1	0.01	F
<b>Dynamic Tests</b>				
SRL 202/pH 7 Buffer		0.28 (80°C)		G
SRL 165 <sup>e</sup> /pH 10.5 Buffer		0.05 <sup>a</sup>		H
SRL 165 <sup>e</sup> /pH 10 Buffer		0.08 (70°C)		I
R7T7/DIW		1.03		J
SRL 131/DIW		2.5		K

<sup>a</sup> Estimated

<sup>b</sup> Values determined from results of both static and dynamic tests

<sup>c</sup> Tuff groundwater: major components are Si(45), Na(55), HCO<sub>3</sub>-(120) in ppm

<sup>d</sup> Granite groundwater: major components are Si(11), Ca(9.8), Na(9.2) HCO<sub>3</sub>-(66) in ppm.

<sup>e</sup> Analog glass without iron

See Cunnane (1993), Volume 2, page 75, for references.

## 3.5.1.6.4 Glass Release from a Waste Package

Adapting data from batch and flow-through tests, two water-contact modes (flow-through and bathtub) are modeled here. In the flow-through mode, as shown in Fig. 3.5.1-5, it is assumed that the water is flowing down the side of a waste glass log without mixing, and keeping a surface area ( $s$ ) wet. In the bathtub mode, the waste package develops a breach, and water flows in and fills up over time, eventually overflowing, as illustrated in Fig. 3.5.1-6. The water inside the container is assumed to be well mixed.

The units used in the PA model are meters, grams, years, and degrees Celsius ( $^{\circ}\text{C}$ ).

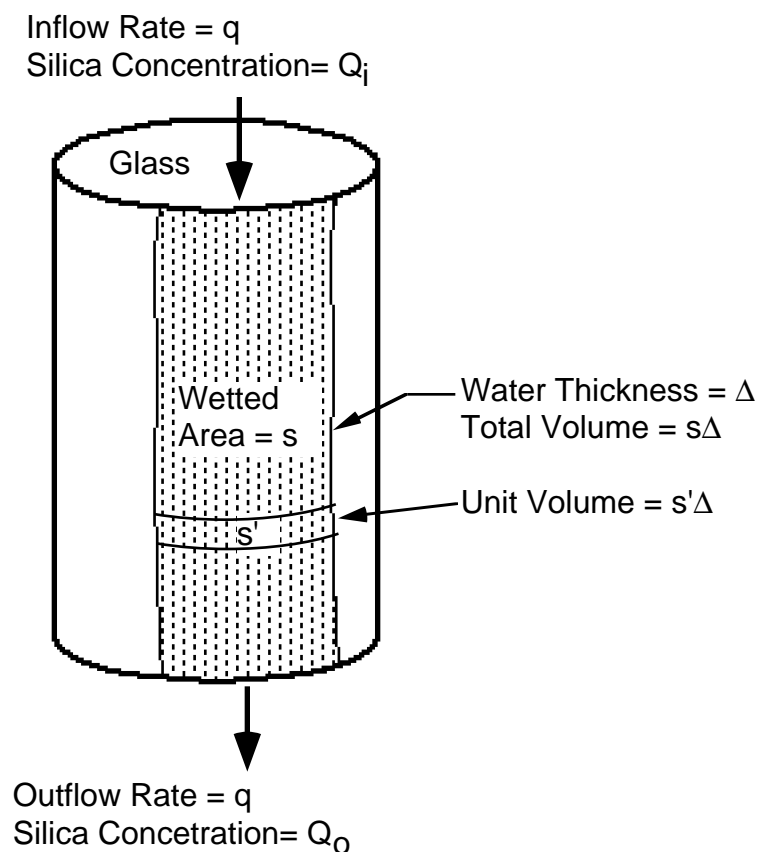


**Figure 3.5.1-5 Flow-through water-contact mode**

Eq. 3.5.1-1 predicts that the dissolution rate will slow down as the dissolution adds to the silica in solution. Silica ( $\text{SiO}_2$ ) is one of the components of glass waste. For example, the DWPF glass contains about 50 wt% of silica (Cunnane, 1993). After water flows inside the waste package, the change of silica concentration in the solution comes from the dissolution of silica released from the glass during alteration process. As the glass dissolves, secondary phases begin to precipitate. A fraction of the silica  $f_p$  contained in the glass will be trapped in the secondary phases—i.e., only  $(1 - f_p)$  of silica in altered glass actually dissolves in the solution. The value of  $f_p$  increases with increasing SA/V ratio and silica concentration in solution. Because there is not sufficient data for consideration of the change of  $f_p$ , a constant intermediate value of  $f_p$  is assumed in this model.

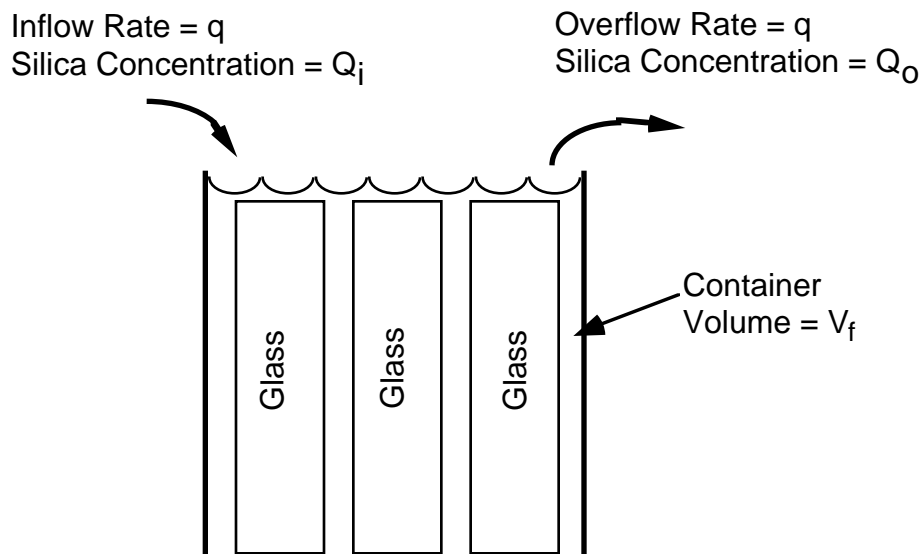


**Figure 3.5.1-6 Bathtub water-contact mode**

On the other hand, the dissolution rate will change because of changes of pH in the solution. The change in pH will be a complex function of the flow rate, buffer capacity of the fluid, and alkali content of the glass. There is insufficient data to obtain a relation for the change of pH due to the dissolution of glass, and only the initial pH value of the inflow groundwater is used in the calculation. This is probably true for the flow-through mode with a high flow rate.

#### 3.5.1.6.5 Flow-Through Mode

The area of the glass log wetted by water ( $s$ ) is usually unknown in the flow-through, water-contact mode. It is to be determined within the model for in-package hydrology. A larger wetted area generally produces a larger release. For glass, the larger area produces a slowdown of alteration rate because of the silica in solution nearing saturation. The two effects oppose each other. Also there is a minimum long-term alteration rate for the rate. The net release rate resulting from these three factors must be evaluated with the numerical model; it cannot be predicted in a simple way.

With a thickness of the water film on the glass of  $\Delta$ , the volume of water covering the glass is  $s\Delta$ . When groundwater of a flow rate of  $q$  covers a portion of surface area as shown in Fig. 3.5.1-5, the time for the water to flow in and out of the package is  $t_{in} = s\Delta/q$ . As the water proceeds downward, the silica increases, and the reaction rate slows. For a steady-state flow condition, the glass-dissolution condition can be considered as a unit volume of water ( $s\Delta$ ) contacting the glass for a duration of  $t_{in}$ . The increase of silica concentration during a time interval  $dt$

$$dQ = \frac{s\Delta f_{si}(1 - f_p)}{s\Delta} \left(1 - \frac{Q}{K}\right) dt \quad (3.5.1-7)$$

where  $f_{si}$  = fraction of silica in glass. Therefore,

$$-\ln\left(1 - \frac{Q}{K}\right) = \frac{kf_{si}(1 - f_p)t}{K\Delta} + C \quad (3.5.1-8)$$

where C is a constant depending on the initial conditions. If the silica concentration of incoming groundwater is  $Q_i$  and that of outgoing is  $Q_o$  after a duration of  $t_{sn}$ , then

$$Q_o - Q_i = K\left(1 - \frac{Q_i}{K}\right)[1 - \exp(-\alpha)] \quad (3.5.1-9)$$

where

$$\alpha = f_{si}(1 - f_p) \frac{ks}{Kq}$$

If  $\beta = ks/Kq$ , one can see that a high water-refresh rate gives a low value of  $\beta$ . When  $\beta$  is high, the system approaches a saturated condition. Also  $f_p$  starts changing toward high values, but there are not very precise data for  $f_p$ . The intermediate value of 0.5 is used.

Because only a fraction of silica  $f_{si}(1 - f_p)$  in the waste glass dissolves in the solution, the total mass of dissolved glass per unit volume of outgoing water should be

$$G_o = \frac{Q_o - Q_i}{f_{si}(1 - f_p)} \quad (3.5.1-10)$$

The dissolution rate (g/yr) from the whole waste glass in the waste package for the flow-through, water-contact mode is

$$R = qG_o = \frac{q(Q_o - Q_i)}{f_{si}(1 - f_p)} = \frac{qK}{f_{si}(1 - f_p)}\left(1 - \frac{Q_i}{K}\right)[1 - \exp(-\alpha)] \quad (3.5.1-11)$$

According to data in Table 3.5.1-2,  $K$  (g/m<sup>3</sup>) can be expressed as a function of  $T$  (°C):

$$K = 6.0 \times 10^{-5} + 1.90 \times 10^{-6} T + 1.25 \times 10^{-8} T^2 \quad (3.5.1-12)$$

When the silica concentration is very near its saturation limit, a long-term rate applies. The mass of glass dissolved in a unit volume of water in a time interval  $dt$  is

$$dG = \frac{s' k_{long}}{s' \Delta} dt \quad (3.5.1-13)$$

The dissolved glass mass per unit volume of water exiting the waste package is

$$G_o = \frac{k_{long} t_{in}}{\Delta} = \frac{s k_{long}}{q} \quad (3.5.1-14)$$

### 3.5.1 Experimental Parameters for Glass Dissolution

---

Thus,

$$R = qG_o = sk_{long} \quad (3.5.1-15)$$

#### 3.5.1.6.6 Bathtub Mode

During filling of the container, it is assumed that the fraction of wetted area increases in proportion to the fraction of the filled volume in the container, as shown in Fig. 3.5.1-6. That is,

$$\frac{A(t)}{V(t)} = \frac{s}{V_f} \quad (3.5.1-16)$$

where

- A(t) = wetted surface area of glass at time t
- V(t) = volume of water in the container at time t equal to q t
- s = total surface area of glass in the waste package
- V<sub>f</sub> = water volume of bathtub when filled

The increment of silica concentration during a time interval before overflowing is

$$dQ = \frac{A(t)}{V(t)} kf_{si}(1-f_p) \left(1 - \frac{Q}{K}\right) dt = \frac{s}{V_f} kf_{si}(1-f_p) \left(1 - \frac{Q}{K}\right) dt \quad (3.5.1-17)$$

The surface area of the glass logs decreases as the glass dissolves. Conservatively, it can be assumed the surface area remains at the initial value during the filling period. Then,

$$-\ln\left(1 - \frac{Q}{K}\right) = \frac{s}{KV_f} kf_{si}(1-f_p)t + C_1 \quad (3.5.1-18)$$

where C<sub>1</sub> is a constant depending on the initial conditions. The time for filling the container is t<sub>f</sub> = V<sub>f</sub>/q. If the silica concentration of incoming groundwater is Q<sub>i</sub>, and that, at the time of overflow, is Q<sub>f</sub>, then

$$Q_f - Q_i = K \left(1 - \frac{Q_i}{K}\right) \left[1 - \exp\left(-\frac{skf_{si}(1-f_p)t_f}{KV_f}\right)\right] = K \left(1 - \frac{Q_i}{K}\right) [1 - \exp(-\alpha)] \quad (3.5.1-19)$$

where  $\alpha = f_{si}(1-f_p) \frac{ks}{Kq}$ .

To estimate the mass of glass dissolved during filling, one considers the possible maximum increase of silica concentration of the solution inside the container:

$$(Q_f - Q_i)_{\max} = K \left(1 - \frac{Q_i}{K}\right) \quad (3.5.1-20)$$

According to Table 3.5.1-2, the silica concentration increase at 90°C is 0.000225 g/m<sup>3</sup>. For 4 glass logs with 0.3 m radius and 2.2 m length inside a container with a radius of 0.80 m and a length of 3.76 m, the bathtub volume,  $V_b$  is 5.072 m<sup>3</sup>. Assuming  $f_{si} = 0.45$  and  $f_p = 0.5$ , one obtains the mass of dissolved glass during filling = 0.000225x5.072/(0.45x0.5) = 0.0051 g. This loss of mass is negligible compared with the initial mass of the 4 glass logs at 6720 kg. Therefore, the assumption of constant surface area of glass is appropriate during the filling period.

After filling (i.e.,  $t > t_f$ ) the change of silica in the water inside the container will be

$$V_f dQ = \left[ skf_{si}(1 - f_p) \left( 1 - \frac{Q}{K} \right) - (Q - Q_i)q \right] dt = [(\alpha K + Q_i) - (\alpha + 1)Q] q dt \quad (3.5.1-21)$$

The loss of mass of glass over a long period after filling can be significant. To deal with changes of surface area resulting from the dissolved mass of the glass logs, calculations can be performed with time steps. Again, the surface area can be conservatively assumed constant as the initial value. Solving the differential equation with the boundary conditions at the time of overfilling, one obtains

$$Q_o - Q_i = \frac{\alpha K}{\alpha + 1} \left( 1 + \frac{Q_i}{K} \right) [1 - \exp(-\tau)] + (Q_f - Q_i) \exp(-\tau) \quad (3.5.1-22)$$

where

$$\tau = \frac{(1 + \alpha)(t - t_f)}{t_f}$$

For a steady state. when  $t \rightarrow \infty$ ,  $\exp(-\tau) \rightarrow 0$ ,

$$Q_o - Q_i = \frac{\alpha K}{\alpha + 1} \left( 1 - \frac{Q_i}{K} \right) \quad (3.5.1-23)$$

The release rate (g/yr) of the waste glass from the waste package for the bathtub mode is

$$R = \frac{q(Q_o - Q_i)}{f_{si}(1 - f_p)} \quad (3.5.1-24)$$

For the long-term silica-saturated condition

$$R = s k_{long} \quad (3.5.1-25)$$

### 3.5.1.7 Solubility-Limited Radionuclide Release from Glass

The following data provide radionuclide solubility limits for the elements U, Pu, Np, Am, Sr, and Cs calculated for SRL-202-type HLW glasses reacting in J-13 water. The data from the calculations are compared with radionuclide concentrations measured in laboratory glass dissolution.

### 3.5.1 Experimental Parameters for Glass Dissolution

Radionuclide concentrations are calculated for four scenarios. Two are closed systems in which the redox state and total carbon were controlled entirely through reactions between J-13 water and the glass reactant. The other two scenarios are for open conditions in which the total carbon and redox state of the fluid are controlled by atmospheric gases assumed to be present in the proposed underground repository at Yucca Mountain. For the open-system simulations, the pressures of carbon dioxide and oxygen gases are assumed to be 0.00032 bars and 0.20 bars, respectively, their average atmospheric values. The compositions of J-13 water and the SRL-202 glass used in the simulations are given in Table 3.5.1-6 and Table 3.5.1-7, respectively.

**Table 3.5.1-6      Composition of J-13 well water used in the simulation  
(Delaney, 1985)**

Component	Concentration (mg/L)	Component	Concentration (mg/L)
Li	0.042	Si	27.0
Na	43.9	NO <sub>3</sub>	9.6
K	5.1	F	2.2
Ca	12.5	Cl	6.9
Mg	1.9	HCO <sub>3</sub>	125.3
Sr	0.035	SO <sub>4</sub>	18.7
Al	0.012	pH	7.6
Fe	0.006		

**Table 3.5.1-7      Composition of SRL-202 glass used in simulation [LL980710651021.049]**

Glass SRL-202 Reduced Component Set						
Oxide	Element	Oxide (wt %)	Oxide (mole %)	Element (wt %)	Element (mole %)	Cation (mole %)
SiO <sub>2</sub>	Si	48.9500	56.53	22.88	17.21	40.72
Al <sub>2</sub> O <sub>3</sub>	Al	3.8400	2.61	2.03	1.59	3.76
B <sub>2</sub> O <sub>3</sub>	B	7.9700	7.94	2.48	4.84	11.44
Mn <sub>2</sub> O <sub>3</sub>	Mn	1.0033	0.44	0.70	0.27	0.64
Fe <sub>2</sub> O <sub>3</sub>	Fe	11.4100	4.96	7.98	3.02	7.14
Na <sub>2</sub> O	Na	8.9200	9.99	6.62	6.08	14.39
K <sub>2</sub> O	K	3.7100	2.73	3.08	1.66	3.94
Li <sub>2</sub> O	Li	4.2300	9.82	1.97	5.98	14.15
Cs <sub>2</sub> O	Cs	0.0720	0.02	0.07	0.01	0.03
CaO	Ca	1.2000	1.48	0.86	0.45	1.07
MgO	Mg	1.3200	2.27	0.80	0.69	1.64
SrO	Sr	0.1100	0.07	0.09	0.02	0.05
MnO	Mn	0.9016	0.88	0.70	0.27	0.64
U <sub>3</sub> O <sub>8</sub>	U	1.9300	0.16	1.64	0.15	0.34

Glass SRL-202 Reduced Component Set						
Oxide	Element	Oxide (wt %)	Oxide (mole %)	Element (wt %)	Element (mole %)	Cation (mole %)
NpO <sub>2</sub>	Np	0.0080	0.00	0.01	0.00	0.00
PuO <sub>2</sub>	Pu	0.0220	0.01	0.02	0.00	0.00
Am <sub>2</sub> O <sub>3</sub>	Am	0.0004	0.00	0.00	0.00	0.00
ThO <sub>2</sub>	Th	0.2600	0.07	0.23	0.02	0.05
<b>Totals</b>		95.8573	100.00	95.86	100.00	100.00

Two types of calculations were carried out for both the closed and open systems. In the first, all possible mineral phases that can form were allowed to precipitate as alteration minerals. This included mineral phases that, for kinetic reasons, generally do not form at low temperatures or over short time periods. In the second simulation, phases (see Table 3.5.1-8) that are known or that are suspected not to precipitate rapidly at low temperatures were suppressed. Note that list in Table 3.5.1-8 includes some highly insoluble actinide oxide phases (PuO<sub>2</sub>, NpO<sub>2</sub>, and Am<sub>2</sub>O<sub>3</sub>), which results in predictions of much higher actinide solubilities for the second case than for the first case. The list also includes phases, such as quartz and andradite, that do not contain radionuclides, but which are known, from observations of natural analogs, not to form readily at low temperatures. One consequence of suppressing these phases is that the solution concentrations of some elements, such as Si and Al, increase to higher values during the simulation than is the case for simulations when the phases are not suppressed. This affects the solubility limits for the radionuclides by changing the amounts of ligands available for complexation, the solution pH, and the concentrations of competing metals. The ultimate effect of the suppression of these phases on radionuclide solubilities is therefore complex, as discussed subsequently.

**Table 3.5.1-8 Phases suppressed in glass dissolution simulation in “metastable” calculation**

Name	Formula	Name	Formula
	Am <sub>2</sub> C <sub>3</sub>		PuO <sub>2</sub>
	Am <sub>2</sub> O <sub>3</sub>		NpO <sub>2</sub>
	AmO <sub>2</sub>	Quartz	SiO <sub>2</sub>
Andradite	Ca <sub>3</sub> Fe <sub>2</sub> (SiO <sub>4</sub> ) <sub>3</sub>	Rhodonite	MnSiO <sub>3</sub>
Dolomite	CaMg(CO <sub>3</sub> ) <sub>2</sub>	Talc	Mg <sub>3</sub> Si <sub>4</sub> O <sub>10</sub> (OH) <sub>2</sub>
K-Feldspar	KAlSi <sub>3</sub> O <sub>8</sub>	Tephroite	Mn <sub>2</sub> SiO <sub>4</sub>
	Np <sub>2</sub> O <sub>5</sub>	Thorianite	ThO <sub>2</sub>
Petalite	LiAlSi <sub>4</sub> O <sub>10</sub>	Tridymite	SiO <sub>2</sub>

Each simulation begins with one liter of J-13 water and one gram of SRL-202 glass. All calculations were performed using the GEMBOCHS version EQ3/6 (Wolery, 1992) V8-R6 composite data file. The glass and water were allowed to react at a fixed rate until the one gram of glass has completely reacted. The system was then composed of a modified water composition in equilibrium with a set of alteration minerals that formed during the reaction. The choice of one gram of glass per liter fluid was arbitrary. Simulations using a smaller



### 3.5.1 Experimental Parameters for Glass Dissolution

amount of glass show that the pH and Eh of the system are not yet dominated by the glass; the system is relatively insensitive to reacting to greater amounts of glass. The results provide an approximation of "bathtub-type" repository situations in which water has breached the glass containment and sits in contact with the glass for extended periods of time under relatively stagnant conditions. A more precise time of reaction is impossible to estimate without including more details (e.g., flow rates) of hydrologic conditions.

Table 3.5.1-9 shows the results of the four simulations: the first part shows the closed system results, and the second part shows the open system results. The line labeled "Total" gives the total amount of radionuclide in the one gram of glass. For each element, this is the conservative maximum available for colloidal transport. The next four lines provide the solubility of each radionuclide (if solubility-limited), the stable phase containing that element that controls the solubility, and the dominant aqueous complex of that element. The first case is for control by metastable solids (as discussed previously), and the second case allows all potential precipitates to form. Note that, because the systems are constrained differently (closed versus open), the solutions for the two cases are at much different values of pH,  $f_{O_2}$ , and  $f_{CO_2}$ . (see Table 3.5.1-9 caption). The radionuclide solubilities are being compared under much different conditions, and the difference in values can provide an indication of the sort of variability in solution concentrations that can be expected for differing repository conditions.

**Table 3.5.1-9 Radionuclide concentrations and equilibrium phases calculated for SRL-202 glass reaction with J-13 water**

Element	U	Np	Pu	Am	Cs	Sr
<b>Closed System (pH = 10.8, log <math>f_{O_2}</math> = -45, log <math>f_{CO_2}</math> = -6.6)</b>						
Total (mg)	16.4	0.07	0.19	0.003	0.68	0.93
Soluble (metastable)	0.5E-3	0.5E-3	0.4E-3	0.7E-4	0.68	0.5E-2
Stable Phase	haiweeite	Np(OH) <sub>4</sub>	Pu(OH) <sub>4</sub>	Am(OH) <sub>3</sub>	—	SrCO <sub>3</sub>
Dominant Complex	UO <sub>2</sub> (OH) <sub>3</sub> <sup>-</sup>	Np(OH) <sub>4</sub> (aq)	Pu(OH) <sub>4</sub> (aq)	Am(OH) <sub>2</sub> <sup>+</sup>	Cs <sup>+</sup>	Sr <sup>2+</sup>
Solubility-Limited	yes	yes	yes	yes	no	yes
Soluble (xtal)	0.8E-3	0.2E-11	0.3E-11	0.6E-4	0.68	0.5E-2
Stable Phase	CaUO <sub>4</sub>	NpO <sub>2</sub>	PuO <sub>2</sub>	Am(OH) <sub>3</sub>	—	SrCO <sub>3</sub>
Dominant Complex	UO <sub>2</sub> (OH) <sub>3</sub> <sup>-</sup>	Np(OH) <sub>4</sub> (aq)	Pu(OH) <sub>4</sub> (aq)	Am(OH) <sub>2</sub> <sup>+</sup>	Cs <sup>+</sup>	Sr <sup>2+</sup>
Solubility-Limited?	yes	yes	yes	yes	no	yes
<b>Open System (pH = 8.9, log <math>f_{O_2}</math> = -0.7, log <math>f_{CO_2}</math> = -3.5)</b>						
Total (mg)	16.4	0.07	0.19	0.003	0.68	0.93
Soluble (metastable)	0.24	0.07	0.03	0.001	0.68	0.02
Stable phase	haiweeite	—	PuO <sub>2</sub> (OH) <sub>2</sub>	AmPO <sub>4</sub> (am)	—	SrCO <sub>3</sub>
Dominant Complex	UO <sub>2</sub> (CO <sub>3</sub> ) <sub>3</sub> <sup>4-</sup>	NpO <sub>2</sub> CO <sub>3</sub> <sup>-</sup>	PuO <sub>2</sub> (CO <sub>3</sub> ) <sub>2</sub> <sup>2-</sup>	Am(CO <sub>3</sub> ) <sub>2</sub> <sup>-</sup>	Cs <sup>+</sup>	Sr <sup>2+</sup>
Solubility-Limited	yes	no	yes	yes	no	yes

### 3.5.1 Experimental Parameters for Glass Dissolution

Element	U	Np	Pu	Am	Cs	Sr
Open System (pH = 8.9, log $f_{O_2}$ = -0.7, log $f_{CO_2}$ = -3.5)						
Soluble (xtal)	1.6	0.07	0.9E-6	0.001	0.68	0.02
Stable Phase	Haiweeite	—	PuO <sub>2</sub>	AmPO <sub>4</sub> (am)	—	SrCO <sub>3</sub>
Dominant Complex	UO <sub>2</sub> (CO <sub>3</sub> ) <sub>3</sub> <sup>4-</sup>	NpO <sub>2</sub> CO <sub>3</sub> <sup>-</sup>	PuO <sub>2</sub> (CO <sub>3</sub> ) <sub>2</sub> <sup>2-</sup>	Am(CO <sub>3</sub> ) <sub>2</sub> <sup>-</sup>	Cs <sup>+</sup>	Sr <sup>2+</sup>
Solubility-Limited?	yes	no	yes	yes	no	yes

All radionuclide amounts in milligrams (mg).

"Total" indicates total amount of radionuclide released from reaction of one gram of SRL-202 glass.

"Soluble (meta)" is amount of radionuclide in one liter of solution (mg/L) in equilibrium with more soluble (metastable) phase indicated as "stable phase."

"Dominant complex" is dominant aqueous species for given element.

"Soluble (xtal)" is amount of radionuclide in one liter of solution (mg/L) in equilibrium with most stable (crystalline) phase labeled "stable phase."

For all four simulations, U, Pu, Am, and Sr were always solubility-controlled, generally to a much lower value than the total element available. Of the actinides, only Np was found not to be solubility-controlled. Under open system conditions, the relatively high solubility of oxidized Np combined with high carbonate concentrations due to additions of CO<sub>2</sub> from air stabilized the NpO<sub>2</sub>CO<sub>3</sub><sup>-</sup> complex to where the least soluble Np phase, NpO<sub>2</sub>, was still a half log unit undersaturated at 0.07 mg/L aqueous Np concentration. Under reducing conditions (closed system), the Np was always solubility-controlled.

An important conclusion from Table 3.5.1-9 is that actinide solubilities are extremely sensitive to whether highly ordered anhydrous crystalline phases (i.e., PuO<sub>2</sub>) or metastable phases such as Pu(OH)<sub>4</sub> control actinide solubilities. These differences can be as high as 7 log units for Pu and Np.

Notice that, unlike the other actinides, uranium solubilities actually decreased when the metastable phases were used to control solubilities. This is true for uranium mainly because of the increased silica concentrations in the metastable-phase-alteration simulations because of suppression of quartz. Greater silica in solution increased the stability of uranium silicate phases such as Haiweeite, which lowered uranium solubility.

Figure 3.5.1-7 graphically depicts the information Table 3.5.1-9. The soluble fraction of total radionuclide inventory available from one gram of glass is plotted for the metastable solids assemblage and for the stable solids assemblage. If the element is not solubility-controlled (i.e., Cs), the entire inventory is available and no bar is shown.

### 3.5.1 Experimental Parameters for Glass Dissolution

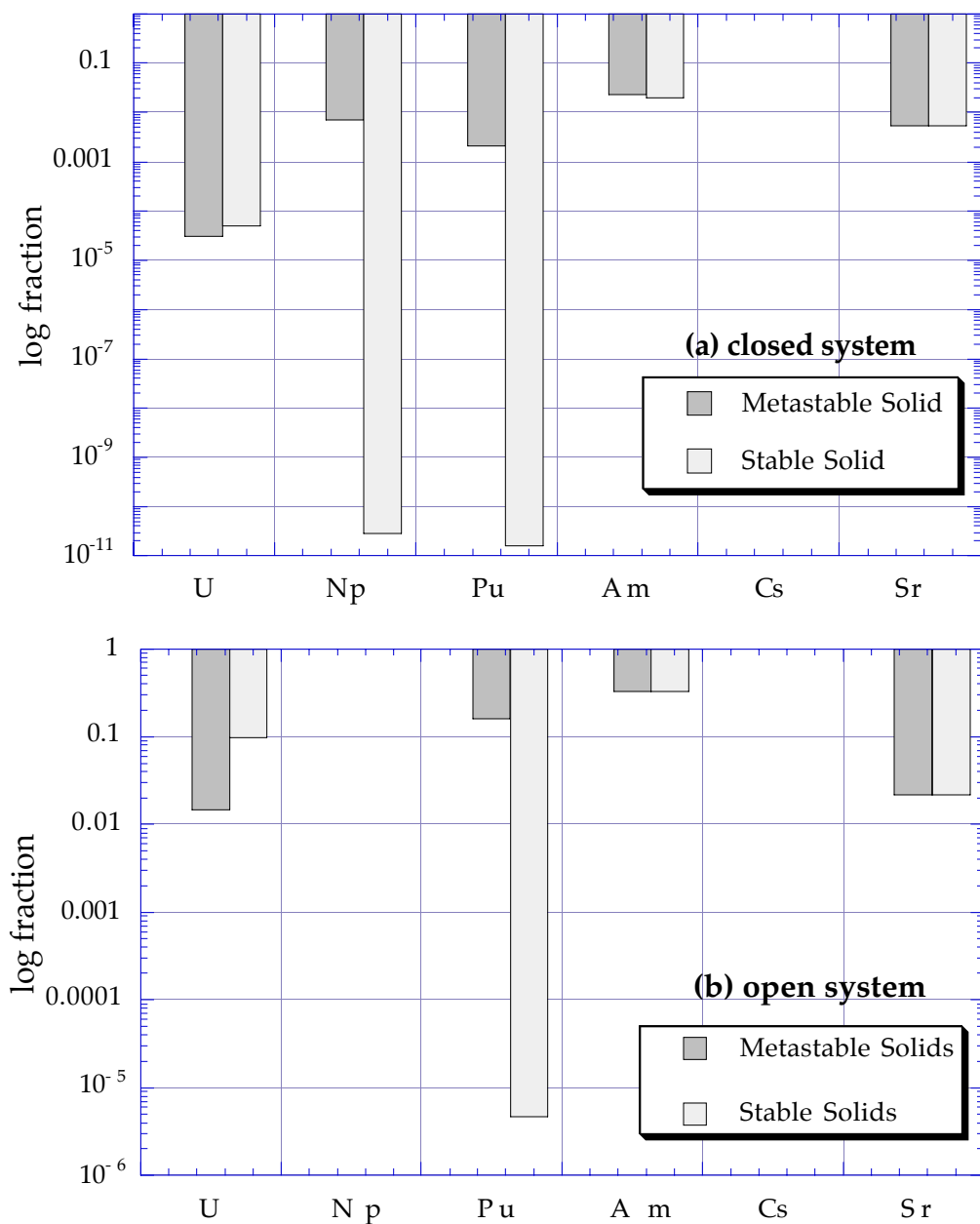


**Figure 3.5.1-7** Histograms showing fractions of radionuclide inventory in glass available for transport for (a) closed-system simulation and (b) open-system simulation. Three cases are shown for each element: (1) no solubility control (all values = 1), (2) solubility control by metastable solids (3) solubility control by stable solids. Data are from Table 3.5.1-9.

#### 3.5.1.8 Comparison With Laboratory Results

Measured actinide releases from long-term drip tests of HLW glasses have been reported by Fortner and Bates (1995). Data from their N2-10 test are shown in Figure 3.5.1-8. These were unsaturated (drip) tests of EJ-13 water onto SRL-165 glass. Unfortunately, for several reasons, these experimental data cannot be directly compared to the model calculations:

- The tests report the entire released inventory of actinides, including soluble, colloidal, and adsorbed masses. The EQ3/6 model calculated only the soluble amounts. Precipitated actinide solids are included in the masses of precipitated secondary phases. EQ3/6 cannot predict the relative amounts of these solids that remain on the glass monolith versus those that flake off and fall to the bottom of the test vessel.
- The tests are of older formulation SRL-165 glasses and cannot be compared directly with the model calculations, which are for the current SRL-202 glass composition.
- The data reported do not include the amounts of fluid in which the total masses of actinides were measured, so they cannot be converted to concentration units needed to determine the relative saturation states of the actinides.

These apparent shortfalls are a consequence of the defined purpose of these tests, which were intended to simulate, as closely as possible, anticipated repository conditions and which were, therefore, not optimum for validating modeling studies. It is still useful to compare trends and relative solubilities of actinides between the experiments and these simulations. The drip-test procedure calls for periodic refreshing of the test vessel with air. The drip-test methodology correlates best with the model's open-system simulations, in which the system stays equilibrated with air. The Fortner and Bates results show that Np is the most soluble actinide; this is in agreement with the simulation results. There is no indication of solubility control of Np release in these tests, which is consistent with the model's calculated results. Am and Pu are generally released at rates 3 to 4 log units slower than Np is released. Their release is probably solubility-controlled. This is consistent with Pu solubility control by some metastable solid somewhat less stable than pure crystalline  $\text{PuO}_2$ . The amount of released uranium is intermediate between Np and Pu; this is also in agreement with the modeling results.

The increased release of Pu and Am occurring after about 8 yr, shown in Figure 3.5.1-8, is thought to be due to spallation of the actinide-containing rinds of alteration minerals to the bottom of the test vessel. The spalled material is potentially available for colloidal transport.

More exact comparison of the model results with the experiments depends on the better characterization of the alteration products that control actinide solubilities (work that is in progress) and on a better estimate of the effective oxidation state and pH of the fluid inside the test vessel. Actinide solubilities are highly dependent on Eh and pH. Overall, the model results are in qualitative agreement with the experimental observations.

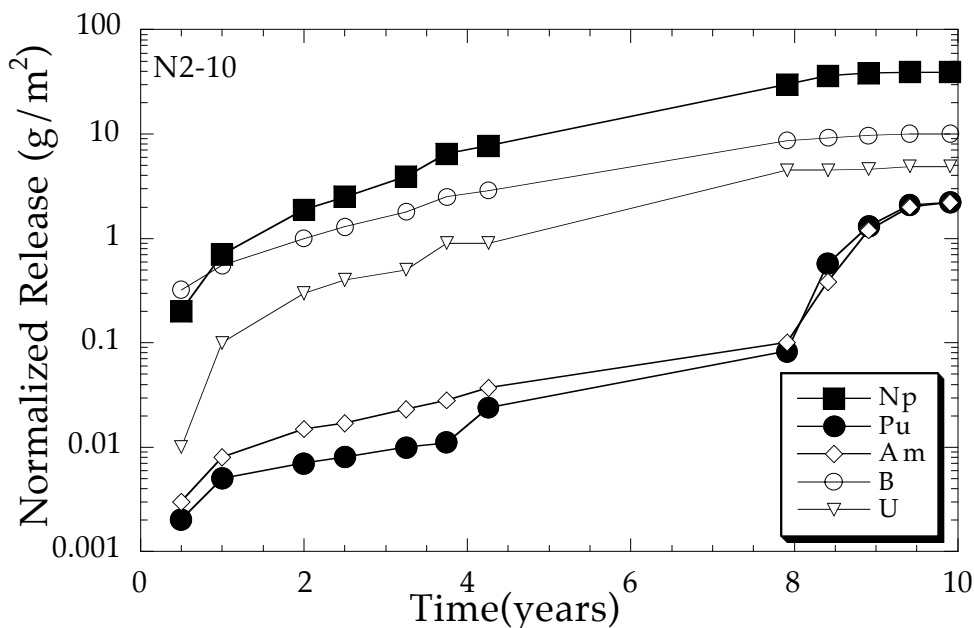


**Figure 3.5.1-8** Experimental data modified from Figure I-7 in Fortner and Bates (1995) showing the normalized release of actinides from SRL-165 glass in an unsaturated (drip) test. Release values shown include cumulative soluble, sorbed, and colloidal release. [LL96010651022.008]

#### 3.5.1.9 Effect of Dissolved Iron on Borosilicate Glass Dissolution

Flow-through borosilicate glass-dissolution experiments were performed in pH-buffered solutions ranging in pH from 6 to 12 and doped with dissolved ferric iron ( $\text{Fe}^{3+}$ ) at 70°C. The iron concentrations were at saturation with amorphous ferric hydroxide ( $\text{Fe}(\text{OH})_3$ ) at each pH. No difference in dissolution rate was found for iron-doped versus iron-free solutions at any pH. This result suggests there will be no deleterious effect of dissolved iron on glass-dissolution rates in a repository for the range of dissolved iron concentrations used in these experiments. However, ferric iron colloids may affect glass-dissolution rates if they cause the removal of dissolved silica from solutions. No iron colloids were present in these tests.

##### 3.5.1.9.1 Introduction

Although solution composition apparently has an important effect on the dissolution rate of borosilicate glasses, there has been little experimental data obtained that can be used to quantify this effect for different elements in solution. Flow-through dissolution tests have been performed on the simple analog SRL-202 glass composition (Table 3.5.1-10) in pH-buffered solutions that have been doped with small amounts of dissolved iron to provide quantification of the effect of dissolved iron on glass dissolution rates. The solution compositions, iron concentrations, and pH buffers used are given in Table 3.5.1-11.

**Table 3.5.1-10** Compositions of glass tested in mole percent oxide and cation mole percent (S-202 glass is a simple analog of SRL-202 glass) [LL980710651021.049]

Oxide/Cation	Mole % Oxide		Cation Mole %	
	SRL-202	S-202	SRL-202	S-202
SiO <sub>2</sub>	55.44	55.6	40.1	40.9
Al <sub>2</sub> O <sub>3</sub>	2.56	8.1	3.7	11.5
Fe <sub>2</sub> O <sub>3</sub>	4.86	—	7.0	—
B <sub>2</sub> O <sub>3</sub>	7.79	8.0	11.3	11.3
Na <sub>2</sub> O	9.79	22.7	14.2	32.3
Li <sub>2</sub> O	9.63	—	13.9	—
CaO	1.46	5.7	1.2	4.1
MgO	2.23	—	1.6	—
MnO	1.10	—	0.6	—
SrO	0.02	—	0.01	—
BaO	0.10	—	0.07	—
NiO	0.75	—	0.5	—
U <sub>3</sub> O <sub>8</sub>	0.16	—	0.3	—

**Table 3.5.1-11** Composition of solutions used in flow-through dissolution tests

pH	Buffer	Iron Concentration
6	0.005 molal Ortho-phthalic acid + KOH	$3.3 \times 10^{-7}$ molal FeCl <sub>3</sub>
8	0.005 molal Boric Acid + KOH	$7.8 \times 10^{-8}$ molal FeCl <sub>3</sub>
10	0.005 molal Boric Acid + KOH	$2.6 \times 10^{-7}$ molal FeCl <sub>3</sub>
12	0.013 molal KOH	$2.2 \times 10^{-5}$ molal FeCl <sub>3</sub>

The effect of solution composition on glass-dissolution rates is incorporated into a kinetic model for glass dissolution with a rate equation of the form shown in Eq. 3.5.2-1. The effects of dissolved species in solution are included in the product term (P). Eq. 3.5.2-1 shows that the solution composition can affect the glass dissolution rate in two ways: through the affinity term or directly on the value of the rate constant. These experiments can be used to determine the coefficients of the product term. They are designed to exclude saturation effects because the solution composition is chosen to be far from glass (silica) saturation.

#### 3.5.1.9.2 Experimental Methods

The glass was dissolved in single-path, flow-through (SPFT) cells using pH buffers of ortho-phthalic acid, borate, and KOH-KCl at ionic strengths of 0.005 molal. Powdered glasses (surface area = 450 cm<sup>2</sup>/g) in 3-ml cells react with buffer solutions at flow rates of 50 to

### 3.5.1 Experimental Parameters for Glass Dissolution

100 ml/day. Experimental data typically show steady-state dissolution rates after a few days. No change in steady-state dissolution rates was found when flow rates were doubled, indicating the systems behaved as continuously stirred reactors in that the dissolution rates were not rate-limited by transport away from the glass reaction surface.

The pH buffers were doped with  $\text{Fe}^{3+}$  (added as  $\text{FeCl}_3$ ) with the concentrations fixed at amorphous  $\text{Fe}(\text{OH})_3$  saturation at each pH. This is likely to be the maximum dissolved iron concentration in repository waters because ferric hydroxide readily precipitates from supersaturated solutions.

A five-component analog of the SRL-202 glass composition, rather than SRL-202 glass, was used in the test. The analog was prepared by adjusting the mole fraction of each component in the analog glass to equal the sum of the mole fractions of the components in the actual glass that were judged to occupy similar structural sites in the glass. This determination was based on crystal chemical principles, including primarily ion size and radius. For example, the sodium content of the S-202 glass was determined by adding the molar concentrations of all the alkalis in the SRL-202 glass. Similar calculations were performed for Ca, Al, and Si in the analog glass. The mole fraction of B was kept equal to that of the waste glass. The simple glasses avoid the problems in data interpretation due to redox reactions during dissolution and precipitation of insoluble secondary phases in real waste glasses. Iron and manganese are particular problems.

#### 3.5.1.9.3 Results and Discussion

The effects on the glass-dissolution rate of doping the buffers with Fe can be seen in Fig. 3.5.1-9, which shows the release rate of silica from the glass as a function of pH for both undoped and doped buffers. Apparently, dissolved iron has little effect on glass-dissolution rates over the pH range and iron concentration range tested. The data points for the iron-doped and undoped buffers lie essentially on top of each other, and their differences in all cases are less than the precision of the experimental method.

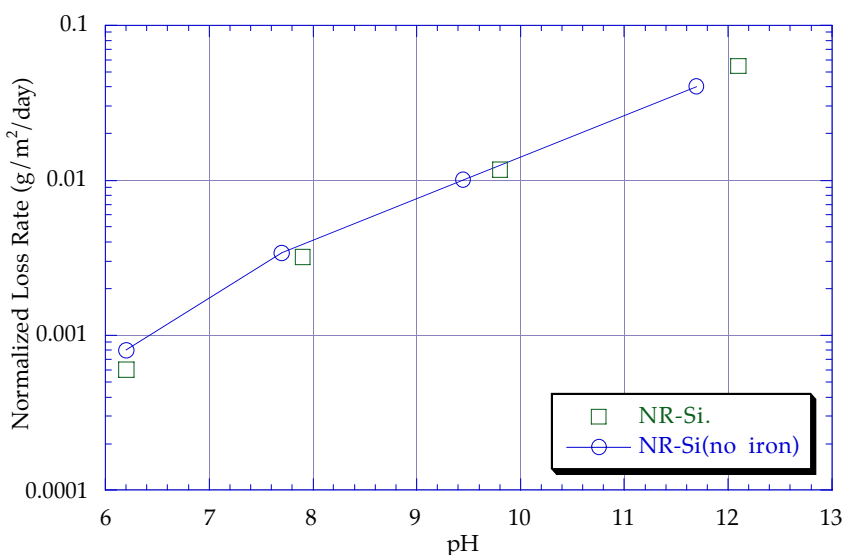


**Figure 3.5.1-9** Normalized loss rate (dissolution rates) for SRL-202 analog glass in pH buffer with and without aqueous Fe present at  $\text{Fe}(\text{OH})_3$  saturation. There appears to be little effect of the dissolved iron on glass dissolution rates. [LL980710651021.049]

These results are consistent with several previous studies of the effect of iron on borosilicate glass dissolution in which borosilicate glass was leached in the presence of various metal phases, including 304L stainless steel, the pour canister material (Bates et al., 1988; Bibler and Jantzen, 1987; Burns et al., 1986). In all of these studies, the iron had little or no effect on the glass-dissolution rate.

Other studies have noted an enhancement of glass-dissolution rates, presumably due to the presence of iron-containing materials in the system (Bart et al., 1987; Inagaki et al., 1996; McVay and Buckwalter, 1982). It is concluded in each of these studies that it is the sorption of silica onto iron colloids, or the sorption of silica onto iron-containing solids, that causes the glass to dissolve more quickly by lowering the silica concentration in solution. The system is therefore farther from silica saturation, and the glass dissolves more quickly under those conditions. Presumably, these later experiments contained iron solids with higher surface areas than did tests where no iron effect was noticed. In some cases, the iron-containing material was much more reactive than 304L stainless steel (i.e., McVay and Buckwalter [1982] used ductile iron, which corrodes much more rapidly and evidently gave rise to iron colloids).

It is concluded that the presence of iron in a waste repository can have a significant negative impact on borosilicate glass performance only if it either leads to the development of colloids that sorb silica or presents a large amount of surface area for silica sorption. In both cases, the amount of colloids or surface area must be sufficient to significantly decrease the concentration of dissolved silica due to sorption. The presence of dissolved iron alone apparently has little effect on the glass dissolution rate.

#### 3.5.1.10 References

- Bart G., H. U. Zwicky, E. T. Aerne, T. Graber, D. Z'Berg, and M. Tokiwai (1987). "Borosilicate glass corrosion in the presence of steel corrosion products." In proceedings from Materials Research Society Symposium. **84**:459–470.
- Bates J. K., W. L. Ebert, D. F. Fisher, and T. J. Gerding (1988). "The reaction of reference commercial waste glasses during gamma irradiation in a saturated tuff environment." *J. Mat. Res. Soc.* **3**:576–597. [NNA.19900125.0073]
- Baxter, R. G. (1983). *Description of defense waste processing facility reference waste form and container*. (Dp-1606). Aiken, SC: Savannah River Site. [NNA.19890327.0057]
- Bibler N. E., and Jantzen, C. M. (1987). "Materials interactions relating to long-term geologic disposal of nuclear waste glass." In proceedings from Materials Research Society Symposium. **84**:47–66. [NNA.19900125.0116]
- Burns D. B., B. H. Upton, and G. G Wicks (1986). "Interactions of SRP waste glass with potential overpack materials." *J. Non-Crys. Sol.* **84**:258–267.
- Cunnane, J. C. (1993). *High-level waste borosilicate glass: a compendium of corrosion characteristics*. (DOE-EM-0177) Washington, DC: U.S. Department of Energy, Office of Waste Management.
- Delage, F., D. Ghaleb, J. L. Dussossoy, O. Chevallier, and E. Vernaz (1992). "A mechanistic model for understanding nuclear waste." *J. Nucl. Mat.* **190**:191–197.



### 3.5.1 Experimental Parameters for Glass Dissolution

---

- Delaney, J. M. (1985). *Reaction of Topopah Spring Tuff with J-13 water: a geochemical modeling approach using the EQ3/6 reaction path code*. (UCRL-53631) Livermore, CA: Lawrence Livermore National Laboratory. [HQS.19980517.2419]
- Fortner, J. A., and J. K. Bates (1995). *Long-term results from unsaturated testing of actinide-doped DWPF and WVDP waste glasses*. (UCRL-CR-122614; DE960072159; B-291561) Livermore, CA: Lawrence Livermore National Laboratory, and Argonne, IL: Argonne National Laboratory. [MOL.19960418.0084]
- Inagaki Y., A. Ogata, H. Furuya, K. Idemitsu, T. Banba, and T. Maeda (1996). "Effects of redox condition on waste glass corrosion in the presence of magnetite." In proceedings from Materials Research Society Symposium. **412**:257–264.
- Johnson, J. W., E. H. Oelkers, and H. C. Helgeson (1992). "SUPCRT92: A software package for calculating the standard molal thermodynamic properties of minerals, gases, aqueous species, and reactions from 1 to 5000 bars and 0 to 1000°C." *Computers and Geosciences*. **18**:890–947. [234273]
- Knauss, K. G., W. J. Beiringer, and D. W. Peifer (1987). *Hydrothermal interaction of solid wafers of Topopah Spring Tuff with J-13 water at 90 and 150°C using Dickson-type gold bag rocking autoclaves: Long-term experiments*. (UCRL-53722) Livermore, CA: Lawrence Livermore National Laboratory. [NNA.19870713.0081]
- Knauss, K. G., W. L. Bourcier, K. D. McKeegan, C. I. Merzbacher, S. N. Nguyen, F. J. Ryerson, D. K. Smith, H. C. Weed, and L. Newton, L. (1990). "Dissolution kinetics of a simple nuclear waste glass as a function of pH, time, and temperature." In proceedings from Mat. Res. Soc. Symp. **176**:371–381. [NNA.19891206.0279]
- McVay, G. L., and C. Q. Buckwalter (1982). "Effect of iron on waste-glass leaching." *J. Amer. Cer. Soc.* **66**(3):170–174. [NNA.19900306.0097]
- O'Connell, W. J., W. L. Bourcier, J. Gansemer, T. S. Ueng (1997). Performance Assessment Modeling for Savannah River Glass HLW Disposal in a Potential Repository at Yucca Mountain. (UCRL-JC-127352) Livermore, CA: Lawrence Livermore National Laboratory. (Presented at the American Chemical Society National Meeting/Symposium on Science and Technology for Disposal of Radioactive Tank Wastes, Las Vegas, NV, September 8–11, 1997) [MOL.19980211.0541]
- Wilder, D. G. (1997). *Near-Field and Altered-Zone Environment Report, Volume I: Technical Basis for EBS design*. (UCRL-LR-124998, Vol. 1) Livermore, CA: Lawrence Livermore National Laboratory. [MOL.19980127.0120]
- Wolery, T. J. (1992). *EQ3/6, A software package for geochemical modeling of aqueous systems: Package overview and installation guide*. (UCRL-MA-110662) Livermore, CA: Lawrence Livermore National Laboratory. [NNA.19921023.0028]

## 3.5.2 Glass Dissolution Models

### 3.5.2.1 Overview of Glass Dissolution

A chemical model of glass corrosion will be used to predict the rates of release of radionuclides from borosilicate glass waste forms in high-level waste (HLW) repositories. The model will be used to calculate the rate of degradation of the glass and to predict the effects of chemical interactions between the glass and repository materials such as spent fuel, canister and container materials, backfill, cements, and grouts. Coupling between the degradation processes affecting all these materials is expected. The glass-corrosion model must therefore be mechanistic and not a simple empirical extrapolation of experimental glass-degradation rates.

This overview is concerned with dissolution behavior of borosilicate glass compositions currently anticipated for use as waste forms under repository-relevant conditions. The models described here cannot be expected to predict glass-corrosion rates under conditions significantly different from these.

Figure 3.5.2-1 illustrates the major processes taking place during glass corrosion. The reaction begins with water diffusion into the glass and alkali ion exchange. Evidence for water diffusion comes from secondary ion mass spectroscopy (SIMS) and ion-probe profiling of reacted glasses that show diffusion profiles for water in a surface zone generally less than 1 micron thick (Abrajano and Bates, 1987; Oversby and Phinney, 1992). Ion exchange is indicated by the early rapid release of alkalis relative to other glass components, which is commonly observed in glass-dissolution tests (Mendel, 1984). Hydration and ion exchange result in the formation of two layers on the glass surface: an inner diffusion layer where concentration gradients for alkalis and water are observed and an outer, hydrated “gel layer” where network hydrolysis (breakage of Si-O-Si) bonds takes place. The gel layer is depleted in alkalis and boron and enriched in insoluble elements such as Al, Ca, Mg, and heavy metals (e.g., actinides).

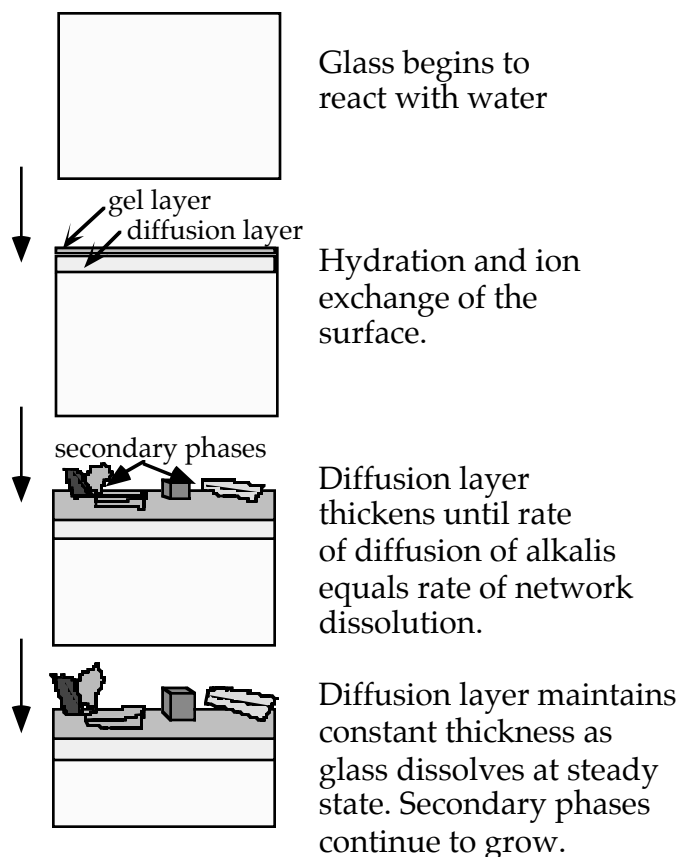


**Figure 3.5.2-1 Glass-dissolution mechanism**

With time, some elements released into solution reprecipitate on the hydrated glass surface and elsewhere as a variety of secondary phases. These phases are commonly clays, zeolites, and metal oxides/hydroxides. The reaction of glass to form secondary phases is driven by the thermodynamically unstable nature of glasses. Water allows glass to react and transform into a set of crystalline phases that are thermodynamically more stable. Water acts as a flux and allows the glass to react at a measurable rate. Under anhydrous conditions, even glass compositions that are relatively nondurable in water are stable for billions of years (Klein, 1986, 1986; Palmer et al., 1988).

Steady-state conditions are commonly observed during glass dissolution in which the rates of water diffusion and ion exchange are equal to the rate at which the glass network dissolves. Steady-state conditions are evidenced by the tendency for the glass diffusion layer to remain constant in thickness while the glass dissolves away and the mass of secondary phases increases with time (Abrajano et al., 1986).

In open-system experiments, the rate of release of most elements is approximately constant or slowly decreasing with time. In closed-system experiments, the release rates slow down more rapidly with time because of "saturation" effects (i.e., the buildup of dissolved glass species in solution) (Fig. 3.5.2-2). Increased silica concentrations are the primary reason for decreased dissolution rates (Chick and Pederson, 1984), although other elements also have effects (Bourcier et al., 1992). Elemental releases from glasses in closed-system tests also show nonstoichiometric behavior: some elements are released much more rapidly than others

(Fig. 3.5.2-2). Most of this nonstoichiometry is due to the precipitation of the less soluble glass components as secondary mineral phases, although a small amount is accounted for in the formation of leached layers.

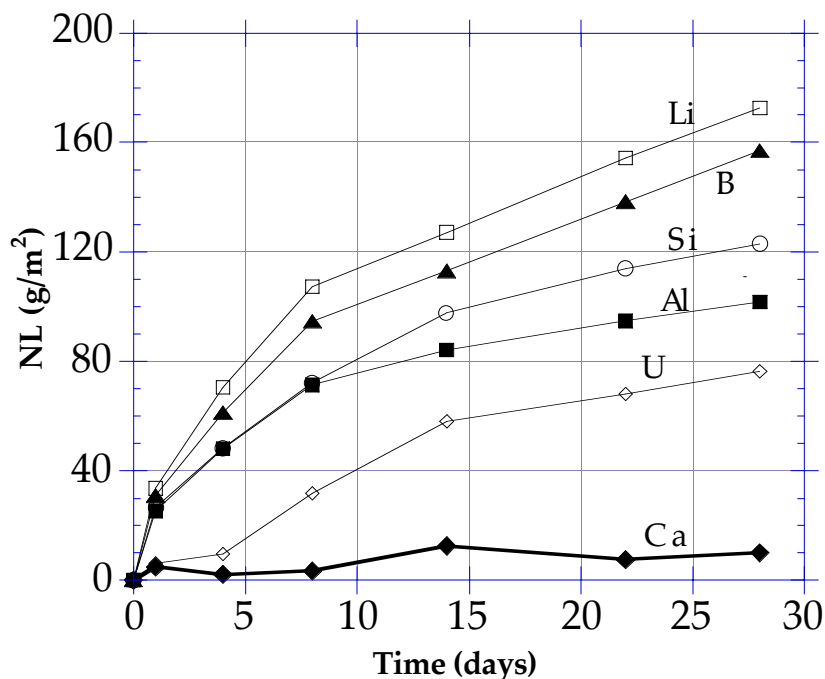


**Figure 3.5.2-2** Normalized elemental release from SRL-165 glass reacted in 0.003m NaHCO<sub>3</sub> at 150°C, surface area to volume (SA/V) ratio 0.01cm<sup>-1</sup> (Bourcier, 1990) [LL980912551021.056; LL981010251021.063]

Nuclear magnetic resonance (NMR) spectroscopy shows that network dissolution reactions taking place in the gel layer are complex. Experiments that are doped with <sup>17</sup>O show that both breakage and reformation of Si-O-Si linkages are taking place (Bunker et al., 1988). Hydrolysis of the highly stressed glass structure allows relaxation and removal of incompatible elements. The original glass is transformed into a hydrous silica-rich phase plus local areas enriched in transition and other heavy metals such as actinides. This alteration layer eventually crystallize into a variety of solid phases.

In some flow-through glass-dissolution tests, the gel layer appears to serve as a transport barrier that limits the overall dissolution rate (Grambow, 1987). In most closed-system experiments, however, elemental release data and electron microscopic examination of the surface layers show that the overall reaction rate is not controlled by diffusion of elements through the alteration layers (Abrajano et al., 1990; Chick and Pederson, 1984; Murakami et al., 1988).

Recent NMR data have also shown that boron in waste glasses is clustered into boron-rich regions (Phillips, 1993). Boron occurs in both three- and four-fold coordination with alkalis in a sodium-di-borate-type structure. The high reactivity and solubility of these zones gives rise to the relatively rapid release of boron from borosilicate glasses in waste glass leach tests.

Rates of glass dissolution may also be strongly affected by certain dissolved elements. For example, dissolution rates of silicate glasses are strongly decreased in the presence of dissolved Mg, Pb, and Zn and strongly enhanced, under some conditions, by dissolved Fe. Likewise, anions such as phosphate and sulfide are known to affect mineral-dissolution rates and may likewise affect glass-dissolution rates. Depending on the specific metal, these effects may be attributable to several processes: the formation of surface complexes, the precipitation of a surface layer providing a transport barrier, or the reaction of dissolved glass species with the dissolved metals causing the precipitation of colloids or secondary phases that affect the glass dissolution affinity (McVay and Buckwalter, 1983). These types of effects are potentially important in repository environments where a variety of dissolved species will be present from other repository materials.

In summary, a model for borosilicate glass dissolution must account for the following processes:

- Kinetically-controlled network dissolution
- Precipitation of secondary phases
- Ion exchange of selected elements
- Rate-limiting diffusive transport through a hydrous surface reaction layer (in some cases)
- Specific glass-surface interactions with dissolved cations and anions

This set of coupled processes should be able to quantitatively predict observations of glass dissolution that include the saturation effect (glass-dissolution rates slows down as dissolved glass species build up in solution), the increase in pH that accompanies glass dissolution in closed-system tests, the variability of glass-dissolution rate as a function of glass composition, and rate-affecting interactions of the glass surface with dissolved cations and anions. First one must look at examples of how the five processes are incorporated into current models and then critically review modeling results using a representative set of examples for modeling of experimental data.

#### 3.5.2.2 Modeling of Glass Corrosion

Current long-term corrosion models for borosilicate glass employ a rate equation consistent with transition-state theory embodied in a geochemical reaction-path modeling program that calculates aqueous-phase speciation and mineral precipitation/dissolution. These models ignore early diffusion-controlled dissolution behavior that is more important for less durable glass compositions such as alkali-silicates and is important only in the very early stages of reaction of borosilicate waste glasses. Diffusion in this case refers to solid-state diffusion of ions through the partially hydrated glass surface layer rather than to diffusion of aqueous species through the more hydrated and restructured gel layer. Therefore, there is no discussion of the many studies that solve the equations for the formation of a moving and thickening transport-limiting surface layer.

##### 3.5.2.2.1 The Rate Law

The rate law commonly used to model network hydrolysis, assumed to be rate-controlling during glass dissolution, has the general form (Aagaard and Helgeson, 1982; Lasaga, 1984):

$$\frac{dn_i}{dt} = Sv_i k \prod_j a_j^{-N_j} \left( 1 - e^{\left( \frac{-A}{RT} \right)} \right) \quad (3.5.2-1)$$

where  $n_i$  is the number of moles of species  $i$  in solution released from the glass,  $t$  is time,  $S$  is the reactive surface area of glass,  $v_i$  is the concentration of species  $i$  in the glass,  $k$  is the rate coefficient for the glass,  $\prod_j a_j^{-N_j}$  is the product of the activities (concentrations) raised to the power of  $N_j$  of dissolved aqueous species that make up the activated complex of the rate-limiting microscopic dissolution reaction,  $A$  is the reaction affinity defined as  $RT \ln(Q/K)$  where  $Q$  is the activity product and  $K$  the equilibrium constant for the rate-determining glass dissolution reaction,  $s$  is a stoichiometric factor that relates the rate-controlling microscopic reaction to the overall solid dissolution reaction (usually it is assumed  $s=1$ ),  $R$  is the gas constant, and  $T$  is the temperature in Kelvin.

The form of Eq. 3.5.2-1 predicts that the dissolution rates of solids have the following characteristics:

- The amount of solid dissolved is proportional to exposed surface area.
- The dissolution rate slows down as the solid approaches saturation.
- The dissolution rate is constant under conditions far from saturation ( $Q/K \ll 1$ ).

An expression having this general form is used in all of the major glass modeling computer codes at this time (e.g., PHREEQE/GLASSOL [Grambow, 1987], EQ3/6 [Bourcier, 1990], DISSOL [Advocat et al., 1990], REACT, [Bourcier et al., 1993], LIXIVER [Delage et al., 1992]).

This rate law implies that, at equilibrium, there is a *reversible* microscopic dissolution reaction that is rate-limiting. However, because glass is thermodynamically unstable and cannot reach saturation, the overall glass-dissolution reaction is clearly not reversible. Therefore, when this rate law is applied to glass dissolution, it must be applied not to the overall reaction, but to some rate-limiting microscopic reversible reaction.

Many of the parameters in Eq. 3.5.2-1 are not known either from theory or from experiments, so that in practice the equation is simplified to

$$\frac{dn_i}{dt} = Av_i k(pH) \left( 1 - \left( \frac{Q}{K} \right)^r \right)^s \quad (3.5.2-2)$$

where the product term  $\prod_j a_j^{-N_j}$  is reduced to include only the pH dependence of the rate coefficient, and the affinity expression is simplified and re-expressed in terms of the saturation index ( $Q/K$ ) of the dissolving solid. This form of rate law is commonly used as an expression to which experimental elemental release data are fitted (i.e., values of  $k$ ,  $K$ ,  $r$ , and  $s$  are determined by regression of experimental data).

Current modeling codes may further simplify Eq. 3.5.2-2. GLASSOL assumes no solution compositional dependence of  $k$ , which is assumed to vary only with temperature. DISSOL, EQ3/6, LIXIVER, and REACT treat  $k$  as a function of both pH and  $T$ . No models account for any further dependencies of  $k$  on solution composition as indicated in Eq. 3.5.2-1.

## 3.5.2 Glass Dissolution Models

---

To use Eq. 3.5.2-2 to predict glass-dissolution rates, one must assume what phase becomes saturated in order to evaluate the Q/K term. Several phases have been tried, ranging from the initial, unreacted glass composition (Bourcier, 1990; Advocat et al., 1990) to the composition of the alkali-depleted surface layer (Bourcier et al., 1990) to simple hypothetical silica (Grambow, 1987; Advocat et al., 1991; Vernaz and Dussossoy, 1992; Michaux et al., 1992). It is clear from these modeling studies that using the unreacted glass composition gives results that deviate from experimental observations (see subsequent text). However, the other two approaches give comparable agreement with experiments.

### 3.5.2.2.2 Secondary Phases

Precipitation of secondary phases takes place as glasses dissolve and the concentrations of species build up in solution. Geochemical modeling codes used to model glass dissolution incorporate algorithms that track saturation states for these possible mineral phases and predict, based on mineral thermodynamic data, the most stable phase assemblage. The types and amounts of phases are continually adjusted during the reaction path calculation to maintain the most stable phase assemblage. While this approach works well for simulations of high-temperature hydrothermal systems, experience has shown that this approach often leads to incorrect phase-assemblage predictions for the lower temperature (<150°C) glass-dissolution tests (Bruton, 1988; Bourcier, 1990). Thermodynamically less stable phases tend to precipitate instead.

Alternative methods of predicting secondary phases have therefore been used in the simulations. One method, termed “inverse modeling,” uses the measured-solution composition to identify which phases are near saturation (Grambow and Strachan, 1988). These phases are assumed to be those actively precipitating and controlling the solution composition, and only these phases are allowed to precipitate during the glass reaction. Another approach is to simply restrict the database of mineral phases allowed to precipitate to those actually observed experimentally. Obviously, neither approach has any predictive capability for secondary phases, but no reliable theory is currently available to enable predictions of the most likely secondary phases in these complex systems (see Steefel and Van Cappellen [1990] for a new approach).

### 3.5.2.2.3 Ion Exchange

The formation of secondary phases is the primary cause for the observed nonstoichiometric release of elements during glass dissolution. The formation of an alkali-depleted surface layer also contributes to nonstoichiometric release and affects the pH of the solution through ion-exchange reactions:



Similar reactions take place for other alkalis, including lithium, potassium, and cesium. The ion-exchanged zone has variable thickness depending on the glass composition and test conditions but is generally 1 to 10 microns thick. The net effect of the ion-exchange reaction is to raise the pH of the surrounding solution. The pH effect is larger as the surface area to volume (SA/V) ratio of the test increases.

Although the ion-exchange process is complex and involves diffusion of ions and water through a partially hydrated and inhomogeneous medium, the chemical effect of the process can be modeled simply. Unless the ion-exchange process is rate-limiting, only the chemical

effects need to be incorporated into the model. A simple method for incorporating this effect first suggested a few years ago (Strachan et al., 1990) was recently reported (Bourcier et al., 1993). In this approach, an ion-exchange reactant is used in addition to the glass reactant in the simulation. This ion-exchange reactant is composed only of the elements released during ion exchange. The mass of this reactant is fixed by the experimentally measured thickness of the ion-exchanged zone. The reactant is allowed to react rapidly at first to simulate the rapid, initial formation of an ion-exchanged zone. The predicted pH and elemental concentration of species using this method agree fairly well with experimental results. The results also show that inclusion of ion-exchange effects is only necessary for simulations of fairly high SA/V ratio.

#### 3.5.2.2.4 Transport-Limited Corrosion

Experimental evidence suggests that, under certain flow-through test conditions, the dissolution rate of some glasses is controlled by transport. Grambow (1987) has hypothesized that it is the transport of silica through the surface alteration layers that is rate-limiting. The transport-limited rate is modeled by a simple diffusion law:

$$r_t = \frac{D}{L}(a_s - a_b) + r_{fin} \quad (3.5.2-4)$$

where ( $r_t$ ) is the dissolution rate,  $D$  and  $L$  are the diffusion constant and thickness of the hydrous alteration layer, ( $a_s - a_b$ ) is the dissolved silica concentration gradient across the layer from the surface (s) to the bulk solution (b).  $r_{fin}$  is the “final rate,” an experimentally estimated empirical parameter to account for the observed finite rate of glass reaction even at “saturation” where using Eq. 3.5.2-1 would predict zero reaction rate.

The affinity-based rate control (Eq. 3.5.2-2) is combined with this simple diffusion-rate control in the GLASSOL (Grambow, 1987). The model tests whether the rate is controlled by transport or surface reaction and makes the appropriate calculation. The LIXIVER code (Delage et al., 1992) has also combined transport and affinity-based rate control. In the LIXIVER model, the thickness and rate of silica diffusion through the gel layer control the concentration of silica at the gel layer/solution interface, and this ion concentration is used to evaluate  $Q$  in Eq. 3.5.2-2. This approach assumes that silica diffusion through the gel layer affects the concentration of dissolved silica at the gel/solution interface, thereby coupling the effects of silica transport and affinity rate control.

#### 3.5.2.2.5 Surface Interactions

Dissolved ions present in solution are known to affect glass-dissolution rates. For example, Mg and Zn are known to decrease glass dissolution rates (Barkatt et al., 1989; Tait and Jensen, 1982), while dissolved iron is known to increase it (Lee and Clark, 1986). Current glass-dissolution models account for the effect of dissolved silica on glass dissolution, but do not account for the effects of other ions. Although silica effects are important, and in most cases dominate over the effects of other ions, this is not always the case; it is necessary to provide for these other ions if the model is to be generally applicable. This is especially important in repositories where the effects of species produced from corrosion of other repository materials, such as metals and cements, are available to interact with the dissolving waste forms.



Three general mechanisms by which dissolved species affect glass alteration rates have been proposed:

1. Ions sorb onto the dissolving glass surface and affect the strength of the Si-O bonds at the glass surface (see Figure 3.5.2-3). It is the hydrolysis of these bonds that controls the overall rate of glass dissolution and radionuclide release. This effect is particularly significant for long-term performance, where the rate at “near-saturation” conditions is likely to be strongly affected by the nature of the glass-solution interface, and therefore the types and concentrations of sorbed species, and the surface charge. Some attempts have been made to understand and model deviations in dissolution behavior believed to be due to surface complex formation (Lee and Clark, 1986; McVay and Buckwalter, 1983; Bart et al., 1987; Grambow et al., 1986; Andriambololona et al., 1992)
2. Dissolved species react with the glass surface to form a protective layer. The protective layer armors the glass surface and reduces the rate of further attack. The overall dissolution process then becomes rate-limited by transport through the protective layer. It is believed that magnesium affects glass dissolution through this process (Barkatt, 1989).
3. Colloids are formed by reaction with the dissolved ion in question and species dissolving from the glass. An example of this is iron. Dissolved iron reacts with silica from the dissolving glass to form iron-silica colloids. The silica-containing colloids act as a sink for silica and maintain a low dissolved-silica concentration in solution. This effectively reduces the glass saturation state and causes the glass-dissolution rate to remain high (see Eq. 3.5.2-1). Note that these colloids will also tend to sorb actinide species and pose a potential migration pathway for otherwise insoluble actinide species.

Qualitative data for the effects of several dissolved metals on glass durability are listed in Table 3.5.2-1. This table summarizes a broad variety of data from experiments that, in many cases, are difficult to interpret because supporting data are lacking. Many of the studies, for example, do not report pH. In some cases, the data conflict; the same dissolved species may cause the dissolution rate to increase in one type of test and decrease in another. In other cases, the glass-dissolution rate may change with time. An aqueous component that first decreases glass-reaction rate may later on enhance it (i.e., the case of lead reported by Zwicky et al. [1992]; see table 3.5.2-1 notes). Another complication is that species may only have an effect if at a sufficiently high concentration to cause precipitation of an armoring surface solid, as is apparently the case for magnesium. At low dissolved Mg concentration, Mg has no noticeable effect (Bourcier et al., 1992); at higher concentrations, where the magnesium-silicate phase sepiolite is supersaturated, Mg greatly decreases the glass-reaction rate, presumably because of precipitation of a surficial Mg-silicate phase such as sepiolite.

Note in Table 3.5.2-1 that there is a lack of data for many metals likely to be present in the repository (i.e., alloying metal in stainless steels such as Cr, Mn, Ni, and Mo).

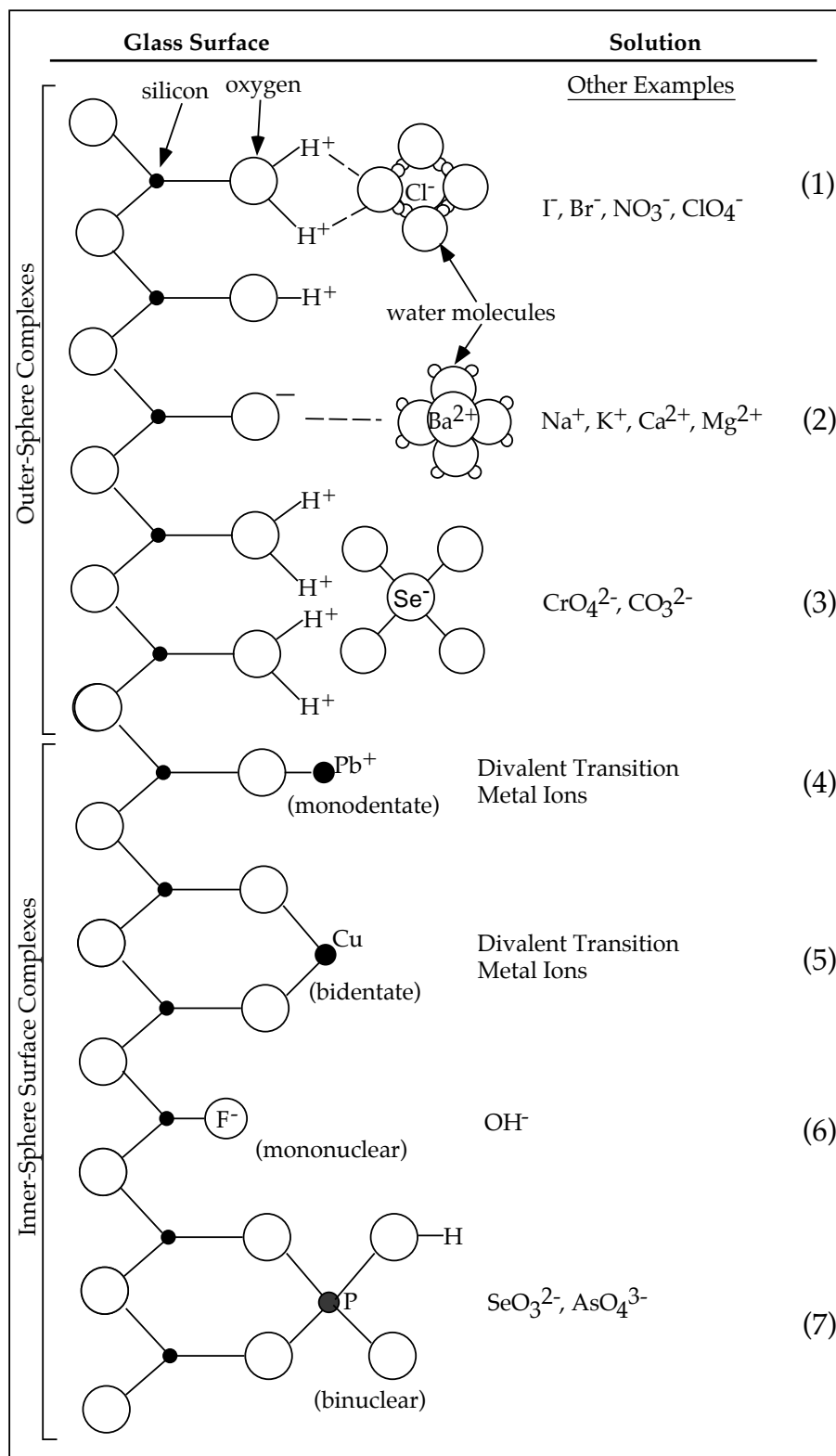


Figure 3.5.2-3 Types of metal complexes on oxide surfaces (Hayes, 1987)

### 3.5.2 Glass Dissolution Models

Although this qualitative information is available, it alone is not sufficient for incorporation of these effects into models of glass dissolution. Experiments are needed to identify the mechanisms through which dissolved species affect dissolution rates and to provide the parameters needed to quantify these effects in the glass-dissolution models. Explicit provision for surface interactions will be especially critical to account for coupled effects of glass with other repository materials in performance assessment (PA) calculations.

**Table 3.5.2-1 Effects of dissolved ions on glass-dissolution rate**

<b>Metal</b>	<b>Low pH</b>	<b>Near-Neutral pH</b>	<b>High pH</b>	<b>Reference</b>
B	none	none	unknown	Bourcier et al., 1992
Mg	none	major –	major –	Bourcier et al., 1992; Barkatt et al., 1989; Lee and Clark, 1986; Sang et al., 1994
Ca	none	none	minor –	Bourcier et al., 1992; Lee and Clark, 1986; Oka et al., 1979
Si	none	major –	major –	Bourcier et al., 1992; Lanza et al., 1988
Al	major -	minor –	none/minor +	Bourcier et al., 1992; Lee and Clark, 1986; Zwicky et al., 1992; Buckwalter and Pederson, 1982
Na	unknown	minor –	minor –	Lee and Clark, 1986
Zn	unknown	minor +	major –	Lee and Clark, 1986; Zwicky et al., 1992; Tait and Jensen, 1982
Li	unknown	unknown	minor +	Feng and Barkatt, 1987
Fe	unknown	major/minor +	major +	Bunker and Arnold, 1983; McVay and Buckwalter, 1983; Bart et al., 1987; Bibler and Jantzen, 1987; Burns et al., 1986; Hermansson et al., 1985; Inagaki et al., 1996
Pb	unknown	major –	major –	Bart et al., 1987; Lehman and Kuchinski, 1985; Burns et al., 1986; Zwicky et al., 1992; Buckwalter and Pederson, 1982
Cu	unknown	unknown	none	Buckwalter and Pederson, 1982
Sn	unknown	unknown	none	Buckwalter and Pederson, 1982
Ti	unknown	unknown	none	Buckwalter and Pederson, 1982

Minor = less than factor of 10 effect; major = greater than factor of 10 effect; + means glass dissolution rate is increased, – means rate is decreased; none = no effect observed; unknown = no data or data uninterpretable

#### 3.5.2.2.6 Effect of Glass Composition

In current models, the effect of glass composition on glass-dissolution rates is accounted for in two ways. Glass has an intrinsic durability related to its composition and structure; quantification of this property affects the rate parameter,  $k$ , in Eq. 3.5.2-1. The glass

composition also affects the value of the equilibrium constant  $K$  in the affinity term of the rate equation. The value of  $K$  used in the model depends on which dissolution reaction is rate-controlling.

Several approaches have been used to try to account for the effect of glass composition on glass-corrosion rate. These include using “hydration theory” (Plodinec et al., 1984; Jantzen and Plodinec, 1984) to calculate both the rate coefficient and the equilibrium constant  $K$  (Grambow, 1984); calculating  $K$  from estimated thermodynamic properties of the surface layer (Bourcier et al., 1990); determining experimentally the rate coefficient from flow-through tests (Knauss et al., 1990); and by empirical fitting to experimental data to determine both  $k$  and  $K$  (Grambow, 1987).

Although the success of hydration theory in correlating glass durability with glass thermodynamic properties has been documented (Jantzen, 1992), the theory has been less successful in making quantitative predictions in glass-corrosion models (Advocat et al., 1990; Bourcier, 1990). When incorporated into glass-corrosion models, the free energies of formation of glasses (which determine the value of  $K$  in Eq. 3.5.2-2) calculated using hydration theory do not predict any slowing of glass-dissolution rate as saturation is approached. The value of  $K$  is predicted to be too large.

Alternatively, Grambow used hydration theory to estimate the rate coefficient in the rate equation (Grambow, 1984) using the expression

$$k_f = X e^{(-E_a / RT)} e^{(-\Delta G_r(\xi) / RT)} \quad (3.5.2-5)$$

where  $E_a$  is the activation energy for dissolution (determined experimentally), and  $\Delta G_r$  is the hydration free energy for the glass-dissolution reaction. The first term in the equation [ $X \exp(-E_a / RT)$ ] is an Arrhenius term that accounts for the effect of temperature on the rate constant. The second term [ $\exp(-\Delta G_r(\xi) / RT)$ ] corrects the rate constant for the effect of glass composition. This approach has had limited success when dealing with the compositional range of real waste glasses. It was eventually dropped from the Grambow model and replaced with experimentally determined values for specific glass compositions.

Another way to apply the hydration free-energy model to glass dissolution is to assume that the rate-limiting step in glass dissolution is the dissolution of the surface, alkali-depleted, hydrous layer. The thermodynamic properties of this layer can be approximated by assuming it is a solid solution of amorphous components (Bourcier et al., 1990). In this method, the hydration free energy is applied to the surface-alteration layer rather than to the unreacted glass, and the components are chosen to be amorphous rather than crystalline to be structurally and energetically more similar to the amorphous surface layer. This model better predicts the experimental glass-dissolution rates than does the hydration free-energy model applied to the unaltered glass. However, the relation between starting glass composition and glass-dissolution rate in this model is complex. The composition of the alteration layer (which is used to calculate the glass-dissolution affinity and the dissolution rate) is affected by the glass composition and by solution composition. No attempt has yet been made to quantify this effect in the glass-dissolution model. The composition of the alteration layer is determined by analysis of reacted glasses.

#### 3.5.2.2.7 Deviant Glass Dissolution Behavior

Several studies have shown that glass-dissolution rates may abruptly increase in rate after showing normal behavior over extended periods of time at what appeared to be nearly constant “final” dissolution rates (Barkatt et al., 1991; Ebert et al., 1993; Patyn et al., 1990; Van Iseghem et al., 1992). These rate changes may be accompanied by abrupt changes in pH and the onset of precipitation of new secondary phases. The rate changes are not well understood, but may be related to physical changes in the surface layers (Sang et al., 1993), secondary phase precipitation (Ebert et al., 1993), or as-yet-unidentified processes.

#### 3.5.2.3 Limitations of Current Models

The most important problems of current models fall into three categories:

1. Most model parameters are obtained from the same experiments as those being modeled.
2. The concept of “silica saturation” lacks precise definition.
3. The long-term release rate is poorly defined and quantified.

These areas need to be addressed with additional experimental and modeling work.

Although the GLASSOL approach has successfully predicted glass-corrosion tests results, some questions have been raised about its suitability for long-term predictions. Curti (1991) used the GLASSOL code to model the dissolution of the French COGEMA and British MW borosilicate glasses (glass produced at British Nuclear Fuel Laboratory) to assess whether GLASSOL can be applied to safety analysis of the Swiss HLW repository. Curti found three areas where improvement was needed before GLASSOL could be suitable for safety analysis:

1. Better accounting for the effects of silica sorption on bentonite backfill
2. Inclusion of provisions for partitioning radionuclides into alteration phases (currently stoichiometric release is assumed)
3. The problem that the final rate of corrosion is poorly defined and has no mechanistic basis

Curti also notes that “a significant drawback of the modeling exercises reported . . . is that the relevant parameters ( $k$ ,  $R_{\text{fin}}$ ,  $K$ ) are derived *ad hoc* from the experiment to be modeled.”

The most serious limitation of these three is that of estimating, both in terms of providing a mechanism controlling this rate and a numerical value to be used in modeling, the long-term or “final” reaction rate. More recent work by Grambow et al. (1992) illustrates this problem using data from dissolution tests in saline fluids and suggests that the rate control may switch from surface-reaction control to water-diffusion control over long time periods. Clearly, the exact mechanism that controls dissolution rates over long time periods is not yet known.

Godon et al. (1989) have observed that R7T7 glass dissolution in contact with 11 different materials shows no systematic “silica-saturation” level. Although the dissolved silica concentration reaches a nearly constant value in each test, that value varies greatly from test to test depending on the type of additional material present. The silica-saturation level, therefore, is not a parameter related to glass composition only, but also depends on test conditions. The silica-saturation level for a particular test probably results from a balance between the rate of formation of silica-containing secondary phases (including colloids) and the rate of release of silica from the glass. The silica-saturation value ( $K$ ) from Eq. 3.5.2-2 is

not a constant for a given glass composition, but will change as a function of test conditions. Thus, long-term predictions based on a constant value of  $K$  in the rate equation are of questionable reliability.

#### 3.5.2.4 Conclusions

It is clear that further progress in developing quantitative, predictive models for glass dissolution depends on obtaining results from systematic, interpretable experiments that confirm and quantify the postulated glass reaction mechanisms. Some work has been done in this area (Trotignon, 1990; Knauss et al., 1990), but much remains to be done. Some specific suggestions for future work are given in Strachan et al. (1994) and include the following:

- **Flow-through tests of glasses in continuously stirred reactors with controlled pHs that are designed to measure the rate constant for glass dissolution over a matrix of temperatures, pHs, and glass compositions**—Similar tests should be performed in pH-buffer solutions doped with relevant cations and anions to systematically determine the effects of dissolved species on dissolution rate. These tests should be combined with surface titrations to characterize glass-surface speciation.
- **Closed-system tests of a matrix of glass compositions with controlled pH (pH stat) to investigate the effect of glass composition on glass-dissolution rate under conditions in which secondary phases form (unlike the flow-through tests)**—These tests should be combined with NMR analysis of unreacted glasses to correlate glass structure and coordination with glass durability, as measured in both the flow-through and the closed-system tests.
- **Additional closed-system tests where stable secondary phases such as calcite, quartz, and clays are added to control solution composition**—The data from these tests should help define and quantify the affinity term in the rate expression.
- **Molecular orbital calculations of glass-surface speciation and molecular-dynamics simulations of glass-dissolution behavior**—These would help constrain macroscopic glass-dissolution models and support validation of proposed dissolution mechanisms.

In all cases, experiments should include as complete an analysis of both solid and aqueous phases as possible. Too many experiments have been performed in which incomplete characterization of either solids or solution phases have made interpretation of the results ambiguous, both for mechanistic interpretation of the results and for use of results in model validation attempts.

The results of these experimental investigations should be combined with additional model development to produce a workable and sufficiently comprehensive glass-dissolution model for use in repository PA simulations.

#### 3.5.2.5 Assessment of Current Methods for Estimating Glass-Dissolution Rates under Silica-Saturated Conditions

Glass-dissolution rates decrease dramatically as glasses approach saturation with respect to the leachate solution. This effect may lower the dissolution rate to 1/100 to 1/1000 of the unsaturated rate. Although rate controls on glass dissolution are best understood for conditions far from saturation, most repository sites are chosen where water fluxes are minimal; thus, the waste glass is most likely to dissolve under conditions close to saturation. Understanding controls on dissolution rates close to saturation is of greater significance for assessing release rates of radionuclides from repositories than understanding controls on dissolution rates far from saturation.

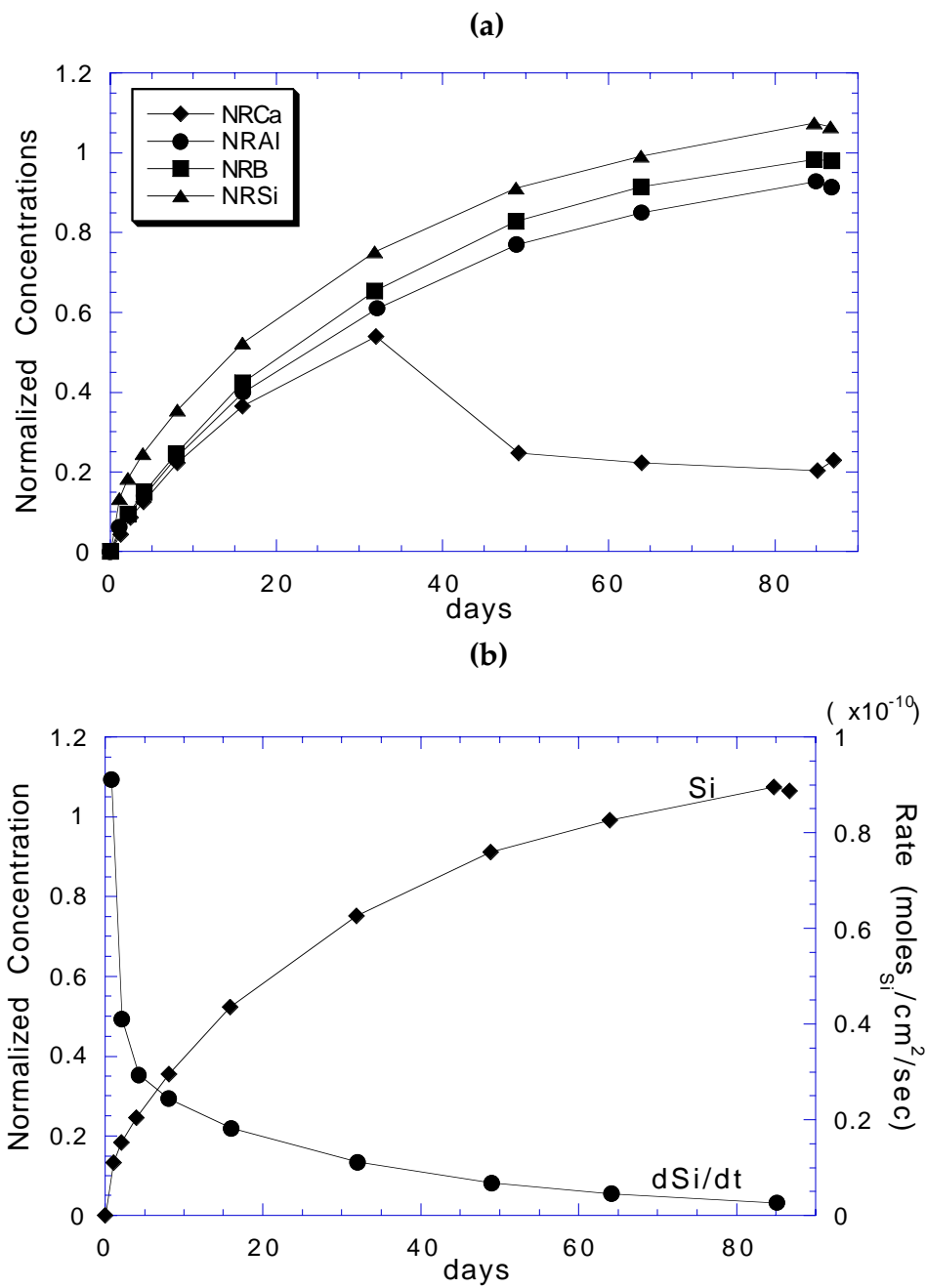
The key term in the rate expression used to predict glass-dissolution rates close to saturation is the affinity term, which accounts for saturation effects on dissolution rates. The form of the affinity term and parameters used to model glass dissolution are clearly critical for accurate estimates of glass performance in a repository.

The concept of saturation with respect to glass dissolution is problematic because of the thermodynamically unstable nature of glass. Saturation implies similar rates of forward (dissolution) and back (precipitation) reactions, but glasses cannot precipitate from aqueous solutions; there can be no back reaction to form glass. However, experiments have shown that, when dissolving, glasses do exhibit saturation effects analogous to saturation effects observed for thermodynamically stable materials. Thus, attempts to model the glass-dissolution process have employed theories and rate equations more commonly used to model dissolution of crystalline solids.

#### 3.5.2.5.1 Current Models of Glass Dissolution under Silica-Saturated Conditions

Because glasses are thermodynamically unstable and Eq. 3.5.2-1 is derived for a solid that dissolves reversibly, a factor called the residual rate is sometimes added to the equation to account for observed, slow long-term rates. This gave rise to the concept of “residual affinity” (Grambow and Strachan, 1983) and some attempts to provide a mechanistic basis to predicting long-term rates under near-saturation conditions (Petit et al., 1990; Advocat et al., 1990). These attempts have been unsuccessful. No mechanistically based model for predicting long-term rates based only on dissolved silica concentration or silica diffusion through a surface-alteration layer has been developed that is consistent with all experimental observations. As shown subsequently, the effects of dissolved species such as Al greatly affect mineral-dissolution rates, in some cases changing them by orders of magnitude. The effects of Al would swamp the observed correlation of long-term glass-dissolution rates with silica content in solution.

In addition, the value of  $\sigma$  in Eq. 3.5.2-1 is assumed to equal one. Analysis of the dissolution rate of a simple borosilicate glass as a function of silica concentration depicted in Figure 3.5.2-4 shows that a value of  $\sigma=0.1$  better fits the experimental data. This value is in the range of values of  $\sigma$  reported for kaolinite  $\text{Al}_2\text{Si}_2\text{O}_5(\text{OH})_4$  (Devidal et al., 1992) and amorphous silica (Jørgensen, 1968). This range of values of  $\sigma$  will clearly make a large difference in the calculated value of the dissolution rate close to saturation. Note, however, that the data from Bourcier et al. (1994), from which a value of  $\sigma=0.1$  was obtained, could be reinterpreted in terms of the effects of increasing Al in solution, using an approach similar to the model of Schott and Oelkers (1995) described subsequently.





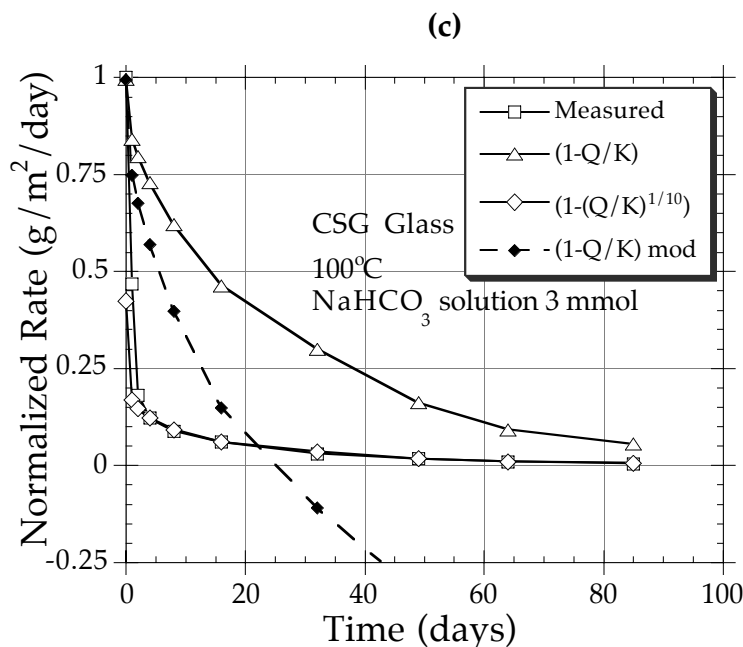


**Figure 3.5.2-4** Experimental data for simple SRL-165 glass analog ( $\text{Na}_2\text{O}$  19 mol%,  $\text{CaO}$  7 mol%,  $\text{B}_2\text{O}_3$  8 mol%,  $\text{Al}_2\text{O}_3$  7 mol%,  $\text{SiO}_2$  59 mol%) dissolving in 3 mmol  $\text{NaHCO}_3$  solution at  $100^\circ\text{C}$  in closed system: Plot (a) shows release data for all elements; (b) shows rate of silica release from slope of silica curve in (a) after release data corrected for pH effect on rate constant and solution volume changes due to sampling. Plot (c) shows attempted fit to data using various affinity functions where both  $\sigma$  and  $K$  were allowed to vary. Best fit is obtained when  $\sigma = 0.1$  ( $n = 10$ ) and  $\log K$  is  $-3.1$  (data are open boxes; calculated values are open diamonds). Open triangles show curve for  $\sigma = 1$ . [LL980608351021.041; LL980912551021.056; LL980912551021.057; LL981010451021.065; LL981010551021.066]

Much recent experimental work on silicate mineral-dissolution rates close to saturation are also inconsistent, with simple affinity control following Eq. 3.5.2-1 (Nagy et al., 1991; Burch et al., 1992; Dove and Elston, 1992; Gin, 1996; Schott and Oelkers, 1995; Berger et al., 1994a, 1994b; Oelkers et al., 1994). In fact, only quartz dissolution has been successfully modeled with this approach. It is clear that the glass-dissolution process is more complicated than any model based entirely on Eq. 3.5.2-1.

### 3.5.2.5.2 Needed Improvement in the Current Models

Although the current, simple models can predict glass-dissolution rates reasonably well in dilute, weakly alkaline solutions typical of groundwaters in repositories, the models fail badly under conditions that deviate significantly from those in the site-specific tests where rate measurements were made. Recent experimental data for glasses (Gin, 1996; Berger et al., 1994b; Bourcier et al., 1992) and analogous aluminosilicate minerals (Devidal et al., 1992; Oelkers et al., 1994; (Berger et al., 1994a; Burch et al., 1992) show rate dependencies that cannot be explained entirely by changing silica concentration, or even as functions of reaction affinity. Numerous papers show the importance of species other than dissolved silica affecting the dissolution rates of silicate minerals. Alkalis such as sodium and dissolved lead

increase the rate of quartz dissolution (Dove and Elston, 1992; Berger et al., 1994a). Aluminum dramatically affects dissolution rates of borosilicate waste glass (Gin, 1996), kaolinite (Devidal et al., 1992), and albite (Oelkers et al., 1994). Flow-through tests of simulated radioactive waste glasses and simple analog composition glasses (Bourcier et al., 1992) show that dissolved aluminum decreases glass-dissolution rates, with the effect being larger at lower pHs (Figure 3.5.2-5). In the same tests, dissolved silica lowered glass dissolution rates above pH 7, but had little effect below pH 7. Dissolved Mg and Ca had no effect at any pH tested when present at 2.5 mmolal concentrations. Clearly the effects of other dissolved species need to be included in the glass-dissolution model.

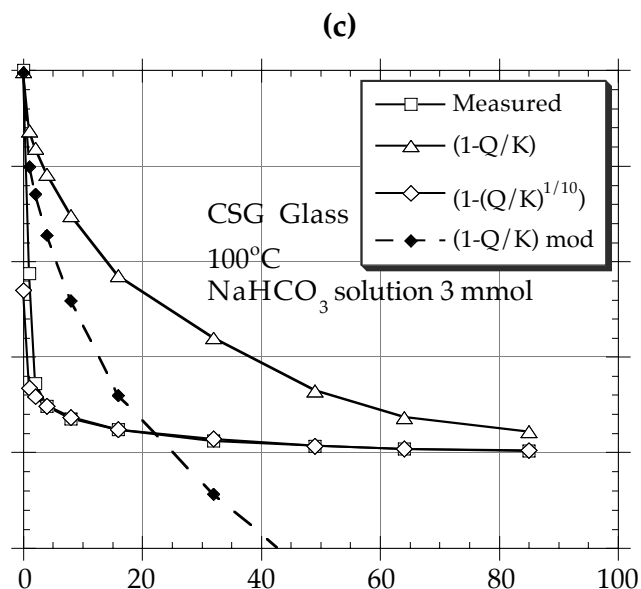


**Figure 3.5.2-5** Dissolution rates of a simplified five-component analog of SRL-165 glass measured in flow-through reactors in pH-buffered solutions doped with 2.5 mM  $\text{Al}(\text{ClO}_4)_3$ , 2.5 mM  $\text{B}(\text{OH})_3$ , and 2.5 mM  $\text{K}_2\text{SiO}_3$ . V-shaped line is regression to data for this glass in undoped buffers. Dissolution rates are decreased by dissolved Si at high pHs, and rates are lowered due to the presence of dissolved Al at low pHs (Bourcier et al., 1992). [LL980912551021.056; LL980912551021.057; LL981919651921.067]

For glasses, some observed deviations from simple rate control by  $\text{SiO}_2(\text{aq})$  were explained by assuming rate control by silica concentrations at the glass–water contact inside a surface gel layer (Grambow, 1987). Silica diffusion through this gel layer controlled the silica concentration at the contact, and the silica concentration at the contact controlled the glass-dissolution rate. By combining this mechanism with the rate law of Eq. 3.5.2-1, Grambow was able to explain observed maxima in flow-through glass-dissolution tests and regress physically reasonable values for the diffusion constant for  $\text{SiO}_2$  in this gel layer. But even with this added term, the model still cannot predict results of recent experiments, particularly experiments that show significant effects of dissolved aluminum (Gin, 1996).

### 3.5.2.5.3 Glasses Versus Crystalline Silicates

Many similarities and parallels between the dissolution behavior of silicate glasses and the dissolution behavior of silicate minerals suggest that recent developments in surface-complexation models for crystalline silicates can be applied to silicate glasses as well.

Figure 3.5.2-6 shows dissolution rates versus pH for albite glass versus albite mineral at 70°C. For both crystalline albite and albite glass, the pH dependence of the rate is identical. However, the glass dissolves one to one-and-one-half orders of magnitude faster than the mineral. As noted previously, the dissolving solid that is rate-limiting for glass–water reactions is an alkali-depleted, partially repolymerized hydrous material. A similar type of material exists on the surface of dissolving minerals such as albite, where several surface techniques have consistently shown a sodium-depleted, partially hydrated layer at the albite–water interface (Hellmann et al., 1990; Casey et al., 1988). The observed layer thickness for albite at near-neutral pHs is 1 to 90 nm, whereas for typical borosilicate waste glasses it is a thicker 10 to 200 nm.

Similar hydrous layers are likely present on other reacting silicate minerals; if they are not observed, it is likely the same mechanisms are operating with both glasses and minerals but at different rates (Petit et al., 1989). For both glasses and minerals, the water contacts an alkali-depleted, partially hydrated surface where the rate-limiting hydrolysis reaction takes place. For all these reasons, it is clear that the basic framework for understanding dissolution-rate control for both silicate glasses and silicate minerals is the same.

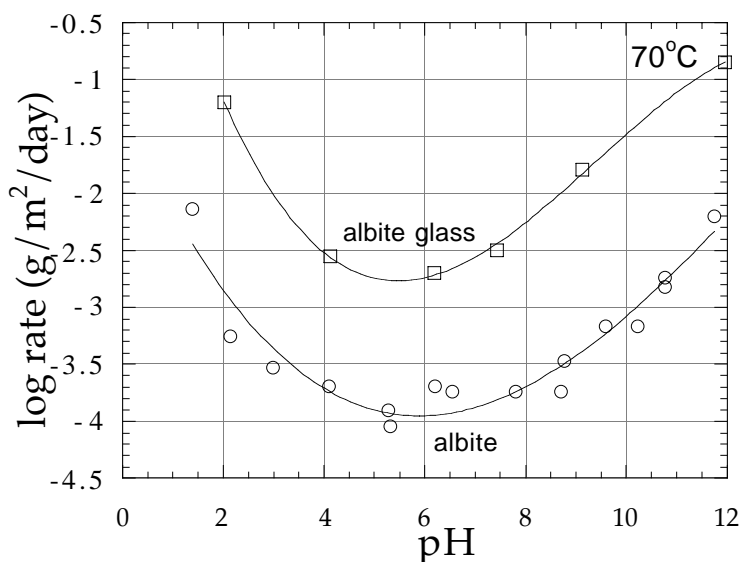


**Figure 3.5.2-6 Comparison of dissolution rates of crystalline albite vs. albite glass in flow-through reactor at 70°C (unpublished data) (Bourcier, 1997) [LL980912551021.056; LL981010751021.068; LL981010851021.069]**

#### 3.5.2.5.4 Dissolution Models for Silicate Minerals

Recent work in developing a mechanistic understanding of silicate mineral dissolution has generated dissolution models with specific provisions for the effects of adsorbed surface species on activated complex. From their data on albite dissolution kinetics, Schott and Oelkers (1995) have proposed a model for aluminosilicate mineral dissolution that includes a functional dependency of dissolved Al on dissolution rates of silicate and aluminosilicate minerals. They propose that the dissolution rate for most silicate minerals is rate-limited by a silica-rich, precursor complex. The dissolution rate is proportional to its concentration. An increase in Al in solution increases the number of Al-rich complexes on the surface of aluminosilicate minerals, thereby lowering the dissolution rate by decreasing the

concentration of the silica-rich precursors. Their rate equation, which incorporates this effect, can successfully predict a wide variety of data from several silicate and aluminosilicate minerals.

A similar modeling approach was developed previously by Berger et al. (1994a) for quartz dissolution in solutions containing dissolved lead and sodium. They proposed a surface-complexation model in which changes in dissolution rates are caused by changes induced in the surface structure due to ionic adsorption. Inner sphere complexes generally decrease rate, outer sphere ionic complexes do the opposite, but both effects change in magnitude in response to pH and reaction affinity. The effects become less significant close to saturation because of competition between electrolyte and silica adsorption on the surface.

It is clear that no comprehensive and generally accepted model exists that explains the existing dissolution data for silicates. But the models that have been proposed are converging on a modified rate law formulation that includes the effects of adsorbed species and accounts for their effects on some rate-limiting, precursor complex. Future experimental studies on glass dissolution should focus on experiments that are explicitly designed to test these models (i.e., Gin [1996] and Berger et al. [1994b]).

#### 3.5.2.5.5 Conclusions

Interpretations of experimental data on the dissolution behavior of silicate glasses and silicate minerals indicate the following:

- Simple affinity control (Eq. 3.5.2-1) does not explain the observed dissolution-rate data for silicate minerals or glasses.
- Dissolution rates can be significantly modified by dissolved cations even under conditions far from saturation where the affinity term is near unity.
- The effects of dissolved species such as Al and Si on the dissolution rate vary with pH, temperature, and saturation state.
- As temperature is increased, the effect of pH and temperature on glass and mineral-dissolution rates decrease, which strongly suggests a switch in rate control from surface, reaction-based (affinity control) to diffusion control (Guy and Schott, 1989; Berger et al., 1994b; Vernaz et al., 1988); this is also consistent with the relative magnitudes of their activation energies ( $E_{a \text{ diff}} < E_{a \text{ affinity}}$ ).

Borosilicate glass-dissolution models need to be upgraded to account for these recent experimental observations. Most important of these are the effects of dissolved species that can sorb on the glass surface and either increase or decrease the dissolution rate. The glass model should be based on current dissolution models for aluminosilicate minerals that are based on a modified transition-state theory rate equation, which specifically accounts for the existence and stoichiometry of a rate-limiting precursor complex. The effects of ionic strength and inner and outer sphere surface complexes must be included in a robust model to predict glass-dissolution rates under repository conditions.

The model for glass dissolution must eventually be incorporated into waste form PA codes. These codes do not generally calculate values for all the parameters that will be needed by any rigorous glass-dissolution submodel. Thus, to simplify submodels of these complex models are needed for inclusion in the PA codes.

### 3.5.2.6 References

- Aagaard, P., and H.C. Helgeson (1982). "Thermodynamic and kinetic constraints on reaction rates among minerals and aqueous solutions I. Theoretical considerations." *Am. J. Sci.* **282**:237–285. [HQS.19880517.2373]
- Abrajano, T., J.K. Bates, W.L. Ebert, and T. Gerding (1986). *The effect of gamma radiation on groundwater chemistry and glass leaching as related to the NNWSI repository site.* (SANL-510-001) Argonne, IL: Argonne National Laboratory. [202939]
- Abrajano, T.A., and J.K. Bates (1987). "Transport and reaction kinetics at the glass:solution interface region: results of repository-oriented leaching experiments." In proceedings from Materials Research Society Symposium. **84**:533–546. [NNA.19900620.0006]
- Abrajano, T.A., J.K. Bates, A.K. Woodland, J.K. Bradley, and W.L. Bourcier (1990). "Secondary phase formation during nuclear waste-glass dissolution." *Clays and Clay Min.* **38**(5):537–548. [NNA.19910903.0114]
- Advocat, T., J.L. Crovisier, B. Fritz, and E. Vernaz (1990). "Thermokinetic model of borosilicate glass dissolution: contextual affinity." In proceedings from Materials Research Society Symposium. **176**:241–248.
- Advocat, T., J.L. Crovisier, E. Vernaz, G. Ehret, and H. Charpertier (1991). "Hydrolysis of R7T7 nuclear waste glass in dilute media: Mechanisms and rate as a function of pH." In proceedings from Materials Research Society Symposium. **212**:57–64.
- Andriambololona, Z., N. Godon, and E. Vernaz (1992). "R7T7 glass alteration in the presence of mortar: Effect of the cement grade." In proceedings from Materials Research Society Symposium. **257**:151–158.
- Barkatt, A., A. Olszowka, W. Sousanpour, M.A. Adel-Hadadi, R. Adiga, A. Barkatt, G.S. Marbury, and S. Li (1991). "Leach rate excursions in borosilicate glasses: effects of glass and leachant composition." In proceedings from Materials Research Society Symposium. **212**:65–76.
- Barkatt, A., E.E. Saad, R. Adiga, W. Sousanpour, A. Barkatt, and M.A. Adel-Hadadi (1989). "Leaching of natural and nuclear waste glasses in sea water." *Appl. Geochem.* **4**:593–603. [NNA.19910424.0078]
- Bart, G., H.U. Zwicky, E.T. Aerne, T. Graber, D.Z. Berg, and M. Tokiwai (1987). "Borosilicate glass corrosion in the presence of steel corrosion products." In proceedings from Materials Research Society Symposium. **84**:459–470.
- Berger, G., E. Cadore, J. Schott, and P. Dove (1994a). "Dissolution of quartz in lead and sodium chloride solutions between 25 and 300°C: Effect of the nature of surface complexes and reaction affinity." *Geochim. Cosmochim. Acta* **58**(2):541–551.
- Berger, G., C. Claparols, C. Guy, and V. Daux (1994b). "Dissolution of a basalt in silica-rich solutions: Implications for long-term alteration." *Geochim. Cosmochim. Acta* **58**(22):4875–4886.
- Bibler, N.E., and C.M. Jantzen (1987). "Materials interactions relating to long-term geologic disposal of nuclear waste glass." In proceeding from Materials Research Society Symposia. **84**:47–66. [NNA.19900125.0016]

- Bourcier, W.L. (1990) *Geochemical modeling of radioactive waste glass dissolution using EQ3/6: Preliminary results and data needs*. (UCID-21869) Livermore, CA: Lawrence Livermore National Laboratory. [NNA.19900501.0161]
- Bourcier, W.L. (1997). "Affinity Functions for Modeling Glass Dissolution Rates." In proceedings from CEA-Valrho Summer Workshop. Méjannes-le-Clap, France: August 31–September 7, 1997. Also UCRL-JC-131186 for Lawrence Livermore National Laboratory, Livermore, CA. [MOL.19980109.0260]
- Bourcier, W.L., W.L. Ebert, and X. Feng (1993). "Modeling surface area to volume effects on borosilicate glass dissolution." In proceedings from Materials Research Society Symposium. **294**:577–582.
- Bourcier, W.L., S.A. Carroll, and B.L. Phillips (1994). "Constraints on the affinity term for modeling long-term glass-dissolution rates." In proceedings from Mat. Res. Soc. Symp. **333**:507–512. Also UCRL-JC-116132 for Lawrence Livermore National Laboratory. [NNA.19940516.0093]
- Bourcier, W.L., D. Peiffer, K. Knauss, K. McKeegan, and D. Smith (1990). "A kinetic model for borosilicate glass dissolution based on the dissolution affinity of a surface alteration layer." In proceedings from Scientific Basis for Nuclear Waste Management XIII. Materials Research Society. **176**:209–216. [NNA.19900522.0148]
- Bourcier, W.L., H.C. Weed, S.N. Nguyen, J.K. Nielsen, L. Morgan, L. Newton, and K.G. Knauss (1992). "Solution compositional effects on dissolution kinetics of borosilicate glass." In proceedings from Seventh Annual Water-Rock Conference. p. 81–84.
- Bruton, C.. (1988). "Geochemical simulation of dissolution of West Valley and DWPF glasses in J-13 water at 90°C." In proceedings from Materials Research Society Symposium. **112**:607–619. Also UCRL-96703 for Lawrence Livermore National Laboratory, Livermore, CA. [NNA.19891026.0021]
- Buckwalter, C.Q., and L.R. Pederson (1982). "Inhibition of nuclear waste glass leaching by chemisorption." *J. Am. Cer. Soc.* **65**:431–436.
- Bunker, B.C., and G.W. Arnold (1983). "The effect of solution pH and ion concentrations on leaching of silicate glass." In proceedings from Materials Research Society Symposium. **15**:151–158. [NNA.19900306.0045]
- Bunker, B.C., D.R. Tallant, T.J. Headley, G.L. Turner, and R.J. Kirkpatrick (1988). "The structure of leached sodium borosilicate glass." *Phys. Chem. of Glasses* **29**:106–120. [NNA.19900215.0017]
- Burch, T.E., K.L. Nagy, and A.C. Lasaga (1992). "Free energy dependence of albite dissolution kinetics at 80°C, pH 8.8." *Chem. Geol.* **105**:137–162. [MOL.19980316.0161]
- Burns, D.B., B.H. Upton, G.G. Wicks (1986). "Interactions of SRP waste glass with potential canister and overpack metals." *J. Noncryst. Solids*. **84**:258–267.
- Casey W. H., H. R. Westrich, and G. W. Arnold (1988). "Surface chemistry of labradorite feldspar reacted with aqueous solution at pH=2, 3 and 12." *Geochim. Cosmochim. Acta* **52**:2795–2807. [NNA.19930105.0003]

- Chick, L.A., and L.R. Pederson (1984). "The relationship between layer thickness and leach rate for nuclear waste glasses." In proceedings from Materials Research Society Symposium. **26**:635–642. [HQZ.19870131.6438]
- Curti, E. (1991). *Modelling the dissolution of borosilicate glasses for radioactive waste disposal with the PHREEQE/GLASSOL code: theory and practice*. Würenlingen, Germany: Paul Scherrer Institute.
- Delage, F., D. Ghaleb, J.L. Dussossoy, O. Chevallier, and E. Vernaz (1992). "A mechanistic model for understanding nuclear waste." *J. Nucl. Mat.* **90**:191–197.
- Devidal, J.L., J.L. Dandurand, and J. Schott (1992). "Dissolution and precipitation kinetics of kaolinite as a function of chemical affinity (T = 150°C, pH = 2 and 7.8)." *Water-Rock Interaction*. Y. K. Kharaka and A. S. Maest (Eds.) Rotterdam, The Netherlands: Balkema. p. 93–96.
- Dove, P.M., and S.F. Elston (1992). "Dissolution kinetics of quartz in sodium chloride solutions: Analysis of existing data and a rate model for 25°C." *Geochim. Cosmochim. Acta* **56**:4147–4156. [235345]
- Ebert, W.L., J.K. Bates, E.C. Buck, and C.R. Bradley (1993). "Accelerated glass reaction under PCT conditions." In proceedings from Materials Research Society Symposium. **294**:569–576.
- Feng, X., and A. Barkatt (1987). "Effects of aqueous phase composition on the leach behavior of nuclear waste glasses." In proceedings from Materials Research Society Symposia. **84**:519–531. [NNA.19900215.0027]
- Gin, S. (1996). "Control of R7T7 nuclear glass alteration kinetics under saturation conditions." In proceedings from Materials Research Society Symposium. **412**:189–196.
- Godon, N., E. Vernaz, J.H. Thomassin., and J.C. Touray (1989). "Effect of environmental materials on aqueous corrosion of R7T7 glass." In proceedings from Materials Research Society Symposium. **127**:97–104.
- Grambow, B. (1984). "Ein physikalische-chemisches Modell für den Mechanismus der laskorrosion—unetr besonderer Berücksichtigung simulierter radioaktiver Abfallgläser." Ph.D. thesis. Berlin, Germany: Freien Universität Berlin. [225985]
- Grambow, B. (1987). Nuclear waste glass dissolution: Mechanism, model and application. (87-02) Stockholm, Sweden: JSS Project, Swedish Nuclear Fuel and Waste Management Co. [NNA.19900215.0035]
- Grambow, B., W. Lutze, and R. Müller (1992). "Empirical dissolution rate law for the glass R7T7 contacting halite- and silica-saturated brines." In proceedings from Materials Research Society Symposium. **257**:143–150.
- Grambow, B., and D. Strachan (1983). "Leach testing of waste glasses under near-saturation conditions." In proceedings from Materials Research Society Symposium. **26**:623–634. [NNA.19870406.0329]
- Grambow, B., and D.M. Strachan (1988). *A comparison of the performance of nuclear waste glasses by modeling*. (PNL-6698) Richland, WA: Pacific Northwest Laboratory. [NNA.199000215.0036]

- Grambow, B., H.U. Zwicky, G. Bart, I.K. Björner, and L.O. Werme (1986). "Modeling the effect of iron corrosion products on nuclear glass performance." In proceedings from Materials Research Society Symposium. **84**:471–481. [HWS.19880517.2449]
- Guy, C., and J. Schott (1989). "Multisite surface reaction versus transport control during hydrolysis of a complex oxide." *Chem. Geol.* **78**:181–204.
- Hayes, K.F. (1987). "Equilibrium, spectroscopic, and kinetic studies of ion adsorption at the oxide/aqueous interface." Ph.D. thesis. Stanford, CA: Stanford University. [223485]
- Hellmann, R., C.M. Eggleston, M.F. Hochella, and D.A. Crerar (1990). "The formation of leached layers on albite surfaces during dissolution under hydrothermal conditions." *Geochim. Cosmochim. Acta* **54**:1267–1281.
- Hermansson H.P., H. Christensen, I.K. Björner, L. Werme, and D.E. Clark (1985). "Variables affecting the leaching of Swedish nuclear waste glasses. *Nucl. Chem. Waste Manag.* **5**:315–332.
- Inagaki Y., A. Ogata, H. Furuya, K. Idemitsu, T. Banba, and T. Maeda (1996). "Effects of redox condition on waste glass corrosion in the presence of magnetite." In proceedings from Materials Research Society Symposium. **412**:257–264.
- Jantzen, C.M. (1992). "Thermodynamic approach to glass corrosion." *Corrosion of Glass, Ceramics, and Ceramic Superconductors*. D. E. Clark and B. K. Zoitos (Eds.) Park Ridge, NJ: Noyes Publications. p. 153-215.
- Jantzen, C.M., and M.J. Plodinec (1984). "Thermodynamic model of natural, medieval, and nuclear waste glass durability." *J. Non-Crys. Solids*. **67**:207–223. [NNA.19900215.0045]
- Jørgensen, S.S. (1968). "Solubility and dissolution kinetics of precipitated amorphous silica in 1 M NaClO<sub>4</sub> at 25°C." *Acta Chem. Scand.* **22**:335–341.
- Klein, L.C. (1986). "Natural glasses in Howardites and Chondrites (Meteorites)." *Advances in Ceramics*, Vol. 20. Westerville, OH: American Ceramic Society. pp. 693–698.
- Knauss, K.G., W.L. Bourcier, K.D. McKeegan, C. Merzbacher, S.N. Nguyen, F.J. Ryerson, D.K. Smith, H.C. Weed, and L. Newton (1990). Dissolution kinetics of a simple analogue nuclear waste glass as a function of pH, time, and temperature. In proceedings from Materials Research Society Symposium. **176**:371–381. Also UCRL-101112 for Lawrence Livermore National Laboratory, Livermore, CA. [NNA.19900320.0195]
- Lanza, F., A. Manara, L. Mammarella, P. Blasi, and G. Ceccone (1988). "Borosilicate HLW glass leaching in silica-saturated solution. In proceedings from Materials Research Society Symposium. **112**:685–691. [NNA.19900306.0091]
- Lasaga, A.C. (1984). "Chemical kinetics of water-rock interactions." *J. Geophys. Res.* **89**(B6):4009–4025. [NNA.1990216.0060; NNA.19921103.0016]
- Lee, C.T., and D.E. Clark (1986). "Effects of solution cations on waste glass leaching." *Advances in Ceramics*, Volume 20. Westerville, OH: American Ceramic Society. pp. 541-550.



- Lehman, R.L., and F.A. Kuchinski (1985). "The effect of various lead species on the leaching behavior of borosilicate waste glass." In proceedings from Materials Research Society Symposium. **44**:179–186.
- McVay, G.L., and C.Q. Buckwalter (1983). "Effect of iron on waste-glass leaching." *J. Amer. Ceram. Soc.* **66**(3):170–174. [NNA.19900306.0097]
- Mendel, J.E. (1984). *Final Report on the Defense High Level Waste Leaching Mechanisms Program*. (PNL-5157) Richland, WA: Pacific Northwest Laboratory. [HQS.19880517.2498]
- Michaux, L., E. Mouche, and J.C. Petit. (1992). "Geochemical modeling of the long-term dissolution behavior of the French nuclear glass R7T7." *Appl. Geochem.* **1**(Special Issue):41–54.
- Murakami, T., R.C. Ewing, and B.C. Bunke (1988). "Analytical electron microscopy of leached layers on synthetic basalt glass." In proceedings from Materials Research Society Symposium. **112**:737–748. [NNA.19900306.0106]
- Nagy, K.L., A.E. Blum, and A.C. Lasaga (1991). "Dissolution and precipitation kinetics of kaolinite at 80°C and pH 3: the dependence on solution saturation state." *Amer. J. Sci.* **291**:649–686. [MOL.19980429.0735]
- Oelkers, E.H., J. Schott, and J.-L. Devidal. (1994). "The effect of aluminum, pH, and chemical affinity on the rates of aluminosilicate dissolution reactions." *Geochim. Cosmochim. Acta* **58**(9):2011–2024. [236030]
- Oka, Y., K.S. Ricker, and M. Tomozawa (1979). "Calcium deposition on glass surface as an inhibitor to alkaline attack." *J. Am. Cer. Soc.* **62**:631–632.
- Oversby, V.M., and D.L. Phinney (1992). "The development of surface alteration layers on SRL-165 nuclear waste glasses." *J. Nucl. Mat.* **190**:247–268.
- Palmer, H.C., K. Tazaki, W.S. Fyfe, and Z. Zhou (1988). "Precambrian Glass." *Geol.* **16**:221–224. [NNA.19900215.0061]
- Patyn, J., P. Van Iseghem, and W. Timmermans (1990). "The long-term corrosion and modeling of two simulated Belgian reference high-level waste glasses—Part II." In proceedings from Materials Research Society Symposium. **176**:299–307.
- Petit, J.C., J.C. Dran, G. Della Mea, and A. Paccagnella (1989). "Dissolution mechanisms of silicate minerals yielded by intercomparison with glasses and radiation damage studies." *Chem. Geol.* **78**:219–227.
- Petit, J.C., M.C. Magonthier, J.C. Dran, and G. Della Mea (1990). "Long-term dissolution rate of nuclear glasses in confined environments: Does a residual chemical affinity exist?" *J. Mat. Sci.* **25**:3048–3052.
- Phillips, B.L. (1993). "Preliminary NMR investigation of sodium borosilicate and analogue SRL waste glasses." *ANL Technical Support Program for DOE Environmental Restoration and Waste Management. Annual Report October 1991–September 1992*. (ANL-93/13) J. K. Bates (Ed.) Argonne, IL: Argonne National Laboratory. pp. 153–164. [NNA.19930907.0056]
- Plodinec, M.J., C.M. Jantzen, and G.G. Wicks (1984). "Stability of radioactive waste glasses assessed from hydration thermodynamics." In proceedings from Materials Research Society Symposium. **26**:755–762. [NNA.199090215.0065]

- Sang, J.C., A. Barkatt, I.G. Talmy, and M.K. Norr (1993). "Increases in leach rate due to possible cracking in silicate glasses." In proceedings from Materials Research Society Symposium. **294**:583–589.
- Sang, J.C., Y., Guo, A. Barkatt, M.A. Adel-Hadadi, G.S. Marbury, and A.A. Barkatt (1994). "Dissolution mechanism of soda-lime silicate glass and of PNL 76-68 in the presence of dissolved Mg." In proceedings from Materials Research Society Symposium. **333**:519–524.
- Schott, J., and E.H. Oelkers (1995). "Dissolution and crystallization rates of silicate minerals as a function of chemical affinity." *Pure and Appl. Chem.* **67**(6):903–910.
- Steeffel, C.I., and P. Van Cappellen (1990). "A new kinetic approach to modeling water-rock interaction: The role of nucleation, precursors, and Ostwald ripening." *Geochim. Cosmochim. Acta* **54**:2657–2677.
- Strachan, D.M., W.L. Bourcier, and B.P. McGrail (1994). Toward a consistent model for glass dissolution." *Radioactive Waste Management and Environmental Restoration* **19**:129–145. [MOL.19960716.0118]
- Strachan, D.M., B.P. McGrail, M.J. Apted, D.W. Engel, and P.W. Eslinger (1990). *Preliminary assessment of the controlled release of radionuclides from waste packages containing borosilicate waste glass*. (PNL-7591) Richland, WA: Pacific Northwest Laboratory. [NNA.19900116.0029]
- Tait, J.C., and C.D. Jensen (1982). "The effect of Zn(II) ion adsorption on the durability of sodium borosilicate glasses." *J. Non-Cryst. Solids.* **49**:363–377.
- Trotignon, L. (1990). "Aqueous corrosion of borosilicate glasses: Nature and properties of alteration layers." Ph.D. thesis. Toulouse, France: Paul Sabatier University.
- Van Iseghem, P., T. Amaya, Y. Suzuki, and H. Yamamoto (1992). "The role of Al<sub>2</sub>O<sub>3</sub> in the long-term corrosion stability of nuclear waste glasses." *J. Nucl. Mat.* **190**:269–276.
- Vernaz, E.Y., J.L. and Dussossoy (1992). "Current state of knowledge of nuclear waste glass corrosion mechanisms: the case of R7T7 glass." *Appl. Geochem.* **1**(Special Issue):13–22.
- Vernaz, E.Y., J.L. Dussossoy, and S. Fillet (1988). "Temperature dependence of R7T7 nuclear waste glass alteration mechanism." In proceedings from Materials Research Society Symposium. **112**:555–563. [NNA.19900306.0125]
- Zwicky, H.U., T. Graber, R. Grauer, and R. Restani (1992). "Cationic corrosion inhibitors for alkali borosilicate glass." In proceedings from Materials Research Society Symposium. **257**:83–90.

## **3.6 Other Release Sources of Radionuclides**

### 3.6.1 Crud

The corrosion products in the coolant of a power reactor form an activated radionuclide subset which, when deposited on the surfaces of a spent fuel assembly, are termed "crud." In reference (1), the crud subset of radionuclides with their specific surface activity was provided as "worst case" estimates for PWR and BWR assemblies; these were estimated irrespective of fuel manufacturer, handling of assemblies, reactor zone, axial location, and burnup. Table I below combines crud data from reference (1) and their half-life data from reference (2). Crud composition and structure are described extensively in reference (2) and summarized in reference (1) as being of two types:

- a) A fluffy, easily removed crud found usually on BWR rods and is composed mainly of hematite ( $\text{Fe}_2\text{O}_3$ )
- b) A tenacious, tightly bound crud found usually on PWR and is composed mainly of a nickel-substituted spinel ( $\text{Ni}_x\text{Fe}_{3-x}\text{O}_4$  with  $x \approx 1$ ).

**Table 3.6.1-1**

Nuclide	Half-life (days)	Crude Activity Density $\mu\text{Ci}/\text{cm}^2$ (reactor shutdown)	
		PWR Fuel	BWR Fuel
$^{51}\text{Cr}$	28	391	35
$^{54}\text{Mn}$	312	380	635
$^{58}\text{Co}$	71	1400	63
$^{59}\text{Fe}$	45	300	87
$^{60}\text{Co}$	1924	140	1250
$^{65}\text{Zn}$	244	N/A	56
$^{95}\text{Zr}$	65	36	30

Because of the relatively short half-lives of the crud radionuclides, the release of crud appears as a potential problem primarily during transportation (Ref. 1 and 2) and preclosure radiological design of repository facilities (Ref. 3). From Table I, the longest half-life is ~5.3 yr for the crud radionuclide  $^{60}\text{Co}$ , which at the end of 1,000 years would have an activity decay multiplier of  $1.6 \times 10^{-57}$ . Thus, the total activity of crud inventory would be small at 1,000 years, even though there exist several square miles of assembly surface (1 sq. mile  $\sim 2.6 \times 10^{10} \text{ cm}^2$ ).

### References

1. R.P. Sandoval, R.E. Einziger, H. Jordan, A.P. Malinauskas, and W.J. Mings, "Estimate of the CRUD Contribution to Shipping Cask Containment Requirements," *Nucl. Tech.*, **98**, 196 (1992).
2. R.P. Sandoval, R.E. Einziger, H. Jordan, A.P. Malinauskas, and W.J. Mings, "Estimate of the CRUD Contribution to Shipping Cask Containment Requirements," SAND88-1358, TCC-0811, Sandia National Laboratories (Jan. 1991).

3. L.J. Jardine, "Preclosure Radiological Safety Analysis for Normal Conditions of the Yucca Mountain Repository," SLTR87-7013, Sandia National Laboratories (April, 1988).

## Conclusions and Recommendations

Data indicating the fraction of crud that might be removed from rods and/or assemblies under varying accident conditions is very limited. Data pertaining to the particle sizes of crud released under varying conditions is also limited. The transport characteristics of the released crud and the respirable fraction that may be of danger to man is therefore not well defined. Despite these limitations, using the available data, the following six conclusions have been reached.

1. The dose evaluation contained in Section 3.3.1 indicate that even if the maximum crud density for BWR fuel is used, the total effective dose equivalent at 1.5 km is 0.48 rem. This is based on the conservative assumptions that the total crud on a BWR assembly is released in a respirable form, and no reduction in the dose occurs during transport of the crud to the site boundary of 5 km. Using the maximum crud density for this estimate is also conservative since there are only a dozen comprehensive measurements of crud characteristics that show discernible amounts of crud, and hundreds of qualitative visual observations of the rods that indicate little or no crud on the rods. That is, the probability is apparently very small of having an incident that would cause a release when handling an assembly in which all rods contain the maximum amount of crud previously observed.
2. Repository operational personnel under normal operations should not be directly exposed to crud. If there are situations in which there might be direct exposures, the personnel involved would probably also be exposed to other stronger sources of radioactivity, such as the fuel material itself. Tables 21 and 22 show that exposure to the maximum amount of crud from one PWR or one BWR rod would provide a radiation exposure of 0.2 R/hr or 2.5 R/hr, respectively. This is much smaller than the dose one would receive from the fuel. It is therefore hard to postulate circumstances where crud would have more than a relatively very marginal effect on the total dose to repository personnel compared to the dose they would receive from the fuel.
3. The data available on crud characteristics is from a small fraction of the total number of irradiated fuel rods. The data in many cases is from rods selected for some reason for additional study. Therefore, the data is probably not representative of "typical" fuel, but probably does provide a conservative estimate for the maximum probable crud amounts.
4. The control of contamination within the reactor cooling system has been studied and methods have been implemented to mitigate the phenomenon. These efforts will cause a decrease in the amount of crud formation on fuel rods and assemblies irradiated in this new operating environment. Therefore, risk calculations using crud characteristic from existing fuel should provide upper bounds on the risk to be associated with fuel irradiated in the future.
5. Crud will spall from bare fuel rods that are being mechanically stressed when being unloaded/loaded into containers or, in particular, while being consolidated. The amount of crud that will spall is not known. This spalled crud will cause contamination in the areas where and when such mechanical processes occur. This

may be expected when removing rods that contain excessive crud from assemblies during the consolidation process. It might be prudent to have a repository procedure such that if observations indicate excessive crud on rods in a particular fuel assembly, that assembly is stored as received, without consolidation. Repository planning has already made provisions for storing unconsolidated assemblies that contain rods with other abnormal conditions. Such a course would decrease crud contamination in the hot cell areas and might provide operational cost savings.

6. Filtration of airborne crud in the hot cells may result in accumulation of crud in the HEPA filters, thus decreasing filter life. The total radiation exposure of operational personnel may be increased due to filtration changes.

### 3.6.2 Hardware

---

### 3.6.2 Hardware

See Section 2.2.2.5

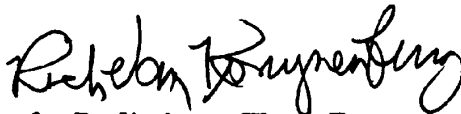
## 3.6.3 Cladding

Interdepartmental letterhead

Mail Station L-352

**CHEMISTRY & MATERIALS SCIENCE DEPARTMENT**

Ext: 2-0456

Corrosion & Electrochemical Processes Section  
Materials Division**MEMORANDUM** - January 23, 1991  
91-02RVKm**TO:** Ray Stout, L-201**FROM:** Rich Van Konynenburg**SUBJECT:** *Carbon-14 Information for Preliminary Waste Form  
Characteristics Document*

In response to your request, here is some information about carbon-14 associated with spent fuel:

According to my current best estimates, the inventory of carbon-14 in spent fuel is as follows:

**BWR**Total:  $3.71 \times 10^{-5} \frac{\text{curies per MTIHM}}{\text{MWd/MTIHM}}$ Zircaloy only:  $1.38 \times 10^{-5} \frac{\text{curies per MTIHM}}{\text{MWd/MTIHM}}$ 

(Nearly half of the BWR zircaloy inventory is in the fuel channel.)

**PWR**Total:  $3.03 \times 10^{-5} \frac{\text{curies per MTIHM}}{\text{MWd/MTIHM}}$ Zircaloy only:  $5.45 \times 10^{-6} \frac{\text{curies per MTIHM}}{\text{MWd/MTIHM}}$ 

Based on the work of Smith and Baldwin, as much as 2% of the total spent fuel <sup>14</sup>C inventory can be released at 350°C in air in 8 hours.

According to recent work in Germany (D. Kopp and H. Münzel, "Release of Volatile Carbon-14 Containing Products from Zircaloy," *J. Nucl. Mater.* 173, 1-6 (1990), oxygen is necessary for volatile <sup>14</sup>C release to occur.

To be conservative, one could assume that sufficient oxygen would be present in the argon fill gas in a waste container to bring about release of the entire 2% of the inventory into the fill gas prior to breach of the container.

RVK:mlm

**Distribution**

Author File

Ballou, L.

L-206

Clarke, W.

L-352



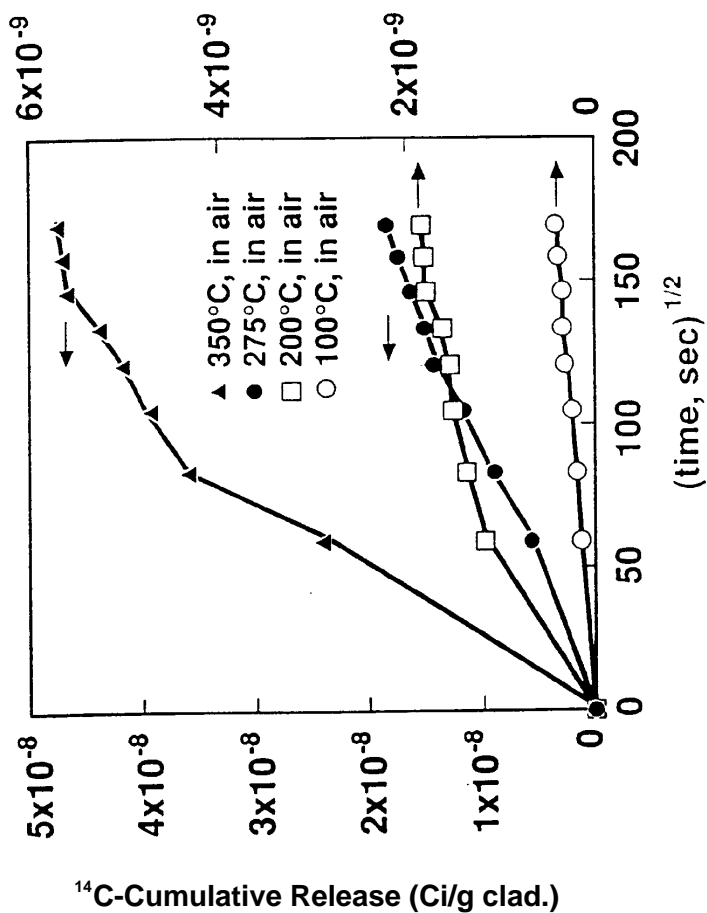


Figure 3.6.3-1 Constant temperature tests, thick oxide (from Harry D. Smith, "Spent Fuel Cladding Degradation," presented to the Nuclear Waste Technical Review Board, August, 1990)

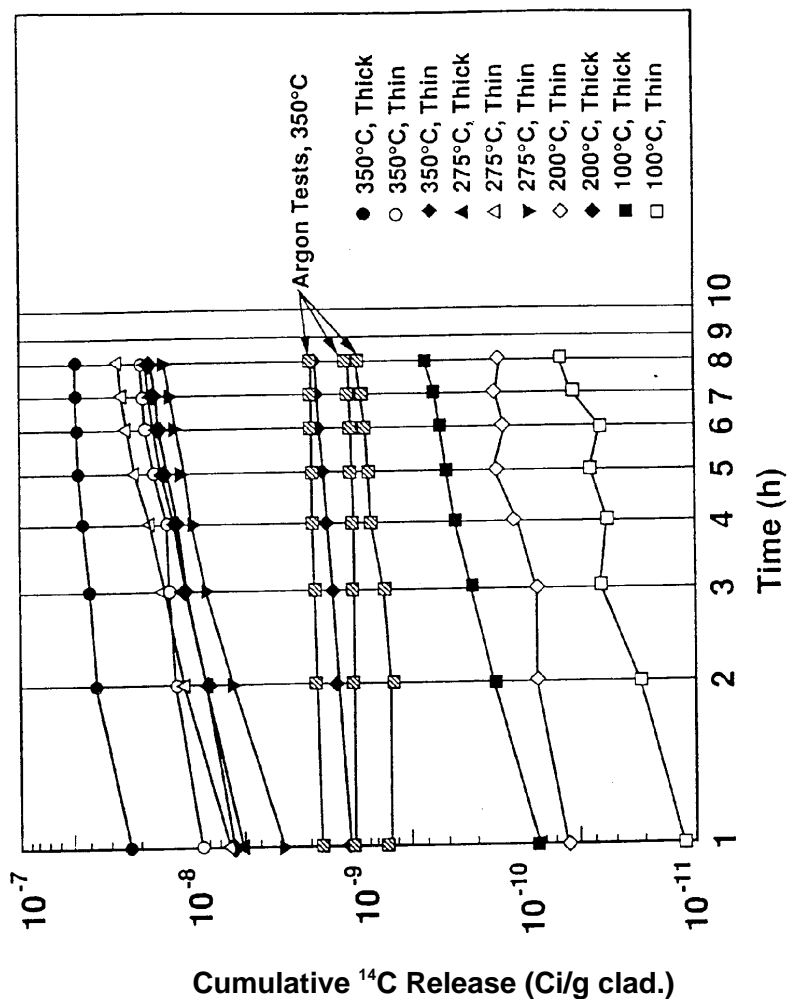


Figure 3.6.3-2 Observed  $^{14}\text{C}$  Release from Zircaloy-4 spent fuel cladding (from Harry D. Smith, "Spent Fuel Cladding Degradation," presented to the Nuclear Waste Technical Review Board, August, 1990)